VIENNA, 2012

ATOMIC AND PLASMA–MATERIAL INTERACTION DATA FOR FUSION

VOLUME 15

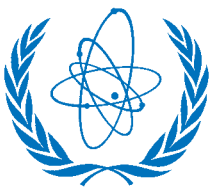

IAEA
International Atomic Energy Agency

The following States are Members of the International Atomic Energy Agency:

AFGHANISTAN
ALBANIA
ALGERIA
ANGOLA
ARGENTINA
ARMENIA
AUSTRALIA
AUSTRIA
AZERBAIJAN
BAHRAIN
BANGLADESH
BELARUS
BELGIUM
BELIZE
BENIN
BOLIVIA
BOSNIA AND HERZEGOVINA
BOTSWANA
BRAZIL
BULGARIA
BURKINA FASO
BURUNDI
CAMBODIA
CAMEROON
CANADA
CENTRAL AFRICAN REPUBLIC
CHAD
CHILE
CHINA
COLOMBIA
CONGO
COSTA RICA
CÔTE D'IVOIRE
CROATIA
CUBA
CYPRUS
CZECH REPUBLIC
DEMOCRATIC REPUBLIC OF THE CONGO
DENMARK
DOMINICA
DOMINICAN REPUBLIC
ECUADOR
EGYPT
EL SALVADOR
ERITREA
ESTONIA
ETHIOPIA
FINLAND
FRANCE
GABON
GEORGIA
GERMANY
GHANA
GREECE
GUATEMALA
HAITI
HOLY SEE
HONDURAS
HUNGARY
ICELAND
INDIA
INDONESIA
IRAN, ISLAMIC REPUBLIC OF
IRAQ
IRELAND
ISRAEL
ITALY
JAMAICA
JAPAN
JORDAN
KAZAKHSTAN
KENYA
KOREA, REPUBLIC OF
KUWAIT
KYRGYZSTAN
LAO PEOPLE'S DEMOCRATIC REPUBLIC
LATVIA
LEBANON
LESOTHO
LIBERIA
LIBYA
LIECHTENSTEIN
LITHUANIA
LUXEMBOURG
MADAGASCAR
MALAWI
MALAYSIA
MALI
MALTA
MARSHALL ISLANDS
MAURITANIA
MAURITIUS
MEXICO
MONACO
MONGOLIA
MONTENEGRO
MOROCCO
MOZAMBIQUE
MYANMAR
NAMIBIA
NEPAL
NETHERLANDS
NEW ZEALAND
NICARAGUA
NIGER
NIGERIA
NORWAY
OMAN
PAKISTAN
PALAU
PANAMA
PAPUA NEW GUINEA
PARAGUAY
PERU
PHILIPPINES
POLAND
PORTUGAL
QATAR
REPUBLIC OF MOLDOVA
ROMANIA
RUSSIAN FEDERATION
SAUDI ARABIA
SENEGAL
SERBIA
SEYCHELLES
SIERRA LEONE
SINGAPORE
SLOVAKIA
SLOVENIA
SOUTH AFRICA
SPAIN
SRI LANKA
SUDAN
SWEDEN
SWITZERLAND
SYRIAN ARAB REPUBLIC
TAJIKISTAN
THAILAND
THE FORMER YUGOSLAV REPUBLIC OF MACEDONIA
TUNISIA
TURKEY
UGANDA
UKRAINE
UNITED ARAB EMIRATES
UNITED KINGDOM OF GREAT BRITAIN AND NORTHERN IRELAND
UNITED REPUBLIC OF TANZANIA
UNITED STATES OF AMERICA
URUGUAY
UZBEKISTAN
VENEZUELA
VIETNAM
YEMEN
ZAMBIA
ZIMBABWE

The Agency's Statute was approved on 23 October 1956 by the Conference on the Statute of the IAEA held at United Nations Headquarters, New York; it entered into force on 29 July 1957. The Headquarters of the Agency are situated in Vienna. Its principal objective is "to accelerate and enlarge the contribution of atomic energy to peace, health and prosperity throughout the world''.

ATOMIC AND PLASMA–MATERIAL INTERACTION DATA FOR FUSION

VOLUME 15

INTERNATIONAL ATOMIC ENERGY AGENCY
VIENNA, 2012

The volumes of ATOMIC AND PLASMA–MATERIAL INTERACTION DATA FOR FUSION are published by the International Atomic Energy Agency normally once a year.

For these volumes, papers, letters and reviews are accepted which deal with the following topics:

— Elementary collision processes in fusion plasmas involving photons, electrons, ions, atoms and molecules;
— Collision processes of plasma particles with surfaces of fusion relevant materials;
— Plasma–material interaction phenomena, including the thermophysical response of materials.

Each submitted contribution should contain fusion relevant data and information in either of the above areas. Original contributions should provide new data, using well established methods. Review articles should give a critical analysis or evaluation of a wider range of data. They are normally prepared on the invitation by the Editor or on prior mutual consent. Each submitted contribution is assessed by two independent referees.

Every manuscript submitted must be accompanied by a disclaimer stating that the paper has not been published and is not being considered for publication elsewhere. If no copyright is claimed by the authors, the IAEA automatically owns the copyright of the paper.

Manuscripts and correspondence should be addressed to: The Editor, ATOMIC AND PLASMA–MATERIAL INTERACTION DATA FOR FUSION, International Atomic Energy Agency, Vienna International Centre, PO Box 100, 1400 Vienna, Austria.

Publisher: International Atomic Energy Agency, Vienna International Centre,
PO Box 100, 1400 Vienna, Austria

Editor: B.J. Braams, Division of Physical and Chemical Sciences

COPYRIGHT NOTICE

Marketing and Sales Unit, Publishing Section
International Atomic Energy Agency
Vienna International Centre
PO Box 100
1400 Vienna, Austria
fax: +43 1 2600 29302
tel.: +43 1 2600 22417
email: sales.publications@iaea.org
http://www.iaea.org/books

Printed by the IAEA in Austria
ATOMIC AND PLASMA–MATERIAL INTERACTION DATA FOR FUSION, VOLUME 15
IAEA, VIENNA, 2012
STI/PUB/023/APID/15
ISBN 978–92–0–131410–9
ISSN 1018–5577
Printed by the IAEA in Austria
July 2012

Foreword

Current designs for nuclear fusion reactors call for the use of the hydrogen isotopes deuterium and tritium as the fuel for the energy producing fusion reactions. Deuterium is plentiful in nature, but tritium undergoes radioactive decay with a half-life of 12 years and does not occur naturally. The use of tritium must be carefully controlled due to its cost and radioactivity and there should be strict limits on the tritium inventory in fusion experiments or in a reactor. These concerns led the IAEA to organize a coordinated research project (CRP) on 'Tritium Inventory in Fusion Reactors'. Between 2002 and 2006, this CRP brought together specialists in fusion materials and plasma-material interaction for the exchange of information and coordination of research activities on the interaction of tritium with plasma-facing materials. This volume of Atomic and Plasma-Material Interaction Data for Fusion is an output of that CRP.

The focal point of the present international fusion energy research programme is the ITER proof of principle experimental reactor now under construction at Cadarache, France, in collaboration with China, the European Union, India, Japan, the Republic of Korea, the Russian Federation and the USA. Small amounts of tritium have in the past been introduced into fusion plasma experiments, notably in the Joint European Torus (JET) and in the Princeton TFTR tokamak, but ITER is the first experiment for which it will be necessary to deal with tritium inventory issues on a scale approaching that of a fusion reactor. The research needs for the final design and the safe operation of ITER were therefore foremost in the mind of the CRP participants, and all contributions to this volume are concerned in one way or another with the choice of plasma-facing materials in ITER, with measurements of tritium inventory, or with means to remove tritium from materials.

The IAEA wishes to thank the authors for their contribution to the CRP and for their efforts in the preparation of this volume. The IAEA officers responsible for this volume were R.E.H. Clark and B.J. Braams.

EDITORIAL NOTE

This publication has been prepared from the original material as submitted by the authors. The views expressed do not necessarily reflect those of the IAEA, the governments of the nominating Member States or the nominating organizations.

The use of particular designations of countries or territories does not imply any judgement by the publisher, the IAEA, as to the legal status of such countries or territories, of their authorities and institutions or of the delimitation of their boundaries.

The mention of names of specific companies or products (whether or not indicated as registered) does not imply any intention to infringe proprietary rights, nor should it be construed as an endorsement or recommendation on the part of the IAEA.

The authors are responsible for having obtained the necessary permission for the IAEA to reproduce, translate or use material from sources already protected by copyrights.

Contents

Introduction and Summary

This volume of Atomic and Plasma-Material Interaction Data for Fusion contains contributions from participants in the IAEA Coordinated Research Project (CRP) "Tritium Inventory in Fusion Reactors" (2002–2006). Tritium, like other isotopes of hydrogen, may be absorbed and trapped in materials, for example the vessel wall within which the fusion plasma is confined. The ease with which plasma-facing materials absorb and release tritium and the ease with which trapped tritium can subsequently be purged from the confining vessel are important considerations for the choice of wall materials. Moreover, nuclear licensing of a fusion experiment or a reactor requires verifiable adherence to inventory limits, and therefore it is essential to be able to measure and monitor the tritium concentration in the surface and sub-surface layers of the materials that are exposed to plasma. Following a recommendation of the Atomic and Molecular Data subcommittee of the International Fusion Research Council (IFRC) the present CRP was initiated in order to gather data and to generate new data relevant to the overall inventory of tritium in fusion reactors. Participants in the CRP convened three times for a Research Coordination Meeting (RCM) at which progress was reviewed and future research plans were formulated. These meetings took place 4-6 November 2002, 18-19 October 2004, and 25-27 September 2006. Summary Reports of these RCMs were produced in the INDC(NDS) series and are available on-line through the A+M Data Unit web pages under *http://www-amdis.iaea.org/publications/INDC/* (Reports 0442, 0495 and 0516.) Following the 3rd and final RCM of this CRP the participants produced a joint paper[1] reviewing the work of the CRP and containing recommendations for ITER. The contributions to the present volume were largely produced following that joint paper.

[1] C.H. SKINNER, A.A. HAASZ, V.Kh. ALIMOV, N. BEKRIS, R.A. CAUSEY, R.E.H. CLARK, J.P. COAD, J.W. DAVIS, R.P. DOERNER, M. MAYER, A. PISAREV, J. ROTH, T. TANABE, Recent advances on hydrogen retention in ITER's plasma-facing materials: beryllium, carbon, and tungsten, Fusion Science and Technology **54** (2008) 891-945.

At the conclusion of the CRP, participants agreed that the increase of stored energy and pulse duration in ITER coupled with the lack of experience in contemporary tokamaks with the plasma facing materials proposed for ITER make the choice of these materials arguably the highest risk factor for ITER. The tritium inventory is a major source term in accident scenarios. Erosion and tritium retention properties are decisive factors in the selection of plasma facing materials. Participants concluded that of the proposed ITER wall materials, tungsten demonstrates the lowest tritium-inventory risk. Carbon presents the greatest risk in terms of tritium inventory, and for the use of carbon, tritium removal techniques will have to be applied. Beryllium presents major retention risk through co-deposits in the presence of oxygen, and tritium removal techniques need also to be developed and applied for Be. Limited understanding of possible mixed material effects increases tritium-inventory risks.

The CRP also led to recommendations for further work (see the summary report of the 3rd RCM and C.H. Skinner, et al., *loc. cit.*). It is important to focus more R&D on the effectiveness of tritium removal techniques from Be and BeO co-deposits with carbon and tungsten impurities. The effect of ion- and neutron-induced damage on tritium trapping, permeation, and retention in tungsten needs to be quantified. There is a need for the capability in the ITER design to make a change of materials in the first wall, due to the concern of unacceptable high tritium inventories with current plasma facing materials. ITER should explore the possibility of using high (400°C or more) temperature for tritium removal and for reduction of tritium inventory; and it would be desirable to design a cooled (room temperature) co-deposit collector in the divertor that is heatable to >700°C for subsequent hydrogen release and removal. Finally, techniques of tritium and dust removal should not be pioneered on ITER. Candidate techniques should be validated in contemporary tokamaks, in particular in JET with its ITER-like wall materials.

Deuterium depth profiles in tungsten materials irradiated with low energy D ions

V.Kh. Alimov[1,2], J. Roth[3], S. Lindig[3]

[1] Institute of Physical Chemistry and Electrochemistry, Russian Academy of Sciences, 119991 Moscow, Russian Federation

[2] Tritium Technology Group, Japan Atomic Energy Agency, Tokai, Ibaraki, 319-1195, Japan

[3] Max-Planck-Institut für Plasmaphysik, EURATOM Association, D-85748 Garching, Germany

Abstract

Depth profiles of deuterium trapped in tungsten materials irradiated with low-energy D ions have been measured up to a depth of 7 μm using the D(^{3}He,p)^{4}He nuclear reaction at a ^{3}He energy varied from 0.69 to 4.0 MeV. It was found that D ion irradiation with ion energies well below the displacement threshold modifies the W structure to depths of up to several μm. Plastic deformation of the W matrix caused by deuterium super-saturation within the near-surface layer was considered for the formation of trapping sites for deuterium.

1. Introduction

Due to its favorable physical properties, like low erosion yield and high melting temperature, tungsten (W) is foreseen as plasma-facing material in fusion devices, such as ITER [1]. As plasma-facing material, W will be subject to intense fluxes of energetic deuterium and tritium ions and neutrals. This implantation process leads to concerns about hydrogen isotope inventories after long-term deuterium-tritium plasma exposure. Most of the results on hydrogen isotope retention and recycling for W have been reviewed by Causey and Venhaus [2, 3], and Skinner et al. [4]. However, not much is known about the hydrogen retention in different W materials irradiated with low-energy hydrogen ions and W exposed to low-energy, high flux hydrogen plasma. Available data ([4] and references therein) have shown that the hydrogen isotope retention in W materials for the case of high-flux hydrogen plasma exposure differs from that for ion implantation. Information about the total amount of hydrogen retained in W materials and about hydrogen detrapping energies can be obtained from thermal desorption measurements. However, measurements of hydrogen depth profiles can give detailed information about the depth distribution of defects which are responsible for hydrogen trapping and, therefore, can help to understand the mechanisms of hydrogen-material interactions.

In this paper our data on deuterium concentration in W materials irradiated with low flux D ions and exposed to high flux D plasma are compiled. These data were obtained in the frame of the Coordinated Research Project on "Tritium Inventory in Fusion Reactors" (2003-2006) initiated by the International Atomic Energy Agency. Although many of the data are already published in different articles [5-9], the emphasis here is on the obtained depth profiles of D in W for different material structure and irradiation conditions and the compilation is thought to be useful for the understanding of diffusion and retention processes in the presence of radiation induced traps.

2. Experimental

Four types of W materials were investigated:

(i) Single crystal (SC) tungsten produced by double electron-beam zone melting. The manufacturer, State Institute of Rare Metals (Moscow), quoted the purity as about 99.9 at.% with the main impurities being H (0.02 at.%), C (0.05 at.%) and O (0.05 at.%). The macro-crystallite sizes were in the range of 10-20 mm. The specimens were cut from a W rod by spark cutting and were 0.8-0.9 mm thick. The sample surface was parallel to the (100) crystallographic plane.

(ii) High purity (99.6 at.%) polycrystalline (PC) tungsten, produced by Plansee AG (Reutte, Austria), a reduced-rolled, powder-metallurgy product with principal chemical impurities: O (0.035 at.%),

C (0.046 at.%), N (0.026 at.%), H (0.092 at.%), Fe, Mo, P, Si, Ca, Na (0.178 at.%). The grain sizes were estimated to be in the range of 2-20 μm (coarse-grained W).

(iii) Hot-rolled polycrystalline W manufactured in Russian Federarion, powder-metallurgy product, 99.0 at.% purity. The principal impurities were H (0.03 at.%), C (0.1 at.%), O (0.2 at.%), N (0.1 at.%), and other impurities – Fe, Al, Si, Ni, Mg (0.5 at.%). The samples were cut from the 0.5 mm thick foil by spark cutting. The grain sizes were 2-5 μm (fine-grained W).

These W samples were mechanically and electrochemically polished. After polishing the single-crystalline samples and coarse-grained polycrystalline samples from Plansee, the samples were annealed at 1573 K for 3.5 h in a vacuum chamber with a background pressure of ~2×10^{-4} Pa during annealing.

(iv) Vacuum plasma-sprayed (VPS) tungsten coating with porosity of 8-9%, 500 μm thick, deposited onto isotropic fine-grain graphite EK 98 with ~20 μm-thick rhenium-containing intermediate layer (deposited by the physical vapor deposition technique). The spraying process was carried out in a controlled low-pressure atmosphere with a subsequent thermal treatment at 1573–1673 K for 1 h. The surface roughness of the VPS W coating was $R_a \leq 4$ μm. According to metallographic images, the grain sizes were 0.5-3 μm, whereas the void sizes were 0.1-2 μm [9]. The samples were cut from the divertor tile manufactured by Plansee AG for the ASDEX Upgrade tokamak and their total thicknesses were approximately 1 mm.

The W samples were subjected to D ion irradiation and D plasma exposure. The irradiation with 200 eV and 1.5 keV D ions was performed in a vacuum chamber connected to a high-current ion source [10] at normal ion incidence. The polycrystalline coarse-grained W and VPS W were bombarded with 200 eV D ions at an ion flux of $(3.6\pm0.7) \times 10^{19}$ D $m^{-2}s^{-1}$, whereas the W single crystal was bombarded with 200 eV D ions at an ion flux of $(1.9\pm0.3) \times 10^{18}$ D $m^{-2}s^{-1}$. Irradiation of the polycrystalline coarse-grained W with 1.5 keV D ions was carried out at an ion flux of $(2.8\pm0.6) \times 10^{19}$ D $m^{-2}s^{-1}$. By electron bombardment from the rear, the irradiation temperature could be varied from 323 to 723 K.

The fine-grained W was exposed to a deuterium plasma generated in a planar dc magnetron with a bias of 450 V [7]. Considering that D_2^+ ions dominate in the plasma, the mean energy of D ions was estimated to be approximately 200 eV. The ion flux was determined from ion current measurements to be $(1.0\pm0.2) \times 10^{21}$ D $m^{-2}s^{-1}$. During plasma exposure the sample was heated by the plasma and the sample temperature increased to the steady-state level after 1-2 min. The temperature was modified by varying the heat conductivity between the sample and cathode and was measured by a chromel-alumel thermocouple welded to the front surface of the sample outside the irradiation area.

The deuterium profiles up to a depth of around 7 μm were determined by nuclear reaction analysis (NRA). The D concentration within the near-surface layer (at depths up to about 0.5 μm) was measured by means of the $D(^3He,\alpha)H$ reaction at a ^3He energy of 0.69 MeV, and the α particles were energy-analyzed with a small-angle surface barrier detector at the laboratory scattering angle of 102°. The α spectrum was transformed into a D depth profile using the program SIMNRA [11]. To determine the D concentration at larger depths, an analyzing beam of ^3He ions with energies varied from 0.69 to 4.0 MeV was used. The protons from the $D(^3He,p)^4He$ nuclear reaction were counted using a wide-angle proton detector placed at a scattered angle of 135°. In order to extend the D concentration to depths of several micrometres, the program SIMNRA was used for the deconvolution of the proton yields measured at different ^3He ion energies. A deuterium depth distribution was assumed taking into account the near-surface depth profile obtained from the α particle spectrum, and the proton yield as a function of incident ^3He energy was calculated. The shape of the D depth profile was then varied using an iterative technique until the calculated curve matched the measured proton yields [12].

The D depth profiles in the polycrystalline coarse-grained W sample irradiated with 1.5 keV D ions to a fluence of 5×10^{23} D/m^2 were determined after ion irradiation and after annealing of the sample at fixed temperatures for 10 minutes. The annealing temperature increased with a step of 50 K, and after each complete annealing procedure the D profile was measured.

The surface morphology of the ion-irradiated and plasma-exposed W samples was investigated by a scanning electron microscope (SEM).

3. Results

3.1. W materials irradiated with low flux D ions

The depth at which deuterium is retained in W materials irradiated with 200-1500 eV D ions can be conditionally divided into three zones: (i) the near-surface layer (up to a depth of about 0.2 μm), (ii) a subsurface layer (from about 0.5 to about 6 μm), and (iii) the bulk (> 6 μm).

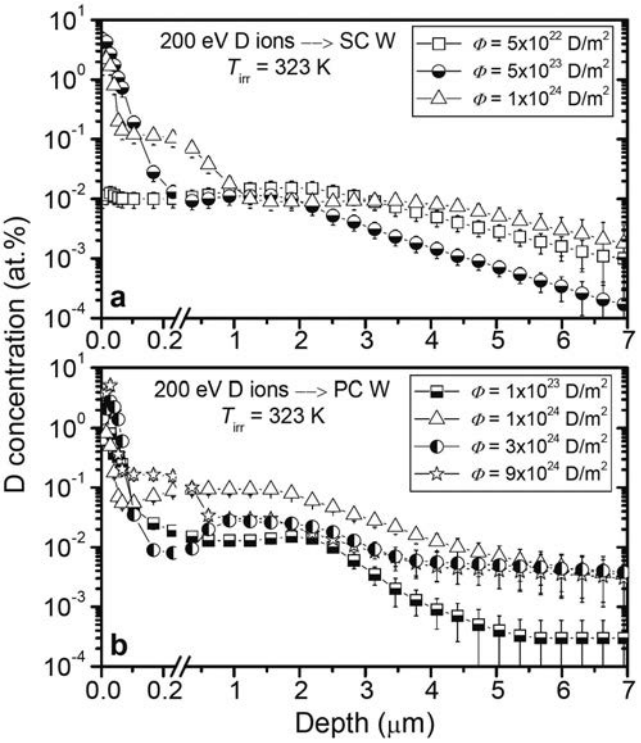

FIG. 1. Depth profiles of deuterium trapped in single crystal W (a) and polycrystalline coarse-grained W (b) irradiated with 200 eV D ions at 323 K to various fluences [5, 6].

In the single crystal W irradiated with 200 eV D ions at 323 K, an increase of the ion fluence, Φ, from 5×10^{22} to 5×10^{23} D/m^2 leads to an increase of the near-surface D concentration by a factor of more than 100, from 0.01 to about 5 at.% (Fig. 1 (a)). The drastic increase of the D concentration can only be explained by a sudden structural change during the low-energy D ion irradiation, providing traps for D retention. The concentration within the sub-surface layer is about 0.01 at.% for all ion fluences used (Fig. 1 (a)), whereas the D concentration in the bulk (at depths beyond 6 μm) is below 10^{-3} at.%.

In the polycrystalline coarse-grained W, the D concentration in the near-surface layer is in the range from 1 to 5 at.% for fluences increasing from 1×10^{23} to 8.9×10^{24} D/m^2 (Fig. 1 (b)). Within the sub-surface layer, as the fluence is increased to 1×10^{24} D/m^2, the D concentration reaches its maximum value of 0.1 at.%. A further fluence increase leads to a decrease in the D concentration to about 0.03 at.%. The D concentration in the bulk increases with the ion fluence and reaches a steady state value of about 3×10^{-3} at.% at $\Phi = 1 \times 10^{24}$ D/m^2 (Fig. 1 (b)).

The release of deuterium from the sub-surface layer of the polycrystalline W may be connected with the appearance of blisters and flaking and accompanying porosity development (Fig. 2). Note that blisters were not observed on single crystal W surfaces irradiated with 200 eV D ions, and the D concentration did not show a release of deuterium with increasing fluence.

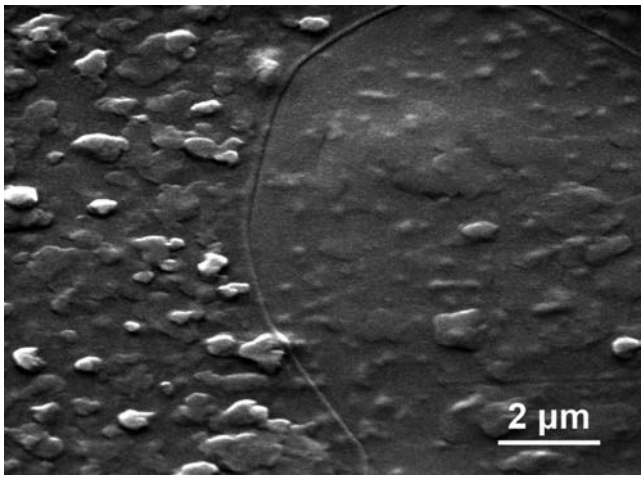

FIG. 2. SEM image of polycrystalline coarse-grained W surface irradiated with 200 eV D ions at 323 K to a fluence of 8.9×10^{24} D/m^2 [5, 6]. The surface was analyzed at a tilt angle of 45 degree.

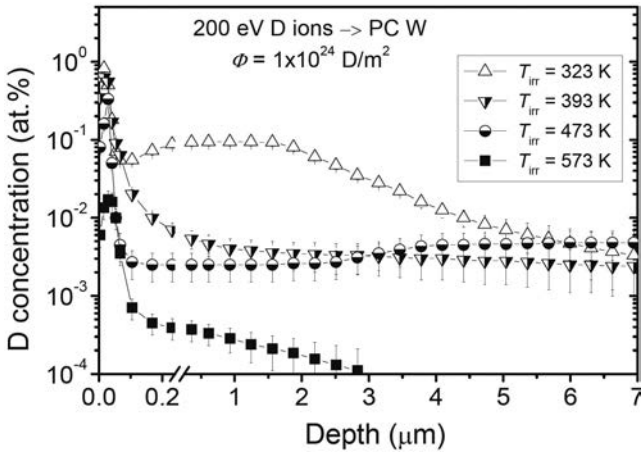

FIG. 3. Depth profiles of deuterium trapped in polycrystalline coarse-grained W irradiated with 200 eV D ions at various temperatures to a fluence of 1×10^{24} D/m^2.

The D depth profiles in the polycrystalline coarse-grained W irradiated with 200 eV D ions to a fluence of 1×10^{24} D/m^2 at irradiation temperatures, T_{irr}, in the range from 323 to 573 K are shown in Fig. 3. The D concentration in the near-surface layer remains unaltered up to T_{irr} = 393 K and then decreases as the irradiation temperature increases. In the sub-surface layer, the D concentration decreases from 0.1 at.% at T_{irr} = 323 K down to about 3×10^{-3} at.% at T_{irr} = 393-473 K (it is notable that this concentration remains practically unchanged within this temperature range). At the irradiation temperature of 573 K, the D concentration at depths of 1-3 μm is $(1\text{-}3) \times 10^{-4}$ at.%. In the bulk, the D concentration is $(3\text{-}5) \times 10^{-3}$ at.% at T_{irr} = 323-473 K and is well below 10^{-4} at.% at T_{irr} = 573 K (Fig. 3).

Irradiation of the polycrystalline coarse-grained W with 200 eV D ions to a fluence of 1×10^{24} D/m^2 at elevated temperatures leads to the formation of blisters on the surface (Fig. 4). The shapes of most blisters are almost spherical-like with sizes ranging from 0.3 to 3 μm depending on the irradiation temperature. As the

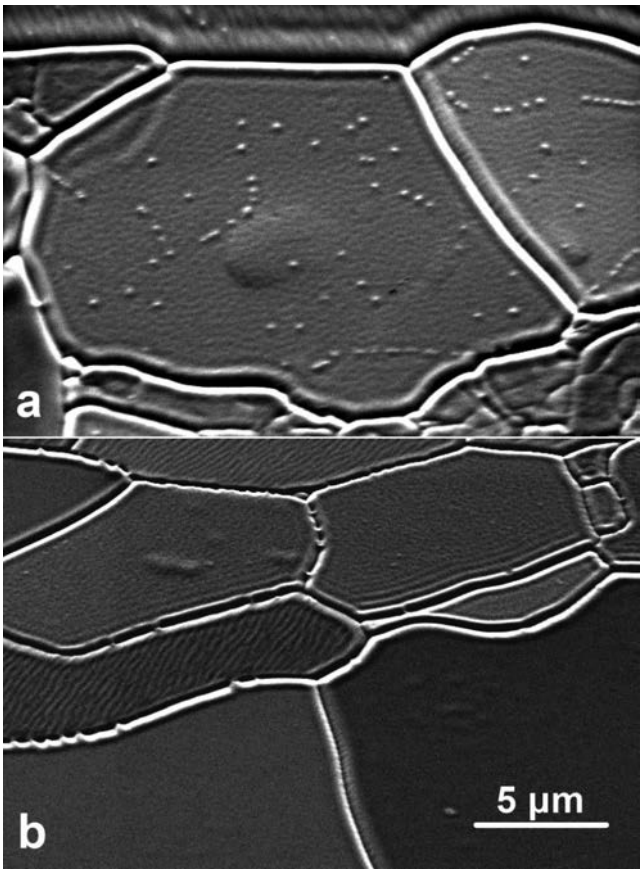

FIG. 4. SEM images of polycrystalline coarse-grained W surface irradiated with 200 eV D ions to a fluence of 1×10^{24} D/m^2 at 323 K (a) and 573 K (b). The surfaces were analyzed at a tilt angle of 45 degree. The scale bar (b) is the same for both images.

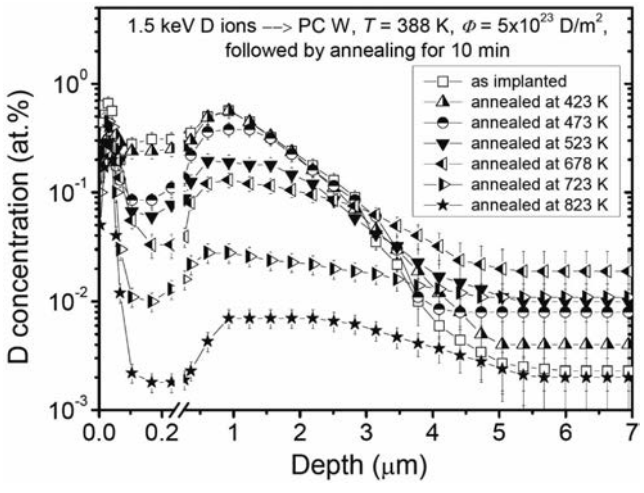

FIG. 5. Depth profiles of deuterium trapped in polycrystalline coarse-grained W irradiated with 1.5 keV D ions at 388 K to a fluence of 5×10^{23} D/m^2 and then annealed at fixed temperature for 10 min [6].

irradiation temperature increases, the blisters become sparser.

The dependence of the D concentration on the temperature of post-irradiation annealing can provide information about the nature of traps which are responsible

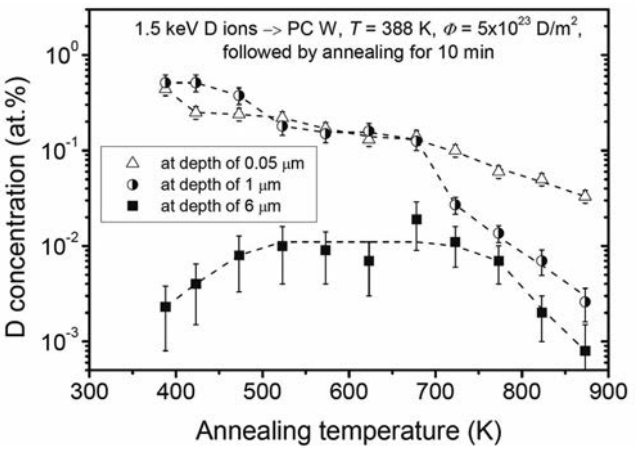

FIG. 6. Deuterium concentration in the near-surface layer (at a depth of 0.05 μm), in the sub-surface layer (at a depth of 1 μm), and in the bulk (at a depth of 6 μm) of polycrystalline coarse-grained W irradiated with 1.5 keV D ions at 388 K to a fluence of 5×10^{23} D/m^2 and then annealed for 10 min, as a function of the annealing temperature.

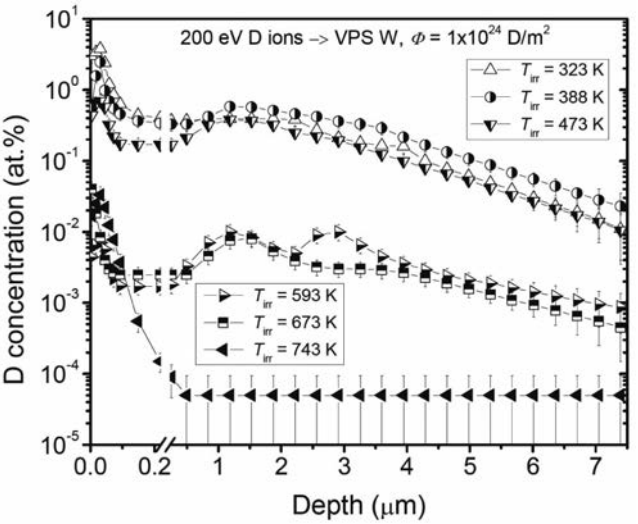

FIG. 7. Depth profiles of deuterium trapped in porous (8-9%) vacuum plasma-sprayed W coatings irradiated with 200 eV D ions to a fluence of 1×10^{24} D/m^2 at various temperatures.

for the capture of deuterium. Changes of D depth profiles in the polycrystalline coarse-grained W irradiated at T_{irr} = 388 K with 1500 eV D ions to a fluence of 5×10^{23} D/m^2 caused by isochronous annealing (for 10 min) are shown in Fig. 5. To observe a variation of the D concentration in the near-surface layer, in the sub-surface layer and in the bulk, values of the D concentration at depths of 0.05, 1 and 6 μm as functions of the annealing temperature are plotted in Fig. 6. It is evident that there are two ranges of the annealing temperatures at which the D concentration in the near-surface and sub-surface layers reduces: 400-500 K and above 680-750 K. As for the bulk, the D concentration at a depth of 6 μm rises initially as the annealing temperature increases, then demonstrates a constant value of about 10^{-2} at.% at annealing

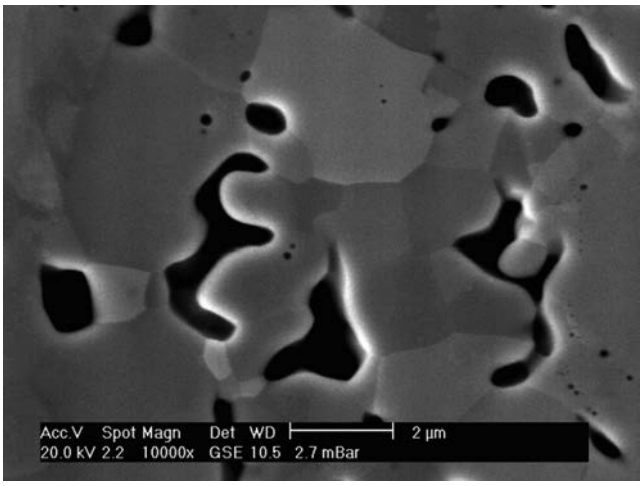

FIG. 8. Metallographic cross-section image of porous vacuum plasma-sprayed W coating. The degree of porosity is 8-9%.

temperatures of 523-723 K, and after that decreases down to below 10^{-3} at.% at 873 K (Fig. 6).

In the porous VPS W irradiated with 200 eV D ions to a fluence of 1×10^{24} D/m^2 at temperatures in the range from 323 to 743 K, there are two temperature ranges when the D concentration decreases significantly: from 473 to 593 K and from 673 to 743K (Fig. 7). The high D concentration in the near-surface layer (1-4 at.%) and in the sub-surface layer (0.4-0.6 at.%) observed after D ion irradiation at 323-473 K can be explained by the accumulation of molecular deuterium inside closed voids (Fig. 8) and by chemical adsorption of D atoms on the void walls.

3.2. W materials exposed to high flux D plasmas

Deuterium depth profiles in the single crystalline and polycrystalline fine-grained W samples exposed to low-energy (200 eV/D), high-flux (1×10^{21} D m^{-2}s^{-1}) D plasmas to an ion fluence of 2×10^{24} D/m^2 are shown in Fig. 9. In the single-crystalline W exposed to the D plasma at T_{exp} = 303 K, the D depth profile demonstrates a sharp concentration maximum near the surface, a concentration minimum and a second maximum with the D concentration of about 0.7 at.% at a depth of around 0.1 μm. At depths beyond 1-2 μm, the D concentration decreases with depth (Fig. 9 (a)). As the exposure temperature increases, the D concentration at the near-surface maximum reduces from about 1 at.% at T_{exp} = 303 K to about 0.4 at.% at T_{exp} = 533 K, while the second concentration maximum shifts into deeper layers and, at $T_{exp} \geq 413$ K, is localized at a depth of about 1 μm. After the exposure at temperatures in the range from 373 to 463 K, the D concentration at the second maximum is 0.3-0.5 at.%. In the bulk, a drastic decrease in the D concentration occurs at exposure temperatures between 463 and 533 K (Fig. 9 (a)).

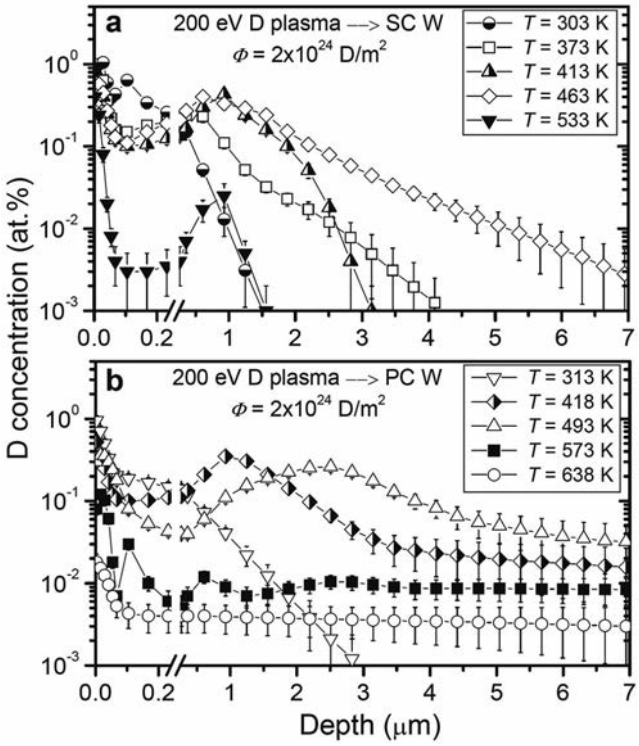

FIG. 9. Depth profiles of deuterium trapped in single crystal W (a) and polycrystalline fine-grained W (b) exposed to a low-energy (200 eV/D), high flux D plasma to an ion fluence of 2×10^{24} D/m^2 at various temperatures [6-8].

In the polycrystalline fine-grained W exposed to a D plasma at 313 K, the D depth profile is characterized by a sharp near-surface concentration maximum (about 1 at.%) and decreasing concentration tail (Fig. 9 (b)). After exposure at temperatures of 418-493 K, the D profile demonstrates, in addition to the near-surface peak, a maximum D concentration (0.3-0.4 at.%) in the bulk (at a depth of about 1 μm for T_{exp} = 418 K and at a depth of 2.5 μm for T_{exp} = 493 K). Between the surface and the maximum D concentration in the bulk, a concentration minimum is observed. At T_{exp} = 418-493 K the D concentration at depths beyond 5 μm is (2-4) $\times 10^{-2}$ at.% (Fig. 9 (b)). Note that in the polycrystalline coarse-grained W irradiated with 200 eV D ions, the D concentration at these depths is (2-4) $\times 10^{-3}$ at.% (Fig. 3). Turning back to the polycrystalline fine-grained W, at $T_{exp} \geq 573$ K the D concentration becomes uniform at depths of 0.5-7 μm and is about 10^{-2} at.% at T_{exp} = 573 K (Fig. 9 (b)) and 2×10^{-4} at.% at T_{exp} = 783 K (not shown in Fig. 9 (b)).

After exposure to the D plasma at elevated temperatures blisters are formed on the surfaces of both the single crystal W and polycrystalline fine-grain W (Fig. 10). For the single crystal W exposed at T_{exp} in the range from 373 to 533 K the mean diameter of the blisters is 3-5 μm and does not depend on the exposure temperature. The maximum areal density of blisters is observed at T_{exp} = 413-463 K, whereas at T_{exp} = 533 K only solitary blisters are present on the surface of the

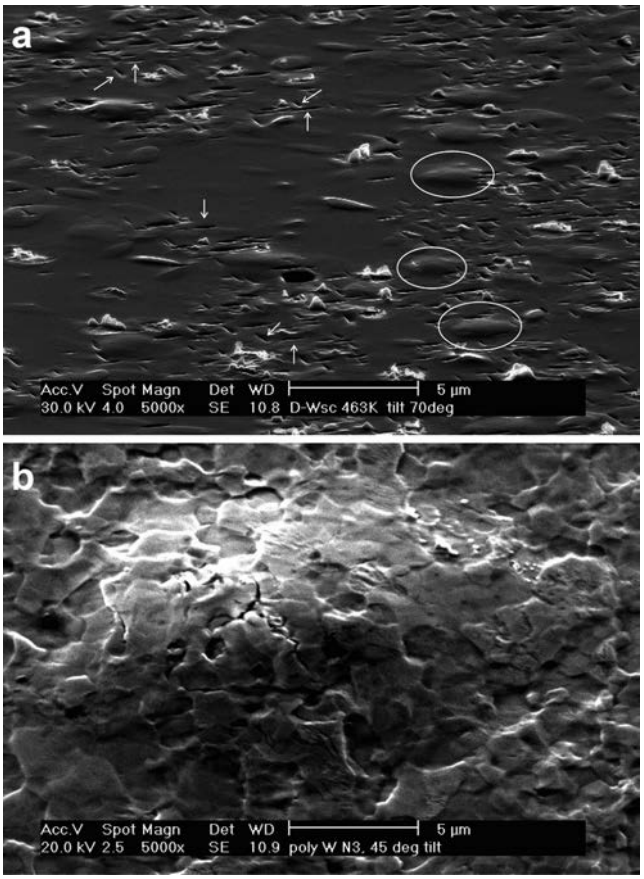

FIG. 10. SEM micrographs of single crystal W (a) and polycrystalline fine-grained W (b) exposed to a low-energy (200 eV/D), high ion flux D plasma to an ion fluence of about 2×10^{24} D/m^2 at 463 K (a) and 493 K (b) [7, 8]. The surfaces were analyzed at tilt angles of 70 (a) and 45 (b) degrees. Some of the blisters on the surface of single crystal W (a) are marked by ovals, some of the etching pits are indicated by arrows.

single crystal W. For the polycrystalline W the mean blister size is about 3 μm at T_{exp} = 313 K and grows to a maximum value of about 30 μm at T_{exp} = 573 K. Cracks are observed on the surface of blister lids and the release of D_2 molecules becomes evident from the concentration minimum of the D depth profile between the near-surface and sub-surface maxima (Fig. 10 (b)). At exposure temperatures above 650 K blisters are not formed on the surface of the polycrystalline W.

4. Discussion

The high deuterium concentration in the sub-surface layer and the formation of blisters allows the conclusion that irradiation with low-energy D ions or exposure to a low-energy, high ion flux D plasma modifies the surface to depths up to several micrometres, for both single crystals W and polycrystalline W. It has been shown with sputter residual gas analysis that in single crystal W exposed to a low-energy D plasma at 373 K some deuterium is accumulated in the form of D_2 molecules [6]. It could be supposed that D_2 molecules (or rather D_2-filled voids) are formed in the sub-surface layer as well (up to depths of several micrometres). According to van Veen et al. [13], the D_2 gas inside the voids is expected to be released during annealing at 400-600 K (detrapping energy ≈1.0 eV), whereas the D atoms bound on the inner surface of voids (binding energy ≈1.7 eV) is expected to be released at 700-900 K. Actually, the D depth profiles in the porous VPS W (Fig. 7) show that the D concentration in the sub-surface layer starts to decrease significantly at exposure temperatures above 500 K, thus confirming the results of van Veen et al. [13]. In the single crystal W and polycrystalline fine-grained W exposed to the low-energy, high flux D plasma the D concentration at depths of 1-3 μm starts to decrease significantly at exposure temperatures above 500 K (Fig. 9), confirming the assumption that D_2-filled voids are formed.

As seen in Fig. 6, the D concentration in the bulk of polycrystalline W starts to decrease at annealing temperatures above 700 K. Therefore, it can be concluded that deuterium retained in the bulk is accumulated as D atoms chemisorbed on the inner walls of voids present initially in polycrystalline W samples.

The depths of D accumulation (several micrometres) are much larger than the deuterium implantation range (several nanometres). Moreover, deuterium ions with energies less than 800 eV are not able to produce displacement damage in tungsten [14]. A review of hydrogen bubbles in metals by Condon and Schober [15] outlines a possible mechanism of void formation - the mechanism of near-surface plastic deformation caused by the deuterium super-saturation within the near-surface layer. During D ion irradiation or D plasma exposure, the D concentration in the implantation zone greatly exceeds the solubility limit and stresses the matrix lattice until plastic deformation with formation of voids and vacancy clusters occurs to alleviate these tensions [14, 15]. This deformation is assumed to be responsible for the sudden increase in trapping sites for deuterium (vacancies, vacancy complexes and macroscopic cavities) at depths of several micrometres and the concurrent accumulation of deuterium, both in the form of D_2 molecules and D atoms. The formation of the deuterium-filled cavities and D retention are thought to be caused by a combination of the stress-induced plastic deformation, D diffusivity, D trapping and de-trapping processes. It may be suggested that the stress-induced plasticity of tungsten appears at high concentrations of soluble hydrogen and increases with increasing temperature. For long-term irradiations, the diffusing D atoms recombine on the cavity surfaces, thus increasing the gas pressure inside these cavities. Near room temperature, as more deuterium is deposited, cooperative fracture between the cavities suddenly

becomes an easy way of relieving their overpressure, thus initiating cracks, allowing internal gas release. At elevated temperatures a high deuterium pressure inside the cavities leads to extrusion of metal and formation of blisters.

Traces of the plastic deformation within the sub-surface layer of the single crystal W are observed on the surface as etching pits (Lüders bands) oriented along a certain crystallographic plane (Fig. 10 (a)). These etching pits are created due to preferential sputtering of dislocation lines intersecting the surface. According to Savitsky and Burkhanov [16], at plastic deformations of 6-10% the dislocation lines in the bcc lattice are parallel to the direction of the closest packing. But at a higher degree of the deformation, a texture is formed.

For polycrystalline W irradiated with 200 eV D ions, changes in the D concentration with increasing fluence result from W structure modifications caused by the low energy ion irradiation. As the ion fluence increases, the concentration of gas-filled voids within the sub-surface polycrystalline layer (1-5 μm) increases, and after a certain fluence interconnected porosity starts to develop. This leads to the release of a fraction of the molecular deuterium. This is demonstrated by the decrease of the D concentration at $\Phi > 1 \times 10^{24}$ D/m^2 (Fig. 1 (a)).

As illustrated in Fig. 1, after irradiation with 200 eV D ions at a low flux of about 4×10^{19} D/m^{2}s, the maximum concentration of deuterium (rather D_2 molecules) at depths of 1-3 μm in the polycrystalline W specimen is at least one order of magnitude higher than that in the single crystal W. This suggests that the initial structure of the W material plays a major role in the stress-induced void formation. Possibly, the grain boundaries serve as preferential sites for void nucleation and growth. However, after exposure to the high-flux (about 1×10^{21} D/m^{2}s) D plasma, the maximum D concentration in the sub-surface layer (at depths of 1-3 μm) is the same for both the single crystal and polycrystalline W (Fig. 9). Apparently, for high-flux D ion implantation, the formation of the stress-induced defects depends on the W structure to a lesser degree than for low-flux implantation.

Interestingly, in polycrystalline W irradiated with 200 eV D ions at low flux (about 4×10^{19} D/m^{2}s), the D concentration in the sub-surface layer decreases drastically as the irradiation temperature increases from 323 to 393 K (Fig. 3). However, in the case of irradiation with an ion flux of about 1×10^{21} m^{-2}s^{-1}, the decrease in the D retention begins at about 500 K (Fig. 9). Evidently, the ion flux affects the temperature where the D concentration in the sub-surface layer reaches its maximum. The possible reason for the temperature dependence of the D concentration on the ion flux is a balance between the incident flux and temperature dependent D atom diffusion rate out of the implantation zone [17].

5. Summary

Depth profiles of deuterium trapped in W materials irradiated with low-energy D ions have been determined up to a depth of 7 μm using the D(^{3}He,p)^{4}He reaction at a ^{3}He energy varied from 0.69 to 4.0 MeV. The proton yield as a function of incident ^{3}He energy was measured and the D depth profile was obtained from the measured proton yields by deconvolution with the program SIMNRA.

The depth at which deuterium is retained in W materials can be conditionally divided into three zones: (i) the near-surface layer (up to a depth of about 0.2 μm), (ii) the sub-surface layer (from about 0.5 to about 6 μm), and (iii) the bulk (> 6 μm). At high ion fluences ($\geq 1 \times 10^{24}$ D/m^2) and irradiation temperatures below 500 K, most of the deuterium retained within the near-surface and sub-surface layers is accumulated in the form of D_2 molecules. Depending of the W structure and irradiation conditions, the maximum D concentration in the sub-surface layer can reach 0.1-1 at.%. In the bulk of polycrystalline W, deuterium is accumulated as D atoms chemisorbed on the inner walls of voids present initially in the sintered and hot-rolled W.

D ion irradiation with ion energies well below the displacement threshold modifies the W structure to depths of up to several μm, in both single crystals and polycrystalline W. Plastic deformation of the W matrix caused by deuterium super-saturation within the near-surface layer is considered for the formation of trapping sites for deuterium.

References

[1] FEDERICI, G., et al., Key ITER plasma edge and plasma–material interaction issues, J. Nucl. Mater. **313-316** (2003) 11.

[2] CAUSEY, R.A., VENHAUS, T.J., The use of tungsten in fusion reactors: a review of the hydrogen retention and migration properties, Phys. Scripta **T94** (2001) 9.

[3] CAUSEY, R.A., Hydrogen isotope retention and recycling in fusion reactor plasma-facing components, J. Nucl. Mater. **300** (2002) 91.

[4] SKINNER, C.H., et al., Recent advances on hydrogen retention in ITER's plasma-facing materials: beryllium, carbon, and tungsten, Fusion Sci. Technol. **54** (2008) 891.

[5] ALIMOV, V.Kh., ROTH, J., MAYER, M., Depth distribution of deuterium in single- and polycrystalline

tungsten up to depths of several micrometres, J. Nucl. Mater. **337-339** (2005) 619.

[6] ALIMOV, V.Kh., ROTH, J., Hydrogen isotope retention in plasma-facing materials: review of recent experimental results, Phys. Scripta **T128** (2007) 6.

[7] ALIMOV, V.Kh., et al., Deuterium retention in tungsten exposed to low-energy, high-flux clean and carbon-seeded deuterium plasmas, J. Nucl. Mater. **375** (2008) 192.

[8] ALIMOV, V.Kh., et al., Surface modification and deuterium retention in tungsten and molybdenum exposed to low-energy, high flux deuterium plasmas, Advanced Materials Research **59** (2009) 42.

[9] DESCHKA, S., et al., Manufacturing and high heat flux loading of tungsten coatings on fine grain graphite for the ASDEX-upgrade divertor, J. Nucl. Mater. **233-237** (1996) 645.

[10] ECKSTEIN, W., GARCÍA-ROSALES, C., ROTH, J., OTTENBERGER, W., Sputtering Data, Tech. Rep. IPP 9/82, Max-Planck-Institut für Plasmaphysik, Garching (1993).

[11] MAYER, M., SIMNRA User's Guide, Tech. Rep. IPP 9/113, Max-Planck-Institut für Plasmaphysik, Garching (1997).

[12] ALIMOV, V.Kh., MAYER, M., ROTH, J., Differential cross-section of the D(^{3}He,p)^{4}He nuclear reaction and depth profiling of deuterium up to large depths, Nucl. Instr. and Meth. B **234** (2005) 169.

[13] VAN VEEN, A., DE VRIES, J., SEGERS, D., ROZING, G.J., "Hydrogen defect interaction in tungsten observed with positron annihilation", Positron Annihilation (AIN, P.C., SINGRU, R.M., GOPINATHAN, K.P., Eds), World Scientific Publ. Co., Singapore (1985) 543.

[14] HAASZ, A.A., POON, M., DAVIS, J.W., The effect of ion damage on deuterium trapping in tungsten, J. Nucl. Mater. **266-269** (1999) 520.

[15] CONDON, J.B., SCHOBER, T., Hydrogen bubbles in metals, J. Nucl. Mater. **207** (1993) 1.

[16] SAVITSKY, E.M., BURKHANOV, G.S., Single Crystals of Refractory and Less-Common Metals and Alloys, Nauka, Moscow (1972) (in Russian).

[17] VENHAUS, T., CAUSEY, R.A., DOERNER, R.P., ABELN, T., Behavior of tungsten exposed to high fluences of low energy hydrogen isotopes, J. Nucl. Mater. **290-293** (2001) 505.

Results of the NERD installation upgrading

S.V. Artemov, Ya.S. Abdullaeva, A.A. Karakhodzhaev, G.A. Radyuk, V.P. Yakushev

Institute of Nuclear Physics, Academy of Sciences of Uzbekistan,Tashkent, 702132, Uzbekistan

Abstract

Improvement of the neutron elastic recoil detection (NERD) technique for hydrogen isotope concentration depth profiling, which can be applied for tritium inventory in thermonuclear reactors, is described. The use of 14 MeV neutrons provides a number of essential advantages which allow us to analyse deep regions of the sample. Improving analytical characteristics of the method is achieved by decreasing, as much as possible, the gamma and charged particles background in the measured energy spectra. To decrease the false coincidences count rate and worsening of energy resolution we turned down the traditional fast-slow arrangement of the spectrometer and used fast branch of the electronics down to the last spectrometric amplifier that produces the spectrometric signal for ADC.

1. Introduction

The project goal is to upgrade the NERD (Neutron-induced Elastic Recoil Detection) method, which is developed for study of tritium and other hydrogen isotopes content and concentration profiles in materials. It is supposed that the NERD method can be used to diagnose tritium concentrations in thermonuclear reactor materials.

Many experimental methods exist now for the study of material-hydrogen systems. Nevertheless, only a few, such as the ion beam analysis (IBA) [1, 2], are able to probe the hydrogen directly and measure its distribution in the near-surface region without destruction of the sample. The NERD method, which allows one to analyse a deep region in a sample, was developed in the Institute of Nuclear Physics of Academy of Sciences (Uzbekistan) [3]. The information on the depth and concentration of hydrogen in a sample is contained in the energy spectrum of H-ions knocked out by monochromatic fast neutrons. The method allows one to measure the concentration for all hydrogen isotopes simultaneously along the thickness of the sample.

In the framework of the IAEA Co-ordinated Research Project "Tritium Inventory in Fusion Reactors" we have improved the neutron method for determination of tritium content and the profile of its concentration in various materials.

2. Experimental technique

The method is based on spectrometry of the protons, deuterons and tritons (nuclei of hydrogen isotopes) knocked out by fast monochromatic neutrons from the analysed sample. Neutrons with the energy ~14 MeV are generated at interaction of the 150 keV deuterons with tritium as a result of the reaction

$$D + T \rightarrow n + {}^4He$$

A telescope consisting of two or three semi-conductor detectors (ΔE and E) is used for identification of the recoiled charged particles and definition of their energy. The scheme of measurement is shown in Fig. 1.

Neutrons do not lose their energy in a sample. However, the recoiled charged particles (p, d, t), passing through substance, lose energy and have different specific energy losses. The particles knocked out from the

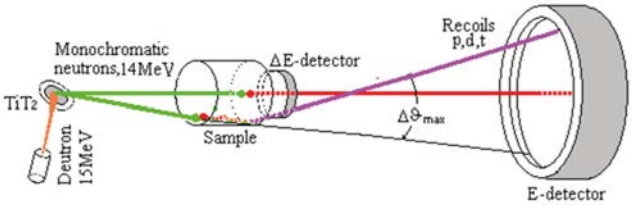

FIG. 1. Scheme of measurement.

surface of a sample have the maximal energy. If a neutron interacts with the nucleus H, D or T deeper in the sample then the recoil p, d or t have smaller energy. The deeper the collision occurs, the less is the energy of the particle. This circumstance is used for hydrogen profiling.

We have improved the analytical characteristics of the installation which realized this method using the T+d neutron generator NG-150. The following lines of action have been fulfilled [4, 5]:

- Significantly decreasing the charged particles and gamma radiation background in the recoil energy spectra;
- Decreasing the neutron scattering on their way to the studied sample [6];
- Using the fast spectrometric electronics up to the final pulses treatment.

Mechanical improvements. We almost completely removed, the background of charged particles in spectra by using graphite as a constructional material for the box of the telescope of detectors, because the thresholds of the reactions "^{12}C+n→charged particle" are very high.

The background of gamma radiation arises as a result of neutron interaction with the constructional elements and protection walls. It was reduced by moving the metallic units and material of the radiation protection as far as possible from the telescope of the detectors.

The share of scattered neutrons, which lower the energy resolution, was diminished by reducing to the minimum the amount of material on the way of the neutrons to the analysed sample and using material that has a small cross-section for elastic scattering of neutrons (as shown in Fig. 2).

Improvement of electronics. A large level of the background pulses, which give false coincidences, leads to decreasing both the sensitivity and the depth resolution of the method. We have achieved precise operation of the fast electronics due to the specially developed electronic modules: the charge sensitive preamplifiers with short output signal and fast linear gates [7]. Charge sensitive preamplifiers have an output pulse duration of not more than 380 ns and big loading ability (4-5 × 10^5 pps). The linear gate has a time of switching of ~20 ns and a dynamic range not less than 10^2. Duration of the driving pulse can be varied from 300 up to 1000 ns.

Due to these actions we can replace the telescope with three-detector system by a two-detector variant and simplify sufficiently the electronics of the spectrometer if the analysed samples have relatively large hydrogen concentrations. Thus we can increase the depth of analysis of the method in such cases.

The modified block scheme of the electronics of the spectrometer is shown in Fig. 3. Practically, placing of the electronics is divided into two parts. The first one is located near the neutron generator and reaction chamber of the NERD installation before the cable

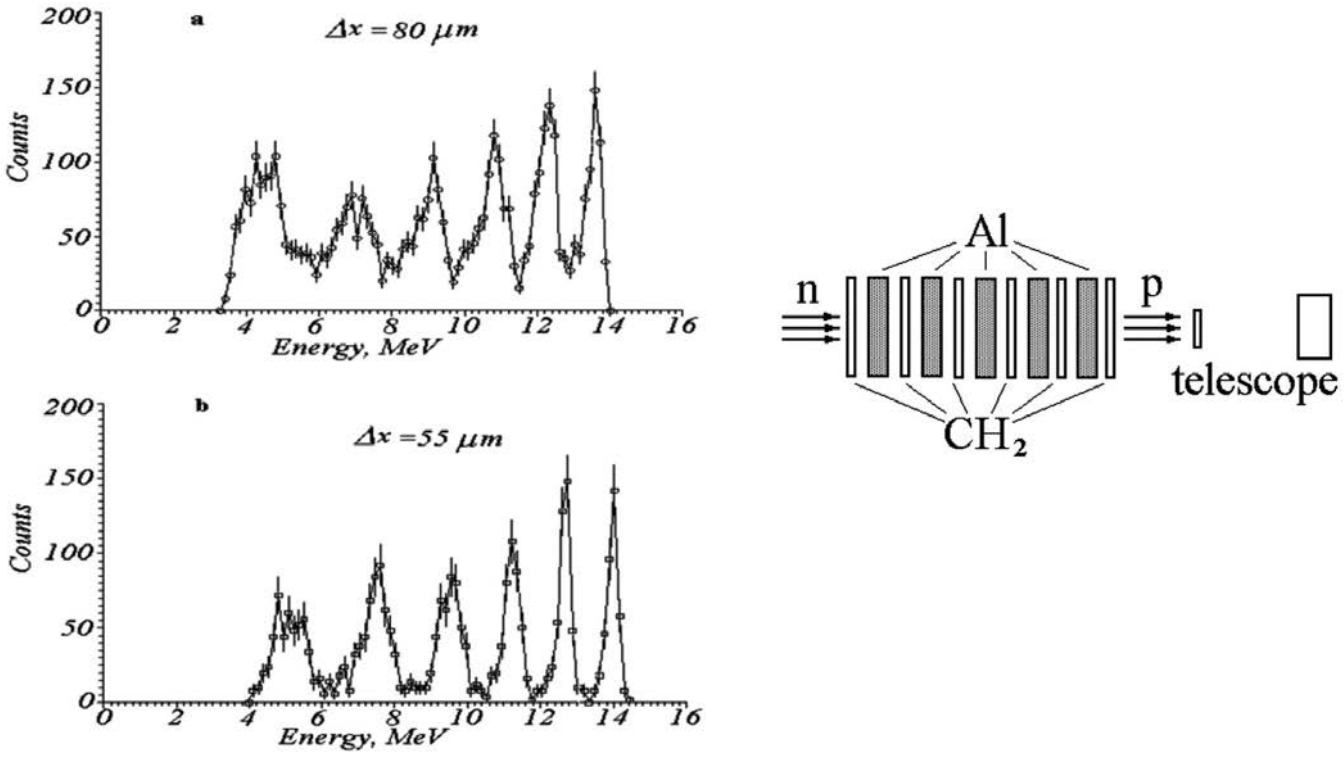

FIG. 2. Illustration of the influence of removing the material on the energy resolution of the spectrometer. Energy spectra of the recoiled protons at analysis of the sample T2 assembled of 6 CH_2 films (thickness 40 μm) separated by 5 Al foils with thicknesses 160 μm. The shape of the proton spectrum before (a) and after (b) modification.

communications. It consists of two preamplifiers CSPA (of ПУ-21 type) and fast-filter amplifiers FPA (1501). The latter one (after the cable channel, separated by the dashed line in Fig. 3) contains the basic part of the electronics and consists of three functional branches.

The first spectrometric branch executes gaining the fast spectrometric signals by the amplifiers 2111, then lets pass the signals through a linear gate, shapes them and gains the reformed slow signal by amplifiers 1101. Then the analog spectrometric signals are transformed to the digital form by the ADC-712 module and transferred to the PC for analysis.

The second driving branch contains the fast amplifiers 1501 independent of the spectrometric ones, the discriminators 1502, the coincidence circuit and fast linear gates (keys).

The third (monitoring) branch provides selection of the big amplitude pulses corresponding to the detection of alpha particles from the $^{28}Si(n,\alpha)^{25}Mg$ reaction which occurs on the material of the ΔE-detector. It consists of the fast discriminator 1502 and the pulse counter 401.

In such mode of the spectrometer one can provide the independent adjustment of all three functional branches that essentially reduces the time of adjustment of the spectrometer directly on a neutron beam. The shape of the fast spectrometric signal is unipolar (without drop to the opposite polarity), has a rise time 70 ns and an overall duration of not more than 400 ns. The time resolution of the coincidence circuit is 100 ns. Duration of the driving pulse of the fast linear gates is 600 ns. The form of the slow spectrometric pulses is bipolar. The integration and differentiation time i equal to 1 μs.

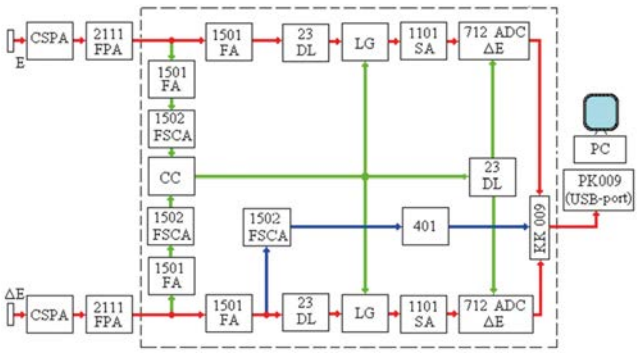

FIG. 3. Block scheme of the spectrometer.

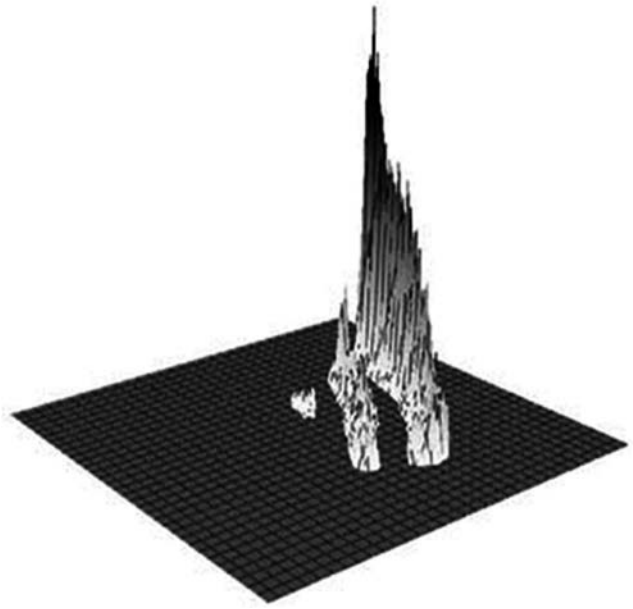

FIG. 4. Three-dimensional matrix of events for the sample containing hydrogen, deuterium and tritium.

3. Procedure of the analysis

The analysis of a sample for the content and profile of concentration of hydrogen is realized in three stages. Let us illustrate it for the analysis of a special complex sample, containing hydrogen, deuterium and tritium. The telescope of detectors consists of two silicon semi-conductor detectors (the ΔE detector with thickness 100 μm and E-detector of full energy absorption with thickness 1300 μm). The sizes of the detectors and relative arrangement of the neutron source and ΔE and E- detectors in this variant of the spectrometer are such that the geometrical resolution of the system makes 350 keV [8].

Firstly the spectrometric signals from detectors are processed by electronics and collected as a two-dimensional matrix in coordinates ΔE, E + ΔE. The three-dimensional image of the matrix of events accumulated at irradiation of this sample by neutrons is shown in Fig. 4. It is visible that particles p, d, t are grouped within independent areas that are well separated from each other. The foots of "mountains" corresponding to each hydrogen isotope have a hyperbolic form and their extent depends on the depth range in which these isotopes are located. The highest hyperbole corresponds to protons, knocked out by neutrons from hydrogen. The hyperbole is long because hydrogen is located inside a sample in all of its thickness. The next hyperbole corresponds to deuterons, which is shorter because deuterium is dispersed not so deeply in the sample. To the left, the stain corresponding to tritons is visible. Tritons are located by a stain instead of a hyperbole because tritium is situated only on a surface of the sample.

The second stage of the analysis consists in treatment of the matrix. Each group of particles is transformed into the energy spectrum of the corresponding recoiled particles. Then the energy spectrum is recalculated into the depth profile function which is the dependence of quantity of each hydrogen isotope on the depth of its location. The profiles of the concentration of hydrogen, deuterium and tritium are shown in Fig. 5. One can see that hydrogen (^1H), deuterium (^2D) and

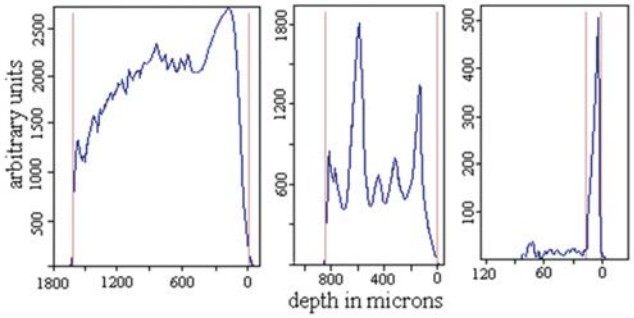

FIG. 5. Profiles of the concentration of hydrogen (on the left part of the figure), deuterium and tritium (on the right) for the special sample.

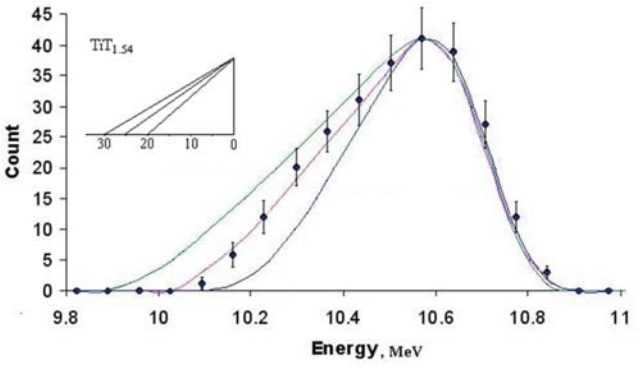

FIG. 6. Energy spectra of tritons: experimental (points) and simulated (curves) spectra for various accepted depths of tritium location (20, 25 and 30 μm).

tritium (^{3}T) are visible up to 1700 μm, ~800 μm and ~30 μm on depths of the sample, respectively.

The third stage of the treatment consists in finer analysis of each spectrum. It consists of modelling the energy spectrum with use of the Monte Carlo method assuming the roughly obtained profiles of concentration at the second stage of analysis. It is usually called for in cases when the experimental energy (and profile) resolution is not good enough to obtain the details of the concentration profile. Such analysis of the tritium content in thin sample is shown in Fig. 6.

We have assumed in this case that the concentration of tritium decreases linearly with depth (see insertion in the figure), and simulated the energy spectra of tritons for various maximal depths. It is visible from the figure that assumptions are justified well and the most probable is the concentration linearly decreasing down to 25 μm from the sample surface. So use of the program of Monte-Carlo simulation allows to obtain considerably better resolution. One can see that in Fig. 6, where we can distinguish depths that differ by ~5 μm.

4. Definition of parameters of the modernized NERD installation

The energy resolution in the measured spectra of recoils is determined mainly by the geometrical resolution and includes the own resolution of the detectors and the spreading of the energy of neutrons as the result of scattering of neutrons on constructional materials before interaction with the analysed sample. Operating with the spectrometer on a neutron beam has shown that for the optimal relation between rapidity of the analysis and energy resolution the overall energy resolution of the spectrometer is ~350 keV.

To check the real depth resolution we investigated a complex sample, consisting of two titanium layers of thicknesses 1.82 μm separated by aluminum foil of thickness 52 μm. The concentration of tritium in titanium was 1.6 atoms T per Ti atom. The energy spectrum of tritons obtained from this sample is shown in Fig. 7. Two peaks, corresponding to tritium in the Ti layers, are reliably separated. So we can conclude, that the experimental depth resolution on tritium for the samples of materials with atomic weight ≤30 does not exceed 17 μm.

The sample also contains two similar titanium layers saturated with deuterium and separated by aluminum foil with thickness 120 μm. They were placed before the mentioned tritium composition. Therefore the recoiled deuterons should pass through the TiT+Al combination of layers before entering to the telescope. The energy spectrum of the knocked-out deuterons is shown in Fig. 8. One can see that the experimental depth resolution for deuterium is not worse than 34 μm in this case.

As one can see from Fig. 7, the height of the peaks corresponding to presence of tritium (1.6 atoms of tritium per atom of titanium) exceeds the level of the background approximately 15 times. The depth resolution is ~20 μm. It means that the effective concentration of tritium is ~0.16 of atom T per atom Ti (the real thickness of the TiT layer is ~2 μm). It means that we can experimentally find the tritium in the titanium if its concentration is ~1 atom of tritium per 100 atoms of titanium (1 at.%) in this case if tritium is dispersed uniformly in the volume of the sample. The sensitivity of the analysis by the NERD method is limited by interfering nuclear reactions on nuclei of the chemical elements of the matrix of the analysed sample. It varies for various materials over a wide range from ~0.1 at.% up to 10 at.%. The background of the reactions on the matrix nuclei can be taken into account by measuring the energy spectra of charged particles from the same sample without the hydrogen. Otherwise for improvement of the situation we have developed a program for simulation of the energy spectra of nuclear reactions on a matrix which allows one to subtract this background from the experimental spectra [9, 10].

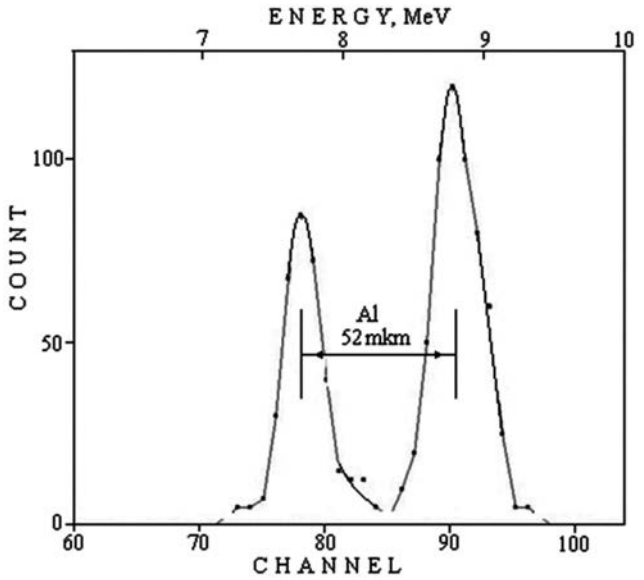

FIG. 7. Energy spectrum of tritons from the sample containing two layers saturated by tritium.

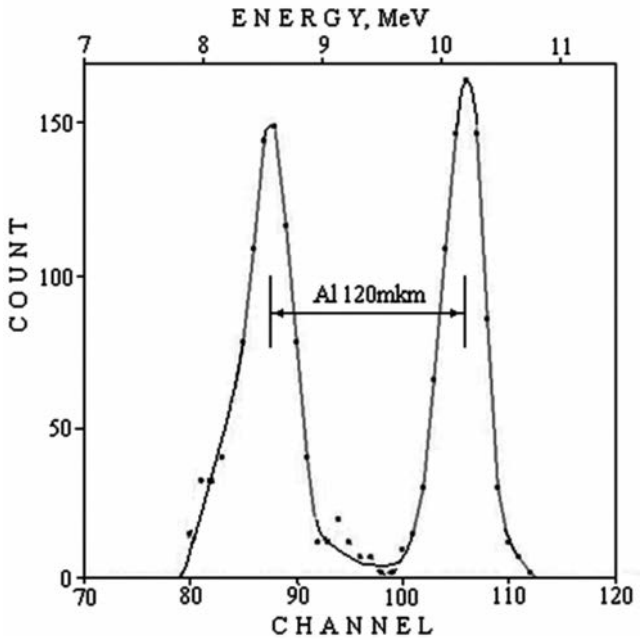

FIG. 8. Energy spectrum of deuterons from the sample containing two layers saturated by deuterium and situated behind the tritium-containing layers.

5. Conclusions

As a result of our activity in the framework of the CRP "Tritium Inventory in Fusion Reactors" on improvement of the analytical properties of the NERD method and its adaptation to the tasks of tritium inventory in the thermonuclear machines, the following was done.

– Expansion of the dynamic diapason of a spectrometer has allowed one to obtain the maximal depth of the analysis. The depths of analyses are different for various materials. They are larger for the light elements and smaller for heavy ones and are: for tritium in tantalum 60 μm and in boron 160 μm; for deuterium in tantalum 140 μm and in boron 430 μm; for hydrogen in tantalum 300 μm and in boron 1000 μm.
– The depth resolution in the profiles of hydrogen isotope concentration which is defined by the energy resolution of the method was improved by reducing the contribution of the scattered neutrons. The typical depth resolution in the profiles of hydrogen isotopes (in percentage of the maximal analysable depth) are: for tritium ~10%; for deuterium ~8%; for hydrogen ~6%.
– The sensitivity of the analysis was increased by taking into account the distortion of the energy spectra of tritium recoils induced by the background (n,t) reactions on the matrix nuclei.

The reliability of the analysis as a whole was increased by comparing the measured and simulated energy spectra of the recoiled tritons.

The installation may be utilized for analysis of tritium and other hydrogen isotopes content and depth profiles in samples of various materials including the intrinsic elements of thermonuclear reactors, especially if deep samples need to be analyzed.

References

[1] LEICH, D.S., TOMBRELLO, T.A., A technique for measuring hydrogen concentration versus depth in solid samples, Nucl. Instr. and Meth. **108** (1973) 67-71.

[2] LANFORD, W.A., TRAUTVETTER, H.P., ZIEGLER, J.F., KELLER, J., New precision technique for measuring the concentration versus depth of hydrogen in solids, Appl. Phys. Lett. **28** (1976) 566-568.

[3] KHABIBULLAEV, P.K., SCORODUMOV, B.G., "Determination of hydrogen in materials", Nuclear Physics Methods, Springer Tracts in Modern Physics **117**, Springer Verlag, Berlin/Heidelberg (1989) 1-87.

[4] RADYUK, G.A., ARTEMOV, S.V., ABDURAKHMANOV, A.Kh., YAKUSHEV, V.P., ZAPAROV, E.A., "Improvement of the neutron-induced elastic recoil detection spectrometer on basis of neutron generator NG-150", Abstract Book of International Conference "NUCLEUS 2004", Belgorod (Russia), June 2004, p. 284.

[5] RADYUK, G.A., et al., "Improvement of the NERD spectrometer on definition of hydrogen isotopes concentration", Abstract Book Third Eurasian

Conference on Nuclear Science and its Application, Tashkent, Uzbekistan (October 5-8, 2004) pp. 69-70.

[6] ARTEMOV, S.V., et al., "NERD-method to study profiles of tritium concentration in interior elements of a fusion reactor", Summary Report of Second IAEA Research Co-ordination Meeting on Tritium Inventory in Fusion Reactors, 18-19 October 2004, IAEA Headquarters, Vienna, Austria, Report INDC(NDS)-0495 (IAEA, Vienna, March 2006), pp. 25-38.

[7] ARTEMOV, S.V., et al., "Fast spectrometer for analysis of concentration profiles of the hydrogen isotopes in materials", Book of Abstracts International Conference on Current Problems in Nuclear Physics and Atomic Energy, NPAE-Kyiv 2006 (May 29 – June 03, 2006), Kiev, Ukraine (2006) pp. 170-171.

[8] ARTEMOV, S.V., et al., "Modernized spectrometer for the hydrogen content analysis in samples", Book of Abstracts, VI International Conference on Modern Problems of Nuclear Physics, 19–22 September 2006, Tashkent (2006) pp. 261-262.

[9] ARTEMOV, S.V., KAYUMOV, M.A., RADYUK, G.A., YAKUSHEV, V.P., "Procedure of account of the background reactions in the NERD-method for definition of concentration profiles of hydrogen isotopes", 5th International Conference on Nuclear and Radiation Physics, Almaty, Kazakhstan, September 26-29, 2005, pp. 210-218.

[10] ARTEMOV, S.V., KAYUMOV, V.F., RADYUK, G.A., YAKUSHEV, V.P., ZAPAROV, E.A., "Expansion of Opportunities of the NERD-Method for Definition of Content and Concentration Profiles of Hydrogen in Materials by Using the Monte-Carlo Simulation", Book of Abstracts, VI International Conference on Modern Problems of Nuclear Physics, 19–22 September 2006, Tashkent (2006) p. 72.

Studies of hydrogen retention and release in fusion materials

R.A. Causey

Sandia National Laboratories, Livermore, CA 94550, USA

Abstract

The work performed at Sandia in connection with the IAEA coordinated research project "Tritium Inventory in Fusion Reactors" is summarized.

1. Hydrogen release from 800 MeV proton-irradiated tungsten [1]

In collaboration with Brian Oliver of Pacific Northwest Nuclear Laboratory and Stuart Maloy of Los Alamos National Laboratory, experiments on the hydrogen release from 800 MeV proton-irradiated tungsten were performed [1]. The tungsten rods were irradiated with 800 MeV protons in the Los Alamos Neutron Science Center (LANSCE). The release kinetics of the hydrogen was analyzed using the TMAP4 computer code.

The tungsten disk samples were prepared at Los Alamos National Laboratory (LANL) by cutting the tungsten rod. The tungsten rod was formed by powder metallurgy and had an elemental composition of 99.96% tungsten with the major impurities being Mo at 100 μg/g and C and O at 30 μg/g each. The proton fluence for the in-beam sample (1Wh) was 1.1×10^{21} p/cm^2, and for the out-of-beam sample (1Wc) it was 4×10^{19} p/cm^2. Calculated displacement rates were 7.9 and 0.31 dpa, respectively. The radial temperature of the rods is estimated to have ranged from 440 to 450 K at beam center and approximately 310 K out of the beam. The specimens for hydrogen analysis were cut from each disk using small diagonal cutters. Each specimen was cleaned in acetone and air-dried, and the mass determined using a microbalance with calibration traceable to the National Institute of Standards and Technology (NIST).

Hydrogen release measurements were conducted at Pacific Northwest National Laboratory (PNNL) using a gas mass-spectrometric analysis system. The analysis procedure involved dropping the individual specimens, under vacuum, into a small cylindrical ceramic crucible. Prior to analysis, the analysis crucible was pre-heated to approximately 1300 K under high vacuum for several days. During the pre-heating and subsequent analysis, the sample chamber was maintained at approximately room temperature. Hydrogen release was measured as a function of time using a quadrupole mass spectrometer connected to the crucible volume. Calibration of the system sensitivity was accomplished using a calibrated hydrogen leak source with a stated absolute uncertainty of ±15%. Calibration measurements were conducted before and after each sample analysis, and showed an overall reproducibility of 2–3%.

Hydrogen measurements were conducted on sections taken from two of the disk samples and on two samples of unirradiated tungsten material from the same batch. In these measurements, the temperature of the sample was ramped from 300 up to 1500 K in an essentially linear profile of either 50 or 100 K/min depending on the expected total hydrogen in the sample. The release curves for the tungsten controls and sample 1Wc are similar in that they show a single major release peak at about 550 K. There is also a small release peak in sample 1Wc at about 1400 K. The release curve for the high proton dose sample (1Wh) looks quite different with a small peak at 550 K, but the majority of the hydrogen starts to come out at 900 K and peaks at 1400 K. The release of hydrogen from the tungsten samples was modeled using the TMAP4 developed at INEL [2]. TMAP4 is a finite-difference computational code capable of simultaneous calculation of hydrogen migration and thermal transport through materials. The 1-D model is developed by first defining a material of a certain thickness, then defining all transport parameters appropriate to hydrogen migration, trapping, and release from the material. These parameters are diffusivity, recombination rate coefficient, and trapping. A review of these parameters and others affecting hydrogen retention and migration in tungsten has been given by Causey and Venhaus [3]. Based on this review, the diffusivity of hydrogen in tungsten given by Frauenfelder [4],

i.e., $D=4.1 \times 10^{-7}\exp(-0.39\ eV/kT)\ m^2/s$, was used in the simulations. It is also assumed that recombination will not slow the release process during the thermal desorption experiments.

The last parameter affecting the release rate of hydrogen is trapping. There are several types of defects that might lead to trapping of hydrogen in tungsten; dislocation at cell boundaries [5], vacancies [6], and voids [5–7]. Anderl et al. [5] showed a direct correlation between the removal of dislocations on cell boundaries and a decrease in the number of hydrogen traps. The trap energy was estimated to be 1.3–1.5 eV. Eleveld and Van Veen [6] showed that the energy of the trap associated with the vacancies was 1.4 eV. Lastly, Van Veen et al. [8] and Eleveld and Van Veen [6, 7] showed hydrogen to be trapped at voids with an effective energy of 1.4 eV. It should be noted that it is a coincidence that dislocations, vacancies, and voids all trap hydrogen with a trap energy of 1.4 eV. Assuming a trap energy of 1.4 eV to be correct, the trap concentration and the level of trap filling were the only fit parameters used in the present TMAP model. The trap density was adjusted to give a 'best fit' to the measured hydrogen release profiles, and the percentage of traps filled was adjusted to yield the total measured hydrogen content. Only that portion of the hydrogen release associated with the high-temperature trap was modeled.

The low-temperature release peaks at about 550 K, noted in both the unirradiated material and in the proton-irradiated material, are assumed to be associated with a non-bulk surface or near-surface trapping mechanism. From the work of Anderl et al. [6], it is known that 1.3–1.6 eV traps exist at moderate levels (70 appm) throughout all unannealed tungsten samples. The samples used in this experiment were not annealed. If bulk trapping of hydrogen at a low-energy trap (0.5–0.7 eV) existed for a tungsten sample, thermal desorption of hydrogen from that sample would exhibit a release of some of the hydrogen at a lower temperature, but the majority of the hydrogen would be released at higher temperatures as a result of re-trapping of the hydrogen in the higher energy traps on its way to the surface. The unirradiated sample in the present work showed most of the hydrogen release in a single low-temperature peak, suggesting the hydrogen must have originated at the surface, perhaps associated with a thin oxide layer. The two control samples also showed a release peak at lower temperature, and this hydrogen is also believed to be associated with a small amount of surface trapping. Such surface trapping cannot be modeled by TMAP. Thus, for the purposes of comparison with the TMAP code, only that portion of the hydrogen release associated with the high-temperature trap was modeled. Deconvolution of the release profile for the two proton-irradiated samples yields total integrated hydrogen releases from the high-temperature traps of 80 appm for sample 1Wc and 1690 appm for sample 1Wh. For these irradiated samples, a trap density of 7.5% was empirically arrived at to yield a best fit to the high-temperature release profiles for both samples. It should be noted, however, that reasonable fits to the data could also be obtained with trap densities as low as 4%. This level of trap density is significantly higher than observed by Anderl et al. [6] for unirradiated, unannealed material, suggesting that most of the traps are created by the energetic proton beam. While trapping at this level seems difficult to imagine, it must be remembered that the 1.4 eV trap can be dislocations, vacancies, or voids. This is a material that has undergone proton damage equal to 7.9 dpa at a relatively low irradiation temperature. In the modeling for each sample, the trap filling level was adjusted to give a total hydrogen concentration in agreement with that measured, i.e., 80 and 1690 appm, respectively. The measured hydrogen releases were normalized to the TMAP data using the calculated surface area of each sample assuming a slab geometry with no correction for edge effects.

2. Sputtering and co-deposition of silicon carbide with deuterium [9]

With a moderately low effective atomic number and excellent thermal properties, silicon carbide is a serious candidate material for use as a plasma-facing material for fusion reactors. As a plasma-facing material, silicon carbide will have its silicon and carbon atoms sputtered by the energetic hydrogen isotope ions and neutrals escaping from the plasma. If the silicon and carbon atoms co-deposit with the hydrogen isotopes from the plasma, a large inventory of these isotopes could build up on the walls of the plasma chamber. If part of the hydrogen fuel is tritium, large inventories of tritium in the fusion device would create safety concerns.

The purpose of this experiment was to provide a direct comparison of the co-deposition rates of silicon carbide with that of graphite for a specific exposure condition. The direct comparison was performed by first striking a Penning discharge between two parallel graphite plates in a vacuum chamber backfilled with deuterium gas. Energetic deuterons striking the graphite plates sputtered atoms from the plates out onto the vacuum vessel walls, where they were co-deposited with the deuterium. The experiment was then repeated with the graphite plates replaced by silicon carbide plates. While the conditions necessary to permit a Penning discharge limit the measurements to a single incident energy, and require gas pressures greater than that typical of accelerator experiments, the experiment did allow a direct comparison of the co-deposition properties of the two materials.

Both the silicon carbide and graphite samples were manufactured POCO products. The graphite was POCO AXF-5Q, the same material as that used in the TFTR reactor. The silicon carbide (converted from graphite) was a high purity material (<5 appm impurities) with a density of 1.77 g/cm^3. The plasma used in this experiment was generated by a Penning discharge. The configuration consists of two parallel plates at equipotential that serve as cathodes. Along the rims of the plates are electrically isolated concentric shields that serve as anodes. There is a solenoid magnetic field perpendicular to the set of electrodes. A small stainless steel catcher plate was located ≈5 cm from the plasma, and collected only a minor fraction of the sputtered atoms. A majority of the sputtered atoms were deposited on the walls of the vacuum vessel. The total volume of the deuterium plasma experiment as determined by pressure rise during the addition of a fixed amount of gas was 59.2 l.

For a typical experiment, the vacuum vessel was first pumped down to its base pressure of 6×10^{-5} Pa, isolated from the pump, and then backfilled with deuterium gas to a pressure of ≈6.6 Pa. Upon initiation of the discharge, the pressure inside the chamber was monitored using a capacitance manometer. Once the pressure in the chamber was reduced by co-deposition down to a pressure of ≈3.3 Pa, the discharge was terminated. The gas was then slowly pumped out of the vessel through a connecting mass spectrometer. The mass spectrometer was used to measure the impurities that had accumulated in the chamber during the discharge. In all cases, the only significant impurity in the deuterium gas was protium. Typically, the fraction of the remaining gas that was protium varied from about 20% to 40%. This recorded gas fraction was used in the data analysis to correct for the total hydrogen isotope removal rate by the plasma. It is believed that the protium was generated primarily by the decomposition of water vapor by the plasma. It must be remembered that the vacuum vessel was backfilled with deuterium, and disconnected from the pumping system for times greater than 30 min. In earlier trial experiments, the protium production had been even greater. It was only through extended baking of the vacuum vessel along with glow discharge cleaning that the protium production was lowered to these reported values. While it is believed that the protium was generated primarily by decomposition of water vapor, the ratio of hydrogen to water in the system at the end of an experiment was measured to be 200 to 1. This ratio would suggest that water vapor (or oxygen) did not play an important role in the erosion of the graphite and silicon carbide.

A discharge current density of either 1 mA/cm^2 or 2 mA/cm^2 was used for all of the experiments. With the ions being primarily D_2^+, the particle flux to the cathodes was either 1.3×10^{16} or 2.6×10^{16} D/cm^{2}s (not including neutrals, if present). The power supply for the Penning discharge was used in the current regulated mode, but some deviation above and below the average current still occurred. As part of the data analysis, the current was averaged over the total plasma exposure time to correct for the noted deviations. During a typical experiment, the bias voltage required to maintain the set current started at ≈700 V and dropped to about 600 V by the end of the experiment. This implies an average energy of the D atoms to be ≈325 eV/D. The voltage decrease was thought to be at least partially due to the pressure decrease in the chamber during the experiment. During an experiment at the higher 2 mA/cm^2, the cathode temperature would increase from room temperature up to a maximum of ≈500 K during a typical 30 min plasma exposure. The maximum temperature was ≈100 K lower for the 1 mA/cm^2 samples. At the end of the silicon carbide plasma exposure, the catcher plate with the collected film was removed from the system and transferred in air to a sputter Auger analysis system. Auger analysis was used to determine the relative concentrations of the elements in the redeposited film as a function of depth.

The slopes of the curves of pressure versus time (or coulombs) are the co-deposition probability of the two different materials (probability that a hydrogen isotope atom will be removed through co-deposition per ion striking the sample surface). Each curve began with enhanced pumping at the onset due to additional wall pumping effects. Several of the experiments were immediately preceded by helium glow discharge cleaning of the chamber walls. A side effect of this cleaning was removal of the hydrogen from the near-surface of pre-existing co-deposited layers on the walls. Once the actual experiment began, a sizable fraction of the deuterium ions striking the cathode samples were reflected out onto the walls. A carbonaceous layer depleted of hydrogen has a very high sticking coefficient for impinging hydrogen ions or neutrals. After saturation of the near surface of these layers, further pumping would occur only with additional carbon deposition. For that reason, the recorded slopes were based only on the data in the second half of each experiment.

Averaging the values of the slopes in the determined curves, the co-deposition probability is 0.072±0.006 for silicon carbide and 0.106±0.015 for graphite. The ratio of the average co-deposition probability for silicon carbide to that for graphite is 0.68±0.14. The implication of these results is that silicon carbide used as a plasma-facing material in a next-step fusion device will generate only about 2/3 as much tritium inventory in the co-deposited layer as that for graphite under plasma conditions similar to those used in these experiments.

Prior to a discussion on the comparison of the co-deposition probabilities of the two materials, the magnitudes of the co-deposition probabilities themselves

require consideration. By definition, the co-deposition probability is the sputtering coefficient times the hydrogen to carbon ratio in the co-deposited film. According to the studies of Balden and Roth [10] and Roth [11], the sputtering coefficient for 325 eV deuterium on graphite at 500 K is ≈0.03. Multiplying the sputtering coefficient by 0.4 [12] (the expected D/C ratio in the carbon co-deposited film), a co-deposition probability of 0.012 is calculated. This calculated probability is a factor of 8.8 less than the value of 0.106 determined in these experiments. While the absolute determination of sputter or co-deposition rates was not the intent of this study, this difference must be addressed. In an almost identical experiment by Hsu and Causey [13], a catcher foil that subtended most of the solid angle for the sputtered carbon was placed around the Penning device. The authors used nuclear reaction analysis of the film to account for a co-deposition probability of ≈0.083. Rutherford backscatter was used to verify that sufficient carbon was present on the foil to account for this amount of deuterium co-deposition. Based on films found outside the catcher foil at the ends of the vacuum vessel, the authors speculated that some sputtered carbon had also escaped from around the catcher foil. Additional deposition outside of the catcher foil could easily bring the co-deposition probability up to the newly measured value of 0.106. From the combination of experiments, it appears that enhanced sputtering occurs under the conditions used in these experiments. The logical explanation is that the enhanced erosion and co-deposition is due to the higher gas pressures used in the experiments. Operation of a plasma in a gas at this pressure is certain to produce a significant quantity of atomic hydrogen in and around the plasma. As shown by Haasz et al. [14], the erosion rate of graphite is significantly increased when atomic hydrogen is present during hydrogen ion implantation (chemical erosion dominates the erosion process). For a $[H_o/H^+]$ ratio of 10, the graphite erosion rate was seen to increase by an order of magnitude over that due to ions alone. While the 500 K temperature used in the experiments reported here is below the temperature for the peak production of methane, methane is still the likely hydrocarbon produced by the chemical erosion. Due to interference by OH, H_2O, HDO, and D_2O, no attempt was made to detect deuterated methane in the chamber at the termination of the plasma discharge.

As stated above, the measured sputtering coefficient for carbon is ≈0.03 [10, 11]. From the work of Plank et al. [15] and Balden et al. [16], the sputtering yield of silicon carbide for the same conditions is also ≈0.03. Balden et al. [17] and Balden and Mayer [18] examined the co-deposition of deuterium with silicon doped carbon. The ratio of D/(Si+C) in the collected films varied from about 0.4 to about 0.75, depending on the Si/(Si+C) ratio in the film. A value of 0.7 was determined for the case of Si/C=1. Based on these results, silicon carbide should be sputtered and co-deposit with deuterium at a rate equal to or greater than that for graphite. This calculated ratio of 1.0 or greater for silicon carbide co-deposition to that of graphite does not agree with the ratio of 0.68 determined in these experiments. It is perhaps not meaningful to even compare the results of these experiments to those performed under other conditions. If one accepts the premise that enhanced sputtering is occurring in these experiments, then a comparison to sputtering results dominated by physical sputtering does not make sense.

3. Deuterium retention and release from highly irradiated annealed tungsten after exposure to a deuterium DC glow discharge [19]

In collaboration with Brian Oliver at Pacific Northwest National Laboratory (PNNL) and Stuart Maloy at Los Alamos National Laboratory, experiments were performed on the retention and release of deuterium in highly irradiated annealed tungsten after exposure to a deuterium glow discharge. The divertor of the ITER fusion reactor will be made of tungsten, and will see very high neutron fluences during the ITER lifetime. The deuterium and tritium retention properties during that lifetime will depend on the damage done by the neutrons. In an earlier report [1], we examined the protium release from tungsten that had been irradiated by 800 MeV protons in the Los Alamos Neutron Science Center (LANSCE) beam line. Those experiments showed the high-energy protons to generate 1.4 eV traps to a density >1 at.%. In the experiments reported here, identical samples were annealed at 1273 K for 6 h, and then partially loaded with deuterium, to examine the effect of annealing on these traps. The DIFFUSE [20] computer code was used to determine the density and energy of the traps controlling retention and release. The tungsten samples were cut from tungsten target rods irradiated with 800 MeV protons in LANSCE between September and November 1996. Each sample was a thin disk 0.25 mm thick, formed by powder metallurgy, and had an elemental composition of 99.96% tungsten with the major impurities being Mo, C, and O. Proton fluence ranged from 1×10^{21} and 4×10^{19} p/cm^2, with displacement rates of 8 and 0.3 dpa. Irradiation temperature was 440 and 310 K. A number of control samples were also made from unirradiated rods from the same lot.

Before the deuterium glow discharge exposure, the samples were vacuum annealed to remove residual hydrogen isotopes formed during the irradiation. Annealing was done for 1 h (control sample) and 6 h (irradiated samples) at 1273 K. From earlier measurements [21], protium generation in the tungsten was

expected to range from 400 to 2000 appm, with deuterium and tritium levels being lower. Following annealing, each sample was exposed in a deuterium glow discharge. The sample was placed on a tungsten rod electrode which had the same diameter as the sample. Deuterium was continuously leaked into the system through a needle valve, while the chamber was being pumped. Deuterium pressure in the chamber was maintained between 0.5 and 1 torr. Discharge voltage was 1 kV; discharge current averaged about 100 μA. Each sample was exposed to the discharge for 6 h for a total deuterium fluence of 2.5×10^{20} D/cm^2. At 0.5 to 1 torr pressure, the average energy of the deuterium ions striking the tungsten surface is estimated to be less than 100 eV. To accommodate this reduction in energy, the deuterium was assumed to be distributed only over the first 4 μm for the modeling.

Hydrogen isotope release was measured using a specialized gas mass spectrometric system [22]. The samples were heated in a ceramic crucible whose temperature was linearly increased from 300 to 1430 K at a rate of 50 K/min. Gas release was measured as a function of time using a quadrupole mass detector tuned for mass 2 (H_2), 3 (HD), and 4 (D_2) amu. Calibration of the system was accomplished using a hydrogen (H_2) leak source. Deuterium sensitivity was determined from measurements on a separate H_2/D_2 gas source. Sensitivity for HD was calculated assuming a $(1/M)^{1.25}$ relationship.

For metals exposed to a hydrogen plasma, the parameters that determine both the amount of retained hydrogen and the subsequent release are diffusivity, recombination rate coefficient, and trapping energies and densities. Of the several formulas given in the literature for the diffusivity of hydrogen in tungsten, the formula given by Frauenfelder [4] ($D=4.1 \times 10^{-7}\exp(-0.39$ eV/kT) m^2/s) is considered to be most correct. Frauenfelder's experimental techniques were designed to minimize errors introduced by impurities and traps. The release rate of hydrogen from a surface is determined by the square of the surface concentration times the recombination rate coefficient. In the case of tungsten, it is not apparent that there is any holdup of hydrogen at the surface. Thus, it has been recommended [3] that an infinite value be assumed for the recombination rate coefficient, which is equivalent to assuming a boundary condition of C=0 at the surface. The number of trap sites for hydrogen in tungsten is strongly affected by the thermal history of the sample. Unirradiated tungsten samples annealed at 1273 K are known to have significantly fewer trap sites than unannealed samples [5]. A trap energy of 1.4 eV is assumed in this analysis, as it was in Ref. [1].

Our modeling of the results included all aspects of the experiment that had an effect on the deuterium release data. This included the 6h glow discharge, the 3–5 d waiting period between the discharge exposure and the outgassing, and the outgassing itself. In the thermal desorption of the unirradiated sample, a major peak at 530 K was accompanied by a minor peak at 450 K, and a small broad peak at relatively high temperatures. Only by assuming the 1.4 eV traps to be distributed over the large area of the first 30 nm with a concentration of 20 at.% could a reasonable fit to the low energy peak be achieved. It is believed that this trap density came from machining. The broad higher temperature peak was well fitted by the assumption of uniform 1.4 eV traps over the entire 300 μm thickness of the sample.

The thermal desorption spectra for both of the irradiated samples were very similar even though the radiation dose was considerably different. The desorption spectra shows three peaks: a distinct peak at about 400 K; another distinct peak at 530 K; and a shoulder type peak centered at about 800 K. The second and third peaks are due to the same traps described for the unirradiated sample. For the DIFFUSE code, the assumption of a machining-induced trap of 1.4 eV over the same 30 nm at a density of 8 at.% predicts a relatively sharp peak, closely resembling the experimental data. The lower trap density for this near-surface trap (8% vs. 20% for the unirradiated sample) is possibly due to the longer anneal at 1273 K (6 h vs. 1 h) for the irradiated samples. The higher temperature peak was modeled assuming a uniform distribution of 1.4 eV traps at a density of 4 appm. This density is only slightly higher than for the unirradiated sample, and suggests that the anneal was very effective at removing irradiation-induced traps. The inability to more accurately model this high temperature peak was likely due to a small fraction of deuterium also trapped at higher energy traps, perhaps chemisorbed on void surfaces.

The lowest temperature peak was the most interesting as it was almost totally absent for the unirradiated sample. This difference leads to the conclusion that the irradiation, or conditions present during the irradiation, significantly increased the responsible trap. Because these samples were irradiated with 800 MeV protons, the damage should be uniform throughout the relatively thin samples. Repeated modeling could not generate a release peak at this temperature using a uniformly distributed trap. Consider, however, that for the ≈2.5 months that the tungsten was irradiated, it was immersed in water at a temperature of 440 K. According to Fromm and Gebhardt [23], the diffusivity of oxygen in tungsten at this temperature is 1.5×10^{-16} cm^2/s. Thus, oxygen from the cooling water should have diffused 0.6 μm into the sample during the proton irradiation. Assuming that the oxide related traps were uniformly distributed over the outer 0.6 μm, it was determined that a 0.95 eV trap at a density of 0.35 at.% gave a reasonable fit to the experimental data.

The most surprising result of the present work was the absence of irradiation-induced traps in the irradiated samples. In earlier experiments [1] using identical samples, thermal desorption spectra were obtained for the protium already in the samples from the irradiation. To match these data, it was necessary to assume 1.4 eV traps at a concentration >1 at.%. In the present experiments, it was necessary to first anneal the irradiated samples to remove proton-generated deuterium and tritium that would have interfered with the signal from the deuterium implanted during the glow discharge exposure. From the work of Anderl et al. [8], it was known that annealing tungsten reduces the dislocation density on cell walls, with a one-to-one reduction in the 1.4 eV traps. The surprise was that a temperature of only 1273 K for 6 h could effectively remove all such traps from a highly irradiated tungsten sample. The results also suggest that hydrogen trapping at voids is not as prevalent as had been assumed prior to the experiments. If voids had played an important role in the trapping of protium in the earlier [1] samples, then these traps would still be active in these later experiments, and the overall level of trapping would have been much higher. It is not possible to anneal out voids in tungsten by heating to only 1273 K, so any voids present would have still remained.

4. Deuterium retention and release from molybdenum exposed to a Penning discharge [24]

In collaboration with Don Cowgill and Chris Kunz of Sandia National Laboratories, the retention and release of deuterium from molybdenum exposed to a Penning discharge has been measured. While molybdenum presents a problem of becoming highly radioactive when exposed to neutrons, it is still used as a plasma-facing material in fusion reactors where the neutron yield is below that of DEMO sized reactors. As a plasma facing material, molybdenum is subjected to intense fluxes of energetic deuterium and tritium ions and neutrals. This implantation process leads to concerns about tritium inventories in the molybdenum after long-term exposure to the DT plasma. The purpose of the experiments reported here was to determine the fractional retention of deuterium implanted into molybdenum at moderate temperatures.

The plasma used in these experiments was generated by a Penning discharge. The configuration consists of two parallel plates at equipotential that serve as cathodes. Along the rims of the plates are electrically isolated concentric shields that serve as anodes. There is a solenoidal magnetic field perpendicular to the set of electrodes. A 25.4 mm diameter button heater electrically isolated from the biased sample by a 1 mm thick sapphire disk was used to heat the sample.

In these experiments, a discharge current density of 12.5 A/m^2 was used. With the ions being primarily D_2^+, the particle flux to the cathodes was 1.5×10^{20} D/m^{2}s (not including neutrals, if present). A bias voltage of 1200 V was required to maintain the Penning discharge. Again assuming primarily D_2^+ source ions, the energy of the individual bombarding deuterons was 600 eV. The deuterium gas pressure in the system was held at 2.25 Pa and the magnetic field strength at 250 G. Each plasma exposure was conducted for 1 h. After removal from the implantation chamber, the samples were allowed to sit in room temperature air for approximately 10 days before placing them in a thermal desorption system. The samples were then elevated from room temperature up to 1373 K on a linear ramp of 1.67 K/s. A mass spectrometer was used to monitor the mass 3 (HD) and mass 4 (D_2) peaks. The samples used in this study were 99.95% molybdenum from EagleAlloys. These samples were left in the as received condition after cutting, but were annealed in vacuum at a temperature of 1273 K for 1 h prior to plasma exposure. The disk samples were 50 mm in diameter and 2 mm thick.

It is important in the understanding of the results presented here that it be realized that the retention of deuterium in the molybdenum consists only of trapped deuterium. The mobile component diffuses out of the samples in the first few hours after termination of the experiment. The fractional retention of the implanted deuterium that remained in the samples varies from a high of 1×10^{-4} at 573 K down to a level of approximately 4×10^{-6} at 773 K. The thermal desorption spectra of the samples exposed at 573 K and 673 K were used in an attempt at modeling the release as a function of temperature. Assuming the diffusion to be given by the expression provided by Perkins [25] ($D=4.8 \times 10^{-7}$ exp(-0.39 eV/kT) m^2/s), and assuming 1.4 eV [26-29] to be the correct trapping energy did not give a proper fit to the data. It was obvious that a higher energy trap was controlling the release. A much better fit was achieved when an additional trap energy of 2.1 eV was assumed to occur in the 573 K sample and a 2.9 eV trap for the 673 K sample. In both cases, the higher energy traps are assumed to extend from the surface to a depth of 50 nm, approximately 2.5 times the implant range. Assuming both traps to extend beyond the implant zone was based on the belief that mobile vacancies would extend outside of that area. Overall, the fitting results were not strongly affected by assumptions on the density or location of the 1.4 eV traps. The trap energy of 2.1 eV and trap density of 1.5×10^{-2} atomic fraction for the 573 K sample were fitting parameters necessary to generate even reasonable agreement between experimental results and computer results. A trap energy of 2.9 eV with a trap density of

3.5×10^{-3} were the parameters necessary for the 673 K sample. It is interesting to note that the 573 K sample released deuterium both at temperatures below and above that of the main peak. It is hypothesized that perhaps the release at temperatures below the peak is the transition away from the release controlled by the 1.4 eV trap, and the release at temperatures above the peak is the transition to the higher 2.9 eV trap seen for the 673 K sample. The samples implanted at 723 K and 773 K showed only the 2.9 eV desorption peak.

To understand these experiments' results, it is necessary to be able to explain what physical phenomenon could result in such high temperature trapping as well as what could shift the apparent trap energy by 0.8 eV when increasing the implant temperature by only 100 K. The first task is easier than the second. Sakamoto et al. [30] observed microbubbles in samples implanted with 4 and 8 keV protons at temperatures of 573 K and above, but no such microbubbles at lower temperatures. Based on the similarities of the implant conditions for their experiments and ours, we conclude that our samples also developed microbubbles during the implantation. We have evidence from the work of Van Veen et al. [8] that atomic hydrogen can be chemisorbed on the surfaces of voids in proton irradiated tungsten. In that case, the release of the hydrogen was effectively controlled by a 1.8–2.1 eV trap. The 0.8 eV shift in the activation energy is simply not understood. Possibilities include changes in the void size or the movement of impurities to the void wall surfaces.

The interesting shift in trap activation energy should not overshadow the primary result. The primary result is the very low retention fraction noted for all of the samples. Retention fractions of 10^{-4}–10^{-6} as reported here will strongly limit the tritium inventory of molybdenum in next-step devices. Molybdenum used in next-step devices such as ITER would almost certainly be operated at temperatures above the 773 K maximum temperature used in these experiments. The elevated temperatures would lead to tritium retention fractions in those applications being even lower than the values measured in these experiments.

5. He-O glow discharge at elevated temperatures for removal of the co-deposited C/H layer [31]

In collaboration with Chris Kunz, Bill Wampler, Don Cowgill, and Bernice Mills, all of Sandia National Laboratories, He-O glow discharge along with heating has been attempted as a way to remove fusion reactor co-deposited layers. The co-deposition of carbon with the deuterium and tritium fuel in tokamaks presents a tritium inventory problem to fusion plant designers. Unless disruptions can be controlled, graphite or carbon composites must be placed in the bottom of the tokamak divertor to allow the vacuum vessel to survive the tremendous energy deposition during a disruption. With carbon present, nearby surfaces where the rate of deposition is greater than the erosion rate will have co-deposited layers of carbon and hydrogen isotopes growing indefinitely. Since ITER will be operating with a mixture of tritium and deuterium, the co-deposited layer has a high potential for generating an excessive tritium inventory. If we combine the high tritium inventory with the fact that the a-C:H co-deposited layer is not stable at elevated temperatures in the presence of air [32], we have a potential environmental hazard in the event of an accidental vacuum loss when the tokamak vessel is hot.

Removal of the co-deposited carbon/hydrogen layer by He-O discharge at room temperature has been attempted in the past. Hsu [33] compared the glow discharge removal rate of a co-deposited layer using several different types of gases. Of nitrogen, hydrogen, helium, and oxygen, only oxygen (in the form of He-O) was found to have a measurable removal rate. He determined an effective removal rate of approximately 5 atoms of carbon for each oxygen ion striking the layer. While the film was produced by the plasma decomposition of methane, and was therefore a soft film with a significant fraction of weakly bound atoms, this result certainly suggested that He-O might present a reasonable removal process for the co-deposited layer. In unpublished experiments [34], Cowgill used a He-O discharge to remove a co-deposited layer from a tile taken from the TFTR reactor. These experiments demonstrated a removal rate of ~1.2 μm/r (about 2.5 carbon atoms/O ion) during the initial stage of the experiment, but noted that the removal rate decreased with time. The decrease was attributed to surface texturing. He-O glow discharge was also used directly in the TFTR reactor. Nagy et al. [35] reported that the technique performed well initially, but decreased with time. For the same experiments, Skinner [36] reported the process to release 50 Ci/hr, and to be constant with time. This value should be compared to an initial removal rate of 170 Ci/hr for deuterium glow discharge, but a steady state release rate of only 10 Ci/h. In a somewhat related series of experiments, Jacob et al. [37] performed a systematic study of the removal of a-C:H layers using electron cyclotron resonance discharges (ECR). Several different species were used for the ECR low-pressure discharges (O_2, D_2, H_2, H_2O, and O_2/H_2), but oxygen always showed the highest removal rates. They noted a co-deposited removal rate as high as 1.7 μm/h at 300 K. The authors noted increased yield with increased voltage or temperature, but found the two were not additive.

The experiments reported here add heating during the He-O discharge to see if a more effective removal

rate can be achieved. An area of net deposition on a graphite tile removed from TFTR prior to the DT campaign was used to provide a co-deposited layer similar to that expected for ITER. Small samples cut from these tiles were examined prior to and after exposure to a He-O at temperatures from 373 K up to 513 K for one to four hours. Changes in the layer thickness and near-surface deuterium content were measured.

Samples used in this experimental program were obtained from a graphite tile removed from the TFTR reactor. The tile had remained in the reactor for many months of deuterium operation, and was covered with a relatively thick co-deposited layer. The samples were obtained by slicing an approximately 2 mm thick layer off of the top of the graphite tile. The area of the tile from which the samples were obtained was selected only after microscopy of the entire tile had shown this area to have a relatively uniform co-deposited layer. The samples were first examined microscopically using Auger scanning electron microscopy. They were then analyzed using He^3 Nuclear Reaction Analysis (NRA) to determine the deuterium concentration versus depth to a depth of about 1.2 mg/cm^2. If the film is assumed to have a density of 1.5 g/cm^3, typical of tokamak co-deposited layers, the 1.2 mg/cm^2 would correspond to a thickness of 8 μm. Additionally, 2.5 MeV proton RBS was used to determine the total thickness of the film. The samples were then exposed to a He-O glow discharge at temperatures varying from 373 K to 513 K (the latter being the highest obtainable temperature in the ITER reactor). The gas consisted of 80% helium and 20% oxygen, and was held at a pressure of 13.2 Pa during the discharge. Slowly pumping on the vacuum vessel at the same time as fresh gas was supplied retained the purity of the gas. A voltage of 470 V was required to generate the discharge, and an incident flux of approximately 10^{19} ions/m^{2}s was obtained. After exposure to the discharge, the samples were then analyzed again using the Auger scanning electron microscopy technique and ion beam analyses.

Two different techniques were used to determine the amount of the co-deposited layer removed. The first technique involved direct observation of the sample before and after He-O glow discharge using scanning electron microscopy. The second technique was 2.5 MeV RBS. Additionally, the amount of deuterium removed from the co-deposited layer was determined using nuclear reaction profiling. For the scanning electron microscopy, overlaying the pictures before and after the glow discharge did not reveal any change in the dimensions of the samples. Only in the extreme case of longer running at the higher temperature could any change be noted at all. For that sample, the exposed sample had a surface appearance of having hair or grass.

It is interesting to examine the upper limit of removal as determined by the RBS technique. The sample exposed to the glow discharge for 4 hours at 443 K is considered here. For this sample the upper limit of removal is 5% of 13.3 μm, or 0.667 μm. Based on a density of 1.5 g/cm^3, this distance represents 5×10^{18} carbon atoms removed per cm^2. During the 4 hour exposure, the total fluence was 1.44×10^{19} ions/cm^2. This result would suggest a removal rate of approximately 0.35 carbon atoms/ion. This amount should be compared to the approximately 5 carbon atoms/ion reported by Hsu [33]. There are two possible explanations for this difference in apparent removal rates. One possibility is that the film examined by Hsu was different. That film was produced by the plasma decomposition of methane. Depending upon the deposition conditions, films produced by this technique may have a higher hydrogen content and a lower density. While it is possible that the two different film types do in fact have different removal rates, another possibility is that the removal rate may start out at a very high rate, but decrease with time. This is exactly what was seen by Cowgill [34] in his unpublished study on He-O removal of co-deposited layers. Monitoring of the CO and CO_2 levels in the chamber using a differentially pumped mass spectrometer showed the apparent etch rate of the co-deposited layer to substantially decrease with time. Microscopic examination of his samples after exposure revealed a grass-like or hair-like structure. Glow discharge produces an ion flux that is normal to the sample surface. It is quite likely that this normal angle of incidence creates the special structure that is resistant to further removal. Part of the justification for the present study using increased temperature was to examine whether the oxygen would react with the individual strands of the structure to result in a continuous, high removal rate. The apparent answer is that this does not occur. The initial versus long-term removal rate may also explain the difference in the results seen in the present study and that performed by Jacob et al. [37]. Their maximum removal rate was 1.7 μm/h while the present results were limited to only 0.17 μm/h (0.667 μm/4 hours). Due to there being no reference to time or thickness in their report, it is not possible to conclude that this is the explanation. It would only be necessary for their films to have a thickness less than the length of the grass-like structure for this explanation to hold.

While the above results show He-O glow discharge cleaning with heating to be an ineffective removal technique for a thick co-deposited layer, the results do not show the technique to also fail at removal of the hydrogen isotopes from the layer. To examine the hydrogen isotope removal, nuclear reaction profiling was used. Examination of the profiles from all of the samples appears to suggest some losses of deuterium throughout the first micron or so; it is more likely that the loss of deuterium is restricted to only that very near the surface.

Removal of either 5 nm or 500 nm would appear almost identical due to both being less than the depth resolution of the technique. The energetic oxygen ions from the He-O glow should only penetrate about 5 nm into the deposited layer.

6. Refilling of the depleted co-deposited layer with hydrogen

In a collaboration with Bob Bastasz and Bernice Mills of Sandia National Laboratories, experiments were performed to determine the ease at which the co-deposited layer is refilled with hydrogen after its removal. In this experiment, a tile removed from the TFTR reactor prior to tritium operations was used as the source of co-deposited layers. Visual examination of the tile surfaces revealed areas of net erosion and net deposition. 1 cm × 1 cm samples were taken only from the areas of greatest deposition. One at a time, the samples were placed in an outgassing system connected to a mass spectrometer. The samples were initially heated to 423 K to allow removal of any water vapor before heating to higher temperatures. Rapid heating to temperatures above about 700 K without removal of the water permits the water to react with the carbon in the layer as well as the graphite substrate. After holding the samples at 423 K for more than one hour, the samples were elevated to 1273 K during a 60 second ramp, and then held at that temperature for 60 more seconds. The quantity of deuterium released during the ramp and hold was determined by a calibrated mass spectrometer. The samples were then transferred in air to a system containing an atomic deuterium source. Some of the samples were allowed to sit in air for up to two weeks prior to exposure to the atomic deuterium. The atomic deuterium flux from the source was 3×10^{14} D/s. The results of these experiments are shown in the table below.

Sample number	Initial deuterium	Atomic fluence	Deuterium uptake
S2	1.43×10^{19} D	2×10^{18} D	5.5×10^{17} D (28%)
S1	1.16×10^{19} D	1×10^{19} D	1.2×10^{18} D (12%)
Virgin Graphite	None	2×10^{18} D	2.0×10^{16} D (1%)

It should be noted that the percentages shown in the last column represent the fraction of the atomic deuterium that is absorbed in the depleted layer, not the fraction of sites refilled. From sample S1, 28% of the atomic fluence is absorbed. When the fluence is increased by an order of magnitude, only 12% of the total is absorbed. The conclusion to be drawn from the results is that the layer can be partially refilled, but complete refilling appears to be impossible. It is logical that many of the dangling bonds left when the hydrogen is removed from the layer are healed during the temperature excursion.

There is one other cautionary note that should be sounded. All of the samples were transferred through air after depletion of the deuterium. It is possible that some of the dangling bonds may be occupied by water vapor from the air. If the samples were left in vacuum after depletion, there is a possibility that the remaining bonds could be greater. Additional experiments are warranted.

References

[1] OLIVER, B.M., VENHAUS, T.J., CAUSEY, R.A., GARNER, F.A., MALOY, S.A., Hydrogen release from 800 MeV proton-irradiated tungsten, J. Nucl. Mater. **307** (2002) 1418.

[2] LONGHURST, G.R., HOLLAND, D.F., JONES, J.L., MERRILL, B.J., TMAP4 (Tritium Migration Analysis Program Version 4) User's Manual, INEL Report EGG-FSP-10315, EG&G Idaho, Inc. (June 12, 1992).

[3] CAUSEY, R.A., VENHAUS, T.J., The use of tungsten in fusion reactors: a review of the hydrogen retention and migration properties, Physica Scripta **T94** (2001) 9.

[4] FRAUENFELDER, R., Solution and Diffusion of Hydrogen in Tungsten, J. Vac. Sci. Technol. **6** (1969) 388.

[5] ANDERL, R.A., HOLLAND, D.F., LONGHURST, G.R., PAWELKO, R.J., TRYBUS, C.L., SELLERS, C.H., Deuterium transport and trapping in polycrystalline tungsten, Fusion Technol. **21** (1992) 745.

[6] ELEVELD, H., VAN VEEN, A., Deuterium interaction with impurities in tungsten studied with TDS, J. Nucl. Mater. **191–194** (1992) 433.

[7] ELEVELD, H., VAN VEEN, A., Void growth and thermal desorption of deuterium from voids in tungsten, J. Nucl. Mater. **212–215** (1994) 1421.

[8] VAN VEEN, A., et al., Hydrogen exchange with voids in tungsten observed with TDS and PA, J., Nucl. Mater. **155–157** (1988) 1113.

[9] CAUSEY, R.A., Sputtering and codeposition of silicon carbide with deuterium, J. Nucl. Mater. **313–316** (2003) 450.

[10] BALDEN, M., ROTH, J., New weight-loss measurements of the chemical erosion yields of carbon materials under hydrogen ion bombardment, J. Nucl. Mater. **280** (2000) 39.

[11] ROTH, J., Chemical erosion of carbon based materials in fusion devices, J. Nucl. Mater. **266–269** (1999) 51.

[12] WINTER, J., Surface conditioning of fusion devices by carbonization: hydrogen recycling and wall pumping, J. Vac. Sci. Technol. A **5** (1987) 2286.
[13] HSU, W.L., CAUSEY, R.A., Pumping of hydrogen during plasma-graphite interaction, J. Vac. Sci. Technol. A **5** (1987), p. 2768.
[14] HAASZ, A.A., et al., Synergistic methane formation on pyrolytic graphite due to combined H^+ ion and H^0 atom impact, J. Nucl. Mater. **145–147** (1987) 412.
[15] PLANK, H., SCHWORER, R., ROTH, J., Erosion behaviour and surface composition modifications of SiC under D+ ion bombardment, Nucl. Instrum. and Meth. B **111** (1996) 63.
[16] BALDEN, M., PICARLE, S., ROTH, J., Mechanism of the chemical erosion of SiC under hydrogen irradiation, J. Nucl. Mater. **290–293** (2001) 47.
[17] BALDEN, M., MAYER, M., ROTH, J., Co-deposition of deuterium with silicon doped carbon, J. Nucl. Mater. **266–269** (1999) 440.
[18] BALDEN, M., MAYER, M., Removal of deuterium from co-deposited carbon-silicon layers, J. Nucl. Mater. **283–287** (2000) 1057.
[19] OLIVER, B.M., CAUSEY, R.A., MALOY, S.A., Deuterium retention and release from highly irradiated annealed tungsten after exposure to a deuterium DC glow discharge, J. Nucl. Mater. **329–333** (2004) 977.
[20] BASKES, M.I., DIFFUSE-83, Report SAND83-8231, Sandia National Laboratory (1983).
[21] OLIVER, B.M., et al., High-sensitivity quadrupole mass spectometry system for the determination of hydrogen in irradiated materials, J. Nucl. Mater. **283–287** (2000) 1006.
[22] OLIVER, B.M., et al., Effects of Radiation on Materials: 20th International Symposium, ASTM Special Technical Publication 1405, American Society for Testing and Materials, West Conshohocken, PA (2001).
[23] FROMM, E., GEBHARDT, E., Gase und Kohlenstoff in Metallen, Springer, Berlin (1976) p. 555D.
[24] CAUSEY, R.A., KUNZ, C.L., COWGILL, D.F., Deuterium retention and release from molybdenum exposed to a Penning discharge, J. Nucl. Mater. **337–339** (2005) 600.
[25] PERKINS, W.G., Permeation and outgassing of vacuum materials, J. Vac. Sci. Technol. **10** (1973) 543.
[26] KERIEM, M.S., VAN DER WERF, D.P., PLEITER, F., Hydrogen-vacancy interaction in molybdenum, J. Phys: Condens. Matter **5** (1993) 1801.
[27] NORDLANDER, P., et al., Multiple deuterium occupancy of vacancies in Pd and related metals, Phys. Rev. B **40** (1989) 1990.
[28] TAKAGI, I., WATANABE, S., NAGAOKA, S., HIGASHI, K., Trapping of hydrogen in molybdenum bombarded with helium-3 ions, Fusion Sci. Technol. **41** (2002) 897.
[29] HANSON, A.L., VINCENT, D.H., DAVIDS, C.N., Hydrogen trapping in molybdenum in the presence of radiation damage, J. Nucl. Mater. **98** (1981) 259.
[30] SAKAMOTO, R., MUROGA, T., YOSHIDA, N., Microstructural evolution in molybdenum during hydrogen ion implantation with energies comparable to the boundary plasma, J. Nucl. Mater. **212–215** (1994) 1426.
[31] KUNZ, C.L., CAUSEY, R.A., CLIFT, M., WAMPLER, W.R., COWGILL, D.F., Removal of the codeposited carbon layer using He–O glow discharge, J. Nucl. Mater. **367–370** (2007) 1512.
[32] HAASZ, A.A., DAVIS, J.W., The removal of codeposited layers from TFTR tiles by O_2 gas exposure, J. Nucl. Mater. **256** (1998) 65.
[33] HSU, W.L., Glow-discharge removal of codeposited carbon films in graphite-lined tokamak reactors, J. Vac. Sci. Technol. A **7** (1989) 1047.
[34] COWGILL, D.F., personal communication.
[35] NAGY, A., et al., Tritium recovery from the TFTR vessel, 17th IEEE/NPSS Symposium on Fusion Engineering **1–2** (1998) 317.
[36] SKINNER, C.H., et al., Measurements of tritium retention and removal on the Tokamak Fusion Test Reactor, J. Vac. Sci Technol. A **14** (1996) 3267.
[37] JACOB, W., LANDKAMMER, B., WU, C.H., Removal of codeposited layers by ECR discharge cleaning, J. Nucl. Mater. **266–269** (1999) 552.

Hydrogen retention in mixed materials

R.P. Doerner and the PISCES Team

Center for Energy Research, 9500 Gilman Dr., University of California – San Diego, La Jolla, CA 92093-0417, U.S.A.

Abstract

The deuterium inventory in mixed-material surface layers formed during beryllium-containing plasma bombardment of graphite surfaces is investigated. The beryllium-containing plasma simulates the erosion of first wall material into the ITER SOL plasma and its subsequent flow towards the carbon divertor plates. The experiments are designed to quantify the behavior of plasma-created mixed Be/C and Be/W surfaces. Developing an understanding of the mixed-material surface behavior is crucial to accurately predicting the tritium accumulation rate within the ITER vacuum vessel. A new periodic heat pulse deposition system is also installed on PISCES-B to simulate the transient temperature excursions of surfaces expected to occur in the ITER divertor during ELMs and other off-normal events. These periodically applied heat pulses allow us to study the effects of transient power loading on the deuterium content of mixed-material surfaces that are created during the experiments.

1. Introduction

A bilateral US(DOE)-EU(EFDA) collaboration, focused on experiments performed in the PISCES-B linear divertor simulator [1, 2], utilizes a beryllium-seeded deuterium plasma to investigate mixed-material erosion and co-deposition properties of ITER relevant divertor materials. The experimental program is designed to reduce uncertainties in the prediction of tritium retention in co-deposited mixed materials in ITER and other future burning plasma devices. The beryllium-containing plasma simulates the erosion of first wall material into the ITER SOL plasma and its subsequent flow towards the carbon and tungsten material located in the ITER divertor region.

This paper will summarize the primary, significant results that this collaboration has produced. It will relate these results to the operating conditions expected in ITER and attempt to predict what the consequences of mixed materials on the ITER plasma-facing surfaces might be.

The first, most dramatic result obtained from this collaboration was the suppression of carbon erosion, both physical sputtering and chemical erosion, at very low levels (~0.1%) of incident beryllium impurity ions [3, 4]. Typical deuterium plasma parameters in PISCES-B are: ion flux ~4×10^{22} $m^{-2}s^{-1}$, incident ion energy ~50 eV and surface temperature ranging from 400 to 1300 K. This result was confirmed using both spectroscopic as well as weight loss measurements. These initial measurements focused on the equilibrium state of the plasma-exposed surface. In other words, long fluence plasma exposures were performed, after which the surfaces of the plasma-bombarded targets were examined. In addition, during these large fluence exposures material collectors (referred to as witness plates) were positioned outside the plasma column to collect eroded material [5].

Subsequent experiments have documented the temporal evolution of the mixed beryllium-carbon plasma-created surface [6, 7]. Through focusing on the time-dependent evolution of the surface and its associated plasma–material interactions, we believe we have been able to identify the fundamental mechanisms responsible for the mitigation of carbon erosion from the mixed-material surface. A thin, protective Be_2C layer forms on the plasma-exposed carbon surface, and this surface layer is responsible for the chemical erosion suppression [8]. An ongoing series of experiments is examining the response of the mixed-material surface layer to periodically applied thermal transients [9] with the goal of understanding how such thin surface layers might react to off-normal events in ITER.

In addition to mixed Be/C studies, the issue of alloy formation between beryllium and tungsten is under investigation [10]. Various beryllide (Be_xW) alloys have been observed to form during different plasma exposure conditions. Again by understanding the formation conditions of these alloys, it will increase the confidence in predictions regarding their importance to the ITER design.

This paper will focus on the hydrogen isotope retention properties of the mixed-material surfaces that have been formed during these experimental activities. In addition, the deuterium content in co-deposited material collected during these mixed-material plasma exposures will be described.

2. Deuterium retention in mixed Be/C target surfaces

Information on deuterium inventory and thermal stability of graphite targets following exposure to beryllium-containing deuterium plasma is inferred from gas desorption profiles during thermal desorption mass spectrometry (TDS) [11]. During TDS, targets are heated linearly in vacuum over 1 h to ~1400 K while the partial pressures of deuterium-containing species D_2, HD, D_2O, CD_3 and CD_4 are monitored using a residual gas analyzer. D_2 and HD are typically the prominent desorption species and deuterium retention is calculated from the weighted integral of their partial pressure profiles. A calibrated deuterium leak, assumed applicable also for the mixed isotope HD, facilitates conversion of the desorption integrals into a total retention value.

Fig. 1 shows desorption spectra for two target temperature regimes of ~600 K and ~1000 K. Spectra for targets exposed to pure deuterium and deuterium with f_{Be} = 0.001 plasma are compared. Targets exposed to pure deuterium plasma received a total ion fluence of 4.0×10^{26} m^{-2} while those subject to beryllium contamination plasma received a smaller fluence of only 2.0×10^{26} m^{-2}.

Fig. 1 shows desorption flux trends for the deuterium-containing species, m/e = 3 (HD), 4 (D_2) as the targets are heated under vacuum at a constant rate of temperature increase to 1373 K. There is no convincing trend in CD_4 desorption or any other deuterium species found to be significant. The deuterium uptake in graphite is increased in targets exposed to beryllium-containing plasma compared to pure deuterium plasma. This result has also been confirmed with Nuclear Reaction Analysis (NRA) of the exposed samples [12]. For targets exposed at ~600 K, thermal release is characterized by a release peak ~800 K with more than a factor of 5 increase in the amount of desorbed deuterium in the beryllium-contaminated case. The targets exposed at ~1000 K do not show strong thermal release ~900 K presumably because of the higher temperature during plasma exposure. In both temperature regimes the mixed-material surface shows a reduced temperature for the onset of desorption.

In Fig. 2 retention is plotted against target surface temperature during exposure. Data are shown for graphite targets exposed to both beryllium containing, f_{Be} = 0.001, and pure, deuterium plasma exposures. The plasma fluences vary from 2 to 5×10^{26} D ions m^{-2} in this data set. The data show that retention falls significantly with exposure temperature. However, targets with a mixed beryllium/carbon surface show systematically higher retention than targets without. Retention in targets with a mixed-material surface is increased by ~4 at temperatures below 600 K but this difference is reduced to ~2 at ~1000 K. Interestingly, similar trends are observed

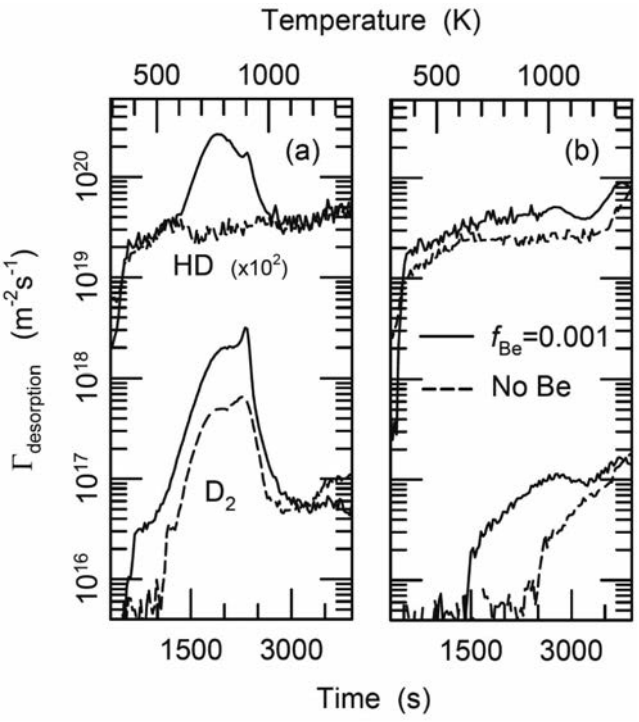

Fig. 1. Thermal desorption spectroscopy profiles for graphite targets exposed to pure and beryllium-contaminated (f_{Be} = 0.001) deuterium plasma at ~600 K (a) and 1000 K (b). The deuterium ion fluence was 4.0×10^{26} m^{-2} for the case without beryllium injection and 2.0×10^{26} m^{-2} for the cases with beryllium injection.

in the reversed scenario. Also shown in Fig. 2 are PISCES mixed-materials retention data from Doerner et al. [13]. In those experiments, pure beryllium targets are exposed under similar conditions to the present study, and retention is compared for plasma exposures with and without deuterated methane (CD_4, ~2 %) injection. As with the present study, retention is increased in beryllium targets with a mixed-material layer and the difference narrows at temperatures beyond 600 K.

Retention measurements made using IBA and TDS techniques show that a mixed material Be/C layer significantly increases hydrogen isotope trapping. NRA measurements show that the deuterium is trapped at shallow depths with most of the deuterium likely located in the mixed-material surface. In spite of this however, TDS thermal release characteristics, as in Fig. 1, show remarkable similarity, possibly suggesting that release mechanisms are tied with carbon rather than beryllium. It is further noted that desorption trends are not reminiscent of pure beryllium [14] or beryllium co-deposits [15]. For graphite targets exposed to pure deuterium plasma, deuterium retention values and dependence on exposure temperature are found to be consistent with data reported in Ref. [16]. In contrast, the presence of a mixed Be/C layer on targets is found to increase deuterium retention up to a factor of 4 at low temperature ~300 K but this difference is less, ~2, at temperatures ~1000 K. These results are at least consistent with retention studies on

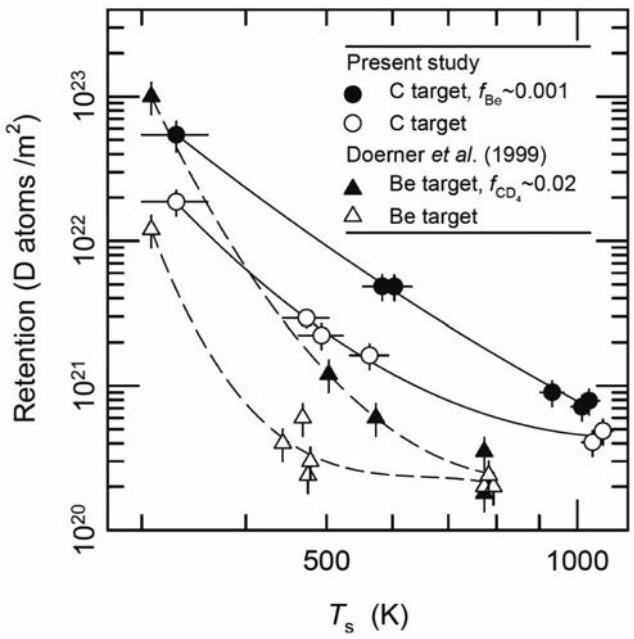

FIG. 2. Deuterium retention in targets as a function of target temperature during plasma exposure. Data are shown for the present study, graphite targets exposed to deuterium plasma with and without beryllium injection (f_{Be} = 0.001) and compared to data from Doerner et al. [13], pure beryllium targets exposed under similar plasma conditions with and without deuterated methane (CD_4, ~2 %) injection. Both data sets reveal increased retention where a mixed beryllium/carbon surface is present.

carbide-doped graphites [17]. However, it must be noted that there are significant chemical and structural differences between the carbidic layers of this study and the doped graphites of Ref. [17].

3. Deuterium retention in co-deposited material

The formation of beryllium carbide surface layers on the graphite targets also affects the redeposited material collected on the witness plate samples. Figure 3 shows the elemental depth profile (obtained using X-ray photoelectron spectroscopy (XPS)) of the redeposited material collected on a tantalum witness plate during exposure of a graphite sample at 1000 K to a 0.1% Be seeding rate plasma [5]. The redeposited material is seen to consist almost entirely of beryllium, with only trace amounts of oxygen and carbon throughout most of the layer. The average deuterium content in this layer is consistent with previous retention measurements in 'clean' redeposited beryllium [18] at low temperature as seen in Fig. 4.

While the hydrogen content of beryllium and carbon co-deposited films is found to be similar during room temperature deposition, the hydrogen content in Be films decreases much faster with increasing deposition temperature than that in carbon films. The temperature dependent release of the deuterium from co-deposisted

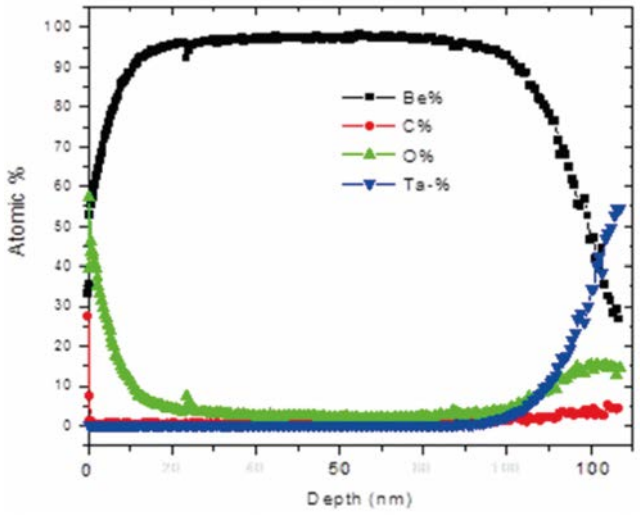

FIG. 3. Elemental depth profile obtained by XPS of the co-deposited material collected on a witness plate coupon during the exposure of a graphite target to beryllium-seeded deuterium plasma at 1000 K.

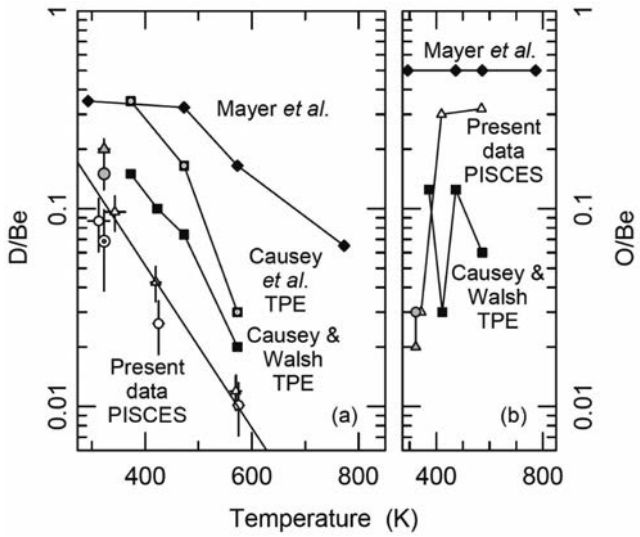

FIG. 4. D/Be (a) and O/Be (b) ratios for deposited material collected on Ta (grey symbols), Mo (dotted symbols) and W (white symbols) witness plate coupons as a function of coupon temperature. Target temperatures are indicated by triangular (~600K) and circular symbols (~1000K). (References: Mayer et al. [17], Causey and Walsh [18], Causey et al. [19], present PISCES data [15]).

material collected during Be seeding experiments is shown in Fig. 5. This data is generated from thermal desorption of the witness plate samples from PISCES-B and can be co-nsidered typical of the release behavior of the accumulated codeposited material in the ITER divertor during a baking cycle. One can see that during a 375°C bake of the ITER divertor (a temperature that is achievable in the ITER divertor after draining of the coolant channels) the D/Be ratio drops to less than 1%. Also shown in the figure for comparison is the temperature dependent deuterium release from co-deposited carbon films [19].

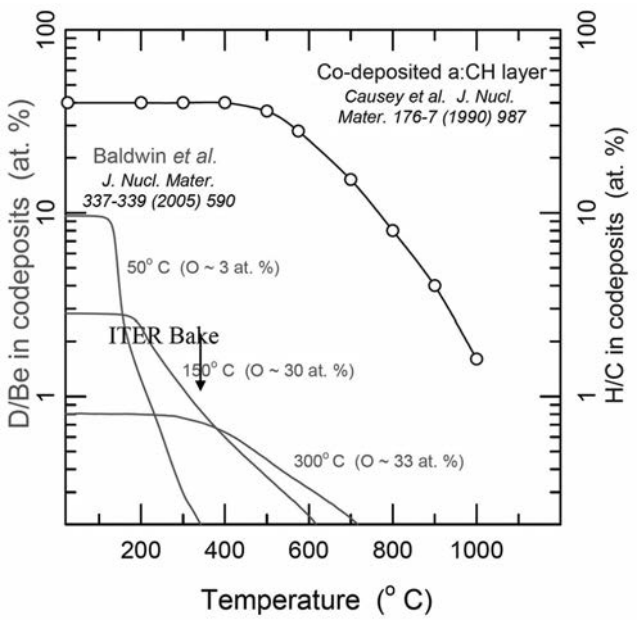

FIG. 5. Comparison of the amount of hydrogen isotope remaining in beryllium based and carbon based co-deposits after thermally annealing to a given temperature. The temperature of an ITER divertor bake, after coolant draining, is also indicated in the plot.

It is interesting to note that the initial temperature of the wall during the deposition of the material affects the release behavior. The deuterium trapped during room temperature collection is released at lower temperature than that collected during higher temperature wall operation. This may be due to the fact that the material structure varies depending on the deposition temperature, or it may be related to the oxygen content of the films (see Fig. 4). Work is continuing in this area to try to isolate the cause of the differences.

Another difference between a beryllium-rich and a carbon-rich co-deposit will be in its location. Beryllium has a high sticking coefficient and will be deposited in locations with line-of-sight views of the erosion location, whereas carbon has been found to migrate into pump ducts, behind tiles and to other non-line-of-sight locations [20].

4. Transient temperature excursion experiments

An important issue related to the formation of mixed-material surfaces in the ITER environment will be their response to off-normal events, such as ELMs and possibly disruptions. Although these events do not occur in the PISCES devices, certain aspects of their occurrence can be simulated. The impact of periodic surface temperature excursions is being investigated during beryllium-seeded plasma discharges by applying a short-duration positive bias to the targets exposed in PISCES-B [9]. Typically, targets are biased negatively in PISCES to provide the ion bombarding energy, however, a positive pulsed bias can be applied to collect electron current, and thereby heat, to the targets repetitively during the plasma exposure. Varying the voltage of the positive bias controls the power flux to the target.

Although these systematic experiments are just beginning, a few observations have already been documented. First, during power fluxes that vary the target temperature from the steady-state value of 800 K, up to 1500 K during the heat pulse (with a heat pulse duty cycle of 1%), the mitigation time of the chemical erosion of the target is seen to decrease dramatically [9]. This behavior is understandable from the mitigation time scaling studies [6] described above (at higher surface temperature the beryllium and carbon atoms in the surface react more readily to form beryllium carbide, thereby reducing chemical erosion). The second result is that the amount of deuterium retained in the targets increases, by roughly 50%, during heat pulse experiments when compared to identical exposures without the application of the positive bias heat pulses. This indicates that the high temperature excursions of the surface are acting to increase the diffusivity of deuterium into the sample, rather than increasing the recombination and release of deuterium from the target surface. The pulsed-power supply system has recently been upgraded to allow the application of higher positive bias voltage pulses to the targets.

5. Be/W mixed-material studies

The other mixed-material system relevant to the ITER device is the Be/W binary mixture. The tungsten beryllide system [21] consists of three alloys (Be_2W, $Be_{12}W$ and $Be_{22}W$) all of which have a lower melting temperature than pure tungsten. The importance of beryllide alloy formation was initially observed in PISCES-B due to the unexpected deterioration of the tungsten crucible used in the beryllium oven during the seeding experiments [22]. Subsequent studies of beryllide formation in tungsten samples exposed to beryllium-seeded deuterium discharges have identified the region of plasma conditions necessary for the alloys to form and grow [10].

In the plasma environment, beryllides begin forming in tungsten surfaces when the temperature reaches about 600°C [10]. However, the diffusion rate of beryllium into tungsten only becomes significant above about 800°C [23]. It has also been demonstrated that the growth rate of the beryllide alloy is restricted when insufficient beryllium exists in the surface [10].

Although there is no information yet available on the deuterium retention characteristics of these mixed Be/W surfaces, one could expect that the high

temperatures necessary for their formation might result in little retention of hydrogen isotopes. This, however, still needs to be experimentally verified and is an ongoing area of research.

6. Summary

Operation of the presently designed ITER device will result in the formation of mixed materials consisting of beryllium, carbon, tungsten and oxygen. The hydrogen isotope retention properties of these beryllium-containing mixed materials have been summarized in this report.

Mixed Be/C surfaces, whether they exist on beryllium or carbon substrates, tend to retain a larger amount of deuterium during low temperature (<700 K) exposure to plasma. However, the difference between the retention of pure and mixed Be/C surfaces tends to disappear during plasma exposure at higher surface temperature (>800 K). Since even the coolest surfaces in ITER will exceed 500 K (the inlet temperature of the coolant), the impact of mixed-material formation on plasma-contacting surfaces will likely be small. However, the mixed-material surfaces that form in ITER will likely determine the material that is eroded and redeposited away from these plasma-contacting locations.

In PISCES-B, and likely in ITER, the co-deposited material is dominated by beryllium eroding from the mixed-material targets. Deuterium is retained at a lower level in, and much more easily removed thermally from, beryllium-rich co-deposits, compared to carbon-rich co-deposits.

Acknowledgements

This work was performed as part of the US-EU Bilateral Collaboration on Plasma–Material Interaction Experiments on C/Be/W Materials that is funded by both the USDOE and EFDA. The dedicated efforts of many individuals both within the US fusion program, as well as throughout the EU, have made this a mutually beneficial collaboration and are gratefully appreciated.

References

[1] GOEBEL, D.M., CAMPBELL, G., CONN, R.W., Plasma surface interaction experimental facility (PISCES) for materials and edge physics studies, J. Nucl. Mater. **121** (1984) 277.

[2] DOERNER, R., BALDWIN, M.J., SCHMID, K., The influence of a beryllium containing plasma on the evolution of a mixed-material surface, Physica Scripta **T111** (2004) 75.

[3] SCHMID, K., BALDWIN, M., DOERNER, R., WILTNER, A., Influence of beryllium plasma impurities on the erosion of graphite, Nucl. Fusion **44** (2004) 815.

[4] SCHMID, K., BALDWIN, M., DOERNER, R., Influence of beryllium plasma seeding on the erosion of carbon, J. Nucl. Mater. **337-339** (2005) 862.

[5] BALDWIN, M., et al., Composition and hydrogen isotope retention analysis of co-deposited C/Be layers, J. Nucl. Mater. **337-339** (2005) 590.

[6] NISHIJIMA, D., BALDWIN, M., DOERNER, R., SERAYDARIAN, R., Parametric studies of carbon erosion mitigation dynamics in beryllium seeded deuterium plasmas, J. Nucl. Mater. **363-365** (2007) 1261.

[7] BALDWIN, M., DOERNER, R., A time resolved study of the mitigation of graphite chemical erosion in deuterium plasmas containing beryllium, Nucl. Fusion **46** (2006) 444.

[8] DOERNER, R., et al., Interaction of beryllium containing plasma with ITER materials, Physica Scripta **T128** (2007) 115.

[9] PUGNO, R., BALDWIN, M., DOERNER, R., HANNA, J., NISHIJIMA, D., ANTAR, G., Saturation in deuterium retention of CFC graphite targets exposed to beryllium-seeded plasmas on PISCES-B, J. Nucl. Mater. **375** (2008) 168.

[10] BALDWIN, M., et al., Be–W alloy formation in static and divertor-plasma simulator experiments, J. Nucl. Mater. **363-365** (2007) 1179.

[11] MINTZ, M.H., JACOB, I., SHALTIEL, D., "Experimental techniques II: Adaptation of new techniques to study surface and bulk properties of H-metal systems", Topics in Applied Physics, Hydrogen in Intermetallic Compounds II, Vol. 67 (L. SCHLAPBACH, Ed.), Springer, New York (1988).

[12] BALDWIN, M., et al., Mixed-material layer formation on graphite exposed to deuterium plasmas containing beryllium, J. Nucl. Mater. **358** (2006) 96.

[13] DOERNER, R., et al., Mixed-material coating formation on plasma-facing components, J. Nucl. Mater. **266-269** (1999) 392.

[14] DOERNER, R., CONN, R.W., LUCKHARDT, S.C., SZE, F.C., WON, J., Outgassing from and deuterium retention in beryllium and Be/C mixed-material plasma-facing components, Fusion Eng. Des. **49-50** (2000) 183.

[15] BALDWIN, M., et al., Composition and hydrogen isotope retention analysis of co-deposited C/Be layers, J. Nucl. Mater. **337-339** (2005) 590.

[16] HAASZ, A., DAVIS, J., Deuterium retention in doped graphites, J. Nucl. Mater. **232** (1996) 219.

[17] MAYER, M., BALDEN, M., BEHRISCH, R., Deuterium retention in carbides and doped graphites, J. Nucl. Mater. **252** (1998) 55.

[18] CAUSEY, R.A., WALSH, D.S., Codeposition of deuterium with beryllium, J. Nucl. Mater. **254** (1988) 84.

[19] CAUSEY, R.A., WAMPLER, W.R., WALSH, D., Comparison of the thermal stability of the codeposited carbon/hydrogen layer to that of the saturated implant layer, J. Nucl. Mater. **176-177** (1990) 987.

[20] FEDERICI, G., et al., Plasma-material interactions in current tokamaks and their implications for next step fusion reactors, Nucl. Fusion **41** (2001) 1967.

[21] OKAMOTO, H., TANNER, L.E., "Beryllium-tungsten phase diagram", Phase Diagrams of Binary Tungsten Alloys (NAGENDRA NAIDU, S.V., RAMO RAI, P., Eds.), Indian Institute of Metals, Calcutta, 1991.

[22] DOERNER, R., BALDWIN, M., CAUSEY, R.A., Beryllium–tungsten mixed-material interactions, J. Nucl. Mater. **342** (2005) 63.

[23] LINSMEIER, C.H., et al., Binary beryllium–tungsten mixed materials, J. Nucl. Mater. **363-365** (2007) 1129.

Carbon for use in fusion reactors

A.A. Haasz, J.W. Davis

University of Toronto, Institute for Aerospace Studies, 4925 Dufferin St., Toronto, Ontario M3H-5T6, Canada

Abstract

Chemical erosion of carbon-based materials in tokamaks leads to the release of hydrocarbon molecules and radicals, which get ionized and dissociated in the plasma edge. Subsequently, the fragmented atoms and radicals get transported and redeposited elsewhere in the torus – in conjunction with the hydrogen fuel – resulting in the formation of co-deposited layers. Here we present results on the chemical erosion of graphite and on the thermo-oxidative technique for the removal of co-deposited layers. These results were obtained under controlled laboratory experimental conditions at the University of Toronto, in the framework of the IAEA Coordinated Research Project on "Tritium Inventory in Fusion Reactors". The topics studied include: (i) chemical erosion of graphite, including tiles removed from DIII-D; (ii) synergistic effects on the chemical erosion yields of graphite due to combined irradiation by low-energy (<100 eV) and energetic (>300 eV) particles, including two special cases of simultaneous irradiation by C^+-H^+ and O^+-H^+; and finally, (iii) the removal of D from lab-produced and tokamak co-deposits (from DIII-D, JET, and TFTR) by thermo-oxidation.

1. Introduction

Carbon has been extensively used in current tokamak fusion reactors for shielding the vacuum vessel from the plasma, e.g., TFTR (US), JET (EU), JT-60 (Japan), ASDEX-UG (Germany), and DIII-D (US-GA). Carbon has also been selected for use in the International Thermonuclear Experimental Reactor (ITER) for high heat flux components in the divertor [1]. Due to its low Z, carbon impurities are less detrimental to the plasma compared to high-Z metals. Due to its excellent thermo-mechanical properties, carbon is able to tolerate high heat loads during off-normal events. Carbon's main drawbacks are its erosion behaviour, its capacity to trap hydrogen, and diminished structural integrity due to neutron irradiation. Erosion can occur due to physical sputtering by ions with energy above the sputtering threshold. Physical sputtering occurs at all temperatures and for all materials, see e.g., Ref. [2]. At temperatures >1300 K graphite also erodes by radiation-enhanced sublimation under energetic particle impact – again above a certain threshold energy [2]. In addition, carbon also erodes via chemical reactions with hydrogen and oxygen impurities. Chemical erosion strongly depends on the graphite temperature and the incident particle energy, see e.g., Ref. [3,4]. Chemical erosion dominates in the reactor divertor where plasma temperatures are a few eV with corresponding H^+ energies of ~10 eV – below the threshold for physical sputtering. The chemical erosion yield of carbon can further be enhanced by the presence of some energetic (>100 eV) H^+ or impurity ions through a synergistic effect [5].

Chemical erosion of graphite leads to the production of hydrocarbon molecules and radicals, which through interactions with the plasma edge can undergo ionization and dissociation. They can then either enter the core plasma or get redeposited on solid surfaces. Carbon redeposition could occur in conjunction with hydrogen, leading to the formation of co-deposited layers. Such layers can reach thicknesses of >100 μm – with large capacity for tritium retention in T-D burning reactors. Indeed, it is the tritium trapped in co-deposits that may limit the operation of ITER, and therefore, research is under-way to develop techniques for the removal of tritium from the co-deposits.

In a parallel article in this book we have presented recent studies performed at the University of Toronto on tungsten as a plasma-facing material in tokamaks. Here, we present recent results on carbon: (i) chemical erosion of graphite, including tiles removed from DIII-D; (ii) synergistic effects on the chemical erosion yields due to combined irradiation by low-energy (<100 eV) and energetic (>300 eV) particles, including two special cases of simultaneous irradiation by C^+-H^+ and O^+-H^+; and finally, (iii) the removal of D from lab-produced and tokamak co-deposits (DIII-D, JET, TFTR) by thermo-oxidation.

2. Chemical erosion of graphite due to H^+, D^+ and T^+

2.1. Low-energy ion irradiation

An extensive database exists for the chemical erosion of graphite by energetic hydrogen ions in the energy range 100-3000 eV; e.g., see the review by Vietzke and Haasz [3] and the IAEA Compendium by Haasz et al. [4]. In this energy range the chemical erosion yield depends on the ion energy and flux density and the graphite temperature, with a maximum around 750-850 K. As the incident ion energy decreases, the relative contributions of the heavy hydrocarbons (C_2H_x and C_3H_y) to the total yield increase [6]. At 3 keV H^+ energy, CH_4 comprises ~90% of the total C yield; at 50 eV it drops to ~50%; and at thermal energy (<0.1 eV H^o atoms) the CH_4 contribution is only about 5-10% [6].

Research during the past decade has been extended to energies below 100 eV H^+ – down to ~10 eV – characteristic of the divertor plasma. We have performed a comprehensive study of chemical erosion of pyrolytic graphite in the temperature range 300-1000 K irradiated by 10-200 eV H^+ and D^+ ions [7]. This work was later extended to include tritium ion irradiation [8]. The use of the three isotopes of hydrogen enabled us to assess the extent of isotopic effects in the chemical erosion of graphite. The findings of these studies are highlighted here – first for the H^+ and D^+ irradiations and then for T^+ (Section 2.2).

As the incident H^+ and D^+ energy is reduced from 200 to 10 eV, the temperature dependence yield curves of the CH_4 and the total number of C atoms (sum of all C atoms in the released hydrocarbons) broaden such that significant yields are seen even at 300 K [7]; see Fig. 1. This room temperature yield is energy dependent with a shallow peak near 50 eV [7]; see Fig. 2(a).

In Fig. 1 the temperature dependence curves show the peak yields (both CH_4 and total C) and the temperatures at which these peaks occur (T_{max}) to shift downwards as the ion energy is reduced. It is interesting to note from both Figs 1 and 2(b) that at ~500 K the yields are nearly energy independent.

2.2. Isotopic effects on chemical erosion

Comparison of the H^+ and D^+ yields [7] show that the isotopic effect illustrated by the D/H yield ratio, was typically in the range of 1-2 [7]; see Fig. 2. The general

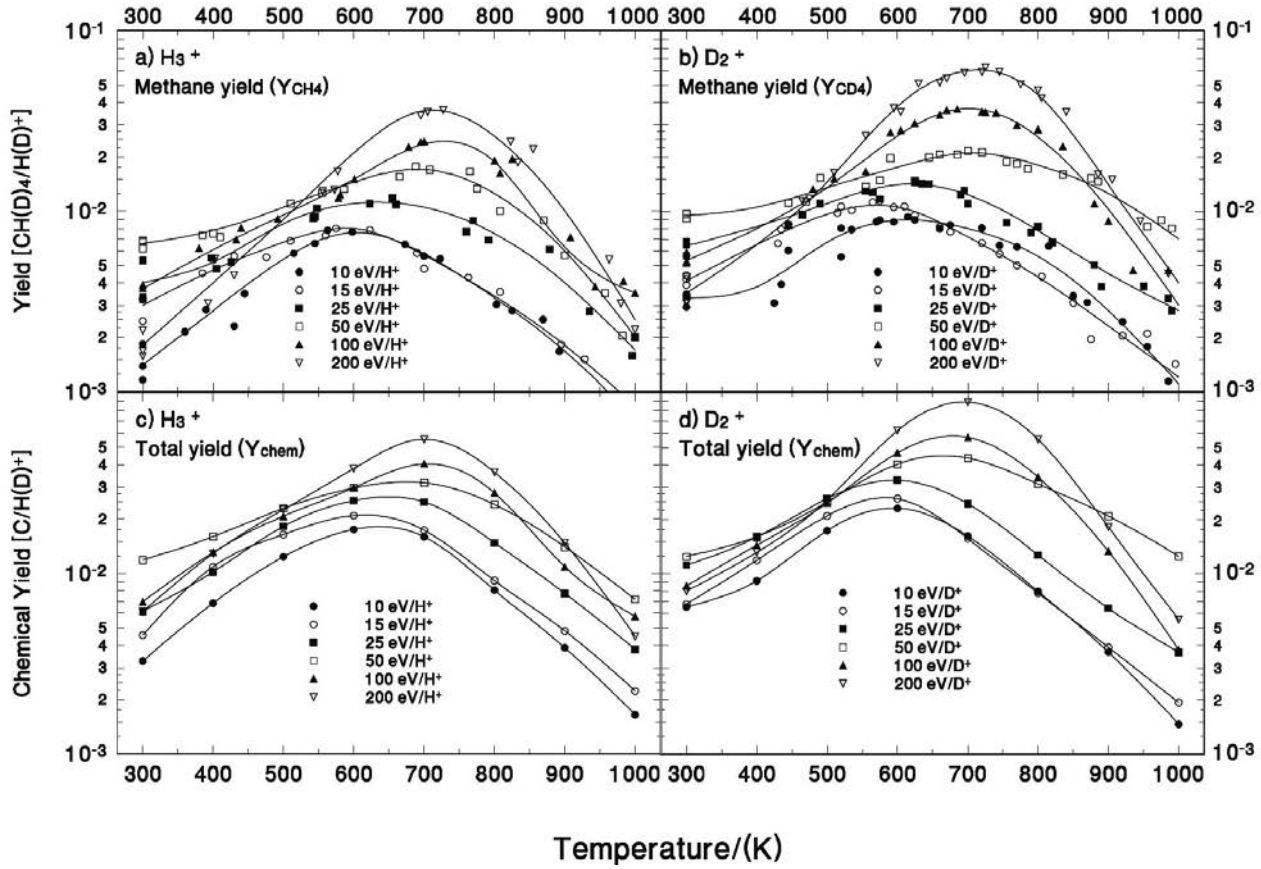

FIG. 1. Methane (a, b) and total chemical erosion (c, d) yields vs. graphite temperature. Y_{chem} is the total number of C atoms in the hydrocarbon reaction products divided by the incident ion flux, i.e., $Y_{chem}=[CH_4+2\times(C_2H_2+C_2H_4+C_2H_6)+3\times(C_3H_6+C_3H_8)]/[H^+]$, with a similar expression for D^+. (Data are from Ref. [7].) Lines are drawn to guide the eye.

trends of yield vs. energy and yield vs. temperature were similar for both H^+ and D^+ irradiations, with the deuterium yields being up to 2 times higher under some energy-temperature conditions: e.g., 300 K graphite temperature and <30 eV ion energy, or at T_{max} (~700 K) and >50 eV [7]. Modelling of the experimental methane yield results [9], assuming a square-root mass dependence, generally fit all of the hydrogen and deuterium yields within the experimental uncertainty of about ±50%. Comparisons of model predictions [9] and experimental data [7] are shown for 15 eV, 50 eV and 200 eV in Fig. 3.

Subsequent experiments with T^+ ions have confirmed the absence of strong isotope dependence for the chemical erosion of carbon [8]. The hydrocarbon yield distributions for 200 eV are similar for H, D and T; see Fig. 4. Within the scatter of the experimental data, the total C erosion yields (i.e., sum of C atoms in the measured hydrocarbons) for the three hydrogen isotopes are essentially the same, with maximum yields at around 700 K [8]. Therefore, based on the results of Refs [7, 8, 9], a square root type isotopic effect is suggested.

The topic of isotopic effect on the chemical erosion of carbon has received considerable attention in the plasma-surface interactions community, and several experiments have been performed in a variety of devices, including ion beams, laboratory plasmas and tokamaks. The measurement techniques used include mass loss, mass spectroscopy and optical spectroscopy [10]. The D-yield/H-yield ratios obtained in these experiments at room temperature and T_{max}, plotted as a function of ion energy, are presented in Fig. 5 [10]; some isotopic effect for H^+ and D^+ is evident, with the deuterium yield being larger [10]. Typically, the observed D-yield/H-yield ratio lies between 1 and 2. This is fully consistent with the square-root of mass dependence proposed by Mech et al. [9], which implies that the erosion due to tritium would not be significantly larger than for deuterium, consistent with the tritium yields measured by Macaulay-Newcombe et al. [8].

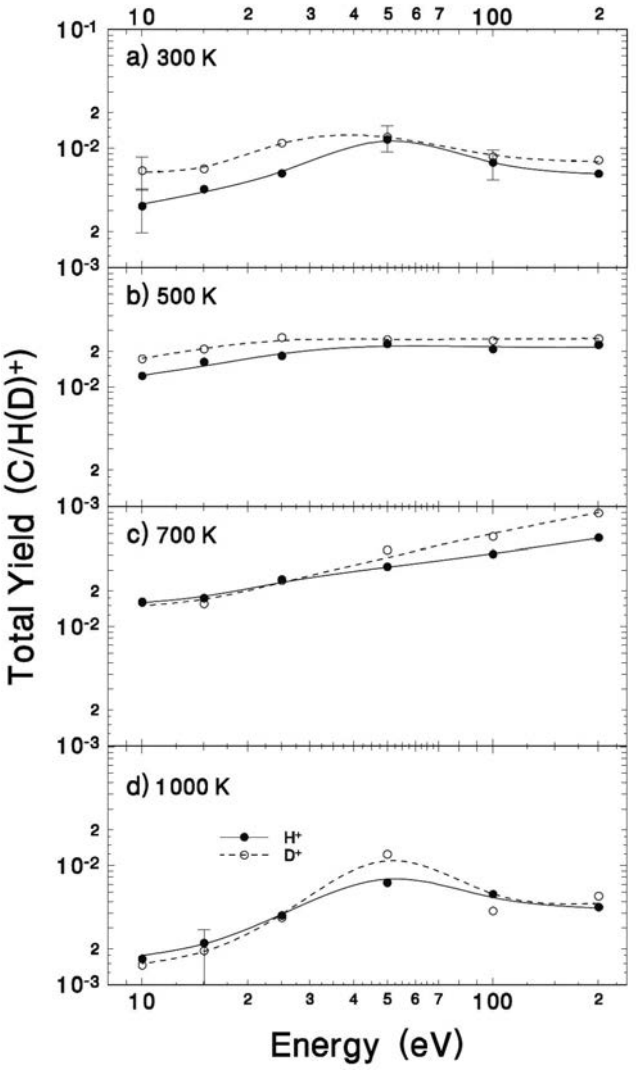

FIG. 2. Isotopic comparison of the total chemical erosion yield, as a function of impact energy, due to H^+ and D^+ impact at four graphite temperatures. (Data are from Ref. [7].)

2.3. *Chemical erosion of graphite tiles removed from DIII-D*

Laboratory experiments were also performed with graphite tiles removed from the DII-D tokamak (General Atomics, San Diego) to assess their chemical erosion behaviour subsequent to extensive plasma exposure and periodic boronizations.

2.3.1. DIII-D midplane tiles

A variety of surface diagnostics of a midplane tile specimen indicated that the surface material consisted of a boron-rich layer of ~2 μm thickness – formed during boronizations – covered with a thin layer of codeposited C/B/D, with 20-40 at % C [11]. Using our low-energy ion beam facility, we have measured initial erosion yields in the range 0.01-0.015 C/D^+ for 50 and 200 eV D^+ at 300 and 500 K; these yields are similar to both pure and B-doped graphite under similar conditions [11]. However, the yields were found to decrease with fluence, consistent with the depletion of C from the thin surface layer [11].

2.3.2. DIII-D lower divertor tiles

Initial studies of the chemical erosion of a graphite tile removed from the inner strike point of the DIII-D lower divertor showed that the erosion yields very quickly reached steady-state values comparable to pure graphite [12]. It is likely that this tile was located in an area of net erosion just prior to its removal. The surface

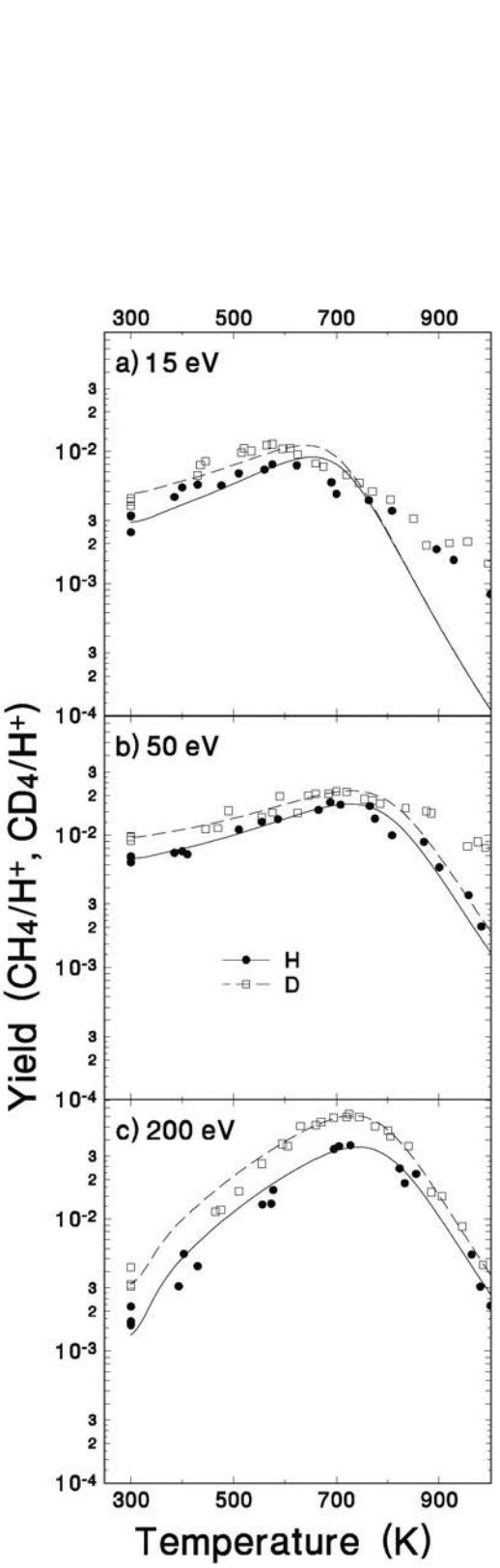

(Left:) **FIG. 3.** Model predictions (lines) and experimental measurements (symbols) for methane production due to H^+ and D^+ irradiation of graphite. (Data are from Refs [7, 9, 10]).

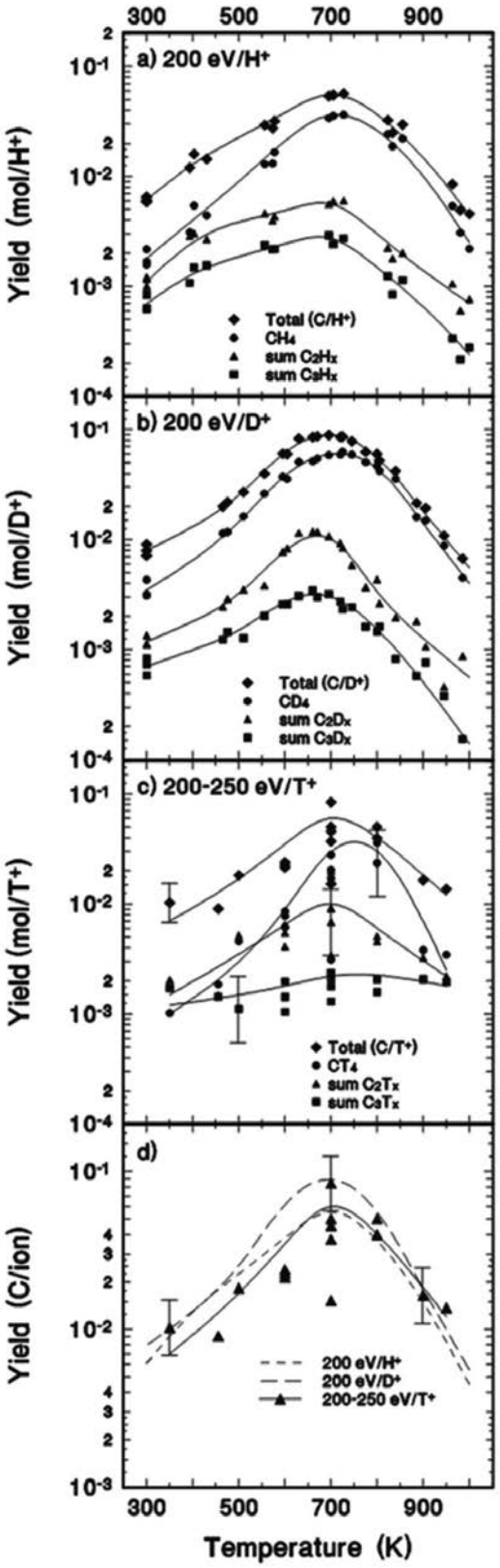

(Right:) **FIG. 4.** Hydrocarbon yields as a function of graphite temperature for H^+, D^+ and T^+ irradiation. (H^+ and D^+ data are adapted from Refs [7, 10] and T^+ data from Refs [8, 10].) For a direct comparison, total C yields from parts (a)-(c) are reproduced in (d). Lines are drawn to guide the eye.

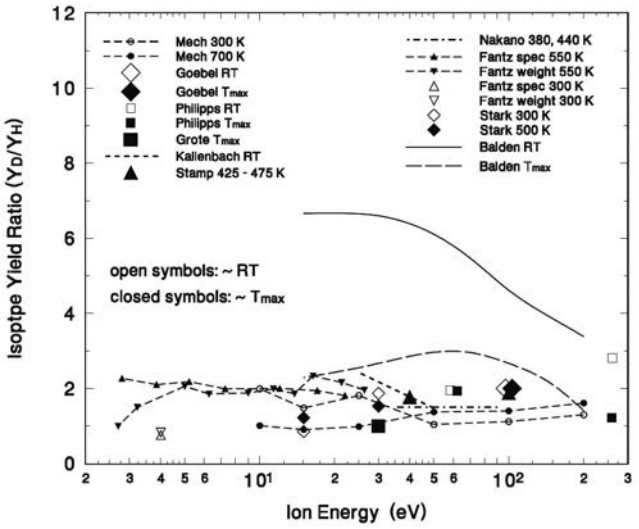

Fig. 5. Summary of isotopic yield ratios determined by various studies in laboratory and tokamak experiments. Sources of the data are given in Ref. [10].

composition of the specimen was primarily carbon with trace amounts of boron; the film thickness was estimated to be ≥5 nm. Visual inspection of the surface confirmed that even at a very low D^+ fluence in our experiment the film was eroded to the graphite substrate [12]. So, based on these initial results, the chemical erosion behaviour of the plasma-exposed divertor tile was very similar to that of pure graphite.

However, spectroscopic analysis of the DIII-D plasma has shown that the brightness of the CD emission band in the lower divertor has decreased by an order of magnitude over the course of eight years of plasma discharges (~23 000 plasma shots) [13]. Over this time period the B_{CD}/B_{CII} ratio has also decreased by a factor of 4. Both of these observations imply that the role of chemical erosion as a carbon source has been progressively reduced. A further implication is that the carbon tiles in the lower divertor might have undergone some surface modification, resulting in a reduced chemical reactivity. Possible causes for the surface changes might be the effect of surface boronizations that have taken place in DIII-D or some sort of *plasma conditioning* of the tiles after extensive plasma exposure [13].

To explore the cause of the apparent reduction in the spectroscopic CD band emissions – and to determine whether the reactor plasma exposure of the lower divertor tiles has affected their chemical erosion characteristics – a controlled study of the chemical erosion of lower divertor tile specimens from both the inner and outer strike point positions was performed [14]. The new results, again, show that the erosion yields (measured as a function of temperature for 15 and 50 eV D^+) are very similar to the yields obtained with pyrolytic graphite and virgin DIII-D tile specimens [14]. These results show no evidence of reduced chemical erosion due to tile surface modification during prolonged DIII-D plasma exposure – ruling out any plasma conditioning effect. The similar chemical erosion yield of pyrolytic graphite and the DIII-D virgin specimen further implies that the DIII-D divertor tiles have not experienced any significant changes in their physical properties due to surface preparation prior to installation in the divertor [14].

3. Chemical erosion of graphite by two-species irradiation: synergistic effect

Multi-species impact is of high relevance for fusion reactors, where, in addition to the hydrogen fuel, the He ash and impurity species (e.g., C and O), and in some cases injected elements, are also present. Combined irradiation of graphite with relatively low-energy H^+ (typically below 100 eV) and energetic (above 300 eV) hydrogenic and non-hydrogenic ions leads to an enhancement of the chemical erosion yield compared to the low-energy H^+-only case. This is due to the additional energy deposition and associated lattice damage by the added energetic ions. An overview of carbon erosion studied in dual-beam experiments has been published by Haasz and Davis [5]. Here we highlight some key findings.

3.1. Erosion of graphite due to simultaneous irradiation by <100 eV H^+ and energetic ions

Experimental studies on the effect of combining thermal H^o (<1 eV) or low-energy H^+ (<100 eV) with energetic H^+ (>300 eV) or non-hydrogenic ions on the chemical erosion behaviour of carbon show that the energetic ions are capable of enhancing carbon's chemical erosion yield via energy deposition and associated lattice damage [5]. However, a mechanism leading to the breakup of hydrocarbons and hydrocarbon precursors within graphite limits the amount of enhancement [15]. We note that different chemical erosion mechanisms have been observed, one dominating for <100 eV H^+ and another dominating above >300 eV; the transition between the two regimes is illustrated in Fig. 6 [5]. It is evident from the figure that for the combination of energetic H^+ and high H^+/H^o flux ratios (>10), methane dominates the hydrocarbon production, while for relatively low H^+ energy and low H^+/H^o flux ratios ($<10^{-2}$), heavy hydrocarbons dominate with methane contributing only ~5% to the total C due to chemical erosion.

The damage causing effect of energetic ions was demonstrated by using chemically non-reactive He^+, Ne^+, and Ar^+ in combination with <100 eV H^+ [5, 17]. In addition to providing fundamental information on hydrocarbon formation, we note that such non-reactive

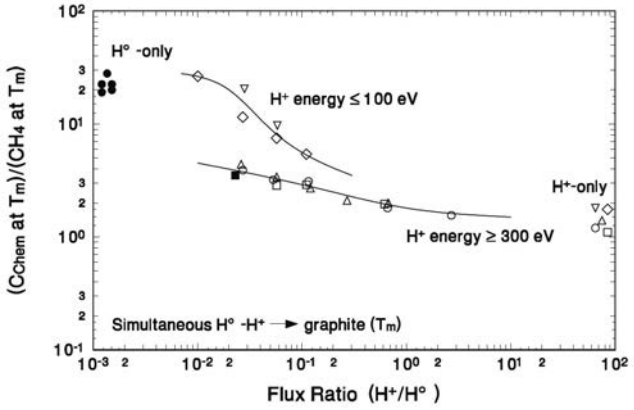

FIG. 6. Ratio of the total hydrocarbon production rate to the CH_4 production rate at their respective T_m as a function of the H^+/H^o flux ratio during simultaneous H^o-H^+ irradiation of graphite. C_{chem} is the sum of C atoms in the C_1, C_2, and C_3 hydrocarbons. (Data are from Refs [5, 6, 16].)

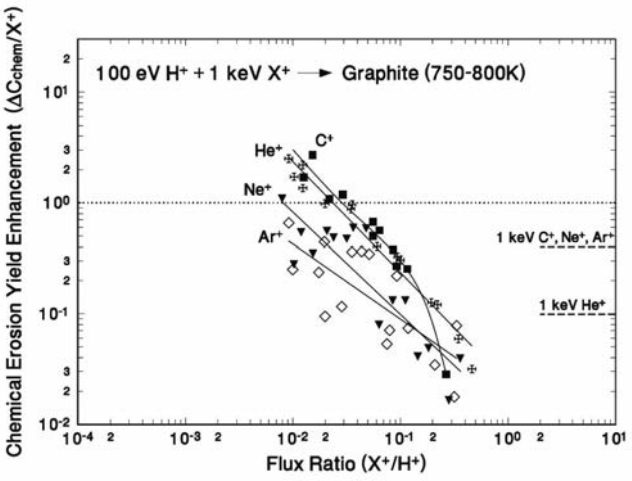

FIG. 7. Total chemical erosion yield enhancement over the 100 eV H^+-only case ($\Delta C_{chem}/X^+$), normalized by the incident energetic X^+ ion flux, during simultaneous irradiation of graphite by 100 eV H^+ and 1 keV X^+ at 750-800 K, as a function of the X^+/H^+ flux ratio; X represents He, C, Ne and Ar. (Data are from Refs [5, 17].) Physical sputtering yields for 1 keV X^+ are shown by dashed lines [20].

ions are also being deliberately introduced into the reactor for plasma cooling [18] or disruption mitigation [19]. The chemical erosion yield enhancement over the 100 eV H^+-only case, per incident X^+, as a function of the X^+/H^+ flux ratio (where X represents He, Ne, Ar, and C) is shown in Fig. 7 [5]; more on C below. We note that the H^+-He^+ and H^+-C^+ cases are similar, reaching greater-than-unity yield enhancement for He^+/H^+ flux ratios of <2%. Although considerable scatter is seen for the H^+-Ne^+ and H^+-Ar^+ cases, similar trends are evident [17]. By comparison, the physical sputtering yield of graphite for 1 keV He^+ is 0.1, and for 1 keV C^+, Ne^+ and Ar^+ it is 0.4 [20].

3.2. *Erosion of graphite due to simultaneous irradiation by C^+-H^+*

A special tokamak-relevant case of synergistic erosion involves thermal H^o or low-energy (<100 eV) H^+ combined with energetic C^+ [5]. Carbon is special since, in addition to producing surface damage, the implanted C actually becomes part of the target graphite and thus can also partake in hydrocarbon formation. Experiments performed at T_m show that the total chemical erosion yield in the presence of thermal H^o or low-energy H^+ (<100 eV) can increase to levels greater than the physical sputtering yield due to C^+ [5]. The hydrocarbon yield enhancement (over the H^o-only case) per incident C^+ ion due to combined H^o-C^+ irradiation exceeds unity for C^+/H^o flux ratios <20% for 1 keV C^+ and <6% for 300 eV C^+ [5]. Unity yield enhancement (over the 100 eV H^+-only case) per C^+ for the case of combined 1 keV C^+-100 eV H^+ irradiation occurs for C^+/H^+ flux ratios of <3% [5]; see Fig. 7. In the divertor region of a tokamak, where the energetic C^+ fluxes are accompanied by orders of magnitude higher fluxes of low-energy H^+ and Franck-Condon H^o neutrals, the resulting erosion yield enhancement may have a significant effect on carbon component erosion, impurity production, and tritium inventory buildup due to co-deposition.

3.3. *Erosion of graphite due to simultaneous irradiation by O^+-H^+*

When graphite is exposed to simultaneous irradiation by H^+ and O^+, in addition to the H^+-induced hydrocarbons and O^+-induced CO and CO_2 formation, water is also formed [21, 22, 23]. No O or O_2 reemission is observed. The combined H^+-O^+ irradiation leads to reductions in the methane and carbon oxide yields obtained with H^+-only and O^+-only irradiations, respectively. These reductions are of the same order of magnitude as the H_2O yield, and all are about an order of magnitude lower than the single-species induced CH_4, CO, and CO_2 yields.

3.3.1. Ion range dependence of reaction product formation

The H_2O yield and the reductions of the other reaction product yields during H^+-O^+ irradiation are independent of the range separation of the H^+ and O^+ ions [22]; e.g., compare ion range ratios corresponding to complete overlap (R_H/R_O=1.2) and total separation (R_H/R_O=4.4) for the H_2O yield and the CH_4 yield reduction in Fig. 8. This leads to the hypothesis that H_2O formation occurs at the end of the O^+ ion range. The absence of re-emitted O or O_2 suggests that there are no free mobile O atoms within the carbon matrix to form O_2 via

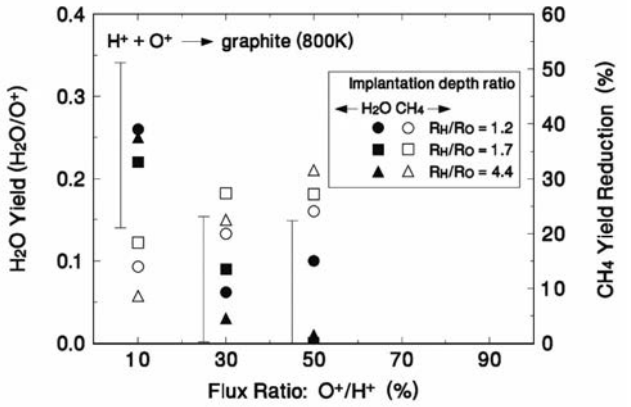

FIG. 8. H_2O yields and CH_4 yield reductions for simultaneous irradiation of pyrolytic graphite at 800 K by H^+-O^+, as a function of O^+/H^+ flux ratio. Ion energies were varied in the ranges of 0.7-3 keV H^+ and 2.5-5 keV O^+ to obtain different ion range ratios. R_H/R_O=1.2 corresponds to complete overlap and R_H/R_O=4.4 to total separation of the ion ranges. (Data are from Refs [5,22].)

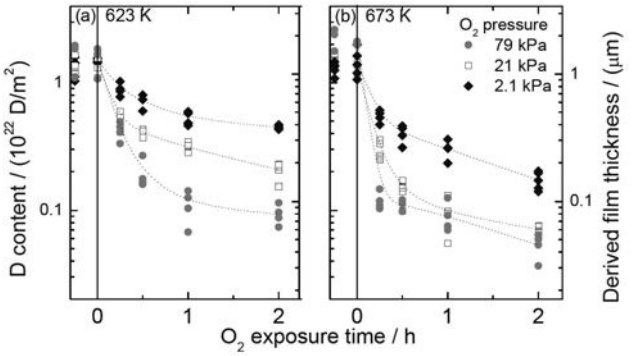

FIG. 9. Measured D content and derived co-deposit film thickness for specimens cut from DIII-D divertor tiles as a function of oxidation time. (Data are from Ref. [25].)

recombination, or more importantly, in the case of H^+-O^+ co-bombardment to react with hydrogen outside of the O^+ range to form water molecules. In contrast, H atoms move freely within the implantation zone [24]. Thus, during simultaneous H^+-O^+ irradiation of graphite, the H atoms can readily react with oxygen even when the end of ion range for H^+ is much greater than that of O^+ [22]. The reaction of hydrogen with available oxygen takes away a portion of the available oxygen supply, resulting in the observed reductions of the CO and CO_2 yields, compared to the O^+-only irradiation case [22].

3.3.2. O^+/H^+ flux ratio dependence of reaction product formation

While the CO and CO_2 yield reductions and the H_2O yield are independent of the H^+-O^+ range separation, they are dependent on the O^+/H^+ flux ratio [22]; e.g., see Fig. 8 for H_2O and CH_4. The smaller the oxygen flux compared to the hydrogen flux, the greater is the reduction of CO and CO_2 yields, and the greater is the H_2O yield per incident O^+. This is likely due to an over-abundance of available hydrogen for low O^+/H^+ flux ratios, leading to more H_2O formation – and thus, to less O being available for CO and CO_2 production [22]. The reduction of CO_2 is higher than that of CO – possibly due to the fact that it takes twice as many O atoms to form one CO_2 than one CO. Therefore, when the oxygen supply is reduced due to H_2O formation, the effect on CO_2 formation is expected to be greater.

The behaviour of CH_4 shows the opposite effect in flux-ratio dependence, i.e., larger reduction at high O^+/H^+ ratios; see Fig. 8. The CH_4 reduction is attributed to methane breakup [15]. In the presence of more energetic O^+ relative to H^+, as is the case for high O^+/H^+ flux ratios, methane breakup increases, leading to larger CH_4 yield reductions.

4. Co-deposit removal by oxidation

Tritium retention in carbon-based co-deposits is a major concern with regard to tritium inventory in next-generation fusion reactors such as ITER [25, 26]. Co-deposits are formed on vessel surfaces – including shadowed areas – via the redeposition of eroded carbon in combination with hydrogen. For example, co-deposition has led to the formation of up to 40 μm thick flakes in the inner leg of the Mark IIa divertor in JET [27]. One of the methods proposed for the removal of tritium from tokamak co-deposits is thermo-oxidation, which removes the co-deposit via the formation of reaction products D_2O, CO and CO_2 [28-30].

Laboratory studies have demonstrated that the co-deposit erosion rates and the associated D removal rates depend on the film structure, oxidation temperature and oxygen pressure, see e.g., Refs [25, 31]. Recent measurements of the remaining D in DIII-D co-deposits, as a function of oxidation time, are shown in Fig. 9 [25]. It is noted that the effect of increasing the temperature and/or pressure leads to increases in the initial erosion rates (Figs 9 and 10) and decreases in the final D content (Figs 9 and 11).

It is evident from Fig. 10 that significantly larger initial erosion rates can be achieved by increasing the temperature – compared with increasing the pressure. For example, increasing the temperature by only 50 K, from 623 to 673 K, at a pressure of 2.1 kPa, results in an erosion rate that is similar to the rate achieved by a ten-fold increase in pressure, from 2.1 to 21 kPa, at 623 K [25]. The highest initial D removal and film erosion rates were obtained at 673 K and 79 kPa [25]. Under these conditions, the D content was reduced by about an order of magnitude in 15 min, roughly corresponding to a film erosion rate of ~10 μm/h; see Fig. 10.

The final D content after prolonged oxidation is seen to decrease with increasing temperature and

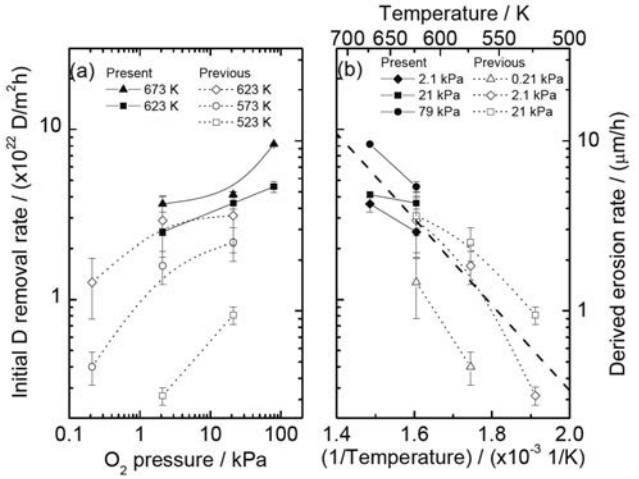

FIG. 10. Dependence of measured initial D removal rate and derived initial co-deposit erosion rate on: (a) O_2 pressure and (b) reciprocal temperature during oxidation. ('Present' data from Ref. [25] and 'previous' data from Refs [31, 32].) The expression $[3.2 \times 10^{26} \times \exp(-0.5\text{eV}/kT)]$ shown by the heavy dashed line in (b) gives an indication of the activation energy for the oxidation process. The names of the 'left' and 'right' ordinates apply to both (a) & (b).

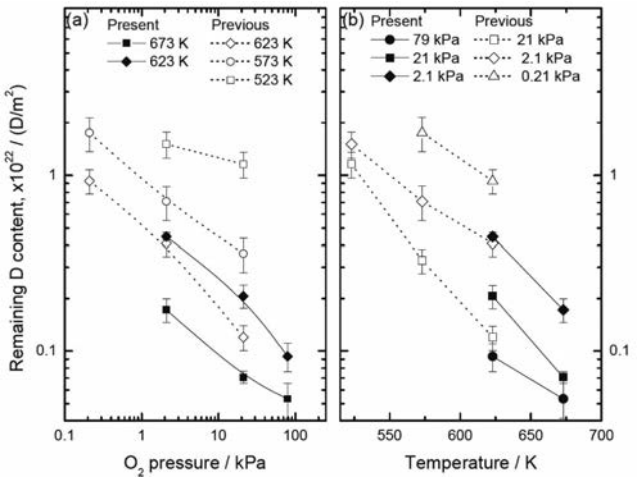

FIG. 11. Final D content as a function of (a) O_2 pressure, and (b) specimen temperature during oxidation. ('Present' data from Ref. [25] and 'previous' data from Refs [31, 32].) For the 'present' data, the remaining D corresponds to 2 h of oxidation; for the 'previous' data, the oxidation times vary, as given in Refs [31, 32].

increasing pressure as shown in Fig. 11. The lowest D content measured was ~5×10^{20} D/m^2 at 673 K and 79 kPa after an oxidation time of 2 h. This level is down by a factor of ~30 from the initial D content of ~1-2 $\times 10^{22}$ D/m^2, with a further decreasing trend with increasing oxidation time [25].

A possible explanation of the reduced oxidation rate with oxidation time is the buildup of impurity elements in the deposited films by the preferential erosion of carbon. For the DIII-D specimens studied [11, 12, 25, 31, 32], the 'amount of D removed' divided by the 'initial D content' is plotted as a function of initial near-surface boron impurity concentration in Fig. 12(a) [25]. Although some metal impurities are also present on most

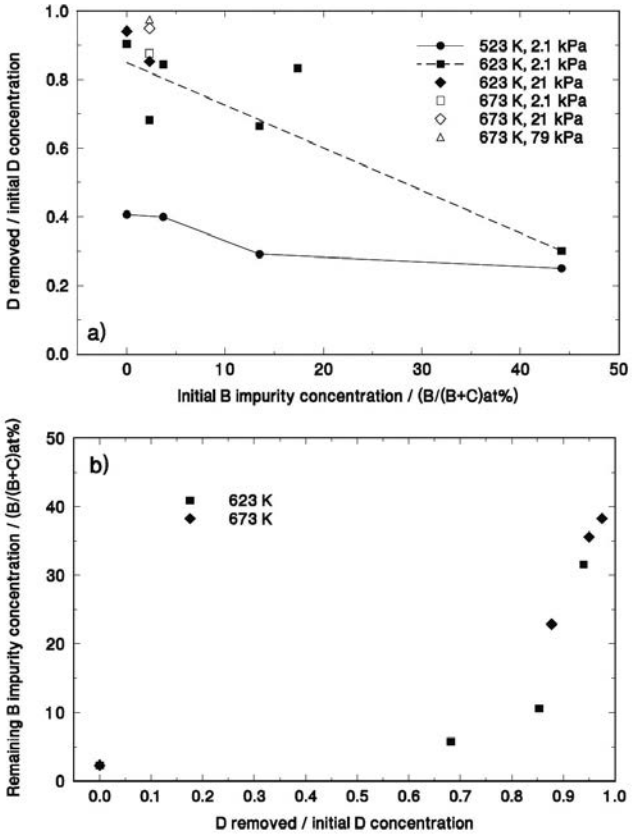

FIG. 12. (a) Amount of D removed by oxidation divided by the initial D content plotted against the initial boron impurity concentration in the near surface of the codeposit. Data are from several sources [11,12,25,31,32]; oxidation times are given in [25]. (b) Data showing the increase in boron concentration of specimens that had an initial B/(B+C) concentration of 2.3 at.% following 2 h oxidation for various temperature and pressure combinations [25].

of the specimens, it is the B that dominates the impurity content. The level of boron impurities following oxidation for specimens with an initial concentration of 2.3 at.% B/(B+C) is shown in Fig. 12(b) [25]. With increasing removal of D, the boron becomes increasingly concentrated, clearly indicating the preferential removal of carbon. The role of B – and other impurities – leading to a reduction in the co-deposit erosion rate requires further investigation. Tungsten surface impurities sputtered onto laboratory-produced 'hard' co-deposits have led to reductions in the oxidative erosion rates [33]. However, about 3 at.% W sputter-deposited onto DIII-D co-deposits had a negligible effect on the oxidative erosion rate [34].

In ITER, if vessel components with largely carbon-based co-deposit accumulation could be selectively heated to ~673 K during oxidation at ~80 kPa O_2 pressure, then based on our maximum erosion rate, tritium-containing co-deposits of ~100 μm thickness – with a few percent impurity content – could be eroded in about 10 h. This estimate is based on the assumption that most of the co-deposit thickness will be eroding at

the highest oxidation rates – until the thin "interface" region between the outer co-deposit and the substrate is reached [25]. We note that the oxidative erosion rate of the graphite substrate is orders of magnitude lower than the rates of tokamak co-deposits [35, 36].

Acknowledgements

The financial support provided by the Natural Sciences and Engineering Research Council of Canada is gratefully acknowledged.

References

[1] FEDERICI, G., et al., Plasma-material interactions in current tokamaks and their implications for next-step fusion reactors, Nucl. Fusion **41** (2001) 1967.

[2] ECKSTEIN, W., "Physical sputtering and radiation-enhanced sublimation", Physical Processes of the Interaction of Fusion Plasmas with Solids (HOFER, W.O., ROTH, J., Eds), Academic Press (1996) 93.

[3] VIETZKE, E., HAASZ, A.A., "Chemical Erosion", Physical Processes of the Interaction of Fusion Plasmas with Solids (HOFER, W.O., ROTH, J., Eds), Academic Press (1996) 135.

[4] HAASZ, A.A., STEPHENS, J.A., VIETZKE, E., ECKSTEIN, W., DAVIS, J.W., HIROOKA, Y., "Particle-induced erosion of Be, C and W in fusion plasmas", Atomic and Plasma-Material Interaction Data for Fusion Vol. 7A, Chemical Erosion of Carbon-Based Materials, IAEA, Vienna (1998) 1.

[5] HAASZ, A.A., DAVIS, J.W., Erosion of carbon in dual-beam experiments, Physica Scripta **T111** (2004) 68-74.

[6] DAVIS, J.W., HAASZ, A.A., STANGEBY, P.C., Hydrocarbon formation due to hydrogen impact on pyrolytic graphite, J. Nucl. Mater. **155-157** (1988) 234.

[7] MECH, B.V., HAASZ, A.A., DAVIS, J.W., Isotope effects in hydrocarbon formation due to low-energy H^+/D^+ impact on graphite, J. Nucl. Mater. **255** (1998) 153.

[8] MACAULAY-NEWCOMBE, R.G., HAASZ, A.A., DAVIS, J.W., Low-energy tritium ion erosion of graphite, J. Nucl. Mater. **337-339** (2005) 857.

[9] MECH, B.V., HAASZ, A.A., DAVIS, J.W., A model for the chemical erosion of graphite due to low-energy H^+ and D^+ impact, J. Appl. Phys. **84** (1998) 1655.

[10] HAASZ, A.A., DAVIS, J.W., Hydrogen isotope effects on the erosion of carbon, Fusion Sci. Technol. **50** (2006) 58.

[11] DAVIS, J.W., WRIGHT, P.B., MACAULAY-NEWCOMBE, R.G., HAASZ, A.A., HAMILTON, C.G., Chemical erosion of boronized films from DIII-D tiles, J. Nucl. Mater. **290-293** (2001) 66.

[12] WRIGHT, P.B., DAVIS, J.W., MACAULAY-NEWCOMBE, R.G., HAMILTON, C.G., HAASZ, A.A., Chemical erosion of DIII-D divertor tile specimens, J. Nucl. Mater. **313-316** (2003) 158.

[13] WHYTE, D.G., et al., Reduction of divertor carbon sources in DIII-D, J. Nucl. Mater. **290-293** (2001) 356.

[14] Wright, G.M., HAASZ, A.A., DAVIS, J.W., MACAULAY-NEWCOMBE, R.G., Chemical erosion of DIII-D lower divertor tiles, J. Nucl. Mater. **337-339** (2005) 74.

[15] CHIU, S., HAASZ, A.A., FRANZEN, P., Energy, flux and fluence dependence of methane breakup in graphite during irradiation, J. Nucl. Mater. **218** (1995) 319.

[16] HAASZ, A.A., et al., Synergistic methane formation on pyrolytic graphite due to combined H^+ ion and H^o atom impact, J. Nucl. Mater. **145-147** (1987) 412.

[17] HAASZ, A.A., DAVIS, J.W., Synergistic chemical erosion of graphite due to simultaneous bombardment by H^+ and other low-Z ions using a dual-beam accelerator, Nucl. Instrum. Meth. **B83** (1993) 117.

[18] JACKSON, G.L., et al., Enhanced confinement discharges in DIII-D with neon and argon induced radiation, J. Nucl. Mater. **266-269** (1999) 380.

[19] WHYTE, D.G., et al., Mitigation of tokamak disruptions using high-pressure gas injection, Phys. Rev. Lett. **89** (2002) 055001.

[20] ECKSTEIN, W., GARCIA-ROSALES, C., ROTH, J., OTTENBERGER, W., Sputtering Data, Report IPP 9/82, Max-Planck-Institut für Plasmaphysik, Garching (February 1993).

[21] CHEN, A.Y.K., HAASZ, A.A., DAVIS, J.W., Two-region model of CH_4, CO, CO_2, and H_2O formation in graphite due to simultaneous irradiation by O^+ and H^+, J. Appl. Phys. **94** (2003) 1617-1628.

[22] CHEN, A.Y.K., DAVIS, J.W., HAASZ, A.A., Chemical erosion of graphite under simultaneous O^+ and H^+ irradiation, J. Nucl. Mater. **266-269** (1999) 399-405.

[23] CHEN, A.Y.K., HAASZ, A.A., DAVIS, J.W., Water formation in graphite and boron-doped graphite under simultaneous O^+ and H^+ irradiation, J. Nucl. Mater. **312** (2003) 16-20.

[24] CHIU, S., HAASZ, A.A., Molecule formation due to sequential and simultaneous exposure of graphite to H^+ and D^+, J. Nucl. Mater. **196-198** (1992) 972.

[25] HAASZ, A.A., TSUI, C., DAVIS, J.W., OCHOUKOV, R., Thermo-oxidation of codeposits from DIII-D divertor tiles, Physica Scripta **T128** (2007) 55.

[26] HAASZ, A.A., DAVIS, J.W., "Hydrogen retention in and release from carbon materials", Nuclear Fusion Research (CLARK, R.E.H., REITER, D.H., Eds), Springer series in Chemical Physics, Springer Verlag, Berlin (2005) 225-248.

[27] PEACOCK, A.T., et al., Dust and flakes in the JET MkIIa divertor, analysis and results, J. Nucl. Mater. **266-269** (1999) 423.

[28] CAUSEY, R.A., CHRISMAN, W.L., HSU, W.L., ANDERL, L., WISHARD, B., Tritium release from a codeposited layer of carbon and tritium during air exposure, J. Vac. Sci. Technol. **A7** (1989) 1078.

[29] HAASZ, A.A., CHIU, S., PIERRE, J.E., GUDIMENKO, Y.I., Thermo-oxidative erosion of amorphous hydrogenated carbon films, J. Vac. Sci. Technol. **A14** (1996) 184.

[30] ALBERICI, S., HINSSEN, H.K., MOORNMANN, R., WU, C.H., Deuterium release rates in a-C:D-layers during oxygen attack, J. Nucl. Mater. **266-269** (1999) 754.

[31] OCHOUKOV, R., HAASZ, A.A., DAVIS, J.W., Pressure dependence of oxidative removal of tokamak codeposits, Physica Scripta **T124** (2006) 27.

[32] DAVIS, J.W., HAASZ, A.A., Oxygen removal of codeposited a-C:D layers from tokamak tiles, J. Nucl. Mater. **266-269** (1999) 478.

[33] DAVIS, J.W., HAMILTON, C.G., HAASZ, A.A., MACAULAY-NEWCOMBE, R.G., Thermo-oxidation of hard carbon films with tungsten impurities, J. Nucl. Mater. **305** (2002) 66-69.

[34] TRUMPOUR, A.P., The effect of sputter-deposited tungsten surface impurity on the thermo-oxidation of codeposited a-C:D layers from DIII-D tokamak tiles, BASc thesis, University of Toronto (2003, – unpublished).

[35] DAVIS, J.W., HAMILTON, C.G., HAASZ, A.A., O_2 erosion of graphite tile substrates, J. Nucl. Mater. **288** (2001) 148-152.

[36] DAVIS, J.W., HAASZ, A.A., Overview of thermo-oxidation of tokamak codeposits, Physica Scripta **T91** (2001) 33-35.

Tungsten for use in fusion reactors

A.A. Haasz, J.W. Davis

University of Toronto, Institute for Aerospace Studies, 4925 Dufferin St., Toronto, Ontario M3H-5T6, Canada

Abstract

Results on hydrogen retention in tungsten obtained under controlled laboratory experimental conditions at the University of Toronto, in the framework of the IAEA Coordinated Research Project on "Tritium Inventory in Fusion Reactors", are presented. The experiments include: (i) hydrogen retention in both polycrystalline tungsten (PCW) and single crystal tungsten (SCW) due to single species H^+ or D^+ irradiation and (ii) hydrogen and helium trapping in PCW due to simultaneous He^+ and $H^+(D^+)$ irradiation. The effects of various parameters on D retention in W were studied: specimen temperature; ion energy, fluence and flux; bulk and surface impurity concentrations; cumulative ion damage due to prior D^+ irradiations; and C^+ implantation prior to D^+ irradiation.

1. Introduction

The materials selected for plasma-facing components in ITER are beryllium for the vessel walls, carbon for the high heat flux target plates in the divertor, and tungsten for the rest of the divertor [1]. The low divertor plasma temperatures currently envisioned for ITER mean that escaping fuel ions will have energies below the threshold for physical sputtering of heavy metals like tungsten. Tungsten's use in ITER has generated considerable interest – both fundamental and applied – in tungsten's hydrogen trapping behaviour. While most of the earlier research, e.g., Refs [2-4], has involved different forms of polycrystalline tungsten (PCW), several recent studies have attempted to separate the effects of various material and experimental parameters. For example, by studying single crystal tungsten (SCW), the trapping of hydrogen in the 'crystal' can be separated from the effects of grain boundaries, dislocations, and other defects in the polycrystalline material. However, even in the case of single crystal specimens the presence of inherent defects and impurities and the modification of the material due to the incident H^+ or D^+ will affect hydrogen diffusion and trapping.

To further control the experimental parameters, some studies have been performed at ion implantation energies below the displacement threshold in W (2050 eV for H^+ [5] and 940 eV for D^+ [6]) to prevent the formation of ion-induced damage. Nevertheless, even for energies below the damage threshold, hydrogen accumulation can occur in the material below the surface, extending to depths much greater than the ion range; e.g., Ref. [3]. This may cause lattice distortion, and under certain combinations of ion flux, fluence and temperature, it may lead to the formation of vacancy clusters or nano-bubbles [7], micro-voids [8, 9], and in some cases blistering [10-13]. While it is evident that surface deformation and blistering is more likely to occur at fluences $>10^{24}$ D^+/m^2 for PCW and even higher fluences for SCW (perhaps as high as $\sim 1 \times 10^{26}$ D^+/m^2), there appears to be some inconsistency regarding the temperature at which such effects occur. The question is whether it is only the temperature, or is it possible that the structure and impurities also play a role in causing the varied observations. In the case of PCW it is possible that both the structure and impurities might play a role. However, in SCW structure is not expected to have a significant effect, leaving impurities – both bulk and surface – as possible causes of surface modifications.

In a parallel article in this book we have presented recent studies performed at the University of Toronto on carbon as a plasma-facing material in tokamaks. Here we shall discuss our recent research on tungsten, primarily focusing on (i) hydrogen retention in both PCW and SCW due to single species H^+ or D^+ irradiation and (ii) hydrogen and helium trapping in PCW due to simultaneous He^+ and $H^+(D^+)$ irradiation. The effects of various parameters on D retention in W will be considered: specimen temperature; ion energy, fluence and flux; bulk and surface impurity concentrations; cumulative ion damage due to prior D^+ irradiations; and C^+ implantation prior to D^+ irradiation.

2. Retention due to single species H^+ or D^+ irradiation

2.1. Polycrystalline tungsten

2.1.1. Fluence and temperature dependence of D retention

Energetic hydrogen ions incident on any material will be implanted in the near surface, within the ion range, from where they can be re-emitted back to the gas phase, but also, they can diffuse further into the bulk, where they can be trapped, and eventually for sufficiently high fluences when bulk saturation occurs, they can be re-emitted from the back surface into the gas phase. The amount of D retained in all of the specimens discussed in this article was measured by thermal desorption spectroscopy, TDS. In the case of a 25 μm thick PCW specimen, at 300 K, the retained amount of D tends to saturation for fluences $>10^{23}$ D^+/m^2 at D^+ energies of 500 eV and 1 keV [3, 14]; see Fig. 1(a). Although the 1000 eV D^+ is slightly above the energy for damage formation (940 eV for D^+ [6]) the saturation levels for the 500 and 1000 eV cases are very similar (~6×10^{20} D/m^2 retained for fluences $>10^{23}D^+/m^2$ [3]). NRA measurements of the near-surface depth profiles show D being trapped far beyond the ion range (few nm) to depths of ~500 nm at both 500 and 1000 eV [3]; see Fig. 2(a).

At 500 K temperature, irradiation of a 25 μm thick PCW foil with 500 eV D^+ did not show signs of saturation even at an incident fluence of 5×10^{24} D^+/m^2; see Fig. 1(a). Given the scatter in the data, the results are consistent with a diffusion-limited trapping mechanism (slope ~0.5). NRA measurements on both the front and back surfaces of a specimen irradiated to a fluence of 10^{24} D^+/m^2 showed relatively uniform D concentrations (0.05-0.1 at.%) throughout the bulk [3]; see Fig. 2(b). Re-emission experiments of a similar 25 μm thick specimen irradiated with 1 keV D^+ to a fluence of 2-3 $\times$ 10^{23} D^+/m^2 showed that re-emission from the front surface at temperatures <1200 K was dominated by D_2, with atomic D^o becoming significant above 1200 K and dominant above ~1800 K; see Fig. 3(a). No re-emission was observed from the back surface at this fluence; see Fig. 3(b) [15].

Deuterium retention in a W-1%La_2O_3 alloy was similar to the D retention behaviour in pure W. The exception is the observed tendency to saturation for 500 eV D^+ irradiation at 500 K for fluences $>10^{24}$ D^+/m^2 [3]; see Fig. 1(a).

The temperature dependence curve of D retention shows increasing retention as the temperature

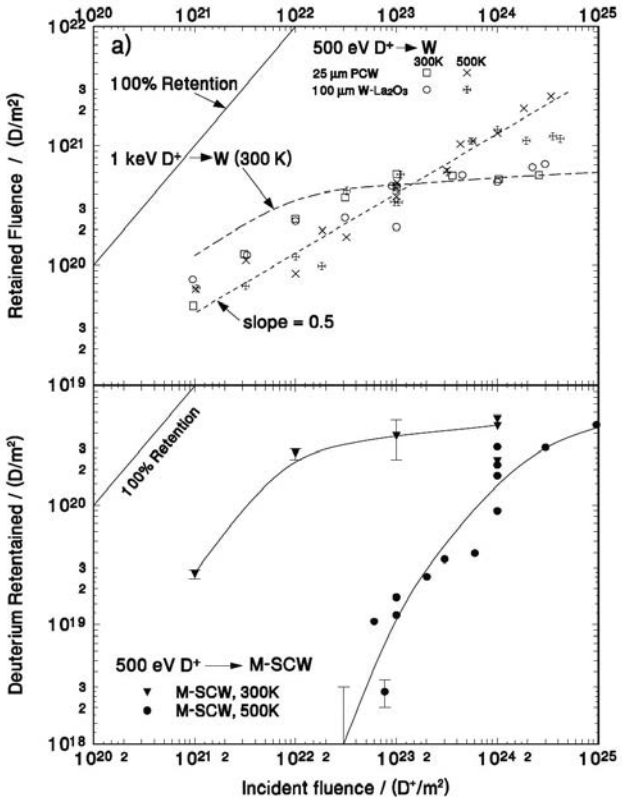

FIG. 1. Fluence dependence of (a) D retention in PCW and W-1%La_2O_3 at 300 and 500 K temperature for 500 eV and 1 keV D^+ irradiations [3]; (b) D retention in M-SCW at 300 and 500 K for 500 eV D^+ [19].

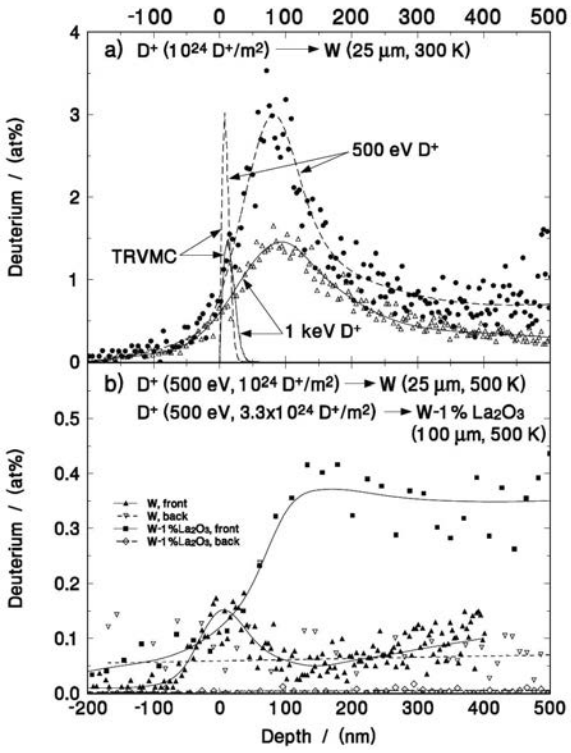

FIG. 2. (a) NRA measurements of near-surface D depth profiles in PCW irradiated by 500 eV and 1 keV D^+ at 300 K. Normalized implantation profiles calculated by TRVMC are shown for comparison [3]. (b) NRA depth profiles in PCW and W-1%La_2O_3 irradiated with 500 eV D^+ at 500 K [3]. Profiles for both front and back surfaces are shown.

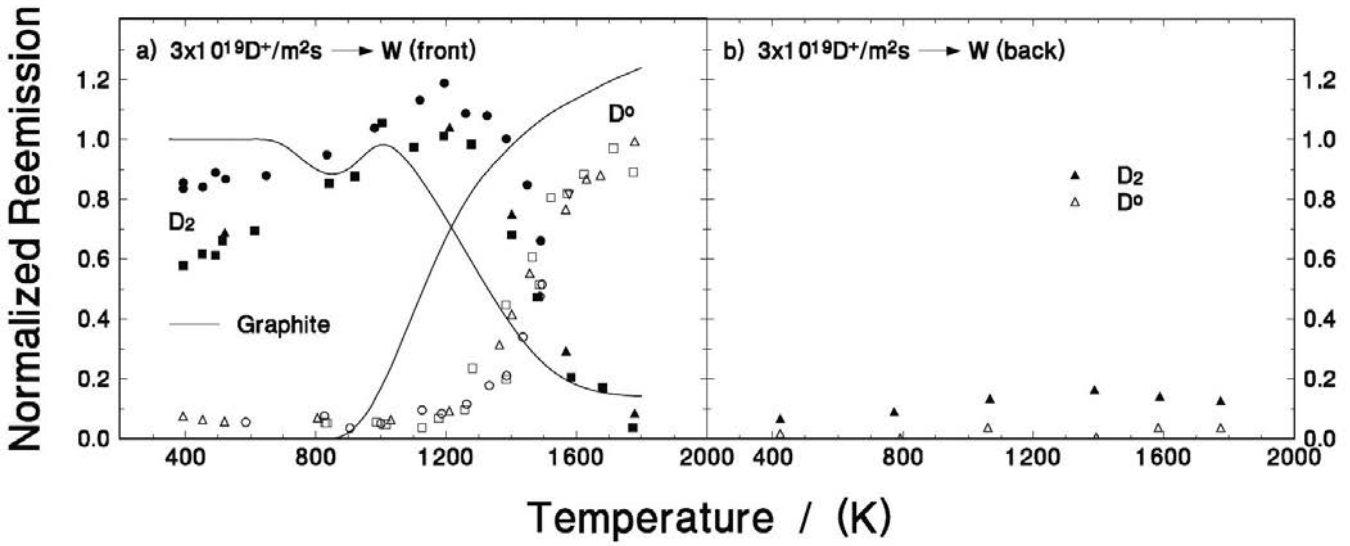

FIG. 3. Steady-state reemission of D^o atoms and D_2 molecules form the front and back surfaces of PCW as a function of specimen temperature during 1 keV D^+ irradiation; the cumulative fluence was (2-3) × 10^{23} D^+/m^2 [15]. The solid lines corresponding to re-emission from pyrolytic graphite are shown for comparison [32].

increases from 300 to ~450 K, reaching a maximum, and then decreasing as the temperature is further increased to ~700 K, where essentially no D is retained [3]; see Fig. 4(a). The large scatter in the data is likely due to the varying implantation history of the specimens, in particular, the effect of cumulative implantations, which was investigated in subsequent experiments [10]; see below.

2.1.2. Effect of ion damage on D retention

The displacement threshold energy for D^+ in W is 940 eV [6]. Therefore, for 500 eV D^+ implantations we do not expect ion-induced displacement damage to occur. However, 500 eV D^+ implantations at 500 K showed an increase in D retention on specimens implanted to a particular incident fluence (e.g., $10^{23}D^+/m^2$), but which have been previously exposed to higher cumulative fluences ($>10^{24}D^+/m^2$) [10]. It is suggested that this increased retention may be due to ion damage caused by means other than atom displacement, namely, swelling-induced stresses and/or precipitation of tungsten hydrides leading to dislocation creation and grain cracking [10]. Such stresses and swelling can lead to macroscopic surface deformation and blister formation. Evidence of surface blisters due to high fluence implantations is seen in Fig. 5. The damage so formed is not removed during TDS (~2100 K), so that more trapping sites are present in subsequent implantations – leading to the observed increase in D retention. This increasing D retention trend, however, changes when microcracks and fissures form in the blisters, leading to escape of deuterium, most likely in the form of D_2 molecules. Surface and cross-sectional SEM views of such a blister formed on 'specimen W7' by 500 eV D^+ with a fluence

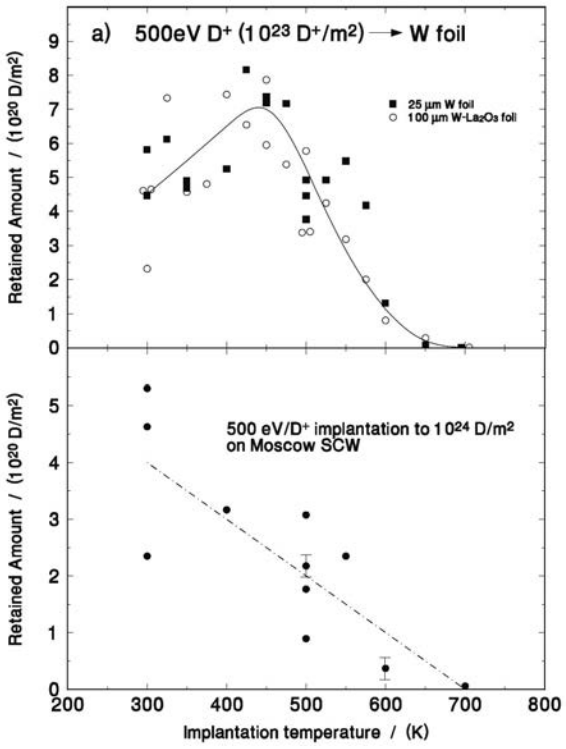

FIG. 4. Temperature dependence of D retention in tungsten irradiated with 500 eV D^+: (a) PCW and W-1%La_2O_3 [3]; and (b) M-SCW [19].

of $10^{25}D^+/m^2$ at 500 K are shown in Figs 5(c) and (d), respectively [10].

2.1.3. Effect of carbon pre-implantation on D retention

The presence of both carbon and tungsten in the ITER divertor will no doubt lead to mixing of these two elements. Materials mixing will be further affected by

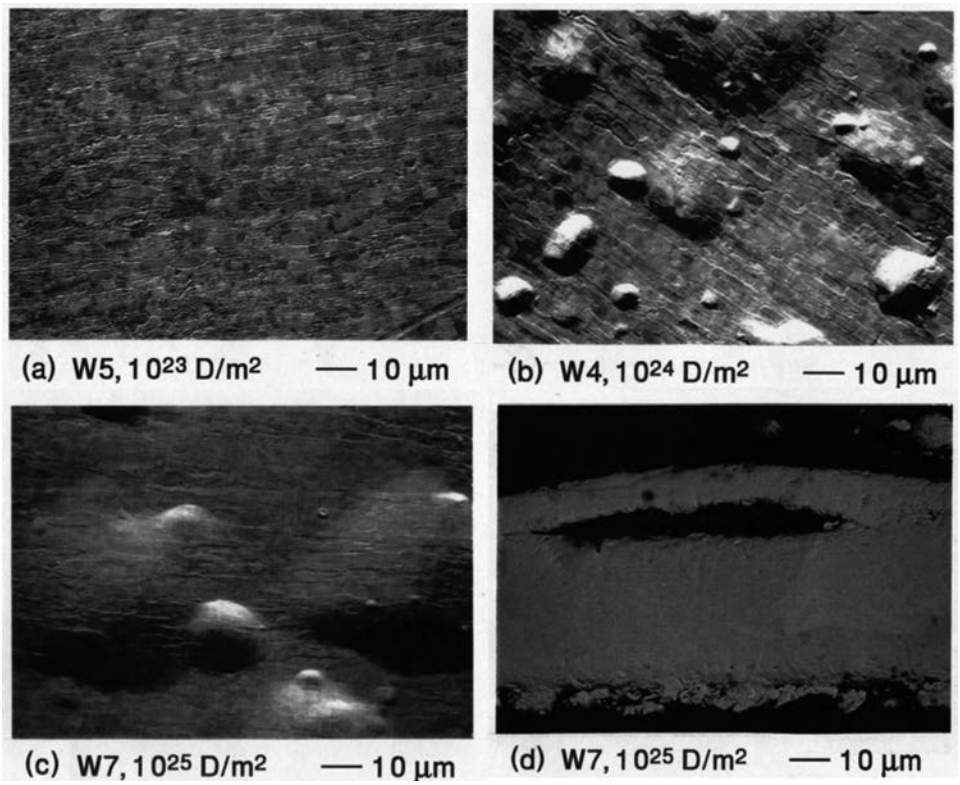

FIG. 5. (a-c) SEM photographs of the front surface of PCW specimens irradiated with 500 eV D^+ at 500 K for different D^+ fluences; (d) cross-sectional SEM of specimen W7 showing a large blister [10].

the transport of eroded beryllium from the vessel first wall – but this will not be discussed here. Regarding tritium inventory, a key question is how the presence of carbon in the near surface of tungsten will affect the trapping of deuterium. Our experiments have shown that D retention in C^+-implanted W strongly depends on the C^+ fluence and the implantation temperature [16]. With high C^+ fluences (>$10^{22}C^+/m^2$) a graphitic surface layer is formed on the W surface. For subsequent low D^+ fluences (~$10^{22}D^+/m^2$) the D retention levels are similar to those seen for pure graphite [17]. However, further D^+ irradiation will lead to preferential erosion of the implanted carbon, and thus the removal of the graphite layer, leaving a WC interface, which was formed during the initial phase of C^+ implantation. Further D^+ irradiation removes the C from the WC interface, eventually leaving pure W [3, 16]. So, basically, we observe three different domains for D retention: (i) D^+ impact on a graphitic surface layer formed by high fluence C^+ implantation; (ii) D^+ impact on a WC surface formed either by low-fluence C^+ or high-fluence C^+ pre-implantation followed by D^+ irradiation to remove the graphite; and (iii) D^+ implantation into pure W when all the C structures are removed from the surface [16]. All of these domains are evident on the curve showing 1 keV C^+ followed by 500 eV D^+ implantations into 25μm PCW at 500 K in Fig. 6.

2.2. *Single crystal tungsten*

In order to understand the basic underlying mechanisms governing hydrogen interactions in tungsten, high purity single crystal tungsten, being almost completely free of grain boundaries and dislocations, is the ideal material to study. While single crystal tungsten will not be used in a fusion reactor, its study will help

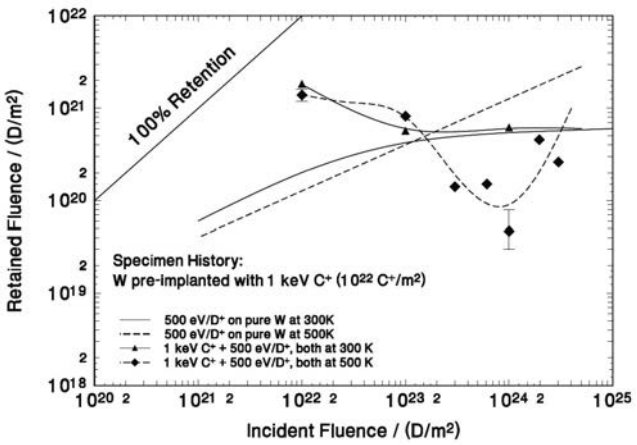

FIG. 6. D retention as a function of incident D^+ fluence for 25 μm PCW foil pre-implanted with 1 keV C^+ to 10^{22} C^+/m^2. Lines are drawn through data corresponding to different implantation temperatures [16]. Reference curves for 500 eV D^+ implantations in pure PCW [3] are shown for comparison.

to determine the role of grain boundaries, impurities, vacancies, porosity and other material characteristics on hydrogen retention, recycling, and permeation.

2.2.1. Fluence and temperature dependence of D retention

Single crystal tungsten specimens used in our experiments were manufactured by Johnson–Matthey (referred to as JM-SCW) and the State Institute of Rare Metals, Moscow (referred to as M-SCW). The quoted impurity content of the JM-SCW was 99.9 wt%, with the main impurities being H (~0.1 at.%), C (~0.5 at.%) and O (~0.5 at.%); the crystal surface orientation was 8.5° from the [001] plane [18]. By comparison, the quoted purity of the M-SCW was 99.9 at.% with the main impurities being the same as for the JM-SCW, but the concentrations were an order of magnitude lower: H (0.02 at.%), C (0.05 at.%) and O (0.05 at.%). The crystal surface orientation of the M-SCW was within 10° of the [001] plane [19]. Most of our single crystal experiments were performed with the higher-purity M-SCW specimens, provided by Dr. V.Kh. Alimov.

The fluence dependence of D retention after a 1775 anneal followed by 500 eV D^+ implantations at 300 and 500 K are shown in Fig. 1(b). At 300 K, the D retention curves for SCW and PCW are very similar; compare Figs 1(a) and 1(b). Initially, the retention increases with increasing D^+ fluence, tending to a saturation level of $\sim 6 \times 10^{20}$D/m^2 for incident fluences above $\sim 10^{23}D^+/m^2$ [3, 19]. At 500 K the retention curves for both SCW and PCW are similar in that they both show an increasing trend with increasing fluence, without reaching saturation even at 10^{25}/m^2. However, they differ in the slope of the curves and the amounts of D retained, with the SCW showing less retention [3, 19], implying significantly less trapping sites in the single crystal.

The temperature dependence of D retention in SCW for 500 eV D^+ implantations with a fluence of $10^{24}D^+/m^2$ shows a decreasing trend in retention with increasing temperature [19]; see Fig. 4(b). This behaviour greatly differs from the PCW case shown in Fig. 4(a), where a maximum at ~450 K is clearly evident [3]. No retention was seen for implantations above 700 K [19], as was also the case for PCW [3].

2.2.2. Flux dependence

Deuterium retention in single crystal tungsten implanted with 500 eV D^+ at 300 K was found to vary significantly at low D^+ fluxes ($<10^{18}D^+/m^2s$) and low D^+ fluences ($10^{21}D^+/m^2$) [20]; see Fig. 7. The prominent decrease in retention for fluxes below $10^{18}D^+/m^2s$ suggests a 'flux threshold' level for D retention. For a higher fluence of $10^{22}D^+/m^2$ the flux dependence is more

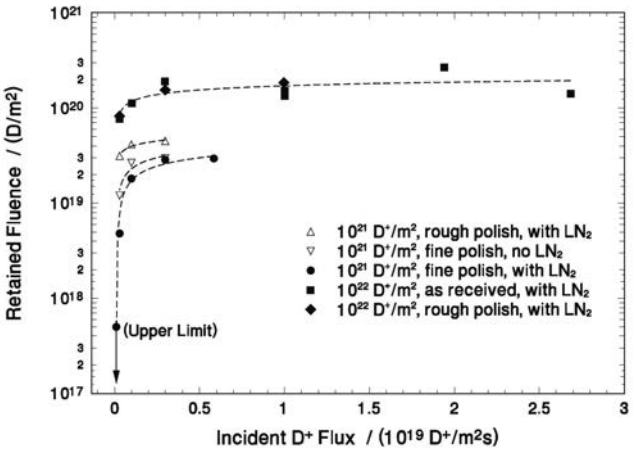

FIG. 7. Deuterium retention as a function of incident D^+ flux at fluences of 10^{21}-$10^{22}D^+/m^2$ at 300 K for various experimental conditions [20].

difficult to observe; see Fig. 7. The suggested explanation for this effect is as follows: under irradiation, a steady state will be established between the incident D^+ flux and the flux of D diffusing out of the implantation zone, such that the local mobile D concentration will depend on the incident flux. Hydrogen trapping is thought to occur only when the local D concentration exceeds a local threshold value, i.e., high enough to cause lattice distortion. Thus, for sufficiently low fluxes, there will not be any hydrogen trapping. For fluxes which lead to mobile D concentrations above the threshold, trapping can occur; however, the rate of trapping does not appear to have any dependence on flux above this threshold value. This threshold effect is present for all fluences studied [20].

2.2.3. Effect of impurities

The impurities that can potentially affect D retention during D^+ irradiation can originate from either the bulk or from the gas phase during irradiation. Differences in D retention have been observed for the high purity M-SCW and the less pure JM-SCW [18, 19]. While the crystal orientation was similar in both materials, the JM-SCW had 10 times higher O and C bulk impurities. The retained D was generally higher in the less pure JM-SCW [19].

SIMS depth profiles of SCW specimens were obtained to see the evolution of surface and bulk impurities at various stages of the experiments: virgin specimen, after annealing to >1700 K, after D^+ implantation, and after TDS at 1775 K. A case of 500 eV D^+ implantation to $10^{24}D^+/m^2$ at 500 K is shown in Fig. 8 [19]. After D^+ implantation all of the elements profiled had gained near-surface peaks; see Fig. 8(b). The peak locations correspond to the D^+ implant zone (~20 nm). It appears that the D^+ implantation has enhanced O and C diffusion

from the surface into the bulk. Since 500 eV D^+ energy was too low to create vacancies, the enhanced diffusion was attributed to lattice strain and dislocations caused by the high concentration of mobile D in a material with very low solubility [21]. Post-implantation TDS (heating to 1775 K) caused a significant reduction of C and O, dropping to the initial post-anneal levels; compare Figs 8(a) and 8(c).

The role of surface impurities was further investigated by controlling the partial pressure of impurities in the background gas during D^+ irradiation [22]. Reduction of the background levels (CH_4, H_2O, CO, O_2, and CO_2) has led to reductions in the near-surface SIMS O and C concentrations and the retained amount of D, and changes in the TDS profiles. The correlation between the reductions of gas impurities and the decrease in the near-surface O and C peaks suggests that O and C from the background gas entered the tungsten to create these near-surface peaks [22]. The thermal energy of the impurity molecules and atoms is insufficient to enter the tungsten, as evidenced by the off-irradiation-spot SIMS analysis that showed no near-surface impurity peaks [22]. However, through elastic collisions, the impacting 500 eV D^+ can transfer up to 200 eV and 250 eV to O and C atoms, respectively [22, 23]. At these energies, O and C can enter the tungsten, but only to depths of a few nm [22, 24]. Collisions with successive D^+ and radiation-enhanced diffusion may allow the O and C to reach depths equivalent to the 500 eV D^+ implant zone, ~20 nm [24].

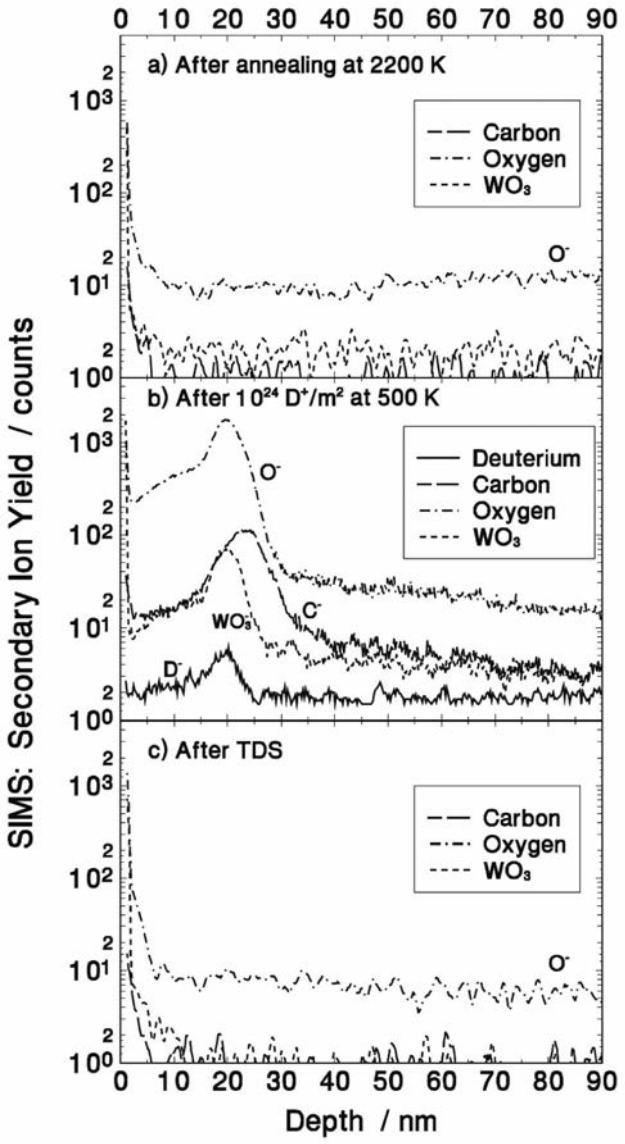

FIG. 8. SIMS depth profiles of M-SCW specimens showing the evolution of impurities after (a) annealing at 2200 K; (b) 500 eV D^+ implantation (10^{24} D^+/m^2) at 500 K; and (c) TDS at 1775 K [19].

The maximum energy transfer from 500 eV D^+ to a W atom is 21 eV – insufficient to create a displacement [5]. However, the energy transfer from O or C is more efficient, such that vacancies can be created by relatively low energy O or C. Deuterium trapping at vacancy-type defects is known to be a significant D retention mechanism in W, see e.g., Ref. [7]. It then follows that by reducing the impurity content in the background gas, and thus the concentration of surface impurities during D^+ irradiation, the number of vacancies created will be reduced, and the amount of D trapped will decrease – as observed in the experiments [22].

Further experiments were performed with SCW to investigate how exposure to background impurities during the various stages of the experiment might affect the measured amount of D released from the specimens during TDS [25]. In the previous experiments discussed above, TDS was performed in a separate vacuum chamber, necessitating specimen transport in air, time delay between implantation and TDS, and as part of the TDS chamber preparation, mild baking (~400 K) of the chamber with the specimen in it. By modifying the ion implantation vacuum system, implantation and TDS could be performed in the same chamber, with more control over the time delay between the two steps [25]. The key findings were: (i) air exposure prior to TDS has negligible effect; (ii) prolonged time delay leads to lower D retention, indicating that during D^+ irradiation some mobile D diffuses deep into the bulk, requiring relatively long post-irradiation times at room temperature to diffuse to the surface and be released; and (iii) in addition to the TDS spectral peaks at 500, 600 and 900 K seen in previous experiments, e.g., Refs [19, 22], a peak was present at ~400 K, indicating the existence of additional lower energy traps. Mild baking of the implantation/TDS chamber (the same in this case), however, resulted in the near elimination of the 400 K peak, as well as a reduction in the total amount of D retained [25] – bringing the retention levels into agreement with previous results, where mild baking was regularly employed [19].

3. D and He retention in PCW due to He^+ and $H^+(D^+)$ irradiations

Under burning plasma conditions, tungsten will be irradiated with the hydrogen fuel (D and T) and the helium ash. Since He is essentially insoluble in all metals, see e.g., Ref. [26], He irradiation often leads to blister formation and subsequent degradation of the mechanical properties of metals, see e.g., Ref. [27]. Such material changes may in turn affect the transport, trapping, and recycling behaviour of hydrogen in tungsten. In order to understand the effect of one irradiating species on another regarding the trapping and retention behaviour of tungsten, we have performed single-species H^+(or D^+), see e.g., Ref. [3], and He^+ [28] irradiations, as well as two-species H^+(or D^+)-He^+ irradiations, both sequential [28] and simultaneous [29]. These experiments were performed with polycrystalline tungsten.

3.1. Sequential (SEQ) irradiations

The objective of this work was to study (i) the effect of deuterium on He trapping in W for sequential D^+-He^+ irradiations, and (ii) the effect of He on hydrogen (or deuterium) trapping in W for sequential He^+-$H^+(D^+)$ irradiations [28]. The amount of He retained in the specimens for He^+-only and SEQ He^+-H^+ irradiations was determined by monitoring the QMS mass-4 (all due to He) signal. The situation for SEQ He^+-D^+ irradiations is complicated by the fact that the QMS used cannot separate the He and D_2 contributions to mass-4. So, to obtain the D retention, the mass-4 D_2 contribution was derived from the difference of measured mass-4 signals for He^+-D^+ and He^+-H^+ irradiations [28].

3.1.1. Sequential irradiations at 300 K

(a) He+-D+: Effect of H+(or D+) post-irradiation on He retention

TDS profiles for He^+-only, D^+-only, SEQ He^+-H^+, He^+-D^+, and D^+-He^+ irradiations at 300 K for several fluence combinations are shown in Fig. 9 [28]; all ion energies are 500 eV. The TDS peaks at >800 K, characteristic of He^+-only irradiation, are not present in any of the SEQ He^+-$H^+(D^+)$ irradiations; see Figs 9(a) and 9(b). This indicates that the incident H^+ and D^+ ions have de-trapped the He from the more energetic traps; compare profiles (1) and (2) with (3) in Fig. 9(a). Instead, He was found to desorb at 500 and 680 K. The 680 K peak is where D would normally be released for D^+-only irradiation; see profile (10) in Fig. 9(c). The absence of peaks >800 K suggests the elimination of He-vacancy (He_nV_m) complexes [28].

He release at 500 K is the only part of the He^+-only TDS spectrum which is largely unchanged by post H^+ or D^+ irradiation. This peak was attributed to He trapped at grain boundaries or within the crystal, possibly at interstitial dislocation loops surrounding He_nV_m complexes [28]. With the He_nV_m complexes now removed by H^+ (or D^+) post irradiation, the unchanged 500 K peak suggests trapping at grain boundaries over interstitial loops [28]. The peak at 680 K which was not observed for He^+-only irradiation may involve He trapping with D (or H), but its reduction with increasing H^+ (or D^+) fluence suggests that it is a remnant of the He_nV_m complex; compare profiles (1) and (2) in Fig. 9(a) and profiles (4) and (5) in Fig. 9(b) [28]. The concept of joint D-He trapping is supported by the nearly overlapping ERD depth profiles of D and He in the near surface (~20-30 nm). This overlapping of the D and He ERD profiles and the absence of D beyond this depth further implies that the pre-implanted He blocks the transport of D beyond the implantation zone; the actual mechanism for this blocking effect has not been identified [28].

(b) He^+-D^+: Effect of He^+ pre-irradiation on D retention

The effect of pre-implanted He on D retention can be seen by taking the difference between the SEQ He^+-H^+ and He^+-D^+ profiles (7) and (8) in Fig. 9(c). This difference, shown by the hatched area in Fig. 9(c), is also plotted in Fig. 9(d), labelled as ΔA (solid line). The ΔA profile indicates that the post-implanted D^+ is released at ~500 K, with the near elimination of the 680 K peak, which is dominant for D^+-only irradiations shown by the dash profile (13) in Fig. 9(d) [28]. This D release at 500 K appears to be largely unaffected by the He presence. It is thought that the post-implanted D^+ breaks apart the He_nV_m complexes and re-traps interstitially with the He atoms [28].

The ΔA profile in the 400-600 K desorption range represents D originating from D trapped within ~35 nm of the near surface. The overlap of He and D ERD depth profiles suggests possible He-D trap configuration. Correspondingly, D release at 680 K (observed for D^+-only) is in part due to D trapping in the bulk. The D content reduction for the SEQ He^+-D^+ irradiation compared to D^+-only is attributed to (i) D being unable to form vacancies at the near surface and (ii) D diffusion being hindered by the He presence in the near surface [28].

(c) D+-He+: Effect of D+ pre-irradiation on He retention

Here the sequence of irradiation is reversed, D^+ first, then He^+. The TDS desorption profiles for SEQ

D^+-He^+ irradiations (Fig. 9(e)) indicate that in the range 800-1200 K, where no D desorption peaks are expected (see D^+-only in Fig. 9(c)), the trapping of post-implanted He is unaffected by the presence of the pre-implanted D, and He is released in the same manner as for He^+-only irradiations; see Fig. 9(e) [28]. Therefore, it appears that the presence of D does not enhance the formation of He_nV_m complexes [28]. (Note that the TDS profile below 800 K is dominated by D release.)

(d) D+-He+: Effect of He+ post-irradiation on D retention

Subtracting the He^+-only profile from the SEQ D^+-He^+ (Fig. 9(e)) gives a good approximation of the D retention profile for the SEQ D^+-He^+ irradiation, shown as ΔB (open squares) in Fig. 9(d) [28]. ΔB represents the D content between 400 and 800 K. The observed reduction in the 680 K peak, compared to the D^+-only case, corresponds to ~40% reduction in D retention; compare profiles (12) and (13) in Fig. 9(d). In previous studies the 680 K peak for D^+-only was interpreted to be D trapped at vacancies at the near surface and extended defects deep in the bulk [19, 30, 31]. Since ERD He depth profiles for 300 K implants show He to be within the near surface (~35 nm), the reduction in the 680 K D peak is attributed to He detrapping of D at vacancies in the near surface [28]. This implies that for D^+-only irradiations, about 40% of the retained D is trapped at vacancies in the near surface [28].

A portion of the remaining D release in the range 400-800 K is interpreted to be D coming from D trapped deep within the bulk beyond the He^+ implantation range. The difference between the ΔA and ΔB profiles in Fig. 9(d) represents D trapped beyond ~35 nm. The D content in the (ΔB-ΔA) difference, corresponding to bulk trapping, represents ~30% of the total amount of D retained for D^+-only implantations [28].

3.1.2. Sequential irradiations at 700 K

(a) He+-D+: Effect of D+ post-irradiation on He retention

For sequential irradiations at 700 K the entire QMS mass-4 release is attributed to He [28] since no D retention is observed at this temperature [3]. Some differences in the TDS peaks are noted for irradiations at 700 and 300 K. Comparison of profiles (3) and (4) with (1) in Fig. 10(a) shows that for 700 K irradiations the post-implanted D^+ does not fully reduce the prominent He peak at ~1000 K, as was the case at 300 K [28]. Also, for 700 K irradiations no He peaks are seen below 800 K, again differing from the 300 K case. It is postulated that during D^+ post-irradiation, He is able to retrap while D is unable to re-trap due to the high temperature. This leads to the observed He release at ~1000 K but not at 680 K, which is attributed to He trapping with D [28].

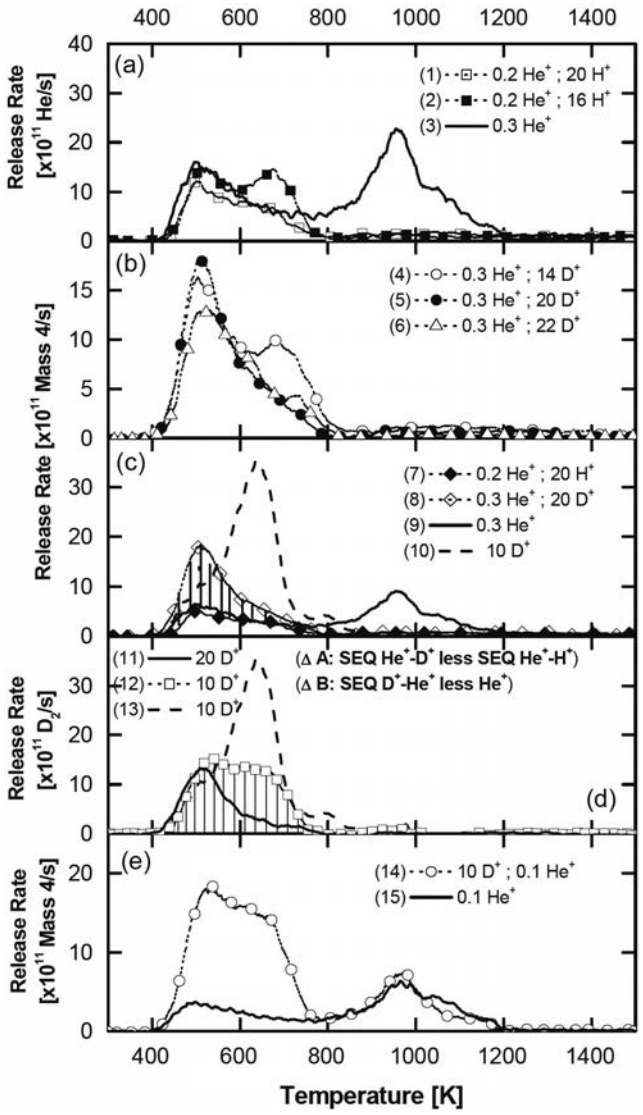

FIG. 9. TDS profiles for 500 eV SEQ irradiations of PCW at 300 K: (a) SEQ He^+-H^+; (b) SEQ He^+-D^+; (c) comparison of two SEQ cases with D^+-only and He^+-only profiles; (d) derived profiles for D release compared with a D release profile obtained for D^+-only irradiation; and (e) SEQ D^+-He^+ where the order of He^+ and D^+ is reversed [28]. Refer to the text for further details regarding the hatched area in part (c) and the D contents designated by ΔA and ΔB in part (d); also see Ref. [28]. (Legend: fluences in units of $\times 10^{22}$ D^+/m^2.)

(b) D+-He+: Effect of D+ pre-irradiation on He retention

It is evident from the TDS profiles shown in Fig. 10(b) that the pre-implanted D^+ has virtually no effect on the trapping behaviour of He. Helium is observed to desorb in a similar manner as if it were implanted alone at 700 K [28]. This behaviour is similar to the 300 K SEQ D^+-He^+ irradiation case presented above; see Fig. 9(e).

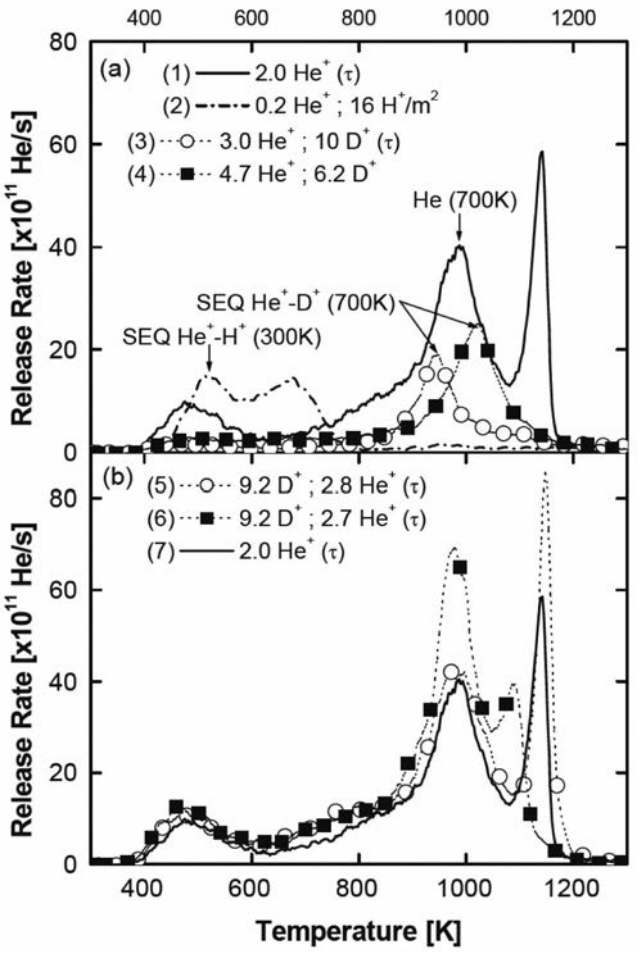

FIG. 10. TDS profiles for 500 eV irradiations: (a) SEQ He^+-D^+ at 700 K, with He^+-only at 700 K and SEQ He^+-H^+ at 300 K; and (b) SEQ D^+-He^+ and He^+-only at 700 K [28]. (Legend: fluences in units of × 10^{22} D^+/m^2)

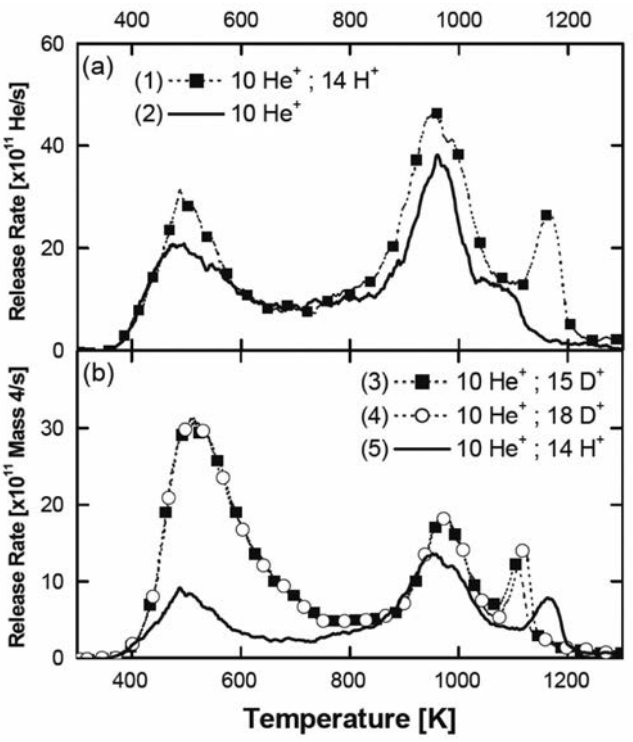

FIG. 11. TDS profiles for 500 eV irradiations at 300 K: (a) SIM He^+-H^+ and He^+-only; and (b) two cases of SIM He^+-D^+ compared with SIM He^+-H^+ [29]. (Legend: fluences in units of × 10^{22} $/m^2$.)

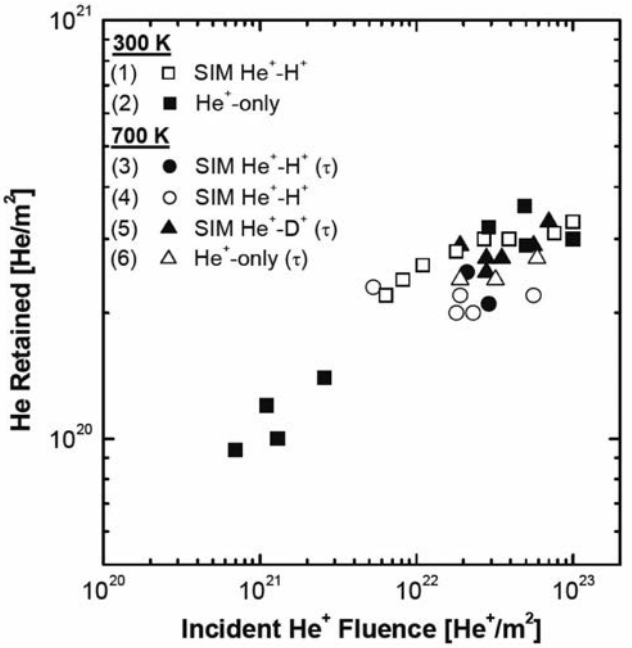

FIG. 12. He retention as a function of He^+ fluence. Profiles labelled with (τ) correspond to specimens held at 700 K for 1 h following irradiations at 700 K [29].

3.2. Simultaneous (SIM) irradiations

3.2.1. Simultaneous He^+-H^+ and He^+-D^+ irradiations at 300 K

The three TDS desorption peaks (near 500, 1000 and 1100-1200 K) characteristic of He^+-only irradiations were also observed for SIM He^+-H^+ and SIM He^+-D^+ irradiations (Fig. 11) [29]. The dominant He release peaks for SIM He^+-H^+ at 500 and 1000 K (Fig. 11(a)) closely follow the He^+-only profiles. Overall, the presence of H^+ does not have a significant effect on the He release profiles. The total He retained also closely follows the He^+-only values and fluence dependence trend; compare data (1) and (2) in Fig. 12 [29].

The most revealing difference between the SIM He^+-H^+ and SIM He^+-D^+ desorption profiles occurs in the temperature range 400-800 K, indicating significant contributions of D_2 to the total mass-4 release in the SIM He^+-D^+ cases; compare profiles (3) and (4) with (5) in Fig. 11(b) [29]. This is the temperature range where D release is observed for D^+-only irradiations at 300 K [19]. The D and He contributions to the spectra can be separated by taking the difference between the SIM He^+-D^+ and SIM He^+-H^+ profiles in the range 400-800 K. This difference, together with a D^+-only profile, is plotted for several He^+ and D^+ fluence combinations in Fig. 13 [29]. Only one desorption peak, centred on ~520 K, is observed; the ~650 K peak characteristic of D^+-only is

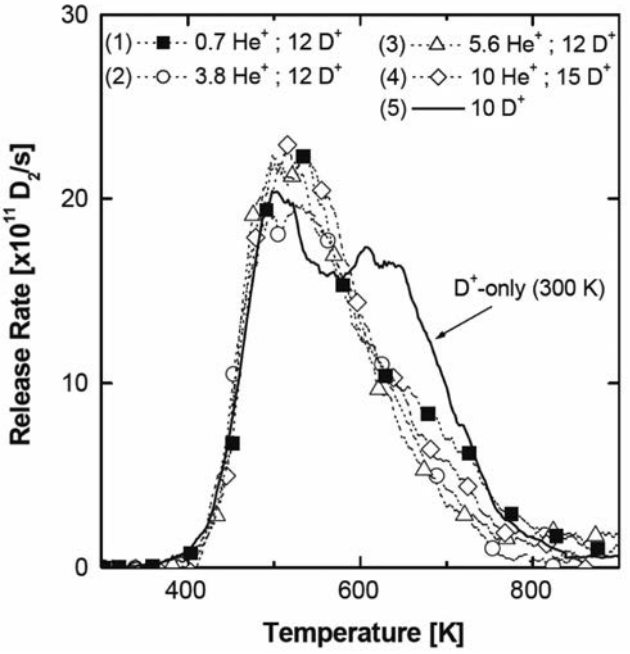

FIG. 13. Derived desorption profiles of D release from SIM He^+-D^+ irradiations at 300 K were obtained by subtracting SIM He^+-H^+ profiles from SIM He^+-D^+ profiles; see Fig. 11. TDS profile for D^+-only irradiation at 300 K is shown for comparison [29]. (Legend: fluences in units of × 10^{22} /m^2.).

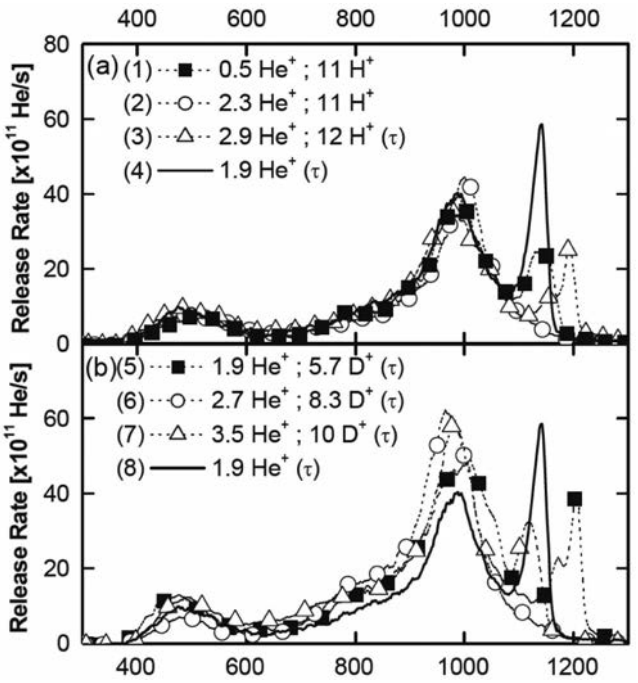

FIG. 14. TDS desorption profiles of He release for different fluence combinations of 500 eV SIM He^+-H^+ and He^+-D^+ irradiations at 700 K. Profiles for He^+-only at 700 K are shown for comparison. (Legend: fluences in units of × 10^{22} /m^2.)

significantly reduced. This indicates that He has modified the nature of some trapping sites.

The total amount of D retained for the SIM He^+-D^+ irradiations was roughly equal to the amount measured for D^+-only [29]. ERD depth profiles of D and He for SIM He^+-D^+ at 300 K show that both He and D are confined to a depth of 30-35 nm [29], similar to the depth profiles seen for SEQ He^+-D^+ irradiations [28]. Deuterium, when implanted alone into tungsten at 300 K, diffuses deep into the bulk (>500 nm) [3]. Hence the shallower D range observed for both SIM He^+-D^+ [29] and SEQ He^+-D^+ [28] irradiations indicates that the presence of He in tungsten limits D diffusion into the bulk. As estimated in Section 3.1.1(d) above, for D^+-only irradiations, the D trapped in the bulk accounts for ~30% of the total D retention [28]. Since the amount of D retained for SIM He^+-D^+ and D^+-only irradiations is nearly equal, and D is confined to within 30-35 nm of the surface for the SIM case, there must be a corresponding increase of ~30% in D retention at the near-surface for the SIM He^+-D^+ case [29].

The exact mechanism of D trapping in tungsten is still unclear, with micro-cavities [8] and vacancy sites [31] being proposed. In the near surface (based on ERD depth profiles), the deuterium desorption spectra were found to be similar for both D^+-He^+ and He^+-D^+ sequential irradiations [28], despite the fact that in the first case He-vacancy complexes are formed while in the latter case they are reduced by D^+. The fact that D trapping does not depend on the existence of He-vacancy complexes suggests that D is not trapped either by chemisorption on the inner surfaces of the He-vacancy complex or by molecule formation within the He-vacancy complex. Rather, the crystal defects created by the high stress fields of the He-vacancy complexes appear more likely to be the trapping sites for D [29].

3.2.2. Simultaneous He^+-H^+ and He^+-D^+ irradiations at 700 K

Similar to the 300 K SIM irradiations (Section 3.2.1), the desorption profiles for SIM He^+-H^+ and He^+-D^+ irradiations at 700 K occur in the vicinity of 500, ~1000, and 1100-1200 K; see Fig. 14. He release at <1100 K for SIM He^+-H^+ closely follows the He^+-only case; compare profiles (3) and (4) in Fig. 14(a). He retention values also closely follow within experimental error; compare data (3) and (4) with (6) in Fig. 12. Thus, the He trapping behaviour appears to be largely unaffected by D and H presence at 700 K.

ERD depth profiles for SIM He^+-D^+ irradiations at 700 K show that He trapping is confined to ~30 nm of the surface and there is no D trapping [29]. Therefore, the mass-4 release for the SIM He^+-D^+ irradiations at 700 K in Fig. 14(b) is entirely attributed to He release. Interestingly, He release at 500 K is observed in both the simultaneous [29] and He^+-only [28] cases despite the fact that irradiations were performed at 700 K. It appears

that He^+ irradiation at elevated temperatures involves some mechanism whereby He atoms in higher-energy traps are transferred to low-energy traps – possibly when the specimen cools.

Acknowledgements

The financial support provided by the Natural Sciences and Engineering Research Council of Canada is gratefully acknowledged.

References

[1] FEDERICI, G., et al., Plasma-material interactions in current tokamaks and their implications for next step fusion reactors, Nucl Fusion **41** (2001) 1967.

[2] SAKAMOTO, R., MUROGA, T., YOSHIDA, N., Retention and desorption of implanted deuterium and high-Z plasma facing materials, J. Nucl. Mater. **233-237** (1996) 776.

[3] HAASZ, A.A., DAVIS, J.W., POON, M., MACAULAY-NEWCOMBE, R.G., Deuterium retention in tungsten for fusion use, J. Nucl. Mater. **258-263** (1998) 889-895.

[4] CAUSEY, R.A., VENHAUS, T.J., The use of tungsten in fusion reactors: A review of the hydrogen retention and migration properties, Phys. Scripta **T94** (2001) 9.

[5] SAKAMOTO, R., MUROGA, T., YOSHIDA, N., Microstructural evolution induced by low energy hydrogen ion irradiation in tungsten, J. Nucl. Mater. **220-222** (1995) 819.

[6] TOKUNAGA, K., TAKAYAMA, M., MUROGA, T., YOSHIDA, N., Depth profile analyses of implanted D in W by secondary ion mass spectrometry, J. Nucl. Mater. **220-222** (1995) 800.

[7] ELEVELD, H., VAN VEEN, A., Void growth and thermal desorption of deuterium from voids in tungsten, J. Nucl. Mater. **212-215** (1994) 1421.

[8] ALIMOV, V.Kh., ERTL, K., ROTH, J., SCHMID, K., Deuterium retention and lattice damage in tungsten irradiated with deuterium ions, Phys. Scripta **T94** (2001) 34.

[9] MACAULAY-NEWCOMBE, R.G., HAASZ, A.A., POON, M., DAVIS, J.W., "An interpretation of the retention of low energy D ions in tungsten", Hydrogen and Helium Recycling at Plasma-Facing Materials in Fusion Reactors (HASSANEIN, A., Ed.), NATO Science Series II: Mathematics, Physics and Chemistry, Vol. 54, Kluwer Academic Publishers, Dordrecht (2002) 145.

[10] HAASZ, A.A., POON, M., DAVIS, J.W., The effect of ion damage on deuterium trapping in tungsten, J. Nucl. Mater. **266-269** (1999) 520.

[11] ALIMOV, V.Kh., ROTH, J., MAYER, M., Depth distribution of deuterium in single crystal and polycrystalline W up to depths of several micrometers, J. Nucl. Mater. **337-339** (2005) 619.

[12] TOKUNAGA, K., et al., Blister formation and D retention on W exposed to low energy and high flux deuterium plasma, J. Nucl. Mater. **337-339** (2005) 887.

[13] WANG, W., ROTH, J., LINDIG, S., WU, C.H., Blister formation of tungsten due to ion bombardment, J. Nucl. Mater. **299** (2001) 124.

[14] HAASZ, A.A., DAVIS, J.W., Deuterium retention in beryllium, molybdenum and tungsten at high fluences, J. Nucl. Mater. **241-243** (1997) 1076-1081.

[15] DAVIS, J.W., HAASZ, A.A., Reemission of deuterium atoms from Mo, Ta and W during D^+ irradiation, J. Nucl. Mater. **223** (1995) 312-315.

[16] POON, M., DAVIS, J.W., HAASZ, A.A., Effect of carbon pre-implantation on deuterium retention in tungsten, J. Nucl. Mater. **283-287** (2000) 1062-1067.

[17] HAASZ, A.A., DAVIS, J.W., Fluence dependence of deuterium trapping in graphite, J. Nucl. Mater. **209** (1994) 155.

[18] HAASZ, A.A., POON, M., MACAULAY-NEWCOMBE, R.G., DAVIS, J.W., Deuterium retention in single crystal tungsten, J. Nucl. Mater. **290-293** (2001) 85-88.

[19] POON, M., HAASZ, A.A., DAVIS, J.W., MACAULAY-NEWCOMBE, R.G., Impurity effects and temperature dependence of D retention in single crystal tungsten, J. Nucl. Mater. **313-316** (2003) 199-203.

[20] POON, M., MACAULAY-NEWCOMBE, R.G., DAVIS, J.W., HAASZ, A.A., Flux dependence of deuterium retention in single crystal tungsten, J. Nucl. Mater. 3**07-311** (2002) 723-728.

[21] FRAUENFELDER, R., Solution and diffusion of hydrogen in tungsten, J. Vac. Sci. Technol. **6** (1968) 388.

[22] POON, M., MACAULAY-NEWCOMBE, R.G., DAVIS, J.W., HAASZ, A.A., Effects of background gas impurities during D^+ irradiation on D trapping in single crystal tungsten, J. Nucl. Mater. **337-339** (2005) 629-633.

[23] THOMPSON, M.W., Defects and Radiation Damage in Metals, Cambridge University Press, Cambridge (1969).

[24] ZIEGLER, J.F., BIERSACK, J.P., LITTMARK, U., The stopping and range of ions in solids, Pergamon, New York (1985).

[25] QUASTEL, A.D., DAVIS, J.W., HAASZ, A.A., MACAULAY-NEWCOMBE, R.G., Effect of post-D^+-irradiation time delay and pre-TDS heating on D

retention in single crystal tungsten, J. Nucl. Mater. **359** (2006) 8-16.

[26] THOMAS, G.J., Experimental studies of helium in metals, Radiat. Eff. **78** (1983) 37.

[27] DAS, S.K., KAMINSKY, M., "Radiation blistering in metals and alloys", Radiation Effects on Solid Surfaces (KAMINSKY, M., Ed.), American Chemical Society (1976) 112.

[28] LEE, H.T., HAASZ, A.A., DAVIS, J.W., MACAULAY-NEWCOMBE, R.G., Hydrogen and helium trapping in tungsten under single and sequential irradiations, J. Nucl. Mater. **360** (2007) 196-207.

[29] LEE, H.T., HAASZ, A.A., DAVIS, J.W., et al., Hydrogen and helium trapping in tungsten under simultaneous irradiations, J. Nucl. Mater. **363-365** (2007) 898-903.

[30] POON, M., Deuterium Trapping in Tungsten, PhD Thesis, University of Toronto, 2004.

[31] FRANSENS, J.R., ABD EL KERIEM, M.S., PLEITER, F., Hydrogen-vacancy interaction in tungsten, J. Phys. Condens. Mat. **3** (1991) 9871.

[32] DAVIS, J.W., HAASZ, A.A., Reemission and thermal desorption of D^o, D_2 and CD_4 from graphite, J. Nucl. Mater. **220-222** (1995) 832-835.

Deuterium trapping and release in carbon materials

A. Pisarev, A. Rusinov, N. Trifonov, Yu. Gasparyan

National Research Nuclear University "MEPHI", Moscow, Russian Federation

Abstract

Deuterium thermal desorption from fine grain graphite MPG-8 and carbon fiber composite NB31 after irradiation by plasma and ion beam and after loading from gas was investigated. It was observed that deuterium accumulation in the two materials was similar in the region of the fluence of 10^{22}-4×10^{24} D^+/m^2, though NB31 retains about twice as much deuterons. The retention in MPG-8 reveals no saturation at high fluence and no flux dependence in the range of $(0.5 \div 3.5) \times 10^{20}$ D^+/m^2s. The difference between polished and unpolished samples, as well as between samples kept in air for various times after irradiation, was within the experimental uncertainty.

1. Introduction

Accumulation of tritium in ITER materials and detritiation of reactor components is the key safety problem of ITER. Knowledge about behavior of hydrogen isotopes in fusion materials is necessary for its analyses. A comprehensive overview of various aspects of hydrogen in plasma facing materials is given in Ref. [1]. Thermal desorption spectroscopy (TDS) is one of the methods giving information about trapping efficiency of hydrogen isotopes in PFM. One of the materials actively investigated for fusion applications is graphite and carbon fiber composite. There are many publications on TDS measurements from carbon based materials, and they demonstrated a variety of shapes of thermal desorption spectra. Experiments on TDS were performed mainly after ion implantation [2-22]. Less has been measured after plasma irradiation [23-37] and after saturation from gas [38-42]. There are few descriptions of TDS made with samples subjected to tokamak plasma [25-27, 33, 34] and to atomic hydrogen [43-45]. The results of the measurements are very different. One can also observe serious differences in TDS after plasma impact, which can be connected with uncertainty of plasma parameters, fluence measurements, sample preparation, etc.

This work is devoted to investigation of deuterium TDS from two carbon based materials, fine grain graphite MPG-8 and carbon fiber composite NB31, irradiated in four different plasma installations, magnetron discharge (MD), radiofrequency discharge (RFD), and two beam plasma discharges (BPD – LENTA and PR-2). Also, TDS after ion implantation and after loading in gas are performed for comparison.

2. Thermal desorption facility

An ultra high vacuum stand with low background during heating the sample was designed for TDS experiments. The scheme of the facility is shown in Fig. 1. There are two chambers: the main chamber (V_1 = 4.1 l) for TDS measurements and an additional one for sample loading separated by a gate valve. The chambers are pumped by turbo molecular pumps TMU-071 attached through valves and dry scroll pumps VARIAN SH100. There is also a quadrupole mass spectrometer (QMS)

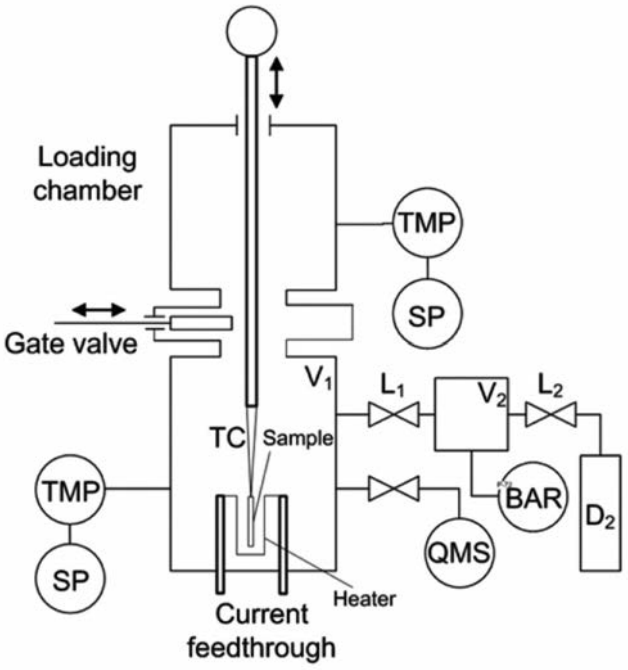

FIG. 1. The scheme of the TDS facility. SP – scroll pumps, TMP – turbo molecular pumps, TC – thermocouple, BAR – baratron, L_1, L_2 – leak valves.

PFEIFFER-VACUUM QMS-200 M1 and QMS calibration system. Carbon samples hang on two thermocouple wires, which are mounted on the bar of a linear feed-through that can move the sample from the loading chamber into the main chamber through the gate valve.

The residual gas pressure in the main chamber is less than 1.3×10^{-9} mbar after a few hours of baking and less than 1.3×10^{-8} mbar after loading the sample. The main component of the residual gas is hydrogen (H_2). The sample is heated linearly with the rate of 2 K/sec to the maximum temperature of 1600-1750 K by radiation from a resistive U-shaped W strip surrounding the sample.

The experimental procedure consisted of the following steps. The main chamber was baked at 200°C for 50 h, while the sample was kept in the loading chamber at room temperature at 10^{-7} mbar. Then the main chamber was cooled down to RT. The ultimate pressure was 10^{-9} mbar. Then the target heater (W strip) was flashed to its maximum temperature for 5 min and cooled down. Then, the loading gate was opened, and the sample was moved into the heating region and linearly heated for TDS measurements.

Preheating of the main chamber and the W strip permitted to reduce the gas release from surrounding surfaces to a negligible level, so that desorption of H_2, H_2O, and CO was small and desorption of deuterium-containing species was negligible even at 1600 K. This was true during control runs both before loading the sample and after TDS measurements.

The data acquisition system permitted to store spectra of 20 masses with a few hundred points in each spectrum. Deuterium-containing masses were interpreted as HD (m=3), D_2 (m=4), HDO (m=19), and CD_4 (m=20). The signal of D_2O (m20) was supposed to be small as is usually the case in hydrogen isotope exchange. The release of CD_3H (m19) was supposed to be much less than HDO, as methane release is usually much less than water release in TDS measurements from graphite. Besides, HD release is less than D_2 release, so CD_3H release is to be less than CD_4 release. There is 0.2% of ^{18}O in oxygen. Therefore mass 20 was corrected having in mind that $H_2{}^{18}O$ is 0.002 of $H_2{}^{16}O$. This correction is important if a significant release of H_2O is observed.

The main TDS chamber was pumped during TDS measurement, so the spectra were obtained in the dynamic regime. The mass-spectrometer was regularly calibrated for measurements of the absolute release rate by using an adjustable leak, which was in turn calibrated by measurements of the pressure rise in a closed volume monitored by a Baratron.

3. Experimental

Samples were made of fine grain graphite MPG-8 (NII GRAPHIT, Russian Federation, 1.85 g/cm^3) and carbon fiber composite NB31 (SEP, Bordeaux, France, 1.9 g/cm^3) with dimensions $10 \times 10 \times 1$ mm. Some samples were polished mechanically, some remained unpolished. Some were degassed in vacuum 2×10^{-5} mbar at 1200°C for 15 min, some not.

Four plasma installations were used for implantation of deuterium: radiofrequency (RFD) plasma discharge [46], beam plasma discharge LENTA [47], beam plasma discharge PR-2 [48] and magnetron discharge [31]. Also, a mass-separated 10 keV D_2^+ ion beam was used. Additionally, a few samples were saturated in deuterium gas at elevated temperatures.

Parameters of the RF plasma discharge were: ion energy 100 eV/D^+, ion flux $1.4–2.6 \times 10^{20}$ D^+/m^2sec, sample temperature 90-150°C, and deuterium pressure $6.7 \cdot 10^{-4}$ mbar. Parameters of the beam plasma discharge were: ion energy 200 eV/D^+, ion flux 2.6×10^{21} D^+/m^2sec, and sample temperature below 50°C. Parameters of the magnetron discharge were: the ion energy 200 eV/D^+, ion flux 1.1×10^{21} D^+/m^2sec, and the sample temperature below 50°C. The energy of the mass-separated ion beam was 5 keV/D^+ (10 keV/D_2^+), ion flux 1×10^{18} D^+/m^2sec, and the sample temperature about 20°C.

Mass spectra of ions in plasma discharges were not controlled in every experiment. Current measurements can be uncertain due to secondary electron emission, non-uniformity of plasma parameters over the plasma-facing surface, and some other factors. These can lead to uncertainty of flux measurements.

4. TDS of various molecules

An example of TDS of the main D-containing species HD, D_2, HDO, and CD_4 from NB31 and MPG-8 after irradiation in BP discharge is shown in Fig. 2.

One can see that deuterium desorbs in a very wide temperature range – from 400 K to above 1500 K with the maximum release rate around 800 K. One can distinguish four peaks: 500 K, 750-800 K, around 1000 K, and 1200-1300 K. Tentative analysis leads to the suggestion that each peak consists of several more narrow peaks, which can be seen in some spectra either as well separated peaks or as shoulders.

One can suggest several reasons of HD release due to recombination of H and D atoms. Atoms can be trapped both in the sample and in surrounding materials, and recombination can take place both on the hot sample and on hot surrounding surfaces. All surrounding surfaces were well annealed, so HD recombination is supposed to be due to recombination of implanted D and absorbed H. Similarly, HDO release is supposed to be due to recombination of D atoms with absorbed HO radicals. Controlled experiments with a tungsten sample, which contains small amounts of H_2 and H_2O,

demonstrated that release of H_2 and H_2O was always small at T<1200-1300 K and high at T>1200-1300 K. Therefore, the release of HD and HDO at T<1200-1300 K can be connected with hydrogen and water absorbed in the samples, while the high temperature part of HD spectra (>1200-1300 K) can be connected with hydrogen and water release from walls.

Release of CD_4 and HDO are peaked around 750-800 K, see Fig. 2, consistent with other experiments on exposure in deuterium plasma [24, 33]. One can also see additional maxima in CD_4 and HDO spectra at about 500-550 K, which appear either as a separate maximum or as a shoulder. One must mention that peak positions of CD_4 and HDO release correlate with peaks of D_2 and HD release.

Release of C_2D_x hydrocarbons is one order of magnitude less than that of CD_4.

The main contribution to D release was from desorption of D_2. The signal of HD was sometimes less, sometimes higher than that of D_2; and HDO signals were 2-3 times less than that of the D_2. The methane signal CD_4 was about 0.3 of D_2 signal. That is, water and methane gave a rather high contribution to the net D release.

After exposure in tokamaks, peak positions are different. Usually, release of D_2 takes place at higher temperatures, as with samples from DIII-D (peak at 1000÷1200 K) [25] and JT-60 (peak at 950 K) [26]. The release of methane often takes place in a broad temperature range with a significant low temperature part, as in our experiments. For example [27], CD_4 release from samples taken from JT-60 was observed in the range from 400 K to 1200 K, though the release of D_2 was from 700 K to 1300 K. The methane spectra can be interpreted as consisting of several peaks [26] with the peaks dependent on the position of the sample in the tokamak.

5. TDS from MPG-8 and NB31

Typical spectra of HD, D_2, HDO, and CD_4 are very similar for the two materials, MPG-8 and NB31, as one can see from Fig. 2. The peak at 750÷800 K always dominates at high fluence. There are some differences in relative amplitudes of the peaks, nevertheless. The release rate from NB31 is about twice higher than that from MPG-8 for all D-containing masses.

Similarity of spectra for the two materials was also observed in experiments on irradiation in RF plasma.

Similarity of TDS from CFC and MPG for all D-containing gases can mean that the trapping sites for deuterium in the two graphite materials are of the same origin. The number of D atoms trapped in CFC is only factor of 2 higher. That is, there is no principal difference in D trapping between powder graphite MPG-8 and carbon fiber composite NB31. Only the number of sites available for trapping can be different in different materials. A difference in the relative intensities of peaks in the two materials can be due to a difference in the relative number of various sites.

6. Trapping sites and mechanisms of release

Powder graphite is compressed of small particles (grains) consisting of small crystallites, while CFC consist of fibers. Hydrogen can be trapped both on the surfaces of the crystallites and inside the crystallites [49]. The space between grains and fibers is partially filled with a binder. The materials are rather porous. Pores can form long channels (open porosity) that make possible transport of gas molecules through the sample. Also pores can form voids far from the surface (closed porosity). There are a lot of dangling bonds in carbon

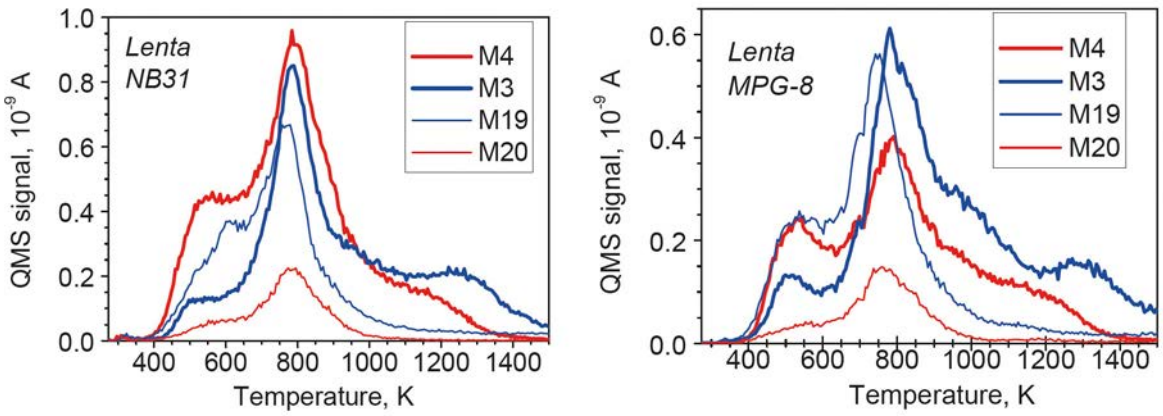

FIG. 2. An example of TDS of D_2, HD, HDO, and CD_4 after irradiation of NB31 and MPG-8 in BPD LENTA at 50°C to the fluence of 1×10^{25} D^+/m^2.

materials, which are primary sites for hydrogen trapping. Voids can accumulate hydrogen also as gas.

Radiation induced defects are in principle the same as natural defects.

The variety of binding energies can be connected with many factors. For example, carbon atoms can have various numbers of dangling bonds, the trapped deuterium atom can be surrounded by various numbers of carbon atoms with free dangling bonds, various numbers of deuterons can be trapped by a carbon atom, dangling bonds can exist on the surface of grains, crystallites, closed pores, and inside the crystal lattice, carbon can be either in crystalline or in amorphous state, free bonds in the lattice can belong both to the lattice and interstitial atoms, various complexes of interstitial atoms and loops, as well as pores can exist, etc. Deuterium can migrate in bulk to distances which depend on the temperature, leading to trapping deep from the open surface both on dangling bonds and in voids. This is why the range of binding energies is wide, TDS are always very broad, and identification of the peak origin is speculative.

The positions of peaks of the various deuterium containing gases HD, D_2, HDO, and CD_4 are very similar. This may mean than the limiting processes of release of these gases are similar. One of the suggestions that can be made is that the limiting step of release of these molecules is detrapping of D atoms trapped by carbon dangling bonds. After detrapping, these D atoms can easily migrate and recombine with other atoms and complexes such as H and D atoms, CD_3 groups, and HO radicals also trapped by carbon dangling bonds.

7. Irradiation in different plasmas

Spectra for the two materials were obtained also after irradiation in another plasma beam facility (PR2), in the magnetron discharge, and in RF discharge. They were different. Examples of spectra after irradiation in the RF discharge and in the magnetron discharge are shown in Fig. 3 and Fig. 4, respectively.

TDS after RF discharge are rather narrow with the peak at 800 K, which always dominates.

The shapes of the spectra after irradiation in the magnetron have own features. The high temperature peak becomes rather high in the D_2 release and not negligible in the CD_4 release, see Fig. 4, contrary to RF and LENTA. The high temperature peak of the D_2 release from NB31 becomes even a dominant one at high fluence of irradiation in the magnetron. The spectra of CD_4 after MD irradiation are very unusual; they look like multipeak spectra with a high low temperature part and not negligible high temperature part.

The high temperature peak is also very high after irradiation in another BPD – PR-2.

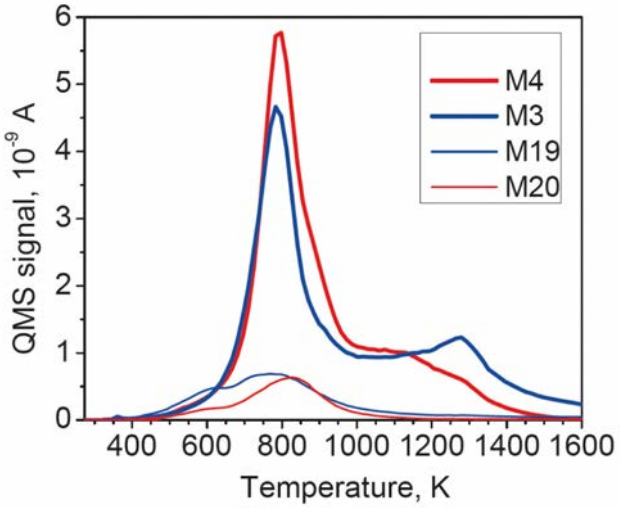

FIG. 3. An example of TDS of D_2, HD, HDO, and CD_4 from NB31 after irradiation in the RF plasma discharge at room temperature to the fluence of 1.9×10^{24} D^+/m^2.

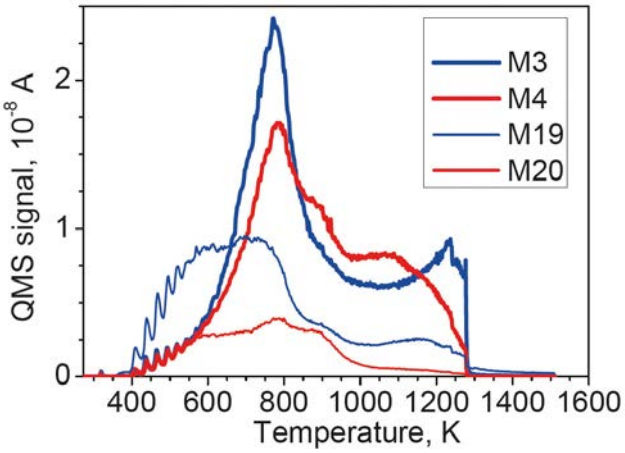

FIG. 4. Thermal desorption spectra of HD, D_2, HDO, and CD_4 molecules from MPG-8 graphite after irradiation in the magnetron discharge to the fluence of 1.7×10^{24} D/m^2. T_{max}=1280 K.

It is important to mention that the position of the peaks is approximately the same in the three installations used. Nevertheless, the relative amplitudes of peaks are different. The difference of TDS after irradiation in different installations can be connected with the difference in plasma parameters. Besides, the contribution of gas absorption can be not negligible.

There are also many factors that complicate the experiments with plasma irradiation. For example, correct flux measurements are never possible, ion and electron stimulated processes are unknown and not controlled, development of the relief, impurity and film deposition are sometimes observed unpredictably. Irradiation in different facilities affects the material in a different way; therefore trapping and release can be rather different, though the trapping sites can be principally similar. Depending on plasma and sample conditions, irradiation by plasma can lead not only to erosion of the surface but also to modification of a thin surface

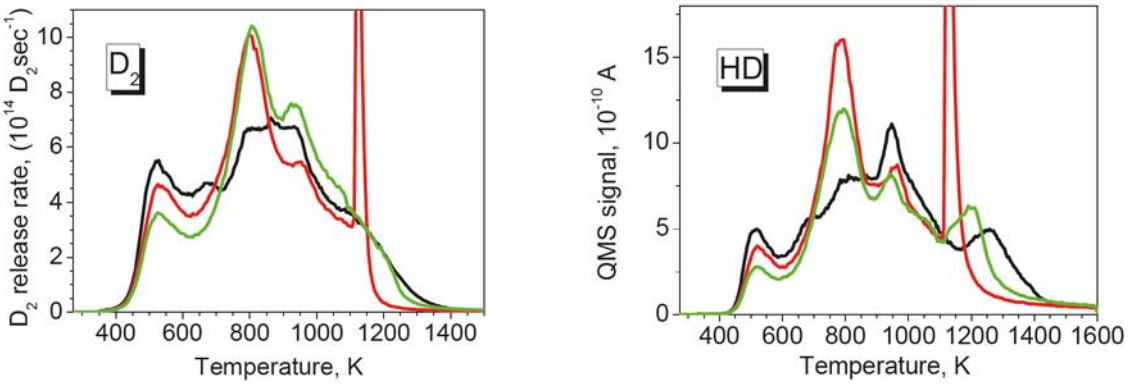

FIG. 5. Thermal desorption spectra of D_2 and HD from 3 samples of MPG-8 irradiated simultaneously by 200 eV/D^+ in LENTA at the fluence of 3×10^{25} D^+/m^2.

layer and appearance of re-deposited films of particles sputtered from surrounding materials. This can definitely influence trapping behavior and change the TDS spectrum.

8. Reproducibility of plasma experiments

Parallel experiments with tungsten irradiated by deuterium ions always demonstrated very good reproducibility of TDS measurements. At the same time, experiments with carbon materials irradiated by plasma in the same facility were often irreproducible. Figure 5 is plotted for demonstration: three samples of MPG-8 were irradiated simultaneously in LENTA, but the relative heights of all peaks are different in the three samples.

Let us mention that a fine structure of the spectra is well seen in Fig. 5. Besides peaks at 500 K and 800 K, one can see peaks at 650 K and 950 K. An abnormal flash at 1100 K in one of the samples was a fault in the temperature programming. The shapes of spectra in Fig. 5 are also different from those in Fig. 2.

This example demonstrates that irradiation by plasma is not well controlled sometimes due to variation of the parameters that are not controlled well. Another reason of the disagreement between "the same" experiments can be connected with the features of the material used. One of the features is that the properties of the material are not uniform. This difference was found in experiments on gas driven permeation through graphite. GDP through graphite wafers was found to be due to molecular gas flow through interconnected porosity [50]. It was observed that the permeation rate was sometimes different for wafer samples cut from different parts of the same graphite block.

9. Ion implantation

The results obtained after plasma irradiation were compared with results obtained after implantation of

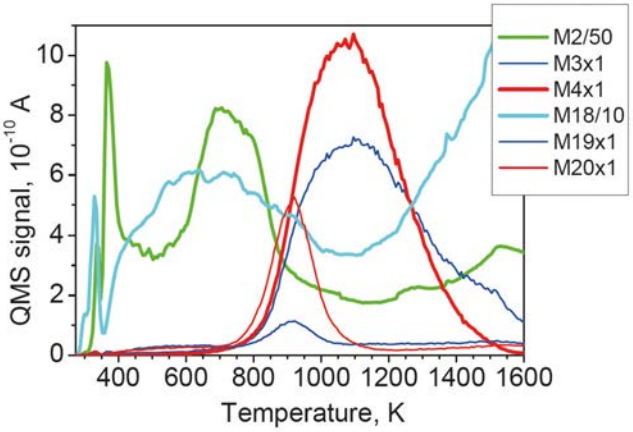

FIG. 6. Thermal desorption spectra from MPG-8 graphite after ion implantation.

10 keV D_2 ions. Figure 6 gives an example of the TDS after ion implantation.

One can see that deuterium is released mainly as D_2 and HD in these experiments. The reason is that the ion fluence is small in ion implantation experiments, while the contents of H_2 and H_2O after exposure of graphite in air are high. Release of D_2 and HD after ion implantation is characterized by broad maxima with faint shoulders. One must also mention that mass 19 and mass 20 correlate, so m19 can be interpreted as CD_3H. The release of hydrocarbons after ion implantation is very small.

Figure 7 shows TDS of D_2 release after irradiation by various fluences. Though the TDS look like a single broad peak, they are not a single peak in fact, as is well seen from the spectrum at the lowest fluence in Fig. 7.

Many early experiments made with ions are described in the literature. TDS of D_2 after ion implantation are usually very broad. They usually start above 700 K and last to 1300-1500 K [4, 11, 16, 22] and sometimes to 2000 K [43]. Usually TDS look like a single peak around 1000-1100K [4, 8, 16], which agrees with our observation. Sometimes the temperature of the peak is either less (950K, [6, 13]) or higher (1200 K, [18]). The position can depend on the rate of the temperature rise as reviewed in Ref. [14].

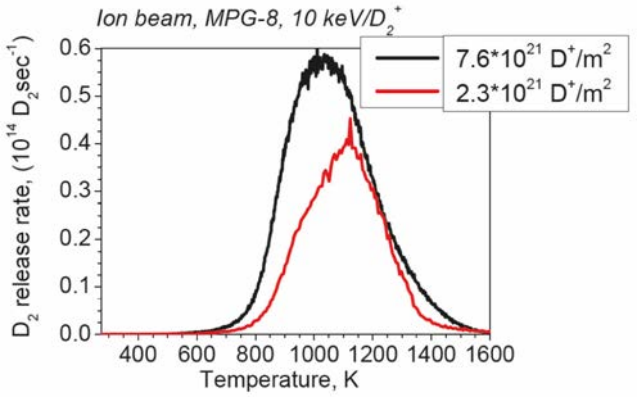

FIG. 7. TDS of D_2 after ion beam bombardment.

The apparently single peak measured in our experiments is not a single peak in fact. It can be tentatively deconvoluted into three peaks with temperatures of about 950 K, 1150 K, and 1350K.

An apparently single peak, which was deconvoluted into two peaks at 850-900 K and 1100 K, was observed also in Ref. [22], a broad peak 700-1300 K had a main maximum at 1000 K and a shoulder at 1200 K in Ref. [8]. A two-peak structure, 1050 K and 1200 K, was observed in Ref. [19].

Multipeak spectra were also observed. Several faint peaks from 900 to 1200 K were demonstrated in Ref. [17]. Three peaks at about 1000, 1100, and 1200 K were seen in Ref. [16]. Five peaks with maxima at 1200-1400 K were identified in Ref. [18].

The number of D_2 and HD peaks and the peak positions scatter in experiments with ions described in the literature. Besides, it is not known a priori if the peaks are connected with radiation damage or with natural defects with high binding energy. Nevertheless, ion implantation experiments usually give release in the high temperature range with maxima from 900 to 1400 K. Usually (not always), one can hardly distinguish between the peaks, so they appear as an apparently single peak with faint peculiarities.

High temperature parts of TDS after plasma experiments and TDS after ion implantation are rather broad, and distinct peaks are rare. Nevertheless, one can mention some features that can be interpreted as peaks. This follows not only from the faint features of the D_2 desorption but also from faint features of HD desorption spectra.

Methane desorption after ion implantation is shown in Fig. 8. The shape of the spectra is typical for the case of ion implantation: there is one narrow peak ($\Delta T_{HWHM}/T_{max}$ = 0.1) with the maximum at about 870÷920 K. In the case of plasma irradiation, methane spectra are much broader, consist of 2-3 peaks, and the main peak position is about 100 K less than at ion implantation.

Methane TDS peaks reported in the literature are usually also in the range of temperatures of 850-950 K (about 850 K in Refs [13, 16, 17], 900 K in Refs [9, 22], 950 K in Refs [6, 11]), though both smaller (800 K in [19]) and higher (1100 K in [43]) temperatures were also observed.

Deutero-methane desorption does not correlate with that of D_2. Methane peak is narrow and appears at smaller temperatures. This is a typical situation for ion implantation that deutero-methane desorption takes place at lower temperatures than desorption of D_2.

10. Flux density

Variation of the flux density during plasma irradiation in the range of (0.5-3.5) × 10^{20} D^+/m^2sec demonstrated that there were no obvious tendencies of TDS variation and deuterium retention at the fluence of 4.5 × 10^{23} D^+/m^2. An example of TDS from MPG-8 irradiated in RFD at various fluxes is show in Fig. 9. One can see only a slight variation typical for plasma irradiation experiments.

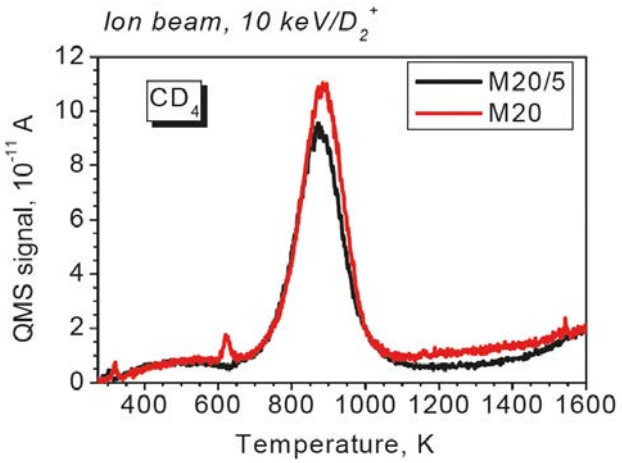

FIG. 8. TDS of CD_4 after ion beam bombardment. Two curves are given at fluences of 7.6 × 10^{20} D^+/m^2 and 2.3 × 10^{20} D^+/m^2. The first curve is normalized by a factor of 5.

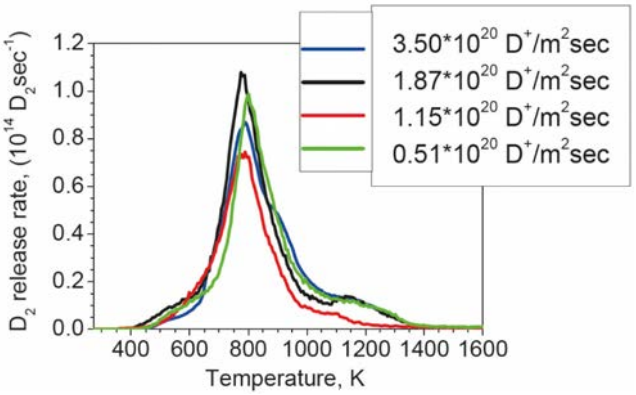

FIG. 9. TDS spectra of D_2 from fine grain graphite after irradiation in RFD plasma at various ion fluxes to the fluence of 4.5 × 10^{19} D^+/cm^2.

Experiments [3] with a high-energy D ion beam also showed no dependence of retention in pyrolytic, pseudo-single crystal and fine grain graphite on the ion flux density in the wider range of 10^{18}÷10^{21} D^+/m^2s.

11. Loading in gas

Loading in gas was performed at the D_2 pressure of 10 kPa and temperatures of 630 K and 830 K for 1 hour. TDS after loading at 630 K are shown in Fig. 10. One can see a very intensive desorption of hydrogen (its signal is divided by 50). Desorption of HD is higher than D_2 in this case, as one can see in Fig. 10, and follows desorption of H_2 in many details.

There are several peaks at 500, 600, 800, 1000, and 1300 K in Fig. 10, which are similar to those after irradiation by plasma. All the traps after loading in gas are natural traps. The variety of peaks after saturation in gas means that a variety of trapping sites with different trapping energies exist in carbon based materials. This means that natural trapping sites cover a whole spectrum of binding energies that was observed in experiments with plasma irradiation and with ion implantation.

After loading at 630 K, deuterium mainly desorbs at low temperatures, and the main desorption peak is at 800 K as in most plasma experiments. After loading at higher temperature of 830 K, deuterium release takes place at higher temperatures with T_m~1100 and 1300 K.

Not many publications on TDS measurements after loading in gas are available. The multiple-peak structure was shown in Ref. [39] in the range of 450-1200 K. Increase in the temperature of loading led to appearance and growth of high temperature peaks in TDS: only low temperature peaks with T_m=550 K and 750 K were observed after loading at 473 K, but peaks around 950 K and 1200 K appeared after loading at 650 K and 1100 K, respectively. The results of Ref. [39] are in good qualitative agreement with our observations. Loading at higher temperatures of 1500 K [40] and 1170 K [41, 42] led to release at even higher temperatures in the interval of 1000-1500 K and 1100-2100 K (T_m=1800 K), respectively.

Variation in the TDS with the temperature of loading can be interpreted in terms of different accessibility of traps [39]: low energy traps are easily accessible even at low temperatures, while high energy traps are accessible only at high temperatures. Trapping sites can exist on boundaries of grains and small crystallites, constituting the grains. They can also be related to closed porosity between grains and in the binder, which is a feature of carbon materials. That is, one can suggest that low energy traps are located closer to the boundaries of grains and small crystallites, while high energy traps are situated deeper in the grains or deeper in the crystallites or deeper in the binder.

One can give another explanation suggesting that traps with various energies exist all over the material, but retention in traps depends on the temperature of loading and the concentration of traps, and traps with different energies compete for trapping of deuterons. Trapping at low temperatures is proportional to concentrations of the trapping sites and does not depend on the binding energies. This means that natural sites, which give the highest peak at 800 K after loading at room temperature, dominate. At a higher temperature, sites with low binding energy do not retain deuterium atoms; therefore only high energy traps can retain deuterons, and high temperature peaks dominate in the spectra. The concentration of the high energy traps is less than that of the low energy traps. Nevertheless, the intensity of the high energy peaks at the high loading temperature is higher than at loading at room temperature. This means that deuterons migrate deeper in the bulk of crystallites and are retained there.

Natural trapping sites are dangling bonds and pores. The variety of peaks in TDS can be connected with the variety of these bonds on the surface and in the bulk. Pores also give various types of trapping: chemisorption on internal surface, and gas phase in the volume.

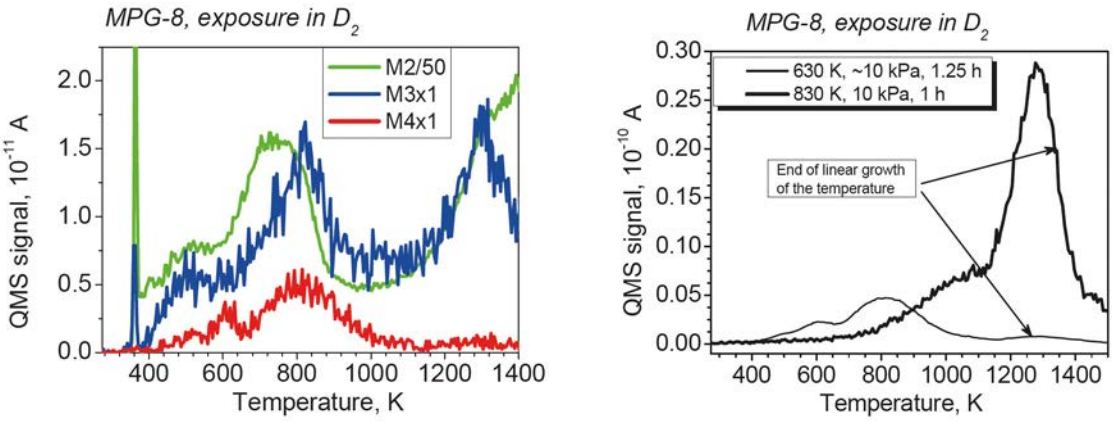

FIG. 10. Thermal desorption from MPG-8, exposed in deuterium atmosphere at 630 K and 830 K and 10 kPa.

Experiments on saturation from gas during milling of graphite powder in various conditions and with various dopants [51-53] demonstrated that mainly two peaks were observed both without and with dopants: 710-740 K and 970-1100 K. One can suggest also the existence of intermediate unresolved peaks between them. Though the position of the peaks is slightly different from those we observe, it is important that the peak temperatures in Refs [51, 52] were the same both with and without dopants and for different dopants. A surprising conclusion can be made that the presence of impurities does not change the binding energy. Though dangling bonds are the sites for hydrogen trapping both in graphite and nanostructurised powder obtained by milling, graphite gives a broad variety of peaks with various binding energies, while powder demonstrates only two prominent peaks.

Trapping in powder produced by arc discharge [32] gave only one peak. Though the temperature of loading was 300 K, the peak temperatures were relatively high. Contrary to Refs [51, 52], presence of W as a dopant in Ref. [32] decreased the peak temperature from about 1100 K without W down to 900 K with W. Surprisingly, no low temperature peaks were observed at all.

Experiments with single wall carbon nanotubes [54], which were loaded in D_2 gas with adding D atoms produced on a hot W surface, exhibited a wide TDS apparently from 500 K to 900 K with several non-resolved peaks. Loading with deuterium demonstrated changes in the system of SWCN. Particularly, prolonged exposure of the SWNTs to the gas with low atomic deuterium concentration affects their size and relative layout, leading to a conglomeration of SWNT bundles into large diameter rope type nanotubes. This means that deuterium leads to modification of the C-C bonds.

12. Comparison of ions, gas, and plasma

Ion irradiation leads to production of a large amount of radiation defects. Therefore, release in TDS after ion implantation is connected with release from radiation defects within the ion stopping range. After loading in gas, a variety of peaks in the range of 500-1300 K are observed. All the traps after loading in gas are natural traps: dangling bonds and pores.

The comparison of TDS after ion beam experiments and after loading from gas may lead to the conclusion that high temperature peaks can be attributed both to radiation induced defects and to natural defects. Radiation induced traps are the same in nature as the natural trapping sites of high binding energy.

TDS after plasma irradiation are as broad as after saturation from gas. The range of temperatures and positions of peaks after loading in gas and after plasma irradiation are similar. Moreover the release at about 800 K dominates both after plasma implantation and after loading from gas at low temperature. This may mean that the trapping sites are similar in the two cases, that is, deuterons from plasma are trapped mainly in natural defects. This can be connected with low energy of ions, which is not high enough to produce many radiation defects. The main part of deuterons after plasma implantation to low fluence is trapped close to the surface, while the main part of deuterons at high fluence is trapped outside the ion range. Nevertheless, the features of TDS are more or less similar at low and high fluence. This means that the energy distributions of the trapping sites are approximately the same at different depths.

One can expect that increase of the temperature of plasma implantation will lead to decrease of low temperature peaks and increase of high temperature peaks, as in the case of saturation from gas. The appearance of high temperature peaks in TDS after plasma irradiation, which we observe in several cases, can be connected with heating of the sample due to failure of the thermal contact between the sample and the sample holder.

13. Fluence dependence

Figure 11 demonstrates the D_2 spectrum evolution obtained after irradiation of MPG-8 and NB31 in the RFD. One can see from MPG spectra that the main peak of D_2 release, which always dominates around 800 K at

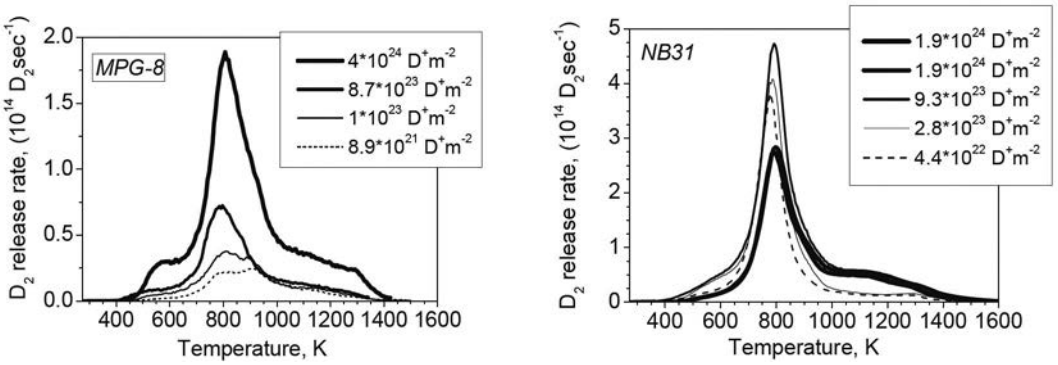

FIG. 11. Release rate of D_2 from MPG-8 and NB31 after irradiation in the RF plasma discharge at 90-150ºC to various fluences.

the high fluence, is not a single peak in fact. One can distinguish at least two more narrow peaks at 800 and 900 K, which are similar in height at low fluence, but the first one rises faster with the fluence and dominates above 10^{24} D/m^2.

Figure 12 demonstrates CD_4 spectra after irradiation in the RFD. One can also see at least two peaks at 600 K and 800 K instead of one peak typical for the case of ion implantation.

Very different variation of TDS was observed when the magnetron discharge was used for implantation, as Fig. 13 demonstrates. One can see that the contribution of the high temperature part becomes dominant at the high fluence.

14. Influence of polishing

Two samples of fine grain graphite MPG-8 having different surfaces were compared. One of them had the surface obtained by breaking a graphite bar. The second sample was polished mechanically. The surface of "broken" samples was very rough, while the polished one was very smooth when examining by SEM. The surface looked like it was almost completely covered by a layer of fine powder. The surface had small regions uncovered by this layer, where one could see the real rough graphite surface. This layer is possibly a carbon dust that arises during polishing, fills pores and hinders roughness. The dust particles have many dangling bonds, which stick particles to each other and to the surface. The powder layer is of about a few microns, so that plasma ions interact only with this layer. The sample with the virgin "broken" surface gave opportunity to plasma particles to interact with the fine grain graphite structure.

The two samples were irradiated in RF deuterium plasma to various fluences, and then TDS were performed. Figure 14 gives a comparison of D_2 and HD spectra from the two samples after irradiation with the fluence of 1.2×10^{24} D/m^2. It is seen that the shapes of TDS are similar, but retention in the polished sample is less. This can be explained by a smaller concentration of dangling bonds in the powder layer on the surface of the polished sample. This can also be connected with a higher surface open for implantation in the "broken" sample with high open porosity.

The similarity of spectra of the polished and "broken" samples may be considered as supporting the suggestion that internal closed porosity in the fine grain graphite is of negligible influence in our experiments.

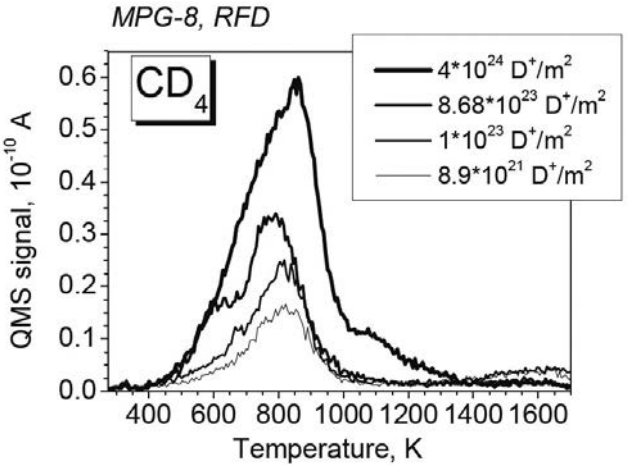

FIG. 12. Thermal desorption of deutero-methane from MPG-8 after RFD plasma irradiation.

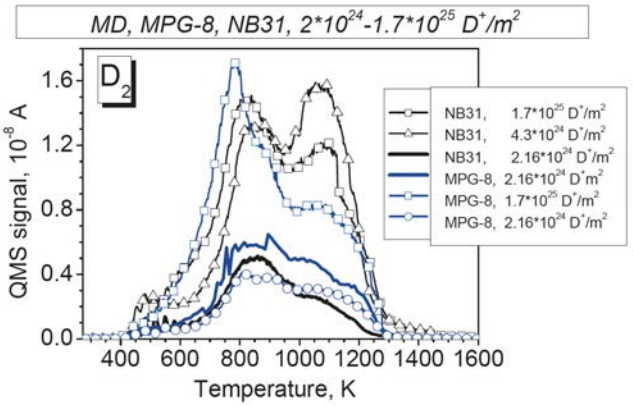

FIG. 13. Comparison of D_2 TDS obtained after irradiation of MPG-8 and NB31 samples in MD at 70°C to various fluences. The time of irradiation is the parameter given in hours.

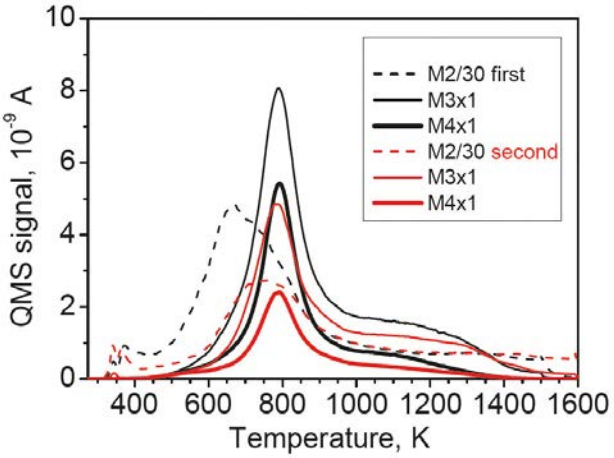

FIG. 14. TDS spectra of D_2 and HD from MPG-8 graphite irradiated in RF plasma to the fluence of 1.2×10^{24} D/m^2. First sample – "broken" surface, second sample – polished surface.

15. Influence of metal impurities

Impurities can change trapping [6, 11]. Deuterium trapping by RG-T graphite was studied to investigate the influence of metal impurities, dopants, and deposits.

RG-T is dense graphite with 3% of Ti. SEM/EDS analysis indicates titanium inclusions with dimensions up to a few μm in graphite.

TDS spectra of D_2 and HD after irradiation by RF plasma are given in Fig. 15. The fluence was 10^{24} D/m^2. The total retention in the sawed surface of RG-T is about 6 times less than that in the broken surface of MPG-8. Though Ti may be expected to increase deuterium trapping, RGT traps less than MPG. This may be connected with a smaller porosity of RG-T.

TDS from RGT were measured in Ref. [19] after ion implantation. The spectrum of D_2 had two peaks – one at about 1000 K, which is typical for ion implantation, and another at 1160 K, which is similar to the high temperature peak in Fig. 15.

In some experiments after plasma irradiation of graphite, abnormally intensive high temperature peaks were observed. This can be connected with the appearance of impurities on the surface of graphite, which were sometimes observed.

TDS from graphite powder milled with metal dopants charged in hydrogen atmosphere investigated in Refs [51,52] demonstrated that TDS consisted of two broad peaks at 730 K and 1050-1100 K both without and with dopants (Fe, Co, Cu, Ni, a few wt%). Tentatively, one could select one more peak at about 900 K. Doping with Co did not change TDS, doping with Fe led to increase of hydrogen content, while doping with Ni and Cu led to decrease of hydrogen content. According to Ref. [16], metallic impurities may influence graphitization of material that changes the absorption of hydrogen. Increase of graphitization leads to decrease of absorption of hydrogen. Various impurities can either increase or decrease the graphitization, therefore, retention of hydrogen can be also decreased or increased.

Anyway, one can conclude that both at loading from gas and from plasma, no new peaks appear due to doping of graphite, that is, doping elements may play a catalytic role in C-H bonding.

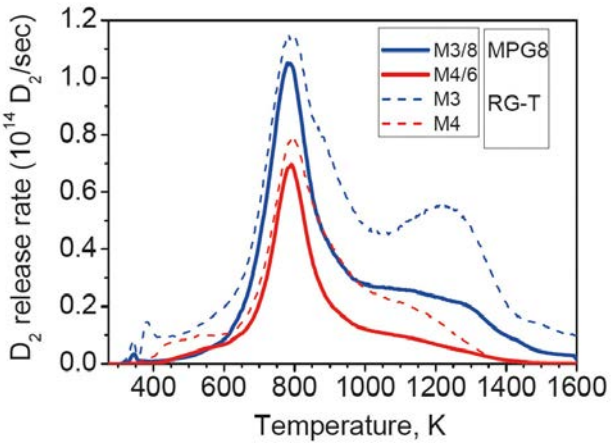

FIG. 15. TDS spectra of D_2 and HD from MPG and RGT graphite after irradiation by RF plasma to the fluence of 10^{24} D/m^2.

16. Decomposition of hard and soft a:C-D films

Carbon films often appear due to irradiation and can contribute to desorption of trapped hydrogen isotopes. Two types of amorphous C-D films were deposited on W samples, which were preliminarily annealed for 1 hour at 900°C, in CD_4 ECR plasma. Soft films were deposited at 10-15 V bias on the W sample, hard films at about 100 eV bias. TDS results are shown in Fig. 16.

TDS from soft carbon films are very different from TDS measured after plasma irradiation of MPG and CFC. All D-containing species (D_2, HD, C_xD_y, HDO) released very rapidly from the soft film, giving a very narrow peak at 750 K (Fig. 16(a)). This release was due to decomposition of the film, which disappeared after TDS measurements.

Release from hard films is very small at temperatures below 700 K, and desorption takes place at higher temperatures (Fig. 16(b)). Desorption of deuterium has the main peak at 850 K, and continues up to 1300 K with several peaks in the spectrum. Deuterocarbons

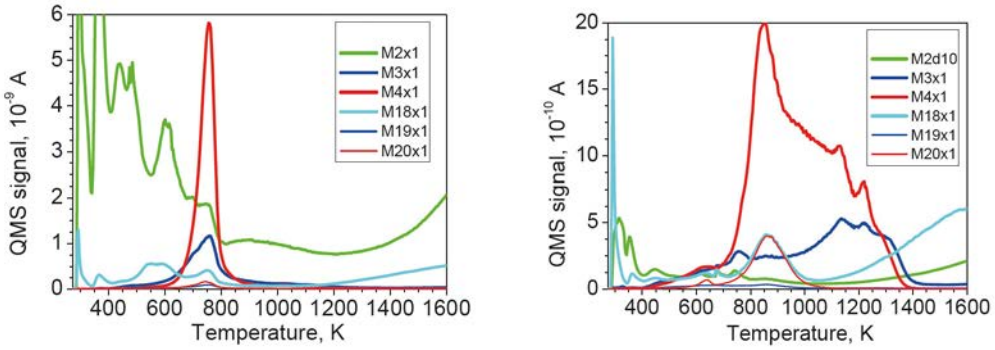

FIG. 16. TDS spectra of H_2, HD, D_2, CD_3 (H_2O), CD_3H (HDO), CD_4 (D_2O) from the sample with soft (a) and hard (b) a:C-D films.

C_xD_y (x,y=1,2,3) release in a single broad peak with T_m=850 K. No hydrocarbon release is mentioned at high temperatures, where D atoms still desorb.

Similar behavior of D_2 and CD_4 in TDS from soft and hard a-C:D films was observed in Ref. [55].

The range of release from hard films is very broad and covers the range of temperatures after plasma irradiation. SEM analyses of the surface after plasma irradiation demonstrate that the surface is modified. Possibly, modified layers are similar in some aspects to hard carbon films from the point of view of deuterium retention and release. One must also mention that even trapping of atoms can lead to modification of carbon based structures as it was observed with nanotubes loaded by deuterium in molecular gas with atomic component.

Deposited carbon films are commonly observed in tokamaks. Measurements with the co-deposited films demonstrated a broad TDS of deuterium. For example, release of D_2 from samples with films co-deposited in JT-60U took place in the range of 550 K to 1250 K in Ref. [33] and 800 K to 1200 K in Ref. [34], dependent on the position of samples in JT-60U.

17. Surface relief in plasma experiments

Carbon materials are very porous, as one can see after sawing or breaking the sample. Dry mechanical polishing leads to production of thin powder particles, which have many dangling bonds. These particles interact through the dangling bonds, fill the porosity, and form a rather stable layer over the surface, making the surface very smooth. The possibility of sticking of carbon powder micro-particles was observed in an optical stereo microscope with the particles, which were much larger than those produced by dry polishing of the surface. Particles were made just by scratching the surface with a needle. They stick to each other forming bizarre 3D patterns, which easily re-arrange when touched by a needle. Polishing with some pastes prevents formation of this layer due to blocking of dangling bonds. Subsequent washing in benzine in the ultrasonic bath removed the paste, so that the porosity became visible even in the optical microscope. Figure 17 demonstrates three surfaces: broken, polished by paste and washed, and dry polished without paste.

Experiments with polished and “broken” samples demonstrated similarity of TDS spectra and a difference in the number of deuterium trapped.

Irradiation of samples by plasma led to transformation of the surface relief. At very high flux density, erosion of the surface was observed, so that porosity and the structure of fine grains appeared. Sometimes this erosion was very strong close to the mask edges, as shown in Fig. 18. The film formed by polishing could be

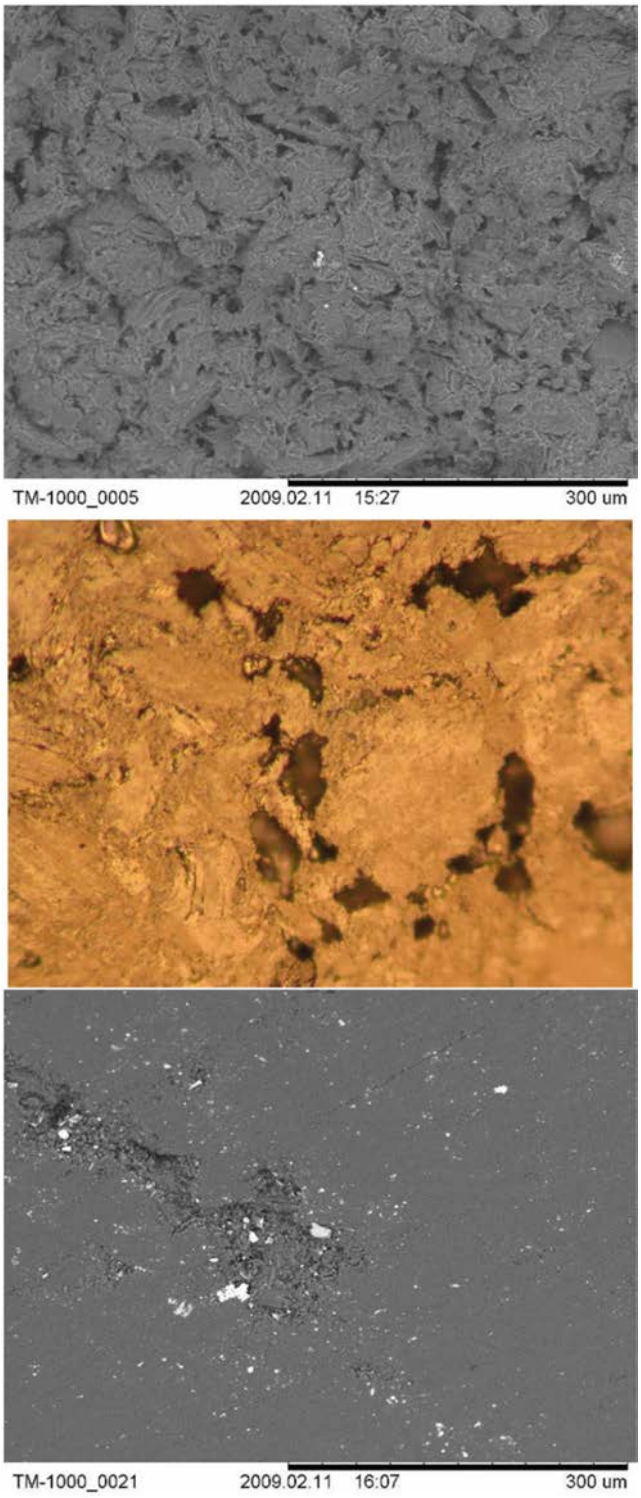

FIG. 17. Surfaces of fine grain graphite: broken, polished by paste and then washed, and dry polished (a region without powder film is shown for demonstration). Horizontal dimensions are 540 μm, 0.4 μm, and 540 μm in the three photos.

either partially or completely removed by plasma irradiation, so that pores became open. The rough relief, which is typical for broken and cut surfaces, became smooth due to sputtering and surface modification (Fig. 19). A part of the eroded carbon can also come back to the surface and be co-deposited with deuterium and some impurities

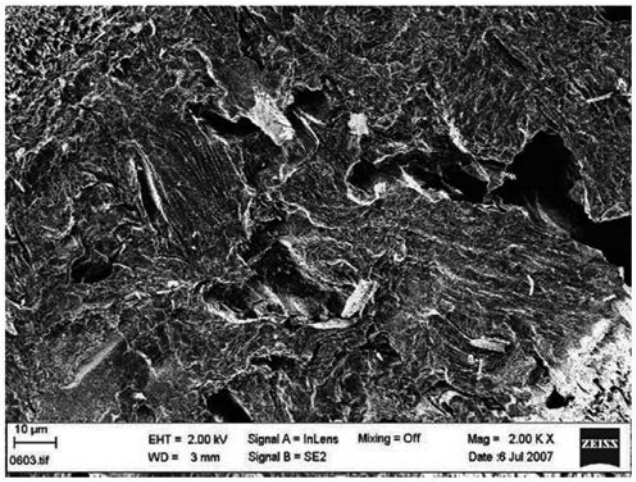

FIG. 18. The surface of MPG-8 sputtered by dense plasma in LENTA.

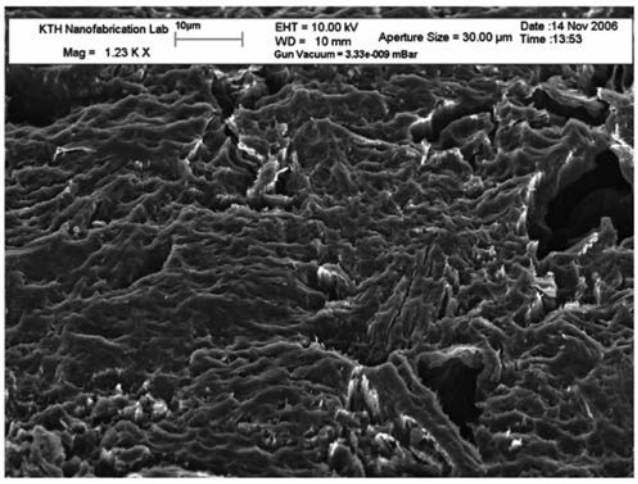

FIG. 19. The surface of MPG-8 modified by irradiation in MD.

on the top surface and inside open pores. As a result, the final surface in different experiments was not the same.

Commonly, some impurities were detected by XPS and EDS. The main impurity practically in all experiments was oxygen. Besides, silicon was often found. Metal impurities also appeared in some experiments; the highest concentration of metal impurities is always at the edge of an irradiation area. Appearance of metal impurities was always unpredictable.

Irradiation in various facilities demonstrated a variety of features on the surface that appeared on some samples unpredictably. Irradiation in the RF discharge was usually more uniform than in other discharges, but occasionally metal droplets appeared on the surface, which was never observed in other plasmas. Peculiar cones and pillars were observed on the surface in the case of the high concentration of metal impurities (Fig. 20).

Irradiation in the beam plasma facilities PR-2 and LENTA also led sometimes to appearance of various surface structures. Some of them are shown in Fig. 21 and Fig. 22.

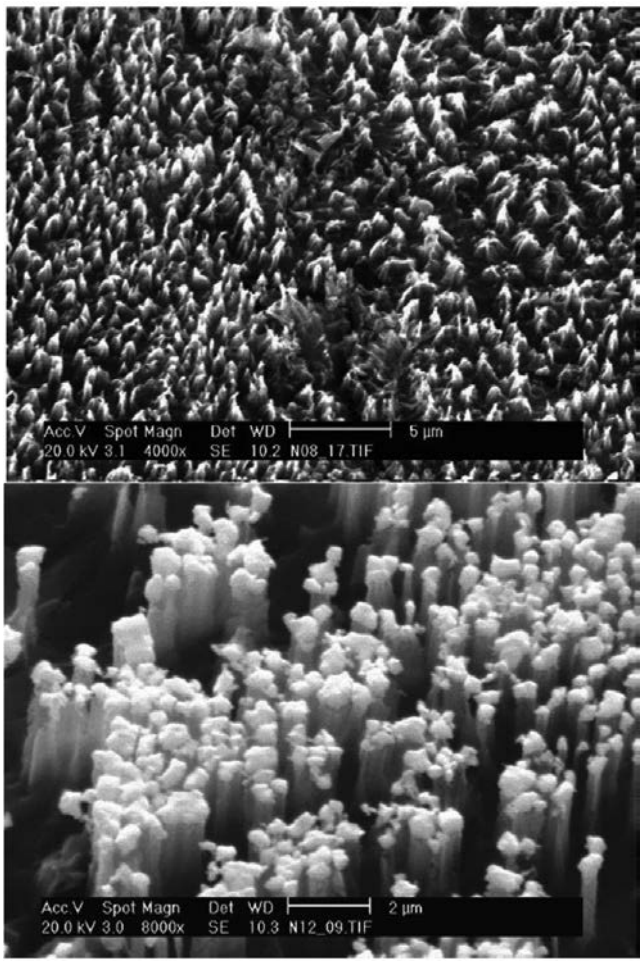

FIG. 20. Structures appeared occasionally on the sample irradiated in the RF discharge.

18. Deuterium trapping

The number of deuterium trapped after plasma irradiation as a function of fluence is shown in Fig. 23.

First, the calibration was tested by using a tantalum irradiated by 10 keV D_2^+ ions (crosses in Fig. 23), which fit well to the 100% trapping in tantalum [57]. Another test was made with implantation of 10 keV D_2 ions in graphite. The retention is about 100% at the low fluence and saturates if the fluence is above 2×10^{21} D^+/m^2. Qualitatively this is in agreement with other observations [2, 3, 11, 38, 56].

The total trapping in NB31 (squares) and MPG-8 (triangles with thick edges) both increases up to the ion fluence of 1×10^{24} D^+/m^2. The retention in NB31 is slightly higher than that in MPG-8. Samples of MPG-8 irradiated in beam plasma discharge to the higher fluence of 3×10^{25} D/m^2 demonstrated a steady increase of retention from 1×10^{22} D^+/m^2 to 3×10^{25} D^+/m^2 (filled triangles in Fig. 23). No saturation of CFC samples at high fluence was found in Refs [7, 23]. One can conclude from these measurements that trapping does not saturate at the high fluence not only in CFCs but also in powder

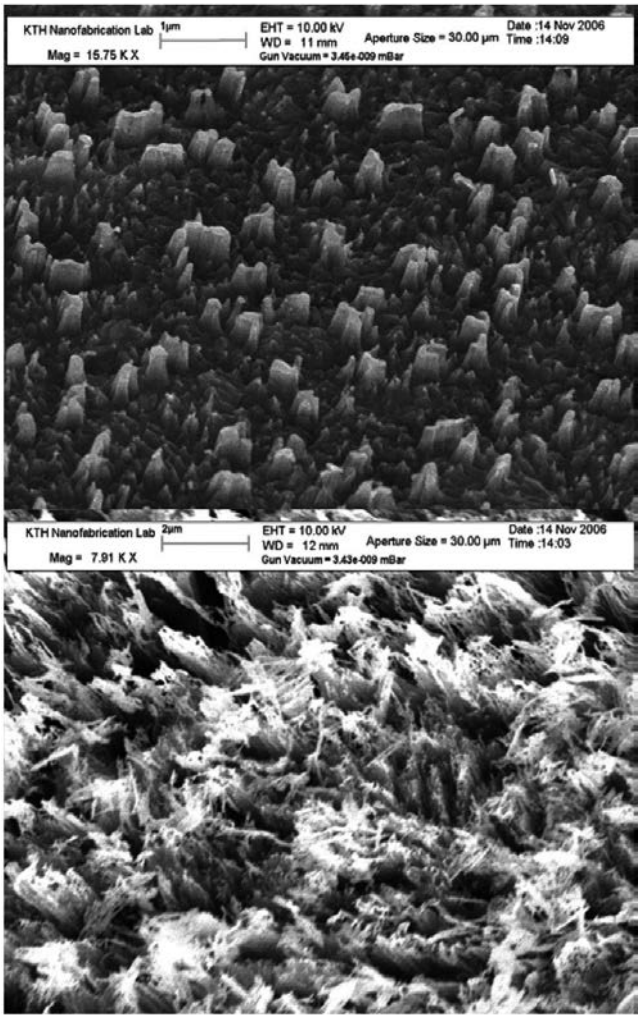

FIG. 21. Some features occasionally appeared after irradiation in BPD PR-2.

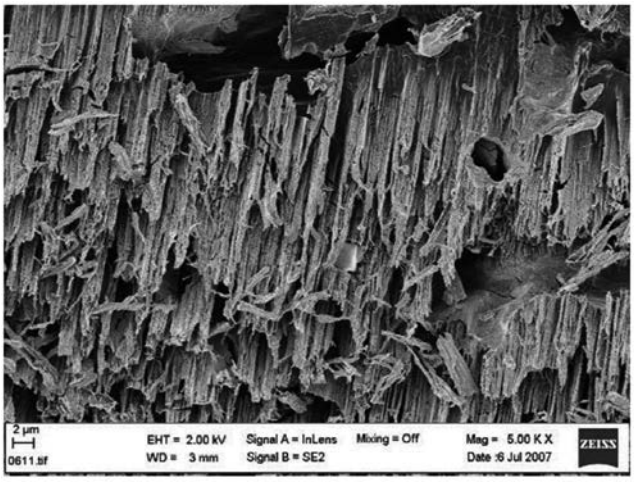

FIG. 22. The boundary near the mask after irradiation in BPD LENTA.

graphite. This should be a general feature of all porous graphite materials.

Trapping of deuterium at low fluence from plasma is less efficient than trapping from the ion beam. This can be connected with the difference in the energy of deuterons (5 keV vs. 100 eV). Approximation of experimental points obtained after 100 eV plasma irradiation to the region of small fluence gives that decrease of the trapping efficiency starts at about $(0.5\text{-}1) \times 10^{20}$ D/m^2 at this ion energy. A similar value of 10^{20} D/m^2 is given in Ref. [56]. In the case of 10 keV D_2 ion implantation, saturation starts at about 2×10^{21} D/m^2. The ratio of the critical fluences at ion and plasma irradiation is about the ratio of ion energies in the two cases, as it should

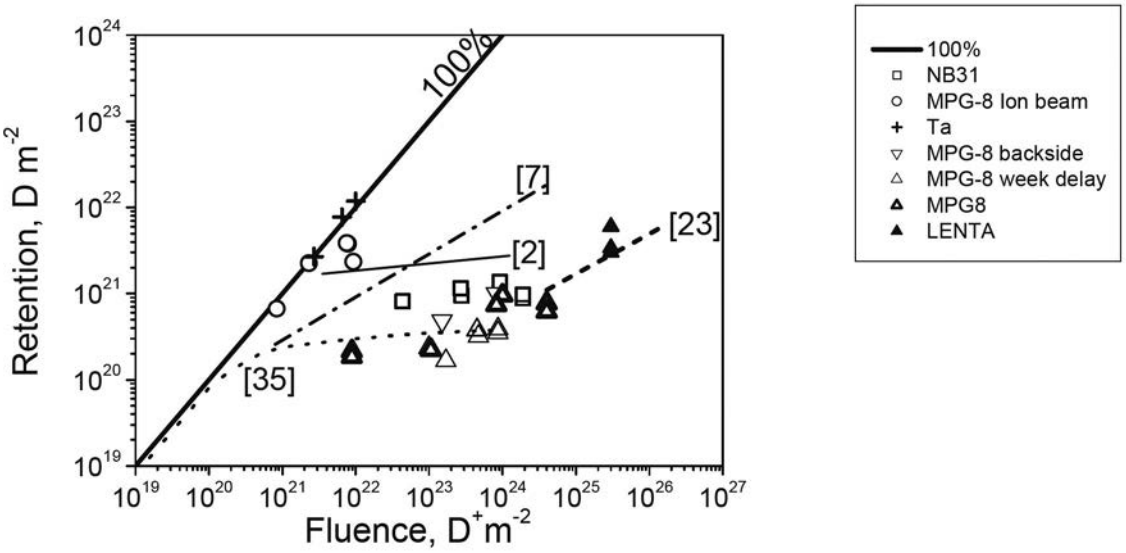

FIG. 23. Fluence dependence of deuterium retention in carbon based materials: MPG-8 irradiated in the RF plasma discharge (triangles with thick edges for irradiation of the polished side, inversed triangles for irradiation of "broken" surface, triangles with thin edges for the samples kept in air for 2-15 days after irradiation), MPG-8 irradiated in the beam plasma discharge (filled triangles), NB31 irradiated in the RF plasma discharge (squares), MPG-8 irradiated by ion beam (circles), tantalum samples irradiated by ion beam (crosses). The experimental uncertainty of TDS measurements is within 30%. The lines are taken from refs. [2, 7, 23, 35].

be if the decrease of the trapping efficiency is connected with saturation of the stopping range of incident ions.

The number of deuterium trapped at the high fluence exceeds the number of deuterium that can be trapped within the stopping range of ions by an order of magnitude. This means that after saturation of the ion range, deuterium is mainly trapped at depths behind the ion range. Long tails of deuterium concentrations were found in many experiments. Penetration up to 3 mm in CFC was reported in Ref. [30] after irradiation in PISCES-A. Recent NRA measurements [31] demonstrated tiles extended beyond 14 μm in NB31 after irradiation in the magnetron discharge to the fluence of 5×10^{24} D/m^2.

Figure 23 shows also approximations of experimental points given in Ref. [23] and [7], which were obtained after implantation of 150 eV ions in N11 from plasma in PISCES-A and after implantation of 200 eV D^+ ions in NB31 from a mass separator, respectively. The difference between the two data sets is remarkable: the trapped number differs by an order of magnitude; and the reason is unclear. Neither energy, nor the temperature differences are of importance. The most remarkable difference is in the ion flux values (3.6×10^{15} D^+/cm^{2}sec in the ion implanter vs. 2×10^{18} D^+/cm^{2}sec in PISCES); measurements made in Ref. [3] gave no distinct flux dependence. Our retention data are closer to those given in Ref. [23], though the flux is rather different.

To check the possible influence of the sample preparation, several additional measurements have been performed. Some of MPG-8 samples were polished mechanically, but some samples (inversed triangles in Fig. 22) were with "broken" surface (see above). The shapes of the spectra from polished and broken samples were always similar. The total retention of deuterium was less for polished samples.

TDS measurements are usually made not immediately after plasma irradiation. To check the possible influence of this delay, several samples were kept in air for 2-15 days after irradiation, but no remarkable difference was observed (triangles with thin edges in Fig. 23). The conclusion was made that keeping in air for a week or two does not lead to remarkable release of trapped deuterium. This conclusion agrees with Ref. [24]. Keeping in air may lead to increase of HD and HDO release and a respective decrease of D_2 release but not to decrease of the D content in samples. Experiments where large amounts of HD and HDO are observed can give a large uncertainty in trapping measurements as the sensitivity of the detector to HD and HDO is not known well.

19. Features of plasma experiments

Analysis of experimental data, both our own and from literature, demonstrates that a wide spread is often observed.

Measurements of TDS spectra were usually reproducible in our experiments. Nevertheless, TDS that did not correlate with other spectra, and even TDS that differed drastically from other spectra, were sometimes observed. These observations demonstrate that plasma irradiation is not as well controlled instrumentally, in comparison with the ion irradiation. Plasma parameters are not always well defined and predictable. Plasma irradiation gives a mixture of particles and their energy. Ions, molecules, and neutrals contribute to deuterium trapping. Secondary ion-electron emission cannot be taken into account in plasma irradiation experiments. Surface modification due to plasma impact, which is different in different facilities, can also be a factor that influences trapping and release. In many experiments, development of specific reliefs on the surface was observed. Deposition of impurities was also often observed, and these impurities were different in different plasma facilities. Formation of C-D films on the surface of irradiated graphite is possible, and this process is sensitive to irradiation conditions.

That is, TDS obtained in different facilities are different even if conditions of the experiment are supposed to be similar. An example of the difference in experimental measurements is given by comparison of Ref. [7] and [23]. Also, a rather large spread is seen between experimental points in Ref. [23], which give the approximation line that tends to too low values of the number of deuterium trapped if extrapolated towards zero.

Differences in TDS after ion implantation and after saturation from gas have been considered above. Experiments with atoms also a demonstrate variety of spectra. A broad spectrum of D_2 (500 K - 2200 K) was observed in Ref. [43] after exposure of graphite to thermal D atoms. Two high temperature peaks at about 1000 K and 1300 K were observed in Ref. [44], but only one main peak at 490 K with faint satellites at 540 and 580 K was found in Ref. [45]. It was observed in Ref. [45] that decrease in the temperature of atoms drastically decreased the absorption efficiency.

One can expect that trapping during plasma irradiation has features of trapping from gas, hot atoms, and ions. This is what we observed in fact.

Not many examples of TDS after plasma irradiation are given in the literature. For example, the spectrum given in Ref. [24] is rather broad (from 400 K to 1200 K). Though it is peaked around 750 K, it may be considered as a superposition of several peaks. A three-peak structure, which was similar to that we observed, was reported in Ref. [29]: two prominent peaks at 800 and 1000 K and a very small peak at 600 K appeared after sequential ^{4}He and D_2 glow discharges at 22ºC and 300ºC. Accumulation after irradiation at 570 K was larger than at 295 K possibly due to deep migration. As in the case of gases and ions, irradiation at elevated temperature led to

release in the high temperature range as observed in Refs. [36, 37] after plasma irradiation of POCO at 1400 K: TDS was in the interval of 1500-2000 K. Only high temperature release of HD and D_2 was reported in Ref. [25] after exposure in DiMES in DIIID, possibly because the temperature was high. Similarly, only high temperature release of H_2 was measured in samples from JT-60 [26].

20. Conclusion

Thermal desorption of deuterium implanted at 50-100ºC in fine grain powder graphite MPG-8 and carbon fiber composite NB31 was investigated. Four different plasma facilities were used for comparison: magnetron discharge, radiofrequency discharge, beam plasma discharge LENTA, and beam plasma discharge PR-2. TDS after implantation of 5keV ions, after loading from gas phase, and TDS from soft and hard deuteron-carbon films were measured for comparison. Releases of HD, D_2, HDO, and CD_4 molecules were measured.

Desorption after plasma irradiation takes place in the range from 400 K to above 1500 K. There are four apparent peaks of D_2 and HD desorption: 500 K, 750-800 K, around 1000 K, and 1200-1300 K. These peaks possibly consist of more narrow peaks. Desorption of HD always dominates at high temperature. There are two peaks of CD_4 and HDO release: 750-800 K and 500-550 K. The peak positions of the CD_4 and HDO release correlate with those of D_2 and HD. Release of C_2D_x hydrocarbons is two orders of magnitude less than that of CD_4. The dominant peak of release of all gases is around 750-800 K. The main contribution to D release is from desorption of D_2 and HD.

There is no principal difference in D trapping between powder graphite MPG-8 and carbon fiber composite NB31. Spectra of HD, HDO, and CD_4 are similar for the two materials, though the relative amplitudes of the peaks are slightly different and the number of deuterium released from NB31 is about twice higher than that from MPG-8 for all D-containing masses. This means that the trapping sites are of the same origin, and only the total and relative number of sites is different in the two materials.

Trapping sites in the two materials are dangling bonds and closed pores. Dangling bonds can exist on surfaces of grains and crystallites, as well as inside crystallites and binder. There are various defects and a variety of binding energies in graphite and composite. Radiation defects produce dangling bonds that make them in principle similar to natural defects.

The positions of peaks of various deuterium-containing gases HD, D_2, HDO, and CD_4 are very similar. This can mean that the limiting processes of release of these gases are similar. It is suggested that the limiting step of release of these molecules is detrapping of D atoms trapped by carbon dangling bonds. These D atoms migrate and recombine with H and D atoms, CD_3 groups, and HO radicals also trapped by carbon dangling bonds.

Irradiation in different facilities affects the material in different way, therefore the shapes of the spectra after irradiation in radio frequency discharge, magnetron discharge, beam plasma discharge PR-2, and LENTA discharge are different, but the positions of the main peaks are the same.

Experiments with carbon materials irradiated by plasma in the same facility were not always reproducible. This can be connected with two factors: (a) the samples can be different as the materials are not homogeneous; (b) unpredictable variations of plasma properties are possible.

In experiments with 5 keV ion implantation, D_2 and HD were mainly observed in TDS. Release is characterized by a broad maximum. The release of deuteron-methane is small.

Experiments with various flux densities in the range of $(0.5\text{-}3.5) \times 10^{20}$ D^+/m^2sec demonstrated that there were no obvious tendencies of TDS variation and deuterium retention.

TDS after loading in gas gave peaks at 500, 600, 800, 1000, 1300 K, which are similar to those after irradiation by plasma. All the traps after loading in gas are natural traps. After loading at 630 K, the main desorption peak appears around 800 K as in most plasma experiments. The natural sites that give the peak at 800 K dominate in carbon materials. After loading at 830 K, the main peaks are at 1100 and 1300 K, and the number of trapped deuterium increases due to migration deeper in the bulk, though the concentration of high energy traps is less than that of low energy traps.

Comparison of TDS after ion beam experiments and after loading from gas may lead to the conclusion that high temperature peaks can be attributed both to radiation induced defects and to natural defects. Radiation induced traps are the same in nature as the natural trapping sites of high binding energy.

TDS after plasma irradiation are as broad as after saturation from gas, and peak 800 K dominates in both cases. That is, deuterons from plasma are trapped mainly in natural defects due to low energy of ions.

TDS of polished and "broken" samples were similar in shape, but different in the number of deuterons trapped.

All D-containing species (D_2, HD, C_xD_y, HDO) released very rapidly from the soft a:C-D films, giving a very narrow peak at 750 K due to decomposition of the film. Release from hard films has the main peak at 850 K and continues up to 1300 K with several peaks in the spectrum. Deuterocarbons C_xD_y (x,y=1,2,3) release

in a single broad peak with T_m=850 K. No hydrocarbon release is mentioned at high temperatures.

Plasma irradiation leads to surface erosion and modification, which was different in different experiments. Sometimes specific features like metal droplets, bunches of carbon nanofibers, carbon columns and pillars, and regions of abnormal erosion appeared.

Trapping of deuterium as a function of fluence was measured up to the fluence of 3×10^{25} D^+/m^2. No saturation with the fluence was observed in NB31 and MPG-8. In general, NB31 traps twice as much deuterium as MPG-8. No flux dependence in the range of $(0.5\text{-}3.5) \times 10^{20}$ D^+/m^2s was observed. Polished and unpolished samples trap different number of deuterium. Keeping in air after irradiation for 2-15 days did not lead to deuterium release. The main part of deuterons at high fluence is trapped outside the ion range.

Plasma parameters (like the energy and fluxes of ions, hot atoms and gas molecules) are not always well defined and predictable. Plasma composition, surface contamination and modification due to plasma impact are not always predictable. This can be the reason for a spread of TDS and accumulation observed in literature as well as that observed in our experiments.

References

[1] SKINNER, C.H., et al., Recent advances on hydrogen retention in ITER's plasma-facing materials: beryllium, carbon, and tungsten, Fusion Sci. Technol. **54** (2008) 891.

[2] HAASZ, A.A., DAVIS, J.W., Fluence dependence of deuterium trapping in graphite, J. Nucl. Mater. **209** (1994) 155.

[3] DAVIS, J.W., HAASZ, A.A., WALSH, D.S., Flux and fluence dependence of H^+ trapping in graphite, J. Nucl. Mater. **176–177** (1990) 992.

[4] HANSALI, G., BIBERIAN, J.P., BIENFAIT, M., Ion beam implantation and thermal desorption of deuterium ions in graphite, J. Nucl. Mater. **171** (1990) 395.

[5] YAMAUCHI, Y., HIROHATA, Y., HINO, T., Hydrogen and helium retention properties of B_4C and SiC converted graphites, Fus. Eng. Des. **39-40** (1998) 427.

[6] MAYER, M., BALDEN, M., BEHRISCH, R., Deuterium retention in carbides and doped graphites, J. Nucl. Mater. **252** (1998) 55.

[7] ROTH, J., et al., Deuterium retention in carbon fibre composites NB31 and N11 irradiated with low-energy D ions, J. Nucl. Mater. **363-365** (2007) 822.

[8] HINO, T., HIRANO, F., YAMAUCHI, Y., HIROHATA, Y., Hydrogen retention and erosion of carbon–tungsten mixed material, Fus. Eng. Des. **49-50** (2000) 213.

[9] LANGLEY, R.A., BLEWER, R.S., ROTH, J., Behavior of implanted D and He in pyrolytic graphite, J. Nucl. Mater. **76–77** (1978) 313.

[10] YAMAUCHI, Y., HINO, T., KOYAMA, K., HIROHATA, Y., YAMASHINA, T., Hydrogen retention properties of low Z and high Z plasma facing materials, J. Nucl. Mater. **241-243** (1997) 1016.

[11] HAASZ, A.A., DAVIS, J.W., Deuterium retention in doped graphites, J. Nucl. Mater. **232** (1996) 219.

[12] ALIMOV, V.Kh., SCHWÖRER, R., SCHERZER, B.M.U., ROTH, J., Thermal desorption of D_2 and CD_4 from bulk-boronized graphites, J. Nucl. Mater. **187** (1992) 191.

[13] GOTOH, Y., YAMAKI, T., TOKIGUCHI, K., SHIMIZU, H., Thermal desorption spectroscopy of pyrolytic graphite cleavage faces after keV deuterium irradiation at 330–1000 K, J. Nucl. Mater. **191-194** (1992) 360.

[14] SAWICKI, J.A., ROTH, J., HOWE, L.M., Thermal release of tritium implanted in graphite studied by T(d, α)n nuclear reaction depth profiling analysis, J. Nucl. Mater. **162-164** (1989) 1019.

[15] MORIMOTO, Y., et al., Study on energetic ions behavior in plasma facing materials at lower temperature, Physica Scripta **T103** (2003) 117.

[16] ATSUMI, H., et al., Surface erosion of graphite by D irradiation, J. Nucl. Mater., **141-143** (1986) 113.

[17] ASHIDA, K., ICHIMURA, K., MATSUYAMA, M., WATANABE, K., Thermal desorption of hydrogen, deuterium and tritium from pyrolytic graphite, J. Nucl. Mater., **128–129** (1984) 792.

[18] KUZMINOV, D.B., KANASHENKO, S.L., GORODETSKY, A.E., ZAKHAROV, A.P., Interaction of deuterium atoms with radiation defects in graphite, J. Nucl. Mater. **185** (1991) 123.

[19] GARCIA-ROSALES, C., ROTH, J., BEHRISCH, R., Sputtering and surface composition modifications of Ti doped graphite RG-Ti at temperatures up to 2000 K, J. Nucl. Mater. **212-215** (1994) 1211.

[20] ATSUMI, H., YAMANAKA, S., SON, P., MIYAKE, M., Thermal desorption of deuterium and helium from ion irradiated graphite, J. Nucl. Mater. **133–l34** (1985) 268.

[21] OYAIDZU, M., et al., Effects of chemical states of carbon on deuterium retention in carbon-containing materials, J. Nucl. Mater. **367-370** (2007) 1522.

[22] MORIMOTO, Y., OKUNO, K., Correlation between annealing effects of damage and implanted deuterium release from graphite, J. Nucl. Mater. **313-316** (2003) 595.

[23] GOEBEL, D.M., et al., Erosion of graphite by high flux hydrogen plasma bombardment, Nucl. Fus. **28** (1988) 1041.

[24] FERNANDEZ, V., BARDON, J., PALMARI, J.P., Study of the influence of air exposure on graphite implanted by low energy high density deuterium plasma, J. Nucl. Mater. **176–177** (1990) 1005.
[25] YAMAUCHI, Y., et al., Deuterium retention of DIII-D DiMES sample, J. Nucl. Mater. **266-269** (1999) 1257.
[26] HIROHATA, Y., et al., Hydrogen retention in divertor tiles used in JT-60 for hydrogen discharge period, J. Nucl. Mater. **337-339** (2005) 609.
[27] YOSHIKAWA, A., et al., Hydrogen retention and depth profile in divertor tiles of JT-60 exposed to hydrogen discharges, Fus. Eng. Des. **81** (2006) 289.
[28] ARKHIPOV, I.I., et al., Bulk retention of deuterium in graphites exposed to deuterium plasma at high temperature, J. Nucl. Mater. **233-237** (1996) 1202.
[29] HIROKI, S., HASEGAWA, Y., KANEKO, K., ABE, T., MURAKAMI, Y., High-resolution mass spectrometric analysis of gases released from graphite during sequential helium and deuterium glow discharge cleanings, J. Nucl. Mater. **224** (1995) 293.
[30] EMMOTH, B., RUBEL, M., FRANCONI, E., Deep penetration of deuterium in carbon based substrates exposed to PISCES-A plasma, Nucl. Fus. **30** (1990) 1140.
[31] ALIMOV, V.Kh., ROTH, J., Hydrogen isotope retention in plasma-facing materials: review of recent experimental results, Phys. Scripta **T128** (2007) 6.
[32] YOSHIDA, H., et al., Deuterium retention in carbon dust and carbon-tungsten mixed dust prepared by deuterium arc discharge, J. Nucl. Mater. **329-333** (2004) 790–794.
[33] HIROHATA, Y., et al., Distribution of hydrogen isotopes retained in the divertor tiles used in JT-60U, J. Nucl. Mater. **367-370** (2007) 1260-1265.
[34] SHIBAHARA, T., et al., Hydrogen isotope retention of JT-60U W-shaped divertor tiles exposed to DD discharges, J. Nucl. Mater. **357** (2006) 115.
[35] BALDEN, M., et al., Deuterium retention by implantation in carbide-doped graphites, Phys. Scripta **T102** (2003) 38.
[36] ZAKHAROV, P., et al., Hydrogen retention in plasma-facing materials and its consequences on tokamak operation, J. Nucl. Mater. **241-243** (1997) 52-67.
[37] ARKHIPOV, I.I., et al., Deuterium retention in codeposited layers and carbon materials exposed to high flux D-plasma, J. Nucl. Mater. **271–272** (1999) 418-422.
[38] DOYLE, B.L., WAMPLER, W.R., BRICE, D.K., PICRAUX, S.T., Saturation and isotopic replacement of deuterium in low-Z materials, J. Nucl. Mater. **93–94** (1980) 551.
[39] ATSUMI, H., TOKURA, S., MIYAKE, M., Absorption and desorption of deuterium on graphite at elevated temperatures, J. Nucl. Mater. **155-157** (1988) 241.
[40] GORODETSKY, A.E., et al., Deuterium trapping by carbon materials for tokamak plasma-facing components, Fus. Eng. Des. **43** (1998) 129.
[41] MARKIN, A.V., GORODETSKY, A.E., ZAKHAROV, A.P., Effect of oxidation on thermal desorption of deuterium sorbed in graphite, J. Nucl. Mater. **248** (1997) 34.
[42] HOINKIS, E., Thermodesorption of deuterium from a porous graphitic carbon, J. Nucl. Mater. **183** (1991) 9.
[43] PHILIPPS, V., VIETZKE, E., ERDWEG, M., FLASKAMP, K., Thermal desorption of hydrogen and various hydrocarbons from graphite bombarded with thermal and energetic hydrogen, J. Nucl. Mater. **145-147** (1987) 292.
[44] PITCHER, C.S., AUCIELLO, O., HAASZ, A.A., STANGEBY, P.C., Interaction of a sub-eV H^0 atom beam with carbon: methane production and hydrogen retention, J. Nucl. Mater. **128-129** (1984) 597.
[45] ZECHO, T., GÜTTLER, A., SHA, X., JACKSON, B., KÜPPERS, J., Adsorption of hydrogen and deuterium atoms on the (0001) graphite surface, J. Chem. Phys. **117** (2002) 8486.
[46] SKOVORODA, A.A., et al., Plasma-driven superpermeation of hydrogen through Nb membranes: bulk effects, J. Nucl. Mater. **306** (2002) 232.
[47] KHRIPUNOV, B.I., et al., "Erosion of fusion materials under high-power steady-state plasma stream on the LENTA facility", 21st IAEA Fusion Energy Conference, Chengdu, China, 2006, Paper EX/P4-3, Book of abstracts, IAEA, Vienna (2006) p. 52.
[48] VIZGALOV, I.V., PISAREV, A.A., GUTOROV, K.M., A mechanism of PFM erosion and redeposition in gaps, J. Nucl. Mater. **363-365** (2007) 833.
[49] ATSUMI, H., Hydrogen retention in graphite and carbon materials under a fusion reactor environment, J. Nucl. Mater. **313-316** (2003) 543.
[50] SPITSYN, A., PISAREV, A., GUREEV, V., SKOVORODA, A., MARTYNENKO, Y., Permeation of hydrogen through MPG-8 graphite, J.Nucl. Mater. **363-365** (2007) 833.
[51] ISOBE, S., et al., Catalytic effect of 3d transition metals on hydrogen storage properties in mechanically milled graphite, J. Phys. Chem. Solids **65** (2004) 535.
[52] ICHIKAWA, T., et al., Hydrogen storage properties on mechanically milled graphite, Mater. Sci. and Engin. **B108** (2004) 138.
[53] ORIMO, S., MATSUSHIMA, T., FUJII, H., FUKUNAGA, T., MAJER, G., Hydrogen desorption property of mechanically prepared nanostructured graphite, J. Appl. Phys, **90** (2001) 1545.

[54] LISOWSKI, W., KEIM, E.G., VAN DEN BERG, A.H.J., SMITHERS, M.A., Thermal desorption of deuterium from modified carbon nanotubes and its correlation to the microstructure, Carbon **44** (2006) 974–982.

[55] SALANCON, E., et al., Redeposition of amorphous hydrogenated carbon films during thermal decomposition, J. Nucl. Mater. **376** (2008) 160.

[56] STAUDENMAIER, G., et al., Trapping of deuterium implanted in carbon and silicon: A calibration for particle-energy measurements in the plasma boundary of tokamaks, J. Nucl. Mater. **84** (1979) 149.

[57] McCRACKEN, G.M., MAPLE, J.H.C., The trapping of hydrogen ions in molybdenum, titanium, tantalum and zirconium, Brit. J. Appl. Phys. **18** (1967) 919.

Review of erosion/deposition and retention of hydrogen isotopes (H, D, T) at divertor area of JT-60U

T. Tanabe[1,2], K. Masaki[3], Y. Gotoh[3], K. Sugiyama[1], Y. Hirohata[4], T. Shibahara[2], Y. Oya[5], T. Hayashi[3], T. Arai[3], N. Miya[3]

[1] Kyushu University, 6-10-1, Hakozaki, Higashi-ku, Fukuoka 812-8581, Japan

[2] Nagoya University, Furo-cho, Chikusa, Nagoya, 464-8603, Japan

[3] Japan Atomic Energy Agency, Naka, Ibaraki 311-0193, Japan

[4] Hokkaido University, Kita-13, Nishi-8, Kita-ku, Sapporo, 060-8628, Japan

[5] Shizuoka University, Shizuoka 422-8529, Japan

Abstract

The present paper summarizes recent studies on erosion/deposition in plasma facing carbon materials, retention of hydrogen isotopes (H, D, and T) and dust collected from the divertor area of JT-60U, and the results are compared with those of JET. The carbon erosion/deposition pattern at the divertor area of JT-60U is similar to that of JET and correlates well with H+D retention profiles in the divertor region, i.e. the deposition dominated inner divertor tiles show high retention, while the erosion dominated outer divertor tiles show low retention. However the retained amount in the redeposited layers is smaller than those observed in JET, which is attributed to temperature rise of the redeposited layers probably owing to their poor thermal contact to the substrate. Carbon deposition on the plasma shadowed area and remote area like pumping ducts is very small and only a small amount of dust is collected. Such low carbon deposition in the remote area in JT-60U could be attributed to the precise alignment of divertor tiles both toroidally and poloidally. It is suggested that divertor geometry could have rather strong effects on carbon deposition or carbon transport.

In D-D discharge machines like JT-60U, tritium produced by D-D reaction does not fully loose its initial energy of 1 MeV and is implanted into the plasma facing wall more than 1 μm in depth. Hence the tritium retention profile is separated from carbon deposition profiles. The implantation of high energy particles could be one important mechanism of tritium bulk retention.

Key words: Carbon, Hydrogen Retention, Erosion, Re-deposition, Divertor, JT-60U

PACS. No. 52.40.Hf (Plasma-wall interactions; boundary layer effects; plasma sheaths)
52.55.Fa (Tokamaks)

1. Introduction

Tritium retention and carbon erosion are critical issues for ITER and have been extensively studied in JET, TFTR and other tokamak machines [1-10]. Because of the following two reasons, (1) erosion of carbon used as PFM is likely too large to use for an appropriate period, and (2) most of the tritium is likely retained in the deposited carbon layers in the divertor region particularly in the plasma shadowed area and hard to remove, the utilization of carbon materials as plasma facing materials in ITER is limited as small as possible. Until now, however, information is limited and little systematic investigations on effects of, for instance, surface temperature, divertor structure, SOL plasmas, isotopic differences and so on, have been carried out.

In JT-60U, studies of plasma-materials interactions (PMI) and plasma facing materials (PFM) have started in 2001 under the joint research between Japanese universities and JAEA [11] and have provided new results [11-45]. The present paper summarizes recent results concerning tritium issues of ITER, in particular erosion/deposition of carbon materials including dust formation and retention of hydrogen isotopes (H, D, and T). Comparing the results of JT-60U with those of JET and TFTR, the mitigation of tritium retention and reduction of carbon erosion/redeposition are discussed.

2. Divertor structure of JT-60U and analyzed carbon tiles

2.1. Divertor structure

JT-60U is a non-circular tokamak device with a vacuum vessel of 3.4 m in major radius and 1.1 m (horizontal)/1.4 m (vertical) in minor radii. In 1997, the divertor structure inside the vacuum vessel was modified from an open divertor geometry to the W-shaped divertor geometry with the inner side pumping to study high-performance plasmas and steady-state operation with deuterium (D) as operating gas [46]. Fig. 1(a) shows a cross-sectional view of the vacuum vessel and Fig. 1(b) poloidal locations of analyzed tiles in the divertor region for the inner side pumping geometry. In 1999, further modification of the divertor structure from the inner side pumping geometry to both sides pumping one was made. Afterward, JT-60U has been operated with the both sides pumping geometry. For the both sides pumping, the outer side pumping slot was introduced between the outer dome wing and the outer divertor tile similar to the inner side pumping slot. Carbon fiber composite materials were used as the divertor tiles and the dome top tiles (CFC:CX-2002U, Toyo Tanso Ltd.) and a part of the baffle tiles (CFC:PCC-2S, Hitachi Kasei Ltd,). All other area was covered with isotropic graphite tiles (IG-430U, Toyo Tanso Ltd.). Temperatures of the tiles located in the divertor area were monitored by AC thermocouples installed 6 mm beneath the tile surfaces as indicated by bold lines in Fig. 1(b).

2.2. Analyzed tiles

In December 1998, a poloidal set of the divertor tiles (exposed to plasma from June 1997 to October 1998) were sampled for the analysis from the #P5 section as indicated in Fig. 1(b), which were referred as the tiles for the inner side pumping. A few tiles of the inner and outer baffle plates and the first wall, which were exposed to discharges from March 1991 to October 1998, were also removed for a tritium analysis.

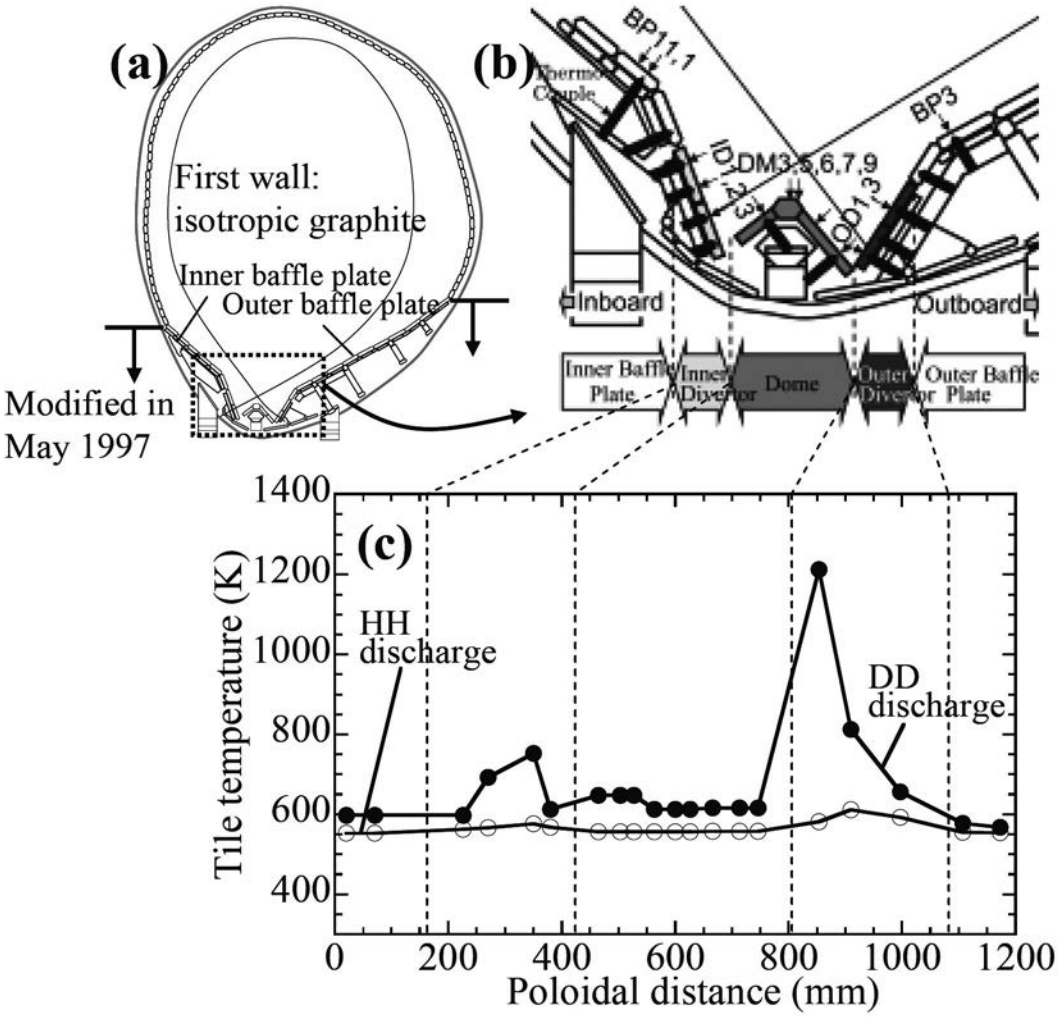

FIG. 1. A cross-sectional view of JT-60U (a), and tiles arrangement for the divertor area (b). Location of samples and thermocouples are indicated. Typical temperature profiles of tiles measured by thermocouples for DD and HH discharges with NBI heating (c) [45].

During the operation period from June 1997 to October 1998, a total of about 4300 discharges were made with the W-shaped divertor geometry with (or without) the inner side pumping. 3600 discharges were deuterium discharges (DD discharges), and more than 300 discharges were with neutral beam injection (NBI) heating with power of 14–23 MW. The total amount of the tritium produced by DD reactions during this period was 18 GBq. During the operation period, two times of boronization were carried out. Before removing the tiles, 700 discharges with hydrogen as an operating gas with H NBI (HH discharges) and a tritium degassing operation by Taylor discharge cleaning (TDC), electron cyclotron resonance (ECR) discharges and glow discharge cleaning (GDC) for six weeks were performed to remove tritium retained in the vessel during the DD discharges [32, 47, 48]. Figure 1(c) gives typical temperature profiles measured by the thermocouples for DD and HH discharges with the NBI heating. The tile temperature rose about 50-600 K during the DD discharges, while the temperature rise during the HH discharges was only 20-100 K, because NBI heating power of the HH discharge was nearly a half of that of the DD discharge.

In 2002, another set of tiles was removed for deposition/erosion profiling, which was exposed to plasmas through 1997 to 2002 for both geometries of the inner side pumping and the both sides pumping. During the period, a total of about 9000 discharges were made and the total time of neutral beam injection (NBI) heating was about 3×10^4 s.

2.3. Analysis

Net deposition thickness and erosion depth on the tiles were estimated from thickness changes of the tile caused by redeposition and erosion by using a micrometer (surface profilometry). Splitting the tiles to give a cross-sectional view, both poloidal distributions in the thickness of, and the sub-μm structures of the redeposited layers were investigated (SEM: Hitachi type S-300H) [20, 30, 43]. Elemental and chemical state analyses were made on the redeposited layers of a thickness around 5 μm by using XPS (ULVAC-PHI: type 5600, Mg K_α X-ray source). For depth profiling, the sputtering rate for the carbon tiles was estimated to be around 0.04 nm/s for argon ion sputter-etching with a beam voltage of 4 kV, a beam current, 13.8 nA, and a luster-area of 3 mm × 3 mm. The details of the XPS analysis were given elsewhere [18, 27].

The depth profiles of hydrogen and deuterium retained in graphite tiles were analyzed by secondary ion mass spectrometry (SIMS) with using cesium ions (Cs^+, 15 keV) as the probing beam a sputtering rate of approximately 1 μm/h [10, 22, 25, 36]. The beam size was about 32 μm and the luster-area was set to be 400 × 400 μm^2. Deuterium analysis was also made by nuclear recoil detection (NRD) [38].

In order to determine the areal distribution of tritium radioactivity, a two-dimensional radiation detector, an imaging plate (IP), was applied because of its high resolution, ultrahigh sensitivity and relatively simple procedure [12-14]. The IP can be used to measure tritium retained within a depth of about 3 μm from the sample surface. Tritium retained in sample tiles was also measured by the full combustion method, i.e. burning the sample in air at 1000°C for 6 h, converting unoxidized tritium into HTO on a hot copper bed (CuO) at 500°C and measuring HTO thus produced by a liquid scintillation counter [19, 33, 34].

To assess the energetic triton loss from the plasma, the Orbit Following Monte-Carlo (OFMC) code [49, 50] was used. In the code, Coulomb collisions between the energetic tritons and the plasma were simulated and the triton orbits were traced in the magnetic fields combined with the axisymmetric field produced by toroidal field ripple.

2.4. Dust sampling

During summer break of JT-60U in 2003, the inside of the vacuum vessel was inspected carefully to observe the deposition of carbon and other impurities on plasma shadowed area and dust/flakes were collected [31]. Little free moving dusts or debris were found on the divertor area or at the bottom of the vacuum vessel. Hence, most of the collected dust is the carbon deposits which were mechanically removed from the vacuum wall not covered by the graphite tiles. Inside of the vacuum ducts for main pumps and cryo-panels of NBI pumping ducts were also examined for tritium retention and deposition of carbon and other impurities.

3. Carbon deposition and erosion

3.1. Divertor area for the inner side pumping geometry

The inner divertor tiles were mostly covered by thick redeposited layers. Figs. 2(a) and (b) are typical cross-sections of the deposited surface of the upper one and lower one of the two inner divertor tiles, respectively [20]. The redeposited layers were clearly distinguished from the substrate and the layers showed columnar structure as seen in the enlarged image in Fig. 2(a). On the columnar structure, the layered structure (Lamellar structure) parallel to the substrate was developed as seen in Fig. 2(b). The thickness of the columnar structured layers was within 30 μm, over which the lamella structure developed to make the maximum thickness of the redeposited layers of 60 μm.

Different from the inner divertor tiles, the outer divertor tiles were mostly eroded, with a maximum erosion depth of around 20 μm. However, the trace of the deposition was observed on the eroded surface in SEM images. Figures 3 (a) and (b) respectively show the poloidal deposition and erosion profiles of the inner divertor and the outer divertor tiles together with frequency histograms of divertor-hit-points. Because there was a bolt hole on the tile for fixing the tile, the deposition profile on the inner divertor had a dip. We believe the deposition profile was a broad single peak as appeared for the both sides pumping geometry in Fig. 4. One can see that the poloidal distributions of the erosion and deposition well correlate with those in the frequency histograms of divertor-hit-points [20].

No continuous redeposited layers were found on the outer dome wing and the dome top tiles, while continuous redeposited layers were found on the inner dome wing tiles at least in the zone close to the dome top. Concerning the dome unit, the observation for the inner pumping geometry was a little different from that for the both sides pumping geometry as described later, which could be attributed to the outer side pumping.

XPS measurements showed that the redeposited layers were mainly constructed of carbon (94-95%) with minor contributions of B: 3-4%, O: 0.4-0.6%, and a little metallic depositions of Fe, Ni, Cr : 0.3-0.6 at.% [20]. It should be noted that oxygen content was very small; accordingly boron atoms in the redeposited layers were mostly bonded to carbon.

The redeposited layers on the inner divertor tiles strongly adhered to the substrate and were hard to remove, suggesting rather high temperature deposition and/or the redeposited layers being subjected to high temperatures during discharges. This is likely the cause of less dust in JT-60U compared to other tokamaks as discussed later.

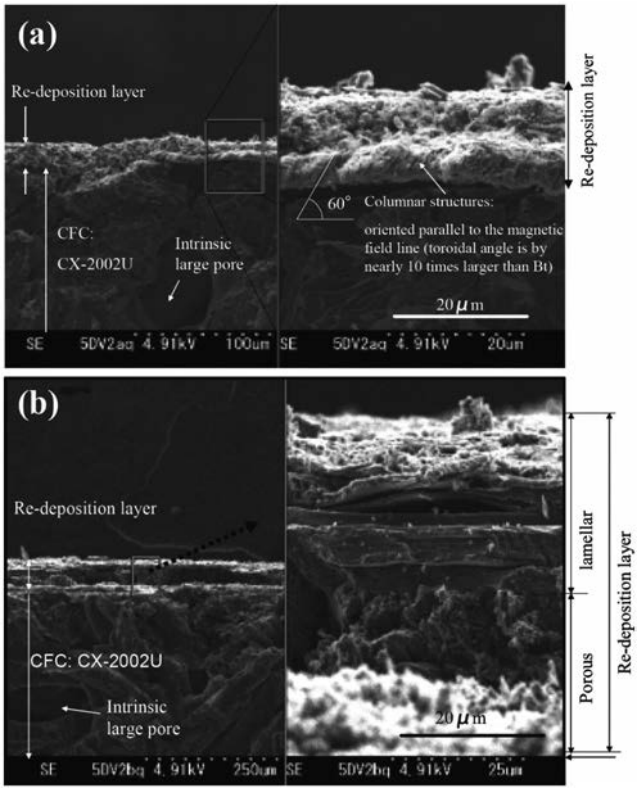

FIG. 2. Cross-sectional SEM images for split tiles of the upper (a) and lower (b) inner divertor tiles. In the right are magnified images [20].

3.2. *Divertor area for the both sides pumping geometry*

Deposition/erosion profiles for the both sides pumping geometry are given in Fig. 4 [43]. One can

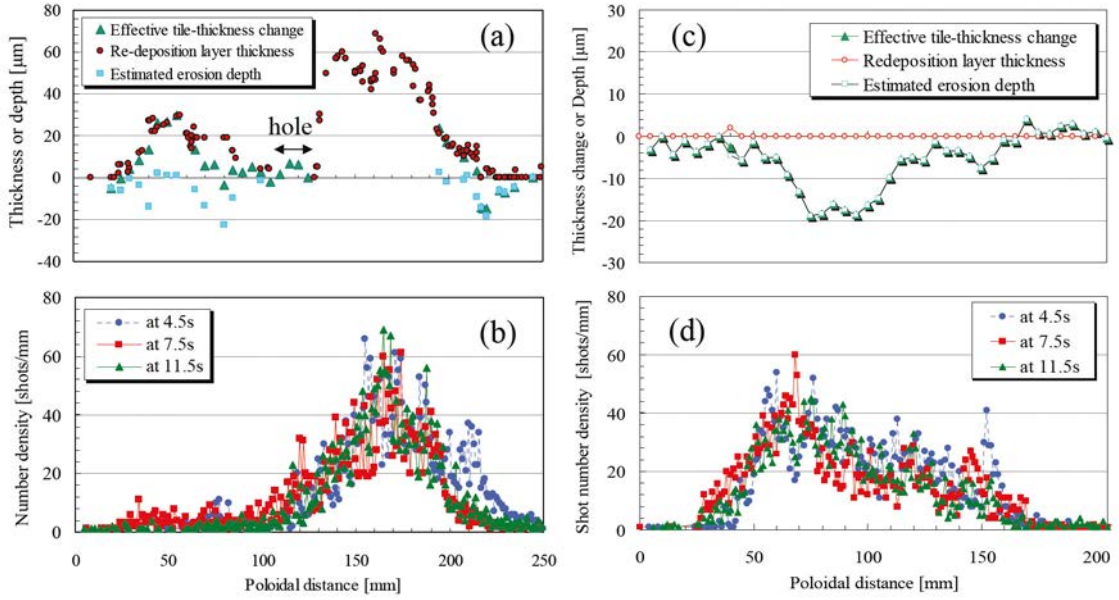

FIG. 3. Deposition and erosion profiles for the inner divertor tiles (a), and the outer divertor tiles (c) together with frequency histograms of divertor-hit-points (b) and (d) for the inner pumping geometry [20].

see that three different toroidal positions show very similar profiles, indicating good symmetry in the toroidal direction, which was also noted in the tritium profiles in Fig. 7. The general appearance of the deposition on the inner divertor and the erosion at the outer divertor is the same as that for the inner side pumping geometry. Deposition dominates the inner divertor tiles with the maximum thickness of the redeposited layers of 230 μm, while erosion dominates the outer divertor tiles with the maximum erosion depth of 70 μm. The poloidal distribution of the thickness of the redeposited layers on the inner divertor tiles was very similar to that of the divertor-hit-points histogram, though the former slightly shifted to the inboard side. The erosion maximum on the outer divertor tiles clearly shifted to the outboard side from the most frequent divertor-hit-point.

Some additional differences are observed between both geometries. Different from the inner side pumping geometry, the deposition profile on the inner divertor makes a broad peak without appreciable dip. The inner dome wing is clearly erosion dominated. The reason for this appearance change of the inner dome wing from the net deposition for the inner pumping geometry to the net erosion for the both sides pumping geometry is not clear. But referring the results that the outer dome wing is clearly deposition dominated with their thickness being significantly increased near the bottom edge, these differences suggest the existence of some eroded carbon flow from the outer divertor to the inner divertor through the dome region for the inner side pumping geometry [43], which might be hindered by the outer side pumping geometry.

Assuming full toroidal symmetry as suggested by the three different deposition profiles in Fig. 4, the total amount of carbon erosion/redeposition in the divertor region was estimated. The increment of carbon by redeposition was 0.36 kg for the inner divertor tiles, –0.09 kg by the erosion for the inner dome wing, –0.25 kg for the outer divertor, and 0.18 kg for the outer dome-wing. The weight of the dust in the divertor region was measured to be 0.01 kg [31, 43]. Adding all above, the net deposition of the divertor area of JT-60U was 0.21 kg, indicating that about 40% [(0.36-0.21)/0.36] of the net deposition of the divertor area must originate from the first wall (main chamber).

According to this net deposition, the carbon deposition rate in the divertor region can be estimated at 9×10^{20} atoms/s, divided by density of the redeposited layers 910 kg/m^3 and the integrated NBI heating time during the 1997-2002 experimental campaigns. The value is a little higher than the 3×10^{20} atoms/s previously determined for the inner side pumping geometry [20], probably because of the higher NBI power for the both sides pumping period. Thus carbon redeposition in the divertor region is estimated to be 560 kg/year assuming a continuous high power pulse operation. Since around 40% of the net deposition on the divertor was attributed to the erosion of the first wall, the net erosion of the first wall for one year high power operation would end up with about 220kg/year [43]. This number is about 1/4 of that estimated for the JET-MkIIA divertor (1000 kg/year) [51].

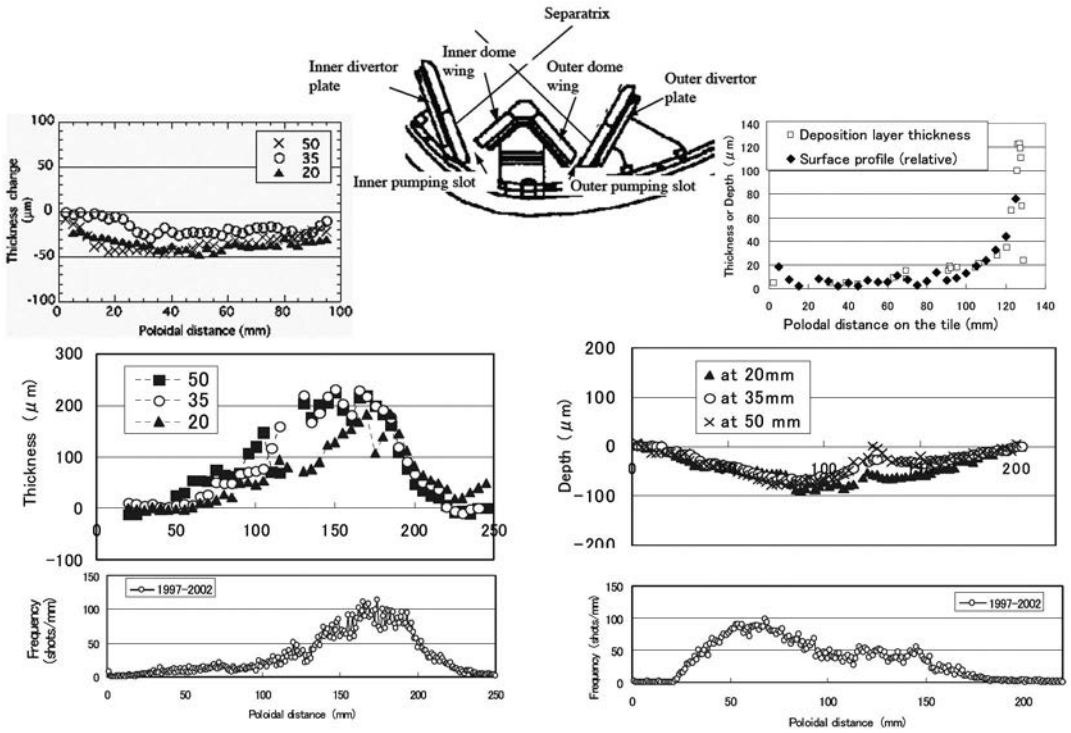

FIG. 4. Deposition/erosion profiles of the inner divertor tiles (a), the inner dome wing (b), the outer dome wing (c) and the outer divertor tiles (d) for the both sides pumping geometry shown in the inset [43].

3.3. *Carbon deposition in remote area*

Careful inspection and dust collection were done in the vacuum vessel for one sector of the divertor region between the poloidal magnetic coils during the summer break in 2002. Although depositions behind the first wall tiles and at the far remote area in the pumping ducts were observed as slight color changes, the deposition was too small to be taken into account. Figure 5 shows the weight of collected dust in various places. Extrapolating the amount of the dust and the removed deposition collected to a whole vessel, the total dust in the vessel was estimated to be around 7 g [31]. This is much less than that observed in JET [4, 5, 52]. Furthermore no appreciable deposition was observed in remote areas like main pumping ducts and even cryo-panels of NBI ducts.

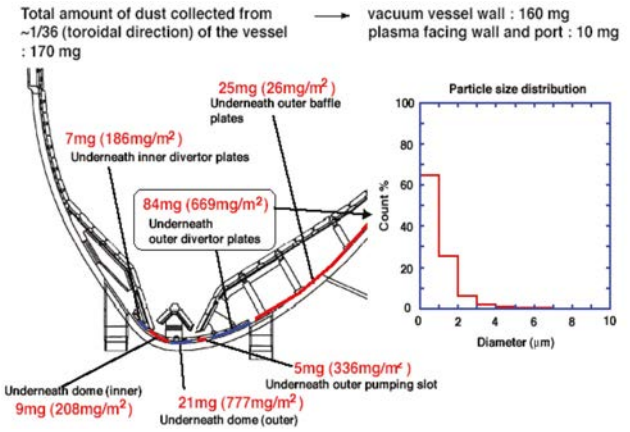

FIG. 5. Collected dusts at various locations in the divertor area (a) and their size distribution (b) [31].

4. Tritium retention in the divertor area for the inner side pumping geometry

4.1. *Plasma facing surface*

Figures 6 (a) and (b) show the poloidal tritium distribution on the divertor area and line profiles measured by IP, where red and blue respectively correspond to high and low tritium retention. No difference was observed for the inner side pumping and the both side pumping. One should note that toroidal distribution is very much symmetric, which is a characteristic feature not only for tritium distribution but also for carbon deposition/erosion (see Fig. 4), quite different from the observation in JET [53-58]. The highest tritium retention was found on the dome top tile, followed by the outer and the inner baffle plates, while tritium retention in the inner and outer divertor tiles was very small [12-14, 21, 24, 26, 37, 41]. The poloidal tritium retention profile is completely different from the carbon deposition/erosion profiles given in Figs 3 and 4, but well correlates with the injection profiles of high energy triton calculated by the OFMC code given in Fig. 6(c) [28].

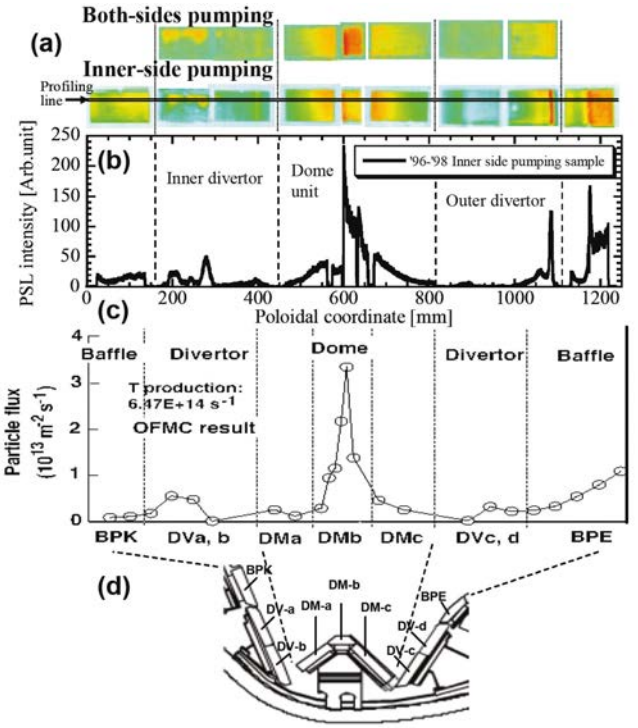

FIG. 6. Tritium retention profiles on tiles of the divertor area for the both sides pumping geometry (a), the inner side pumping geometry (b), their line profiles along two different toroidal positions (c) and profiles of energetic triton fluxes calculated by the OFMC code (d) [28].

The direct implantation of high energy triton [50] was confirmed by the full torus tritium profile of the dome top tiles as depicted in Fig. 7. Except noisy peaks, the intensity shows clear periodicity which is the same as the position of the toroidal magnetic filed coils as indicated in the figure. This periodicity was attributed to ripples loss of high energy tritium owing to the ripple of the magnetic field [53]. The inhomogeneity owing to the ripple loss was more clearly observed on the outer baffle plates as show in Fig. 8, which shows quite good agreement between the profiles of tritium intensity and calculated tritium flux distribution.

The poloidal tritium profile along the first wall also agrees with the simulation, i.e. very high at the midplane and low at the other area as seen in Fig. 9. According to the OFMC simulation, 31% of tritium produced by DD reactions escapes from the plasma without being thermalized and 12% is implanted directly to the divertor area [28]. This is very much consistent with the experimental observation that about 10% of the totally produced tritium was retained in the divertor region.

It is important to note that by removing the redeposited layers on the inner divertor tiles, the tritium intensity increased as shown in Fig. 10. This further confirms that tritium was implanted directly deep inside, as suggested by the simulation. The small retention in the outer divertor, particularly, near the most frequently

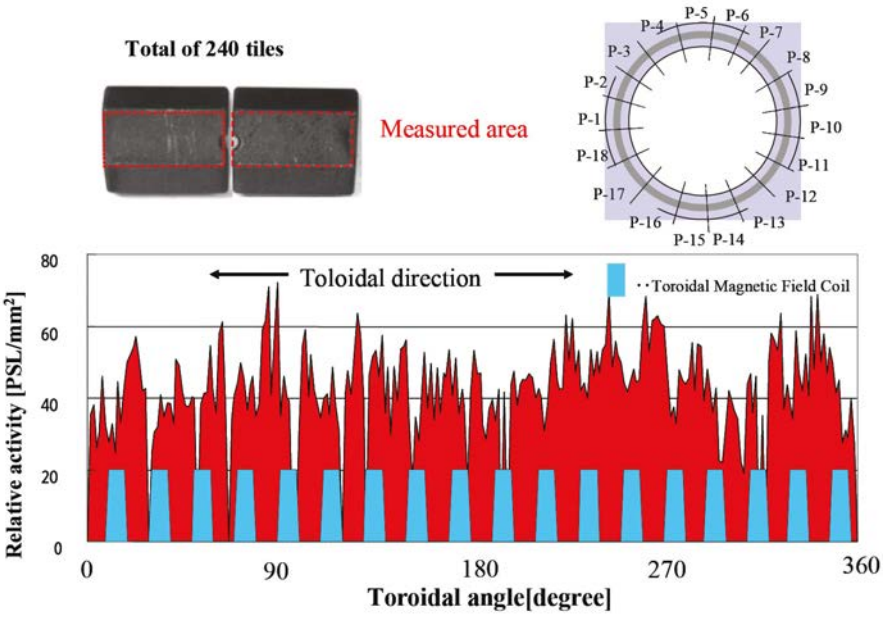

FIG. 7. Full toroidal tritium retention profiles for totally 240 dome top tiles. The locations of the toroidal magnetic coils are also shown in the figure. Both figures show the same periodicity [53].

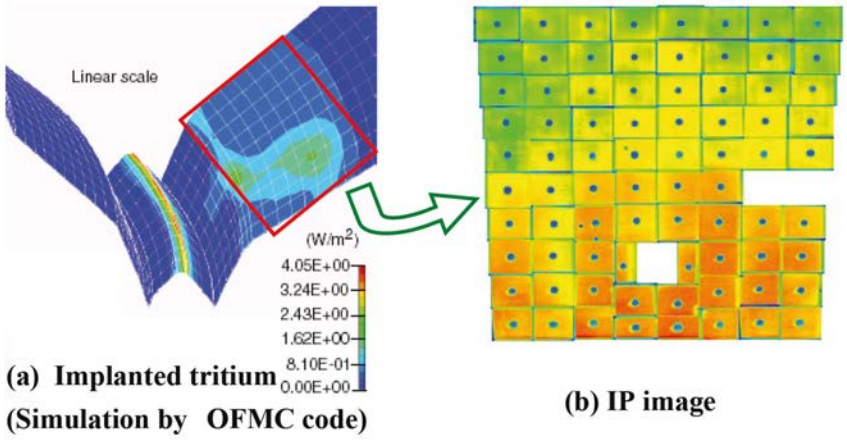

FIG. 8. Tritium profiles on the outer baffle plates in one sector. Profiles of energetic triton calculated by OFMC are also shown for comparison.

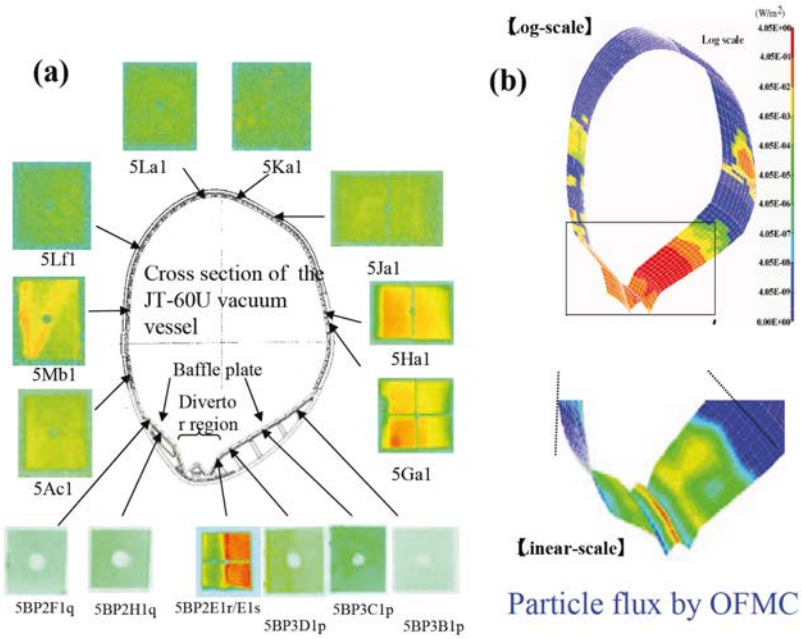

FIG. 9. Tritium profiles for selected first wall tiles (a), together with the profiles of energetic triton injecting flux (b) [28].

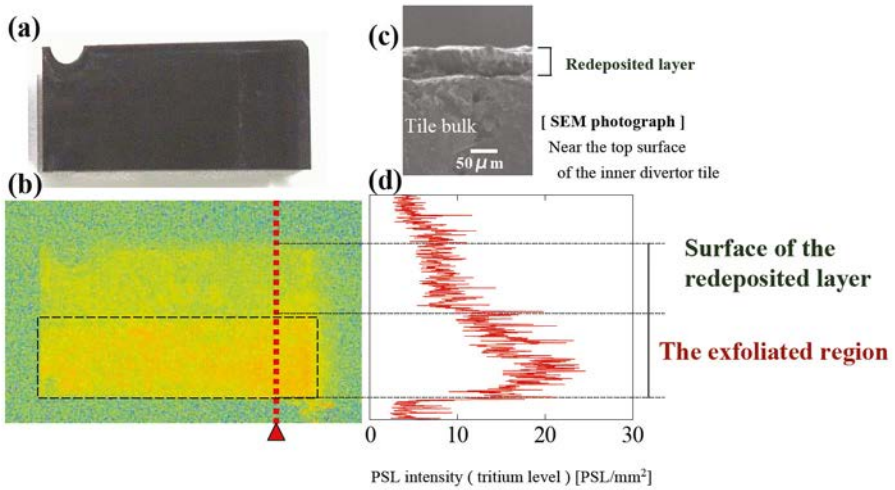

FIG. 10. Comparison of tritium for the original surface of the inner divertor and after removing the redeposited layers on the surface of the inner divertor tile 5DV2ap for the both sides pumping geometry. Top view (a), tritium profile (b), cross-section (c), and tritium line profile (d).

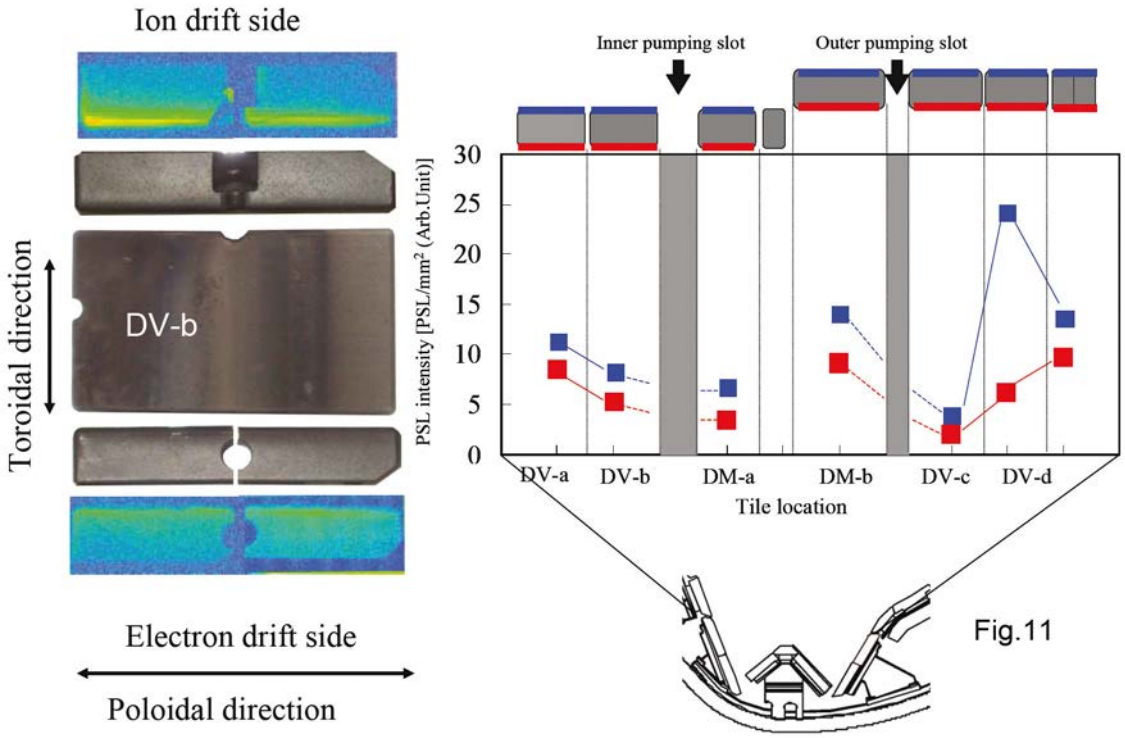

FIG. 11. Tritium profiles of the toroidal facing sides of the inner divertor (5DV3bq), and their poloidal dependence. The ion drift sides retained higher tritium than the electron drift side [41].

divertor-hit-point, is due to temperature increase owing to plasma heat load.

4.2. Tritium on the tile gap and remote area

Tritium retention on the toroidal tile sides (tile gap) for the both sides pumping geometry was clearly observed as shown in Fig. 11 [41]. This means that tritium thermalized in the plasma impinged everywhere. But those once stuck on the plasma facing surface were easily replaced by subsequent deuterium ions from the plasma, while at the plasma shadowed area no replacement was possible and piled up together with carbon deposition. The tritium profile along the poloidal direction is rather homogeneous with higher intensity at the ion drift side and at the outer divertor. Again this profile agrees well with the tritium injection profile calculated by OFMC. The tritium retention profile from the top to deep inside the gap gave two characteristic decays as depicted in Fig. 12. The shorter one is only 3 mm of decay length, while the other is showing very long decay or nearly constant. The shorter decay was attributed to the prompt redeposition of carbon atoms eroded at the

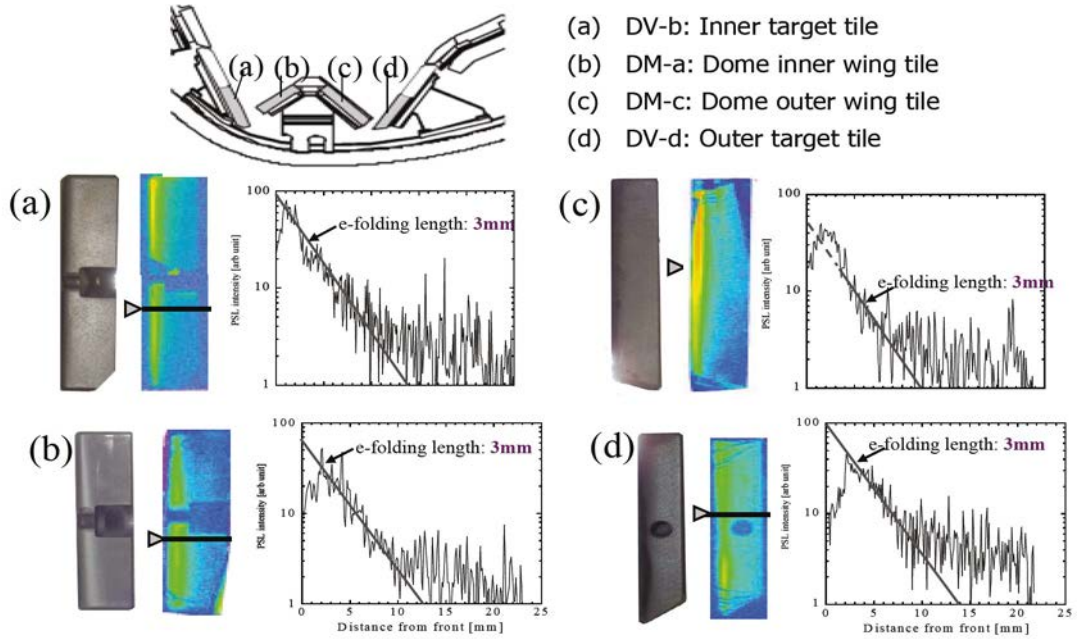

FIG. 12. Tritium profiles of the toroidal facing surface (ion drift side) of the divertor tiles. Photographs, tritium images and line profiles are compared. The locations of the sides are indicated in the inset [41].

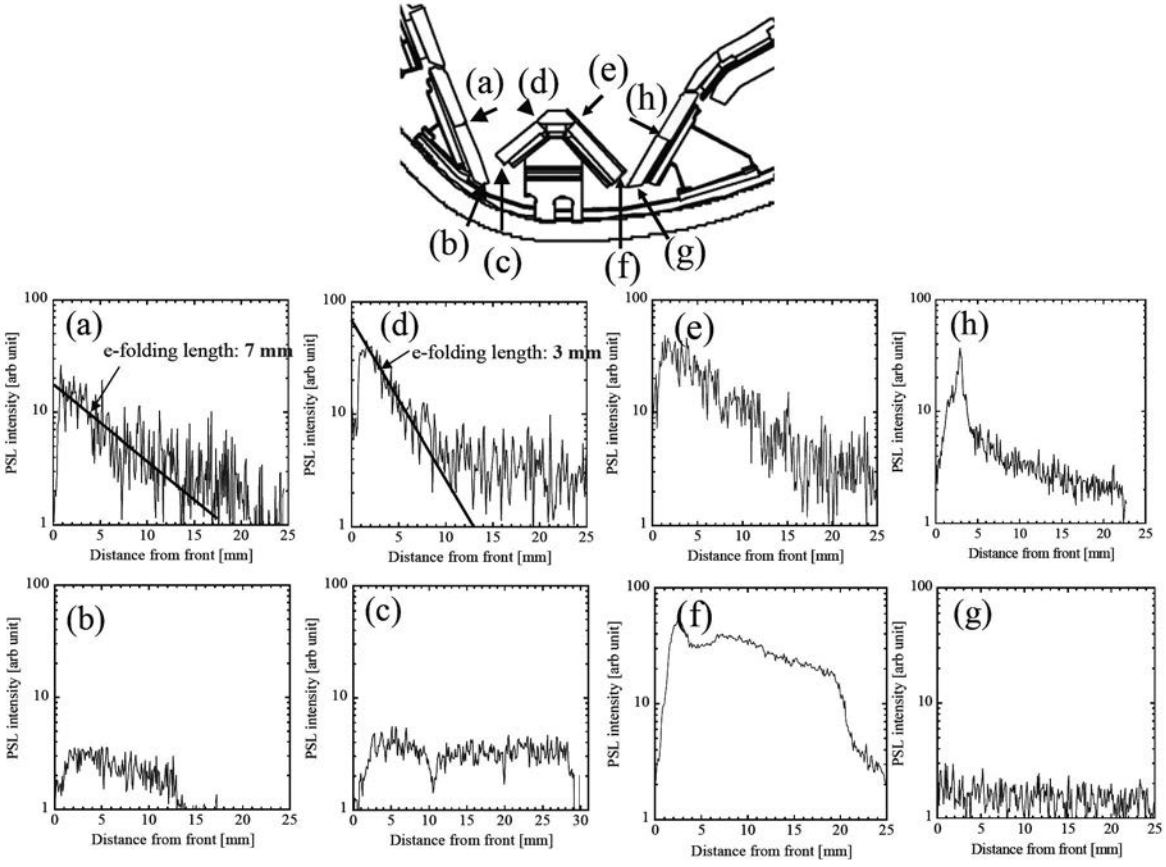

FIG. 13. Tritium line profiles from the top to the rear surface on the poloidal sides of the divertor tiles. The locations of the sides are indicated in the inset [12].

plasma facing surface owing to its gyration after the ionization [41] and similar decay was also observed in tile gaps of bumper limiters in TFTR [56]. The longer decay indicates deep penetration of neutral carbon and hydrocarbon atoms into the gap.

Tritium profiles on the poloidal tile sides were quite dependent on the location as indicated in Fig. 13. In particular, the tile sides facing the pumping slot did not show rapid decay but were rather uniform. According to Gotoh et al. [43], thick redeposited layers were observed

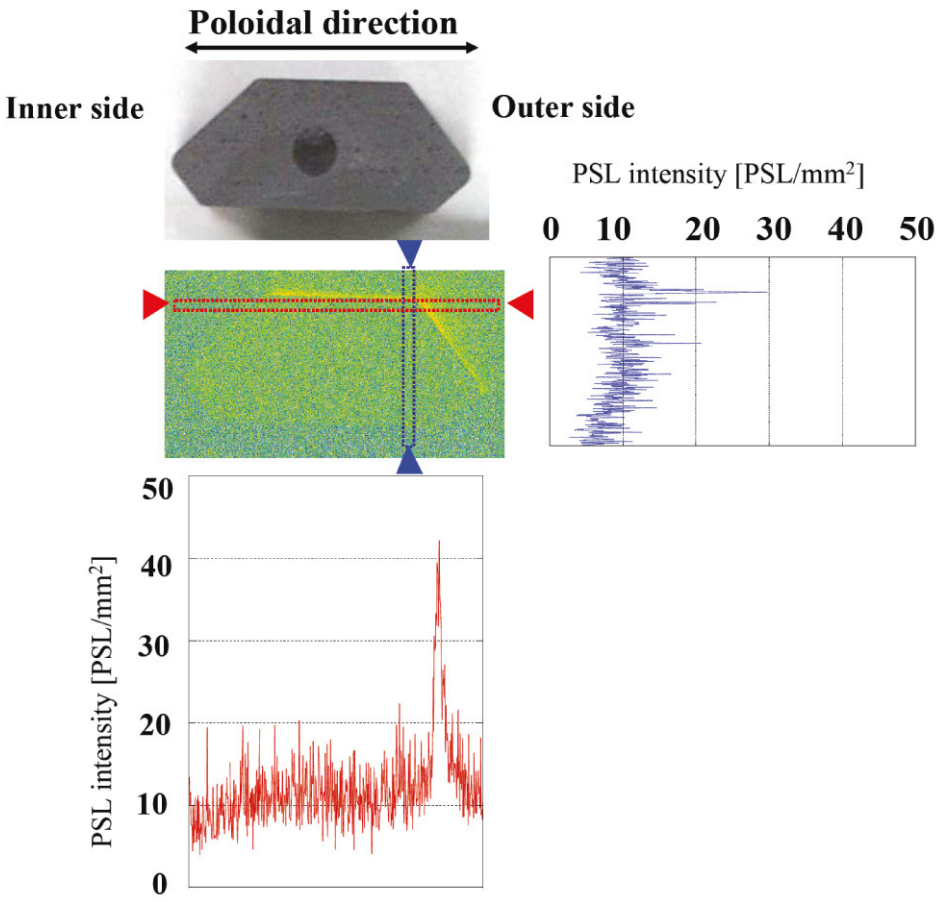

FIG. 14. Tritium profiles on the cross-section of the dome top tile.

in the same place, indicating that tritium was incorporated in the carbon redeposited layers, without replacement by D.

Tritium retention at remote areas like the pumping duct was also measured. Because of little carbon deposition, tritium retention was also very small. The activity owing to the neutron activation of duct materials which clearly decayed with distance from the plasma overwhelmed the tritium activity. Hence tritium exhausted from JT-60U must be in stable chemical forms like hydrogen gas phase (HT) and/or stable hydrocarbons. This would be the cause of less dust and debris in JT-60U compared to other machines and the redeposited layers are strongly adhered to the surface of the duct.

4.3. Tritium retention in the tile bulk

Tritium retained in the tile bulk was also measured by IP measurement for the cross-section of the tile and by the combustion method [19, 34, 35]. Figure 14 shows the tritium profile on the cross-section of the dome top tile obtained by IP. One can see the dominant tritium retention near the surface and a very small retention, only a little higher than the background, in the bulk throughout the tile.

In the combustion measurement, several thin sample plates were cut from the tiles parallel to the surface into the depth direction. Tritium was detected only for the sample including the plasma facing surface, and other samples retained very small amount of tritium, only a little higher than the background level. This indicates that tritium in gaseous form could penetrate into the bulk through open pores but energetic triton did not diffuse into the bulk. Unfortunately, however, the depth resolution was too poor to give the accurate tritium concentration near the surface. It should be mentioned that during combustion of the tiles, the gaseous form of T (HT or DT) was found to be firstly released and then followed HTO release. This means that the sample was hard to be oxidized and gaseous T was thermally released below the oxidizing temperature of the sample, and is very much consistent with the above findings that the tiles were subjected to higher temperature, retaining small hydrogen and no oxygen, and having a rather graphitized structure.

5. H and D retention of the divertor tiles for the inner side pumping geometry

5.1. Depth profiling by NRD and SIMS

Depth profiling of H and D by SIMS clearly showed that H and D were retained in much shallower regions in the tiles than T [32, 36]. Figure 15 shows depth profiles of H and D by SIMS analysis typical for the eroded area on the outer divertor, the dome top area and the redeposited layers on the inner divertor. Deuterium profiles by NRD [38] were quite similar to SIMS profiles. H was retained mostly in the very near surface and the D profile showed its maxima just behind the H profile, indicating that H replaced most of D retained in the near surface region during the HH discharges performed before the ventilation for removal of T. The highest concentration of H and D determined by TDS and NRD [38] was about 0.05 in a (H+D)/C ratio, and averaged concentration throughout the redeposited layers was about 0.03 as given in the next section. This concentration is much less than the H/C observed in most tokamaks [4, 5]. D retention was the highest at the outer dome wing so as the T retention, where no appreciable deposition was observed. This is most probably owing to high energy deuteron injection originated from NBI as discussed in the next session.

5.2. TDS analysis

Desorbed amounts of hydrogen isotopes as hydrogen isotope molecules and hydrocarbons, and the total amount of desorbed hydrogen isotope atoms and the ratio of the desorbed hydrogen isotopes (D/H ratio) for all samples, are compared in Fig. 16 [32, 42, 44]. In the deposition dominated area at the inner divertor (ID1-3) and the outer dome wing (DM7-9), the total retention of hydrogen isotopes (H+D) was larger than those for the eroded area at the inner dome wing (DM3), the dome top (DM5, 6) and the outer divertor (OD1, 3). The largest retention (H+D) was observed at DM9 with 1.4×10^{23} atoms/m^2.

Except for ID3, the amount of hydrogen isotopes desorbed as hydrocarbons was independent of sample locations with less contribution of the total hydrogen desorption for larger hydrogen retaining samples. The largest hydrocarbon contribution of about 1/5 was found at DM9. The amount of H desorbed as H_2 molecules was larger at the redeposited area than that at the eroded area. Although HD desorption was similar to that for H_2, the difference of desorbed amount between the maximum and the minimum was a little larger than that for H_2. The largest release of D_2 was observed for DM9, while the minimum for OD1 was located at the outer divertor.

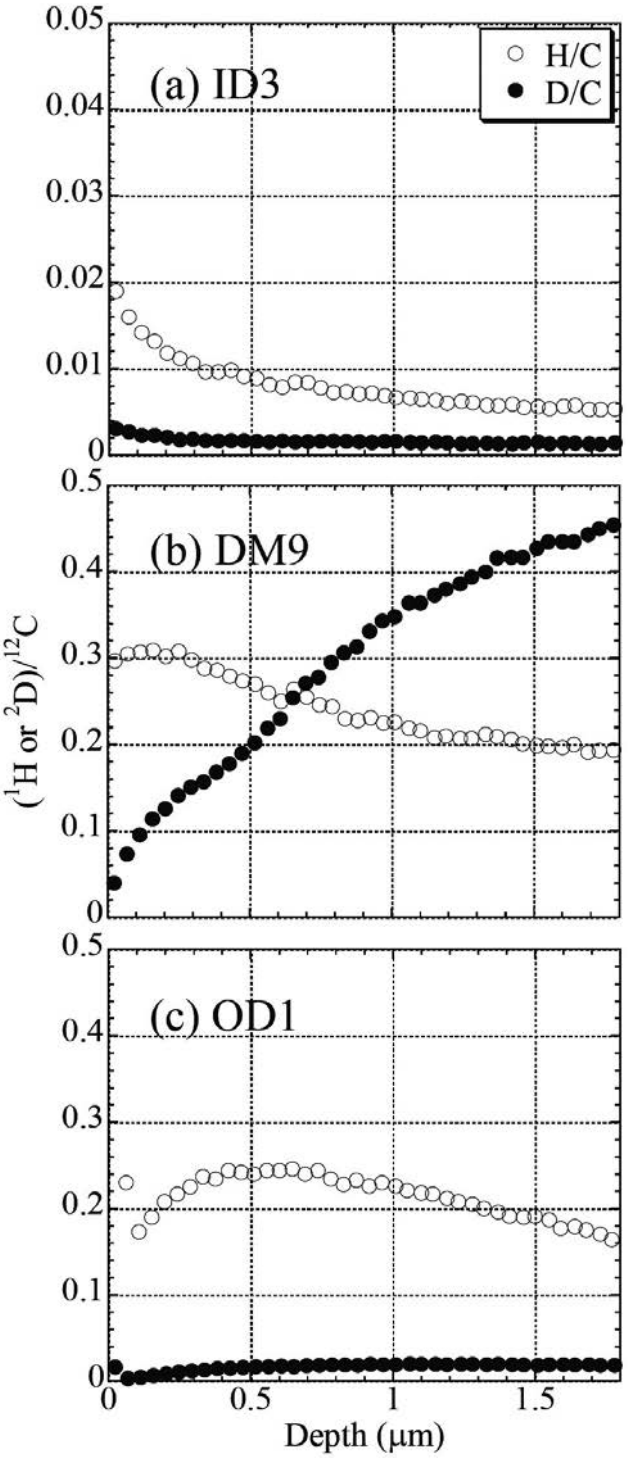

FIG. 15. Depth profiles of H and D determined by SIMS for the redeposited layers on the inner divertor (a), the dome top (b) and the eroded area of the outer divertor (c) [36].

The D_2 desorption for the samples at the inner divertor was smaller than those of H_2 and HD. In Fig. 16, the amounts of the total desorbed H and D for all samples were also compared. All samples except DM3, DM7, DM9 and OD1 show nearly constant D/H ratios of 0.4, but the figure clearly distinguishes D/H of 1.2 for the dome samples from the others. The D/H ratio of the bulk and removed samples (in which the redeposited carbon

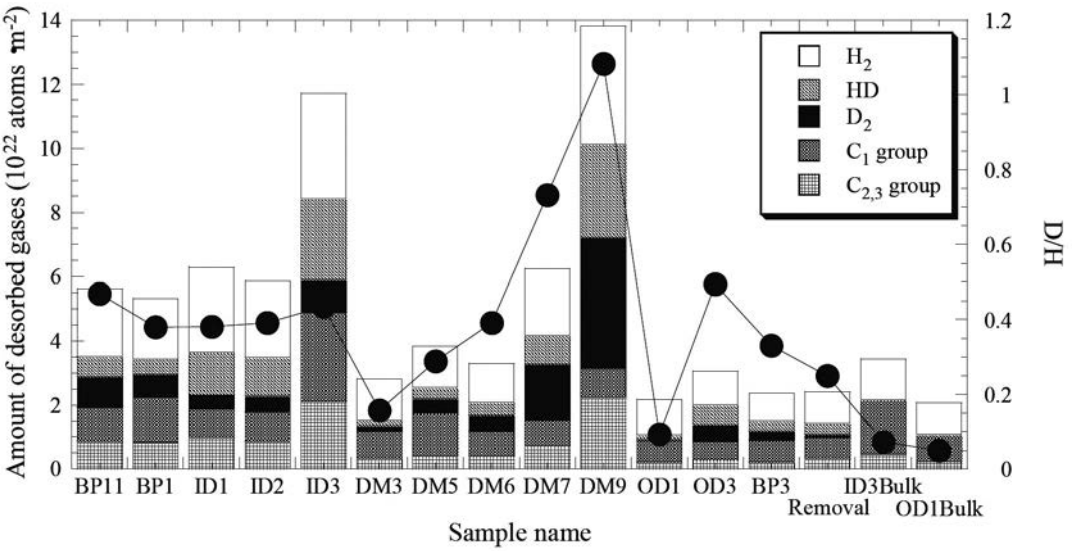

FIG. 16. Poloidal profiles of H, D and hydrocarbons desorbed by TDS for the inner side pumping geometry. The ratios of released H/D are also given [44].

layers were removed) were much smaller than those of the plasma facing samples, indicating less penetration of D atoms into the bulk. This is a clear indication of different retention mechanisms of H and D for the dome area and the other area. In DM9, D retention was also the highest and the highest, D/H for DM9 suggests that D was retained rather deep like tritium. Referring to the highest tritium retention on the dome top tile (see Fig. 6), the largest D retention in DM9 is likely caused by the injection of high energy deuterium originated from D NBI. The energetic deuterium injection originated from NBI would be caused by the ripple loss mechanism, which is large in JT-60U. Hence it could contribute long term tritium inventory, because energetic fuel ions will be rather deeply implanted without saturation.

It is also important to note that the above D/H ratios were much smaller than the ratio of the number of DD discharges and HH discharges, which is about 5 [44]. This indicates that a significant part of D retained during the DD discharge period must be replaced by H during the HH discharges succeedingly made, as discussed in the following section.

Figure 17 shows a good linear relationship between the thickness of the redeposited layers and the total hydrogen isotope retentions for the samples taken from the redeposition dominated inner divertor tiles. This indicates that except on the very near surface, both hydrogen isotopes were uniformly retained throughout the redeposited layers, though the contribution of H on the total retention decreased with increasing thickness. From the gradient of the lines in Fig. 17, the concentrations of hydrogen isotopes in the redeposited layers on the inner divertor tiles were determined to be 0.032 in the (H+D)/C atomic ratio [44]. The value is nearly the same as that obtained for the open divertor tiles of JT-60 exposed to the HH discharges (H/C = 0.030) [29, 45]. Such low hydrogen concentration is well consistent with the TEM observation that the redeposited layers clearly have graphite like spots in their diffraction patterns [30].

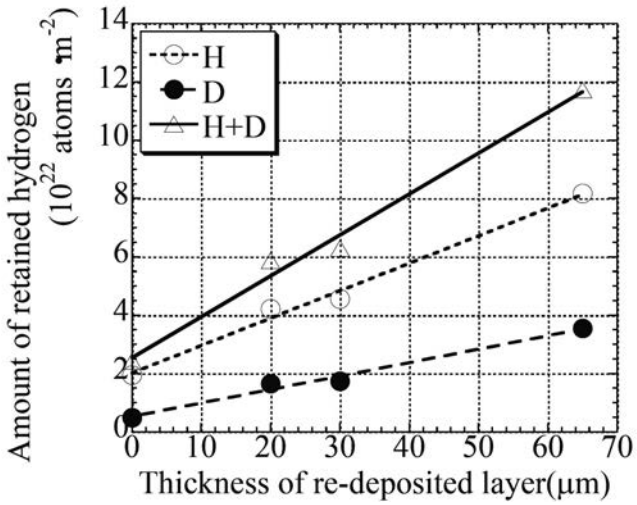

FIG. 17. The amount of totally released H and D by TDS plotted against the thickness of the redeposited layers for the inner divertor tiles [44].

All these observations indicate that the divertor tiles were subjected to substantially high temperature during the discharges. Since JT-60U was normally operated at 573 K and the divertor tiles were only inertially cooled, the temperature of the divertor tiles increased 50 K or more and the surface temperature of the divertor tiles sometimes escalated above 1500 K. This could explain the lower (H+D)/C ratio and appearance of graphitized film like redeposited layers in JT-60U.

6. Discussion

6.1. Carbon erosion/deposition

In Table 1, observations in JT-60U are compared with those for JET with a Mark-IIA divertor [5, 6]. Since carbon sputtering and deposition processes are simple physical and chemical processes, erosion and deposition rates in front of the outer divertor determined by spectroscopy for various machines agree within a factor of two or three [5]. On the other hand, the carbon deposition particularly at the plasma shadowed area is quite machine dependent. Actually the most significant difference between JT-60U and JET is the carbon deposition on the plasma shadowed area. This should be attributed to either or all of the differences in the divertor structure including the position of the pumping slot, discharge conditions, different tile temperatures, different tile sizes, tile alignments for both machines.

In the previous paper [6], we have shown that the tile alignment is critically important to reduce erosion and deposition. Comparing significant toroidal inhomogeneity both for tritium retention and carbon deposition on JET Mark-IIA divertor tiles, those for JT-60 divertor tiles were quite uniform except for the periodicity reflecting the ripple loss. JET experiments with comparison of a Mark-IIA divertor and gas box divertor also show that the geometrical structure is a critical factor to control carbon erosion and deposition [10].

As already noted, sputtered carbon neutrals are immediately ionized and gyrating, most of them return to the sputtered surface within a little distance (prompt redeposition). This is the main cause of the significant deposition in the tile gaps with sharp decay in depth as appeared in Figs 11 and 12. Owing to the magnetic field line in the normal field geometry, the sputtered atom returns to the poloidally inner side (or vertically upper side), as clearly appeared in the deposition profiles of JT-60U (see figs. 3 and 4). In this respect, the heavy deposition at the pumping duct including louvers of the inner divertor of the JET Mark II-A divertor is quite reasonable. When the inner strike point is on the vertical target tile of the gasbox divertor, carbon is not likely transported to the down side, i.e. to the direction of the pumping duct as reported in Ref. [10]. Interestingly, such inner side transport is more clearly seen in the carbon deposition on the outer dome wing tile in JT-60U for the both sides pumping geometry in Fig. 4 [43]. The outer dome wing tile was mostly covered by the depositions and the thickness of the redeposited layers was the largest at the bottom edge. This indicates that the deposition is caused by carbon eroded at the outer divertor and transported to the inner side (directing dome). The heaviest deposition was observed at the bottom side which was not directly facing the plasma [43]. Even in the JET Mark-II A divertor, the inner side of the outer horizontal target tile showed larger tritium retention indicating rather large carbon deposition [54-58].

Once carbon is redeposited at the inner side or the upper direction of the plasma facing surface, they should be succeedingly subjected to ion fluxes resulting in re-erosion. Hence the net erosion could be relieved as observed less deposition in the gasbox divertor than that in the Mark-IIA [59]. These dynamic or repeating cycles of carbon erosion and deposition on the plasma facing surface would result in long range carbon transport from

Table 1. Comparison of JET with Mark-IIA divertor and JT-60U with W-shaped divertor

	JET	JT-60U
Deposition rate at inner divertor	5g/h 6.5×10^{20} atoms/s	9×10^{20} atoms/s for NBI heating time
Erosion rate at outer divertor	2.3 nm/s	0.7 nm/s
D/C in deposits	0.4-0.1	< 0.05
Deposition at remote area	Louvers at inner pumping slot	Beneath outer divertor
Collected dust	1 kg	7 g
Pumping slot	Inner side	Bottom
Tile alignment in toroidal direction	A few mm step between tiles	No step between tiles
Divertor temperature	Below 500 K with base structure water cooled	Above 600 K Only inertially cooled

the outer divertor and the first wall to the inner divertor. However, when carbon is redeposited on the shadowed area as well as the plasma facing area, it must not be re-eroded and hence the redeposition layers will pile up. The smooth alignment of the tiles of JT-60U seems quite effective to reduce the net erosion and deposition on the plasma facing surface, while a few mm step between the neighboring tiles of the JET divertor [60] could not allow escaping of the carbon redeposition at the lower or plasma shadowed side, resulting inhomogeneous profiles of carbon redeposition and tritium retention.

6.2. Mechanism of H and D incorporation in redeposited layers and eroded carbon

Here, the mechanism of hydrogen isotope retention in JT-60U is discussed based on the above findings, taking discharge conditions and tile temperatures into account.

During DD discharges, as already noted in Fig. 1, the maximum temperatures of the tiles of 750, 600 and 850 K were attained respectively for the inner divertor, the outer dome and the outer divertor, and the tile surfaces were further heated up to ~1000 K, ~800 K and ~1400 K, respectively. For a high NBI heating discharge, the local temperature near the outer divertor strike point was further heated up to 1200 K or more from ~573 K during the shot. For the HH discharges, due to less NBI heating power to the divertor area, nearly a half of that for the DD discharges, the highest temperatures of the tiles were nearly 400 K lower than those for the DD discharges.

At the beginning when the redeposition starts on the inner divertor for DD discharges, the deuterium was incorporated in the carbon layers with D/C saturated at the temperature of the redeposited layers. Since the vacuum vessel of JT-60U was kept at 573 K, the tile temperature increased with time during a discharge owing to the plasma heat load, and attained the maximum temperature just before discharge termination. Since the saturated concentration decreases with temperature, the temperature increase would result in hydrogen release from the redeposited layers made during the shot as evidenced by deuterium recovery after termination of the discharge [61]. Hence the D/C in the redeposited layers must be a little smaller than that at the beginning. It should be noted that most of the deuterium impinging on the plasma facing surface must be reflected and re-emitted, because the ratio of deuterium flux and carbon flux will be larger than 10. This means that only a small fraction of the incident deuterium flux remains on the surface. Succeeding discharges would pile up the redeposited layers with similar D/C, but maybe somewhat differently by each discharge depending on the plasma heat load, which enables to distinguish the redeposited layers piled up shot by shot, as clearly shown by Gotoh for the divertor tiles of JT-60 [30]. With pile-up of the redeposited layers by successive discharges, their thermal contact to the substrate became poor [40] and the temperature of the whole redeposited layers would rise higher during a shot. When a particular shot with larger heating power was made, the temperature of the redeposited layers would increase uniformly, resulting in additional deuterium release to homogenize D/C over the whole redeposited layers. This makes D/C in the redeposited layers uniform throughout the layers with such a small value of around 0.03, corresponding to the saturated hydrogen concentration in hydrogen implanted graphite at around 900 K [44].

Succeeding HH discharges would add redeposited layers on the redeposited layers made by DD discharges. Since the heat load of the HH discharge is nearly a half of that of the DD discharges, the temperature increase during the shot would remain less than that for DD discharges. Thus H/C in the newly made redeposited layers by the HH discharges must be larger than D/C for the DD discharges. During the HH discharges, isotope exchanges of D by incoming H would further reduce D/C near the surface region. Accordingly depth profiles of H and D in the redeposited layers become as SIMS depth profiles show. This also happens on the outer dome tile. But the tile temperature was lower than that of the inner divertor, which makes hydrogen concentration a little higher.

Since the redeposited layers showed columnar and porous structure, both D_2 and H_2 can penetrate deep into the tile bulk and be absorbed at so to speak the inner surface or surface of the columnar grains. Thus a certain amount of D retained during the DD discharges would be replaced by H during the HH discharges subsequently made. H_2 penetration also appears the same H/D for the redeposited samples and the bulk samples in Fig. 16. The effect of isotope replacement is discussed separately in Ref. [62].

At the eroded area, in contrast, higher heat load results in smaller D retention but still does not allow D diffusion deep into the bulk, D remaining only near the surface. The HH discharge would add H retention to result in higher (H+D)/C owing to lower heat load for the HH discharges than that of the DD discharges. In addition, some of the D was isotopically replaced by H. Consequently the least D/H as well as the least (H+D)/C appeared for OD1 as seen in Fig. 5.

This continuous replacement of retained hydrogen isotopes with new coming ones is the cause of no T retention near the surface. Because of the less new coming ion flux on the tile gap or plasma shadowed area, T remained near the surface as observed in Figs 11 and 12.

According to this mechanism, retention of hydrogen isotopes on the plasma facing surface will not simply increase with discharge numbers. Actually, global wall saturation was observed at JT-60U [61]. This indicates that tritium retention in the redeposited layers on the plasma facing surface would not be a problem but that at the plasma shadowed region such as pumping slots and gaps of the tiles it must be piled up and could continuously increase.

6.3. Mitigation of tritium retention for carbon machine by modification of divertor structure and operating temperature

For hydrogen implanted in carbon, a temperature of around 500 K is critical, above which hydrogen retention decreases exponentially with temperature, while H/C remains nearly 1 below 500 K [53]. Most of the tokamaks, except JET, TEXTOR and JT-60U, are operated below 500 K and H/C in their carbon deposition is ranging from 0.4 to 1 [4, 5]. Although JET was operated above 500 K, its divertor area was water cooled. Hence large part of the divertor area likely remained below 600 K, except near strike points where high particle flux and heat load easily resulted in over 1000 K.

In JT-60U, which was operated at 570 K with innertially cooled divertor structure, H/C in the deposited carbon on the outer divertor area was below 0.03 [32, 44]. The redeposited carbon layers were not amorphous like but rather well graphitized and not easy to remove [30]. All these were the evidence for the divertor tiles being subjected to high temperatures.

As already mentioned, recent tritium measurements have shown that the deposition on the gap facing the toroidal sides of JET divertor tiles was very small, while the deposition on the plasma facing surface but shadowed by a neighboring tile was appreciable [56, 57]. This means tritium retention at the erosion dominated area would be small, because the eroded area must be subjected to a high particle flux and heat load and hydrogen isotopes near the surface would be saturated during a shot. In addition, hydrogen diffusion in carbon is too small for hydrogen to penetrate deep, except the pore diffusion of molecular species.

Thus to reduce the tritium retention, we should keep the surface temperature as high as possible (well above 800 K). With this higher temperature operation, the chemical erosion on the plasma facing surface would be suppressed and wall saturation would be attained, which prevent continuous increase of tritium retention.

Still, tritium retention on the plasma shadowed area remains a concern, because tritium in this area can not be isotopically replaced even by plasma discharges. In TORE-SUPRA, the hydrogen fueling doubled the exhausting, which was attributed to co-deposition of hydrogen and carbon at the remote area [63]. On all sides of the bumper limiter tiles of TFTR used in its DT discharge campaign, a significant amount of carbon co-deposition with high tritium retention was observed [53]. On the other hand, JET and JT-60U divertor tiles have shown no significant deposition or retention of tritium on the tile sides facing the toroidal gap [55-57]. The lower temperature operation and limiter configuration of TFTR are likely the cause for the large deposition on its tile sides [64]. As already noted, in the JET Mk-IIA divertor [60], there are a few mm steps between the neighboring tiles in the toroidal direction, accordingly the tile surface near the edge shadowed by the neighboring tile was deposition dominated, in other words, the other edge which is nearer to the plasma must be more easily eroded. Thus most of the eroded carbon is transported to the neighboring tile but not escaping down into the gap. In JT-60U, different form JET, all divertor tiles were well aligned to remove the steps between toroidally neighboring tiles and accordingly the deposition/erosion pattern was toroidally very uniform. All above observations clearly indicate that fine alignment between the neighboring tiles in to toroidal direction and removal of open path shining through the plasma could significantly reduce the carbon exhaust to the remote area or pumping ducts.

Another concern is production of tritiated dust, which is believed to originate from the once redeposited layers. Actually the dust collected from JET retained very high tritium [52]. It is important to note that the properties of the carbon deposition critically depend on hydrogen concentration, which also depends on the temperature of the substrate. Hence the carbon deposition retains less hydrogen (tritium) at higher temperature. In addition, the deposition at higher temperatures shows stronger adhesion to the substrates suggesting the less dust formation. As shown in Table 1, the total amount of dust collected in JT-60U [39] was much less than that in JET, owing to less hydrogen retention and stronger sticking of the redeposited layers on the substrate in the former.

Thus JT-60U seems to show a good example to reduce carbon deposition as well as tritium retention. All divertor tiles of JT-60U were well aligned with more or less no steps between the neighboring tiles in both toroidal and poloidal directions, which reduced both the net erosion and redeposition, and kept their temperature above 600K. The divertor geometry of JT-60U also helped to suppress carbon transport to the shadowed area, particularly to the pumping duct. The reduction of the plasma shadowed area by fine tile alignment both in the toroidal and poloidal directions would also help to reduce erosion and redeposition in the tile gap, which is very difficult to remove.

In ITER, unfortunately, the operating temperature will not be high enough, hence tritium retention could

be still high, which can be studied during the hydrogen and deuterium discharge phase. Sophisticated design to maintain the temperature of all plasma facing surface very high with the aid of a plasma heat load could be one solution.

7. Conclusion

The recent results on erosion/deposition including dust formation and retention of hydrogen isotopes (H, D, T) in plasma facing carbon materials of JT-60U, obtained by joint research work between the Japanese university and JAEA, are summarized as follows.

- The inner divertor tiles were deposited, while the outer divertor tiles eroded, and no significant deposition was observed on the plasma shadowed area except on the bottom side of the outer dome wing for the both sides pumping geometry.
- The carbon deposition rate in the divertor region is estimated to be around 9×10^{20} atoms/s normalized for NBI heating time during the 1997-2002 experimental campaigns. Around 40% of the net deposition on the divertor was attributed to the erosion of the first wall; the net erosion of the first wall for one year high power operation could be about 220 kg/year, which is about 1/4 of that estimated for the JET-MkIIA divertor.
- H+D retention in the redeposited layers correlates well with their thickness, and hydrogen concentration in them was uniformly 0.03 in (H+C)/C, except a few μm top surface layers in which it was 0.05.
- Surface D within a few mm in depth is mostly replaced by H, indicating possible T removal by D discharges both for eroded and redeposited tiles.
- Rather high D retention was observed on the outer dome wing probably owing to higher energy deuteron implantation originating from NBI.
- Little deposition and debris were observed in the remote area even in NBI ducts and cryo-panels.
- The tritium profile on the plasma facing surface was separated from the deposition/erosion profile of carbon, because high energy triton was directly implanted a little deeper into the tiles by the ripple loss mechanism. Such energetic fuel implantation into the deeper area could be an additional source for bulk tritium retention.
- Tritium thermalized in plasma was retained in redeposited carbon layers in the tile gaps and on the plasma shadowed area. And the profile of the redeposited layers suggests local carbon transport through prompt redeposition of eroded carbon with higher redeposition for more surface eroded tiles.

JT-60U seems to show a good example to reduce carbon deposition as well as tritium retention. Well aligned tiles with more less no steps between the neighboring ones tiles in the toroidal and poloidal directions could reduce the net erosion and redeposition not only on the plasma facing surface but also on the plasma shadowed area. Higher surface temperature above 600 K reduced the tritium retention. The divertor geometry of JT-60U also helped to suppress carbon transport to the shadowed area, particularly to the pumping duct. Still tritium retention at the plasma shadowed region such as pumping slots and gaps of the tiles remains a concern because it must be piled up and could continuously increase.

Acknowledgement

This work was partly supported by a Grant-in-Aid for Scientific Research, MEXT, Japan, Priority area 467, "Tritium Science and Technology for fusion reactor" http://tritium.nifs.ac.jp/

References

[1] ITER PHYSICS EXPERT GROUP, ITER physics basis, Nucl. Fusion **39** (1999) 2137. Also http://www.iter.org/

[2] FEDERICI, G., et al., Plasma-material interactions in current tokamaks and their implications for next step fusion reactors, Nucl. Fusion **41** (2001) 1967.

[3] FEDERICI, G., et al., Key ITER plasma edge and plasma–material interaction issues, J. Nucl. Mater. **313-316** (2003) 11-22.

[4] SKINNER, C.H., et al., Tritium experience in large tokamaks: Application to ITER, Nucl. Fusion **39** (1999) 271.

[5] PHILIPPS, V., ROTH, J., LOARTE, A., Key issues in plasma–wall interactions for ITER: a European approach, Plasma Phys. Control. Fusion **45** (2003) A17.

[6] TANABE, T., On the possibility of ITER starting with full carbon, Fusion Eng. Des. **81** (2006) 139.

[7] SKINNER, C.H., FEDERICI, G., Is carbon a realistic choice for ITER's divertor?, Physica Scripta **T124** (2006) 18.

[8] COAD, J.P., et al., Erosion/deposition issues at JET, J. Nucl. Mater. **290-293** (2001) 224.

[9] COAD, J.P., et al., Erosion/deposition in JET during the period 1999–2001, J. Nucl. Mater. **313-316** (2003) 419.

[10] COAD, P., et al., Overview of material re-deposition and fuel retention studies at JET with the Gas Box divertor, Nucl. Fusion **46** (2006) 350.

[11] MIYA, N., et al., Major results of the cooperative program between JAERI and universities using

plasma facing materials in JT-60U, J. Nucl. Mater. **329-333** (2004) 74.

[12] TANABE, T., et al., Imaging plate technique for determination of tritium distribution on graphite tiles of JT-60U, J. Nucl. Mater. **307-311** (2002) 1441.

[13] TANABE, T., et al., Surface distribution of tritium on graphite tiles of divertor area in JT-60U, Fusion Sci. Technol. **41** (2002) 877.

[14] TANABE, T., et al., Surface tritium detection by imaging plate technique, Fusion Sci. Technol. **41** (2002) 528.

[15] TOBITA , K., et al., First wall issues related with energetic particle deposition in a tokamak fusion power reactor, Fusion Eng. Des. **65** (2003) 561.

[16] HIROHATA, Y., et al., The depth profiles of deuterium and hydrogen in graphite tiles exposed to DD plasma discharges of JT-60U, Physica Scripta **T103** (2003) 15.

[17] SUGIYAMA, K., et al., Tritium profiles on the surface of graphite tiles used in JT-60U, Physica Scripta **T103** (2003) 56.

[18] OYA, Y., et al., Hydrogen isotope behavior in in-vessel components used for DD plasma operation of JT-60U by SIMS and XPS technique, J. Nucl. Mater. **313-316** (2003) 209.

[19] MASAKI, K., et al., Tritium distribution in JT-60U W-shaped divertor, J. Nucl. Mater. **313-316** (2003) 514.

[20] GOTOH, Y., et al., Analyses of erosion and re-deposition layers on graphite tiles used in the W-shaped divertor region of JT-60U, J. Nucl. Mater. **313-316** (2003) 370.

[21] TANABE, T., et al., Tritium Distribution on Plasma Facing Graphite Tiles of JT-60U, 19th IAEA Fusion Energy Conference, (Lyon, France, 2002) Ex/P2-11.

[22] OYA, Y., et al., Analyses of hydrogen isotope distributions in the outer target tile used in the W-shaped divertor of JT-60U, Physica Scripta **T108** (2004) 57.

[23] NAKAMURA, H., et al., Application of glow discharges for tritium removal from JT-60U vacuum vessel, Fusion Eng. Des. **70** (2004)163.

[24] MASAKI, M., et al., In-out asymmetry of low-Z impurity deposition on the JT-60U divertor tiles, J. Nucl. Mater. **329-333** (2004) 845.

[25] HIROHATA, Y., et al., Depth profile and retention of hydrogen isotopes in graphite tiles used in the W-shaped divertor of JT-60U, J. Nucl. Mater. **329-333** (2004) 785.

[26] SUGIYAMA, K., et al., Tritium profile in plasma-facing components following D-D operation, J. Nucl. Mater. **329-333** (2004) 874.

[27] MORIMOTO, Y., et al., Correlation between hydrogen isotope profiles and surface structure of divertor tiles in JT-60U, J. Nucl. Mater. **329-333** (2004) 894.

[28] MASAKI, K., et al., Retention characteristics of hydrogen isotopes in JT-60U, J. Nucl. Mater. **337-339** (2005) 553.

[29] HIROHATA, Y., et al., Hydrogen retention in divertor tiles used in JT-60 for hydrogen discharge period, J. Nucl. Mater. **337-339** (2005) 609.

[30] GOTOH, Y., et al., Transmission electron microscopy of redeposition layers on graphite tiles used for open divertor armor of JT-60, J. Nucl. Mater. **329-333** (2004) 840.

[31] SHARPE, J., HUMRICKHOUSE, P.W., SKINNER, C.H., Characterization of dust collected from NSTX and JT-60U, J. Nucl. Mater. **337-339** (2005) 1000.

[32] HIROHATA, Y., et al., Retention of hydrogen isotopes in divertor tiles used in JT-60U, Fusion Sci. Technol. **48** (2005) 557.

[33] ISOBE, K., et al., Tritium release behavior from JT-60U vacuum vessel during air exposure phase and wall conditioning phase, Fusion Sci. Technol. **48** (2005) 302.

[34] TAKEISHI, T., KATAYAMA, K., NISHIKAWA, M., MIYA, M., MASAKI, K., Recovery of retained tritium from graphite tile of JT-60U, Fusion Sci. Technol. **48** (2005) 561.

[35] KATAYAMA, K., et al., Release behavior of hydrogen isotopes from JT-60U graphite tiles, Fusion Sci. Technol. **48** (2005) 565.

[36] OYA, Y., et al., Hydrogen isotope distributions and retentions in the inner divertor tile of JT-60U, Fusion Eng. Des. **75-79** (2005) 945.

[37] TANABE, T., et al., Retention of hydrogen isotopes (H, D, T) and carbon erosion/deposition in JT-60U, 20th IAEA Fusion Energy Conference (Vilamoura, Portugal, November 2004), EX/P5-32, 1-6.

[38] HAYASHI, T., et al., Deuterium depth profiling in JT-60U W-shaped divertor tiles by nuclear reaction analysis, J. Nucl. Mater. **349** (2006) 6.

[39] ISHIMOTO, Y., et al., Thermal properties of redeposition layers in the JT-60U divertor region, J. Nucl. Mater. **350** (2006) 301-309.

[40] ISHIMOTO, Y., et al., J. Nucl. Mater., submitted.

[41] SUGIYAMA, K., TANABE, T., MASAKI, K., MIYA, N., Tritium distribution measurement of the tile gap of JT-60U, J. Nucl. Mater. **367-370** (2007) 1248.

[42] HIROHATA, Y., et al., Distribution of hydrogen isotopes retained in the divertor tiles used in JT-60U, J. Nucl. Mater. **367-370** (2007) 1260.

[43] GOTOH, Y., et al., Long-term erosion and re-deposition of carbon in the divertor region of JT-60U, J. Nucl. Mater. **357** (2006) 138.

[44] SHIBAHARA, T., et al., Hydrogen isotope retention of JT-60U W-shaped divertor tiles exposed to DD discharges, J. Nucl. Mater. **357** (2006) 115.

[45] SHIBAHARA, T., et al., Hydrogen retention of JT-60 open divertor tiles exposed to HH discharges, Nucl. Fusion **46** (2006) 841.
[46] HOSOGANE, N., et al., A compact W-shaped pumped divertor concept for JT-60U, Proc. 16th Int. Conf. Fusion Energy (Montreal, Canada,1996), Vol. 3, p. 555.
[47] OIKAWA, A., et al., Tritium experience in JT-60 DD plasma operation, Fusion Sci. Technol. **41** (2002) 612.
[48] OIKAWA, A., private communication.
[49] TOBITA, K., et al., Ripple induced fast ion loss and related effects in JT-60U, Nucl. Fusion **35** (1995) 1585.
[50] TOBITA, K., et al., First wall issues related with energetic particle deposition in a tokamak fusion power reactor, Fusion Eng. Des. **65** (2003) 561.
[51] MATTHEWS, G.F., Material migration in divertor tokamaks, J. Nucl. Mater. **337-339** (2005) 1.
[52] PEACOCK, A.T., et al., Dust and flakes in the JET MkIIa divertor, analysis and results, J. Nucl. Mater. **266-269** (1999) 423.
[53] TANABE, T., et al., Tritium retention of plasma facing components in tokamaks, J. Nucl. Mater. **313-316** (2003) 478.
[54] SUGIYAMA, K., et al., Tritium distribution on the surface of plasma facing carbon tiles used in JET, J. Nucl. Mater. **313-316** (2003) 507.
[55] TANABE, T., et al., Comparison of tritium retention and carbon deposition in JET and JT-60U, J. Nucl. Mater. **345** (2005) 89.
[56] TANABE, T., et al., Tritium retention in the gap between the plasma-facing carbon tiles used in D-T discharge phase in JET and TFTR, Fusion Science and Technol. **48** (2005) 577.
[57] SUGIYAMA, K., et al., Detailed tritium distribution on the JET MK IIA divertor tiles, Fusion Science and Technol. **48** (2005) 573.
[58] PENZHORN, R.D., et al., Tritium in plasma facing components, Fusion Eng. Des. **56-57** (2001) 105.
[59] ESSER, H.G., et al., Effect of plasma configuration on carbon migration measured in the inner divertor of JET using quartz microbalance, J. Nucl. Mater. **337-339** (2005) 84.
[60] ALTMANN, H., et al., "Design of the Mark II Gas Box divertor - a new design concept", Proceedings of the 19th Symposium on Fusion Technology (SOFT), Lisbon, 16–20 September 1996, North Holland, Amsterdam (1997) Vol. 1, p. 483.
[61] TAKENAGA, H., et al., Study of global wall saturation mechanisms in long-pulse ELMy H-mode discharges on JT-60U, Nucl. Fusion **46** (2006) S39.
[62] TANABE, T., et al., Tritium removal by isotopic exchange, J. Nucl. Mater. **390-391** (2009) 705.
[63] GRISOLIA, C., Plasma wall interaction during long pulse operation in Tore Supra, J. Nucl. Mater. **266-269** (1999) 146.
[64] SUGIYAMA, K., TANABE, T., SKINNER, C.H., GENTILE, C.A., Measurement of tritium surface distribution on TFTR bumper limiter tiles, Physica Scripta **T108** (2004) 68.

IAEA
International Atomic Energy Agency

Where to order IAEA publications

In the following countries IAEA publications may be purchased from the sources listed below, or from major local booksellers. Payment may be made in local currency or with UNESCO coupons.

AUSTRALIA
DA Information Services, 648 Whitehorse Road, MITCHAM 3132
Telephone: +61 3 9210 7777 • Fax: +61 3 9210 7788
Email: service@dadirect.com.au • Web site: http://www.dadirect.com.au

BELGIUM
Jean de Lannoy, avenue du Roi 202, B-1190 Brussels
Telephone: +32 2 538 43 08 • Fax: +32 2 538 08 41
Email: jean.de.lannoy@infoboard.be • Web site: http://www.jean-de-lannoy.be

CANADA
Bernan Associates, 4501 Forbes Blvd, Suite 200, Lanham, MD 20706-4346, USA
Telephone: 1-800-865-3457 • Fax: 1-800-865-3450
Email: customercare@bernan.com • Web site: http://www.bernan.com

Renouf Publishing Company Ltd., 1-5369 Canotek Rd., Ottawa, Ontario, K1J 9J3
Telephone: +613 745 2665 • Fax: +613 745 7660
Email: order.dept@renoufbooks.com • Web site: http://www.renoufbooks.com

CHINA
IAEA Publications in Chinese: China Nuclear Energy Industry Corporation, Translation Section, P.O. Box 2103, Beijing

CZECH REPUBLIC
Suweco CZ, S.R.O., Klecakova 347, 180 21 Praha 9
Telephone: +420 26603 5364 • Fax: +420 28482 1646
Email: nakup@suweco.cz • Web site: http://www.suweco.cz

FINLAND
Akateeminen Kirjakauppa, PO BOX 128 (Keskuskatu 1), FIN-00101 Helsinki
Telephone: +358 9 121 41 • Fax: +358 9 121 4450
Email: akatilaus@akateeminen.com • Web site: http://www.akateeminen.com

FRANCE
Form-Edit, 5, rue Janssen, P.O. Box 25, F-75921 Paris Cedex 19
Telephone: +33 1 42 01 49 49 • Fax: +33 1 42 01 90 90
Email: formedit@formedit.fr • Web site: http://www. formedit.fr

Lavoisier SAS, 145 rue de Provigny, 94236 Cachan Cedex
Telephone: + 33 1 47 40 67 02 • Fax +33 1 47 40 67 02
Email: romuald.verrier@lavoisier.fr • Web site: http://www.lavoisier.fr

GERMANY
UNO-Verlag, Vertriebs- und Verlags GmbH, Am Hofgarten 10, D-53113 Bonn
Telephone: + 49 228 94 90 20 • Fax: +49 228 94 90 20 or +49 228 94 90 222
Email: bestellung@uno-verlag.de • Web site: http://www.uno-verlag.de

HUNGARY
Librotrade Ltd., Book Import, P.O. Box 126, H-1656 Budapest
Telephone: +36 1 257 7777 • Fax: +36 1 257 7472 • Email: books@librotrade.hu

INDIA
Allied Publishers Group, 1st Floor, Dubash House, 15, J. N. Heredia Marg, Ballard Estate, Mumbai 400 001,
Telephone: +91 22 22617926/27 • Fax: +91 22 22617928
Email: alliedpl@vsnl.com • Web site: http://www.alliedpublishers.com

Bookwell, 2/72, Nirankari Colony, Delhi 110009
Telephone: +91 11 23268786, +91 11 23257264 • Fax: +91 11 23281315
Email: bookwell@vsnl.net

ITALY
Libreria Scientifica Dott. Lucio di Biasio “AEIOU”, Via Coronelli 6, I-20146 Milan
Telephone: +39 02 48 95 45 52 or 48 95 45 62 • Fax: +39 02 48 95 45 48
Email: info@libreriaaeiou.eu • Website: www.libreriaaeiou.eu

JAPAN
Maruzen Company, Ltd., 13-6 Nihonbashi, 3 chome, Chuo-ku, Tokyo 103-0027
Telephone: +81 3 3275 8582 • Fax: +81 3 3275 9072
Email: journal@maruzen.co.jp • Web site: http://www.maruzen.co.jp

REPUBLIC OF KOREA
KINS Inc., Information Business Dept. Samho Bldg. 2nd Floor, 275-1 Yang Jae-dong SeoCho-G, Seoul 137-130
Telephone: +02 589 1740 • Fax: +02 589 1746 • Web site: http://www.kins.re.kr

NETHERLANDS
De Lindeboom Internationale Publicaties B.V., M.A. de Ruyterstraat 20A, NL-7482 BZ Haaksbergen
Telephone: +31 (0) 53 5740004 • Fax: +31 (0) 53 5729296
Email: books@delindeboom.com • Web site: http://www.delindeboom.com

Martinus Nijhoff International, Koraalrood 50, P.O. Box 1853, 2700 CZ Zoetermeer
Telephone: +31 793 684 400 • Fax: +31 793 615 698
Email: info@nijhoff.nl • Web site: http://www.nijhoff.nl

Swets and Zeitlinger b.v., P.O. Box 830, 2160 SZ Lisse
Telephone: +31 252 435 111 • Fax: +31 252 415 888
Email: infoho@swets.nl • Web site: http://www.swets.nl

NEW ZEALAND
DA Information Services, 648 Whitehorse Road, MITCHAM 3132, Australia
Telephone: +61 3 9210 7777 • Fax: +61 3 9210 7788
Email: service@dadirect.com.au • Web site: http://www.dadirect.com.au

SLOVENIA
Cankarjeva Zalozba d.d., Kopitarjeva 2, SI-1512 Ljubljana
Telephone: +386 1 432 31 44 • Fax: +386 1 230 14 35
Email: import.books@cankarjeva-z.si • Web site: http://www.cankarjeva-z.si/uvoz

SPAIN
Díaz de Santos, S.A., c/ Juan Bravo, 3A, E-28006 Madrid
Telephone: +34 91 781 94 80 • Fax: +34 91 575 55 63
Email: compras@diazdesantos.es, carmela@diazdesantos.es, barcelona@diazdesantos.es, julio@diazdesantos.es
Web site: http://www.diazdesantos.es

UNITED KINGDOM
The Stationery Office Ltd, International Sales Agency, PO Box 29, Norwich, NR3 1 GN
Telephone (orders): +44 870 600 5552 • (enquiries): +44 207 873 8372 • Fax: +44 207 873 8203
Email (orders): book.orders@tso.co.uk • (enquiries): book.enquiries@tso.co.uk • Web site: http://www.tso.co.uk

On-line orders
DELTA Int. Book Wholesalers Ltd., 39 Alexandra Road, Addlestone, Surrey, KT15 2PQ
Email: info@profbooks.com • Web site: http://www.profbooks.com

Books on the Environment
Earthprint Ltd., P.O. Box 119, Stevenage SG1 4TP
Telephone: +44 1438748111 • Fax: +44 1438748844
Email: orders@earthprint.com • Web site: http://www.earthprint.com

UNITED NATIONS
Dept. I004, Room DC2-0853, First Avenue at 46th Street, New York, N.Y. 10017, USA
(UN) Telephone: +800 253-9646 or +212 963-8302 • Fax: +212 963-3489
Email: publications@un.org • Web site: http://www.un.org

UNITED STATES OF AMERICA
Bernan Associates, 4501 Forbes Blvd., Suite 200, Lanham, MD 20706-4346
Telephone: 1-800-865-3457 • Fax: 1-800-865-3450
Email: customercare@bernan.com · Web site: http://www.bernan.com

Renouf Publishing Company Ltd., 812 Proctor Ave., Ogdensburg, NY, 13669
Telephone: +888 551 7470 (toll-free) • Fax: +888 568 8546 (toll-free)
Email: order.dept@renoufbooks.com • Web site: http://www.renoufbooks.com

Orders and requests for information may also be addressed directly to:

Marketing and Sales Unit, International Atomic Energy Agency
Vienna International Centre, PO Box 100, 1400 Vienna, Austria
Telephone: +43 1 2600 22529 (or 22530) • Fax: +43 1 2600 29302
Email: sales.publications@iaea.org • Web site: http://www.iaea.org/books

ISBN 978–92–0–131410–9
ISSN 1018–5577